Dipl.-Ing. Alexander Volk, BSc

Nanocluster and Nanowire Growth in Superfluid Helium Droplets

DOCTORAL THESIS

to achieve the university degree of

Doktor der technischen Wissenschaften

submitted to

Graz University of Technology

Supervisor

Univ.-Prof. Dipl.-Phys. Dr.rer.nat Wolfgang E. Ernst

Institute of Experimental Physics

Graz, January 2016

Für Valentina & Johannes

Study hard what interests you the most
in the most undisciplined, irreverent and
original manner possible.

Richard P. Feynman

Abstract

The helium droplet technique has been established as a powerful tool for the spectroscopic investigation of cold atoms, molecules and clusters during the past decades. Only recently it further evolved towards an instrument for the inert synthesis and soft surface deposition of nanoclusters and nanowires. Since then, the applicability of the technique to the tailored production of metallic nanostructures of various size and composition has been proven by several experiments. However, there has still been a considerable lack of knowledge on the details of the growth process, which starts with the incorporation of metal atoms into a single helium droplet and finally yields the nanoparticles.
The present work addresses this issue by comparison of nanoparticle morphologies obtained from highly resolved electron micrographs to theoretical models. It turns out that the growth process is influenced by the doping rates, with which metal atoms are added to the helium droplets, as well as by the droplet size. Small helium droplets favor the growth of one cluster by addition of single atoms. High doping rates and large helium droplets on the other hand, preferably lead to a multicenter growth scenario, where several clusters are formed simultaneously at different nucleation sites within one droplet and subsequently coagulate to the final nanostructures. In the presence of quantized vortices this leads to the directed growth of nanowires, which conserve the morphologies of the initial building blocks.
In the course of the conducted simulations, the dimer collision times of coinage metal atoms in helium droplets of various size are determined by molecular dynamics simulations combined with helium density functional theory. The obtained values enter a rate-based model describing the growth process in large helium droplets. Further, the universal validity of continuous nanowire growth is proven for the special case of silver, which formerly has been subject of controversy in the literature.

Kurzfassung

Die Heliumtröpfchenmethode hat sich in den letzten Jahrzehnten als mächtiges Werkzeug für die spektroskopische Untersuchung von kalten Atomen, Molekülen und Clustern etabliert. Erst kürzlich entwickelte sie sich zu einem Instrument für die inerte Synthese und sanfte Oberflächendeposition von Nanoclustern und Nanodrähten. Seither wurde die Anwendbarkeit der Methode auf die maßgeschneiderte Herstellung von metallischen Nanostrukturen unterschiedlicher Größe und Zusammensetzung in zahlreichen Experimenten nachgewiesen. Trotzdem blieben nicht zu vernachlässigende Defizite im Wissen um die Details des Wachstumsprozesses, welcher mit der Einlagerung von Metallatomen in ein einzelnes Heliumtröpfchen beginnt und schließlich zu den Nanopartikeln führt.
Die vorliegende Arbeit behandelt diesen Aspekt durch den Vergleich der aus hochauflösenden Elektronenmikroskopieaufnahmen erhaltenen Morphologien der Nanopartikel mit theoretischen Modellen. Es stellt sich heraus, dass der Wachstumsprozess sowohl durch die Dotierraten, mit welchen Metallatome in die Heliumtröpfchen eingebracht werden, als auch durch die Tropfengröße beeinflusst wird. Kleine Heliumtröpfchen begünstigen das Wachsen eines einzigen Clusters durch Hinzugabe einzelner Atome. Hohe Dotierraten und große Heliumtröpfchen wiederum führen bevorzugt zum Szenario eines Vielzentrenwachstums, in welchem sich mehrere Cluster gleichzeitig an verschiedenen Nukleationszentren eines Tröpfchens formieren und anschließend zur schlussendlich vorliegenden Nanostruktur zusammenwachsen. In der Gegenwart von quantisierten Wirbeln führt dies zum gerichteten Wachstum von Nanodrähten, welche die Morphologien der ursprünglichen Bausteine enthalten.
Im Zuge der durchgeführten Simulationen werden die Dimer-Kollisionszeiten von Münzmetallatomen in Heliumtröpfchen verschiedener Größe durch Molekulardynamiksimulationen in Kombination mit Helium-Dichtefunktionaltheorie bestimmt. Die erhaltenen Werte gehen in ein raten-basiertes Modell ein, welches den Wachstumprozess in großen Heliumtröpfchen beschreibt. Weiters wird die universelle Gültigkeit eines kontinuierlichen Nanodrahtwachstums im speziellen Fall von Silber nachgewiesen, was bisher Thema von Kontroversen in der Literatur darstellte.

Articles related to this work

(1) "High resolution electron microscopy of Ag-clusters in crystalline and non-crystalline morphologies grown inside superfluid helium nanodroplets" by **Alexander Volk**, Philipp Thaler, Markus Koch, Evelin Fisslthaler, Werner Grogger and Wolfgang E. Ernst in *The Journal of Chemical Physics* **138**, 214312 (2013).

(2) "Thermal instabilities and Rayleigh breakup of ultrathin silver nanowires grown in helium nanodroplets" by **Alexander Volk**, Daniel Knez, Philipp Thaler, Andreas W. Hauser, Werner Grogger, Ferdinand Hofer and Wolfgang E. Ernst in *Physical Chemistry Chemical Physics* **17**, 24570-24575 (2015).

(3) "Atomic collisions in suprafluid helium-nanodroplets: timescales for metal-cluster formation derived from He-density functional theory" by Andreas W. Hauser, **Alexander Volk**, Philipp Thaler, and Wolfgang E. Ernst in *Physical Chemistry Chemical Physics* **17**, 10805-10812 (2015).

(4) "The impact of doping rates on the morphologies of silver and gold nanowires grown in helium nanodroplets" by **Alexander Volk**, Philipp Thaler, Daniel Knez, Andreas W. Hauser, Johannes Steuer, Werner Grogger, Ferdinand Hofer and Wolfgang E. Ernst in *Physical Chemistry Chemical Physics* **18**, 1451-1459 (2016).

(5) "Molecular dynamics simulation of the deposition process of cold Ag-clusters under different landing conditions" by Philipp Thaler, **Alexander Volk**, Martin Ratschek, Markus Koch and Wolfgang E. Ernst in *The Journal of Chemical Physics* **140**, 044326 (2014).

(6) "Formation of bimetallic core-shell nanowires along vortices in superfluid He nanodroplets" by Philipp Thaler, **Alexander Volk**, Florian Lackner, Johannes Steurer, Daniel Knez, Werner Grogger, Ferdinand Hofer and Wolfgang E. Ernst in *Physical Review B* **90**, 155442 (2014).

(7) "Synthesis of nanoparticles in helium droplets-A characterization comparing mass-spectra and electron microscopy data" by Philipp Thaler, **Alexander Volk**, Daniel Knez, Florian Lackner, Georg Haberfehlner, Johannes Steurer, Martin Schnedlitz and Wolfgang E. Ernst in *The Journal of Chemical Physics* **143**, 134201 (2015).

(8) "Formation of bimetallic clusters in superfluid helium nanodroplets analysed by atomic resolution electron tomography" by Georg Haberfehlner, Philipp Thaler, Daniel Knez, **Alexander Volk**, Ferdinand Hofer, Wolfgang E. Ernst and Gerald Kothleitner in *Nature Communications* **6**, 8779 (2015).

Notes: The articles (1)-(4) are reprinted as part of this work in chapters 4-7.

AFFIDAVIT

I declare that I have authored this thesis independently, that I have not used other than the declared sources/resources, and that I have explicitly indicated all material which has been quoted either literally or by content from the sources used. The text document uploaded to TUGRAZonline is identical to the present doctoral thesis.

Date

Signature

Contents

List of Figures

List of Tables

1 Introduction

The synthesis and subsequent surface deposition of nanoparticles inside of helium droplets (He_N) has been proposed for the first time in 2007.[1] Since then, the technique has experienced increasing interest. Although probably not suited for the production of industrial quantities, He_N exhibit unique properties which are out of reach for most other nanoparticle production routes.

The inert and cryogenic environment given by the droplets allows for sequential doping with foreign species, which subsequently coagulate into nanoparticles. In absence of any chemical agent, template, or electric field, this enables the tailored production of pristine nanoparticles and conservation of the initial compound purities. It is well known that at the very nanoscale, single foreign atoms or molecules can alter the properties of such particles dramatically. Therefore, the He_N technique is especially favorable in all cases where the material properties of nanoparticles should be investigated without any influences from chemical residues. Another peculiarity of the method is the possibility of using virtually any material combination in the nanoparticle synthesis process. Together with a sequential pickup scheme, this could enable the building of *e.g.* core-shell structures of exotic composition. In recent works, the attractive forces of vortices in large He_N have been exploited for the directed growth of nanowires, making the synthesis process even more versatile.

However, although there have been numerous experimental studies exploiting the He_N technique for synthesis and surface deposition of nanoparticles[2–7] and nanowires[8–10] up to now, the growth process of these structures inside the droplets has not been well understood in many cases. When moving to the production of more elaborate compositions, the increasing complexity of the synthesis process makes control over the particle growth process indispensable. The present thesis and related articles[11–18] can be seen as the first step towards closing this gap.

1.1 Organization of this Thesis

The present work has cumulative character. Chapters 1–3 give the reader a basic overview of the used techniques and should serve as an introduction to the topics covered in the following chapters. Chapters 4–7 are reprinted articles, which are published in peer-reviewed journals and represent the scientific results of this thesis. The contributions of all co-authors to these publications are disclosed at the beginning of the respective chapters. Finally, chapter 8 summarizes the novel findings of this work.
A more detailed description of the laboratory infrastructure and the experimental setup, both of which were designed and assembled in the course of this thesis, can be found in chapter 10. This manual has been written to treat technical aspects in greater detail and can be seen as a self-contained document.

1.2 The helium droplet system

Of the two stable helium (He) isotopes ^{3}He and ^{4}He, only the latter is of importance in this work. In the following, "He" and "^{4}He" are used interchangeably, unless otherwise stated.
Since its discovery in 1868 by Pierre J. C. Janssen, helium has repeatedly proven its extraordinary status among the elements. Although relatively rare in the earth's atmosphere ($\approx$ 5 ppm), He is the second most abundant element in the universe. The diatomic $^4He_2$ molecule exhibits only one bound state with an approximate binding energy of 1.176 mK and a calculated mean internuclear distance of $\approx$ 54.6 Å.[19] These numbers are in good agreement with experimental findings,[20] which makes $^4He_2$ both, the largest and weakest bound dimer known.[19]
In its liquid state, He exhibits the lowest boiling point of all liquids at $\approx$ 4.2 K and does not turn solid at atmospheric pressure for temperatures approaching 0 K.[19] Below 2.18 K, helium undergoes a phase transition to the so-called He II phase,[21] in which it is superfluid as discovered by Pyotr L. Kapitza in 1938.[22] Vanishingly small viscosity and extraordinary high heat conductivity,[23] are only two examples of the unusual properties of He II.
In 1961, Becker *et al.* produced the first He droplet beam in a free jet expansion.[24] As determined from rotationally resolved spectra of immersed SF_6 molecules,[25] the droplets cool to a temperature of 0.37 K in vacuum *via* the evaporation of surface atoms. Theoretical calculations further revealed that these temperatures are reached within times shorter than 1 ms,[21,26] which is less than the He_N flight-time in a typical droplet beam apparatus. At these low temperatures, He_N adopt the superfluid phase for $N \gtrsim 60$ as shown experimentally.[27]
The capability of He_N to pick up foreign species was demonstrated by Gough *et al.* in 1985.[28] It turns out that helium droplets pick up literally any species at collision with

the pickup cross-section equaling the geometrical cross section of the droplet. Nearly all atomic dopant species are immersed in the droplet volume, except hydrogen, the alkali metals and some of the alkaline earth elements, which are heliophobic and reside in a dimple on the droplet surface.[21,29,30] A general prediction whether dopants exhibit heliophilic or heliophobic behaviour can be obtained by evaluation of the so-called Ancilotto parameter λ.[31] This parameter is given by the ratio between the energy gain upon solvation of the dopant in the droplet and the energy cost caused by the creation of the associated bubble in the helium. Full submersion is predicted for $\lambda > 1.9$, while heliophobic behaviour can be expected for $\lambda < 1.9$.[31] The He_N confinement potential for heliophilic dopants is very shallow inside the droplet volume (see *e.g.* Fig. 6.2), which allows for free dopant motion below the Landau velocity.[32]
Nowadays, the use of He_N-beams for pickup and subsequent investigation of atoms, molecules and small clusters is well established in spectroscopy.[21,29,33,34] Dopants embedded in He_N are efficiently cooled to the droplet temperature, while otherwise remaining rather undisturbed. The evaporative He-loss associated with the dissipation of the energy introduced by the dopants, is approximately 1600 atoms per 1 eV.[21] This sets a natural size limit for nanoparticles synthesized in He_N. The recent advent of a new generation of closed-cycle refrigerators allows for a very effective cooling of the He nozzle, which enables the production of larger sized He_N (see Sec.1.2.1). This has triggered the exploitation of the He droplets' extraordinary environment for nanoparticle production.

> **Remark:** Although helium droplets are strictly speaking clusters of He atoms, they are entitled as "droplets" throughout this work. This should not only highlight their super(-fluid) state, but also enables a linguistic differentiation between He_N and the embedded nano-clusters.

1.2.1 Creation of the He-droplet beam

Usually, He_N-beams are produced by expanding He gas of high purity through a small orifice into a vacuum region at cryogenic temperatures (for more details on the experimental realization refer to Chap. 2.1). Depending on the nozzle temperature T_0 and the applied He-stagnation pressure p_0, a wide range of droplet sizes is accessible. Fig. 1.1 illustrates how the mean number $\bar{N}$ of He-atoms in a droplet depends on the nozzle conditions. It is evident that larger droplet sizes, as needed for nanoparticle production, can only be obtained by lowering the nozzle temperature.
These temperature changes also affect the type of droplet formation. As indicated in Fig. 1.1, droplet growth is determined by atomic collisions in an adiabatic gas expansion for $T_0 \gtrsim 10\,\mathrm{K}$. At temperatures below $\approx 4\,\mathrm{K}$, droplet formation is caused by the so-called Rayleigh breakup of a liquid He stream leaving the nozzle. Intermediate nozzle

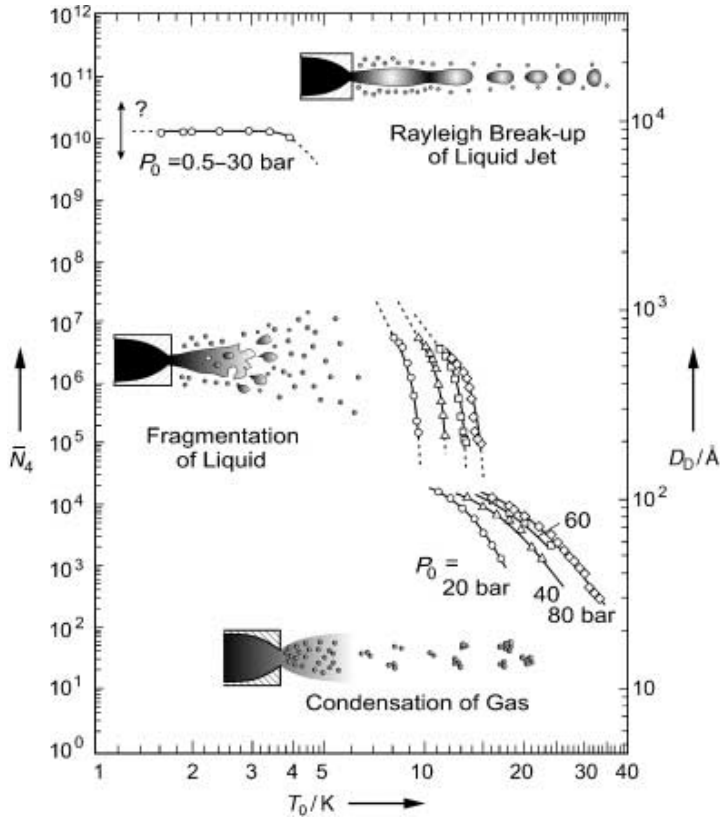

Figure 1.1: Dependence of the He_N size $\bar{N}$ on stagnation pressure p_0 and nozzle temperature T_0. Different types of droplet formation are indicated at the respective temperatures. This graph is reprinted with permission from ref. 21, Copyright (c) 2004 Wiley-VCH Verlag GmbH & Co. KGaA.

temperatures result in droplet formation *via* cavitational breakup of liquid He, induced by enclosed portions of the gaseous phase.[21]
It seems as if the type of droplet formation can influence the obtained He_N system, as shown in the following section.

1.2.2 Quantized vortices in helium droplets

The vanishing viscosity in He II prohibits the transformation of angular momentum, which is transferred to the fluid, into solid body rotation. Instead, angular momentum conservation is assured by the generation of vortices in the fluid. A detailed mathematical treatment of vortices in He II can be found in ref. 35. The most important findings are summarized in the following.
It turns out that vortices can only be created or annihilated at the fluid boundary and that their ends can only be located perpendicular to the fluid surface boundary. In case of a superfluid, vortices are quantized and can carry one quantum of circulation κ each. Vortices carrying $2 \times \kappa$ are energetically unfavorable to two vortices carrying one quantum, *i.e.* the transmission of large angular momenta to the fluid leads to the formation of multiple vortices ordered in a hexagonal array. Foreign species immersed in the superfluid are attracted and eventually captured by the vortex cores due to a surrounding pressure gradient.[35]
Experimentally, these properties of quantized vortices have been exploited for their detection by Williams *et al.* in 1974.[36] In the respective work, electrons were injected into He II in a rotating bucket experiment. The electrons were captured by the vortex cores. As their motion is not suppressed along the vortex cores, and the cores terminate on the fluid surface, electrons could be detected on a fluorescence screen above the He II surface. At the position of vortex cores, the amount of electrons leaving the superfluid was considerably higher, leading to bright spots on the screen. At increasing rotational velocity of the bucket, the number of spots rose in discrete manner, in agreement with the quantized nature of the vortices. The first observation of vortex lattices was achieved by Yarmchuk *et al.* in 1979, using a similar experimental setup.[37] It was not before 2006, when the first imaging of vortices in He II succeeded by using hydrogen tracer particles.[38] Lately, vortices in bulk He II have been extensively exploited for the production and characterization of nanowire bundles and meshes.[39–48]
In He_N the existence of vortices has been predicted theoretically (see *e.g.* ref. 49–52), but was not observed in the experiments until 2012.[8] In the respective work, He_N were doped with silver atoms and the droplet beam was subsequently terminated on a transmission electron microscopy (TEM) grid. The electron micrographs revealed silver clusters aligned along distinct lines, which was led back to the presence of growth guiding vortices. The reason for their late discovery most probably lies in the different type of droplet formation compared to previous experiments. In ref. 8, aligned silver struc-

tures in He_N were obtained at nozzle temperatures around 5-6 K, which is well within a temperature region where liquid helium is present already inside the nozzle in the expansion process (see Sec.1.2.1). Through evaluation of the corresponding Reynolds number, it can be shown that the flow of He through the nozzle is turbulent. Further, the interaction of the liquid with the nozzle wall can transfer an angular momentum to the droplets. This is different from the growth of droplets from atomic collisions in the gas phase as associated with experiments at higher nozzle temperatures and most probably facilitates the effective creation of vortices in He_N. The existence of vortex lattices in large He_N has been proven in X-ray diffraction experiments recently.[53]
Triggered by these findings, several experiments have exploited vortices in He_N as templates for the synthesis of nanowires lately.[4,9,14,16]

1.2.3 Deposition of nanoparticles under soft landing conditions

Surface deposition of the nanoparticles contained in He_N can be achieved by terminating the droplet beam on any suitable substrate. The helium droplets disintegrate upon impact,[54] thereby leaving the enclosed particles on the substrate surface.
Gentle deposition which does not lead to a breakup or to surface implantation of the nanoparticles, is termed as "soft landing" process. As a general rule of thumb, these conditions are likely fulfilled if the binding energy of the atoms making up the particle is larger than the kinetic energy per atom during the impact.[55] For metal dopants, He_N easily meets these criteria under the assumption that the droplet velocity of $\approx 200 - 400\,\mathrm{m/s}$ equals the deposition velocity of the enclosed clusters.[2] On the other hand, recent molecular dynamics (MD) simulations indicate that in case of an attractive interaction between the dopant species and the substrate, the nanoparticles may be reasonably accelerated towards the surface.[15] The influence of the helium surrounding the clusters was neglected in this work. Density functional theory (DFT) calculations in turn, suggest an additional cushioning of the nanoparticle impact by the He_N.[54,56]
Generally speaking, the full dynamics of the deposition process are far from understood. However, the finding of metastable cluster morphologies which have to be preserved from the synthesis process during surface deposition (see Chap. 4), as well as the preservation of nanowire structures upon impact (see Chap. 5 & 7), substantiate the assumption of a soft landing process for the He_N technique.

1.3 Investigated nanoparticles

Throughout the experimental work covered by this thesis, gold (Au) and silver (Ag) were used as dopants. Both metals exhibit good chemical inertness, can be brought into the gas phase easily by evaporation at moderate temperatures (see Sec. 2.2) and adopt the fcc lattice with nearly equal lattice constant in the bulk. Further, the binding energies

of atoms to the respective metal clusters Ag_n and Au_n are very similar.[57]
The properties mentioned above make Au and Ag not only easy to handle in the experiments, but ideal candidates for the exploration of fundamental ideas concerning the He_N technique, such as the synthesis of core-shell particles in a sequential pickup scheme. In general the properties of nanoparticles can remarkably deviate from those of their atomic constituents as well as from the behaviour in the bulk limit (see *e.g.* ref. 58–60). Therefore, it is opportune for investigations on a new synthesis process, to use systems which have already been studied intensively in the literature, as in the case of gold and silver nanoparticles.

Remark: While elongated nanostructures are termed as nanowires throughout this work, the term "cluster" is reserved for (quasi-) spherical arrangements of atoms. In cases where no distinction is necessary, both types of shape are referred to as "nanoparticles".

2 Experimental Methods

In the course of this thesis a new helium droplet apparatus has been set up, which is especially suited to synthesize nanoparticles. The layout of the apparatus is schematically depicted in Fig. 2.1. The generation of the He_N-beam, the doping of the droplets with foreign species and the analysis and/or deposition of the nanoparticles grown inside of the droplets take place in separate vacuum chambers. In the following we denote these vacuum chambers as source chamber (SC), pickup chamber (PC) and measurement chamber (MC), respectively. The setup is described in great detail in the attached manual (see Chap. 10) and further information can be found in the doctoral thesis of Philipp Thaler[61] as well as in the master's thesis of Johannes Steurer[62]. The following sections are intended as an introduction for the reader and should provide the basis for understanding the experimental methods used in Chap. 4, 5 & 7.
It should be noted, that the experiments described in Chap. 4 were carried out on a pre-existing apparatus. Detailed information about the corresponding setup can be found in the doctoral thesis of Markus Koch[63] and in ref. 64.

2.1 Droplet beam generation

The He_N-beam is generated *via* a supersonic jet expansion of highly purified (grade 6) and initially gaseous He through a cooled nozzle. The nozzle is realized by a platinum electron microscope aperture (Günther Frey GmbH) and exhibits a nominal orifice diameter of $5\,\mu$m. The nozzle plate is clamped to an oxygen-free copper block, which is cooled by a closed cycle refrigerator (Sumitomo RDK-408D2). As described in Sec. 1.2.1, the droplet size distribution can be shifted by tuning the nozzle conditions, *i.e.* the nozzle temperature T_0 and the applied He stagnation pressure p_0. In the course of all experiments discussed in this thesis, p_0 was held constant at 20 bar or at 50 bar and T_0 was varied between 11.4 K and 5.4 K. With these settings the desired mean droplet size can be selected in the range of $\bar{N} \approx 3 \times 10^3 - 1.7 \times 10^{10}$, corresponding to droplet diameters $\bar{d}_\mathrm{D} \approx 64 - 1100\,\mathrm{nm}$.
Temperature stabilization is achieved through counter heating of the copper block with an attached power resistor (Arcol HS15). The actual copper block temperature is measured with a silicon diode temperature sensor (Lake Shore Cryotronics Inc., model DT-670B1-BO) and taken as input parameter for a closed loop system. A commercial

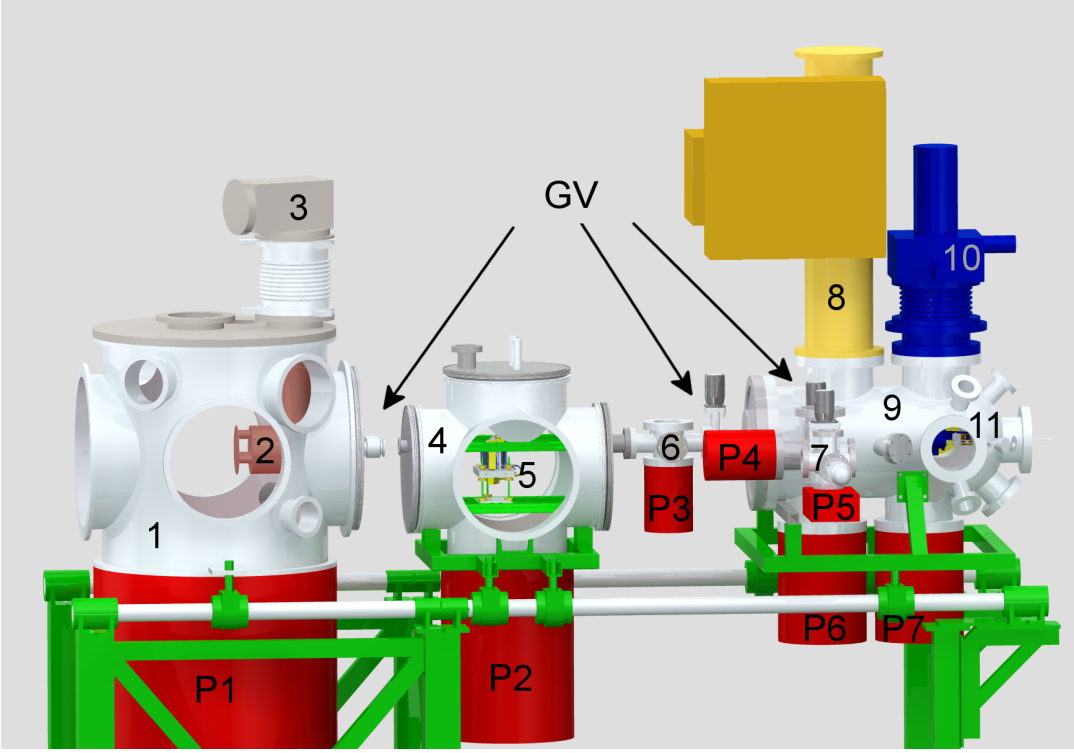

Figure 2.1: Schematic depiction of the He_N- beam apparatus. Source chamber (1) with visible radiation shield (2) of the nozzle and mounted coldhead (3); pickup chamber (4) with resistively heated pickup cell (5); chamber for differential pumping (6); measurement chamber (9) with attached vacuum transfer system (7), time of flight mass spectrometer (8) and manipulator (10) for deposition on various substrates. The holder for TEM grids (blue) and the crystal holder of a quartz crystal monitor are indicated in the region of surface deposition (11). The source chamber is pumped by an oil diffusion pump (P1), while the other chambers are pumped by turbo pumps (P2-P4 & P6-P7). The vacuum transfer system is equipped with an ion getter pump (P5). The chambers can be separated by several gate valves (GV).

controller (Eurotherm 3500) is used to evaluate the required heating current. With this setup the temperature can be held constant within $\pm 0.02\,\mathrm{K}$. Fig. 2.2 shows a photograph of the assembled nozzle setup without radiation shield. The alignment of the nozzle is described in the attached manual (Chap. 10).
After its creation, the He_N-beam passes a $400\,\mu\mathrm{m}$ skimmer into an adjacent vacuum chamber. Naturally, a large part of He atoms streaming out of the nozzle, will not pass

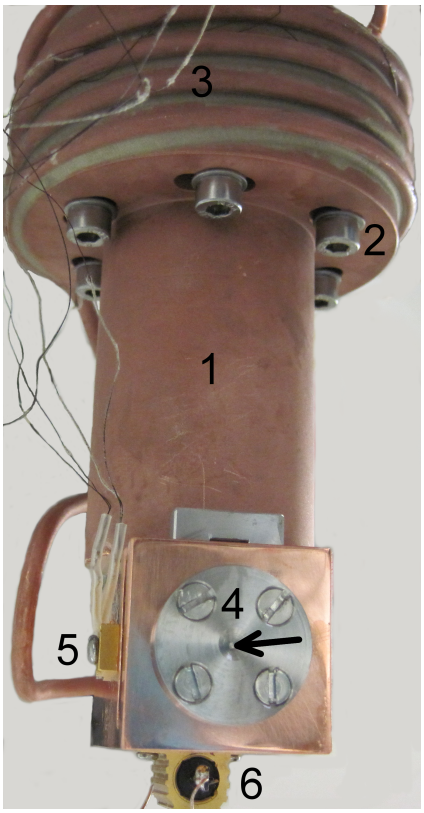

Figure 2.2: The nozzle setup consists of an oxygen-free copper block (1), which is clamped to the second stage of a closed cycle refrigerator (2). Gaseous helium is precooled in a copper tube (3), which is brazed to the copper block. The helium is pressed through an electron microscope aperture (marked by arrow), which is clamped against the copper block with a stainless steel disc (4). The temperature is measured with a silicon diode temperature sensor (5) and can be controlled *via* adaption of the heating current through a power resistor (6).

the skimmer and therefore contribute to the background pressure in the SC. Therefore, an oil diffusion pump with large throughput ($12\,000\,\mathrm{l/s}$) is used to ensure effective pumping and a vacuum pressure not higher than a few $10^{-4}\,\mathrm{mbars}$ at the largest gas loads.

2.2 Controlling of dopant pickup

In the second vacuum chamber (PC) the He droplets are doped with foreign species. For this purpose, it is necessary to create defined regions where the respective species are present in the gas phase, so that they can be picked up by passing He_N. These regions are called pickup cells. A complete overview of the different types of pickup cells available for the apparatus at the moment, can be found in Chap. 10.
For the experiments discussed in this thesis, only Ag or Au atoms are used as dopants. Fig. 2.3 shows the temperature dependence of the vapor pressure for the two metals. As a rule of thumb, noticeable pickup starts at $\approx 5 \times 10^{-5}$ mbar dopant vapor pressure for the smallest droplet sizes used. Resistively heated alumina crucibles (Ted Pella, Inc., Prod. No. 84-27) are used to heat the metals to the desired temperature. In practice it is inconvenient to control the temperature of the crucibles, mainly because the amount of evaporated dopant atoms depends on the filling level of the respective crucible and because small uncertainties in the temperature measurement may greatly influence the present vapor pressure.
A possibility to overcome this problems is to directly track the amount of dopants picked up by the He_N as described in a work of Loginov *et al.*.[2] This approach takes advantage of the fact that during every pickup event energy is transferred to the droplets by the dopants and subsequently dissipated by evaporative cooling. This leads to a shrinking of the droplets and to a reduced He flux into the adjacent measurement chamber. The disintegration of helium droplets upon surface collision leads to a rise of the helium background pressure p_{He} in the MC, which is monitored either with a quadrupole mass spectrometer (QMS, Balzers QMA200/QME200) or with an ionization pressure gauge (Leybold IM 220). To obtain the mean number of dopant atoms per He_N, it is necessary to monitor the relative change in p_{He}, *i.e.* the decrease in pressure for the doped droplet-beam compared to p_{He} obtained for the undoped beam. With increasing doping level, p_{He} in the MC decreases, as helium atoms are evaporated from the droplets already in the pickup chamber. Knowing the initial mean droplet size $\bar{N}$ for the given source conditions, it is then possible to calculate the mean number $\bar{N}_{\mathrm{evap}}$ of helium atoms evaporated per droplet upon doping *via*[2]

$$\bar{N}_{\mathrm{evap}} = \frac{p_{\mathrm{He,undoped}} - p_{\mathrm{He,doped}}}{p_{\mathrm{He,undoped}}} \times \bar{N} \tag{2.1}$$

The mean number of dopant $\bar{n}_X$ atoms per droplet is then given by

$$\bar{n}_X = \bar{N}_{\mathrm{evap}} \times \frac{E_{\mathrm{He}}}{E_X}. \tag{2.2}$$

$E_{\mathrm{He}} = 0.6\,\mathrm{meV}$ is the binding energy of one helium atom to the droplet and E_X is the energy transferred to the He droplet by one dopant of species X. In the case of atomic metal dopants, the kinetic energy stemming from the evaporation process is

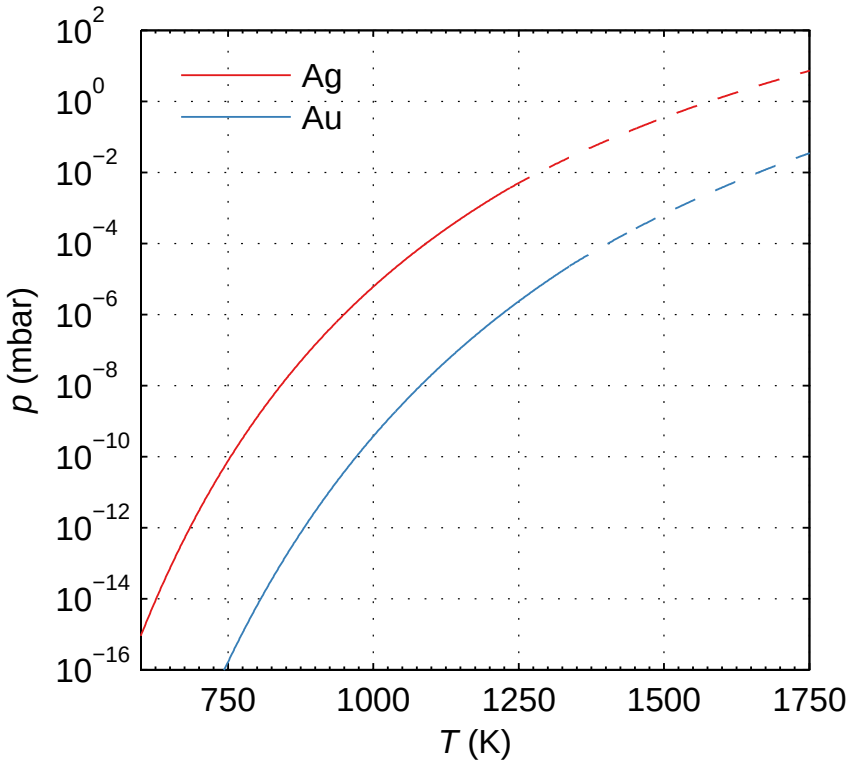

Figure 2.3: Temperature dependence of Ag and Au vapor pressures. Dashed lines indicate temperatures above the melting point of the respective metal. The pressures are calculated using the empirical formula $\log(p/\mathrm{Pa}) = 5.006 + A + BT^{-1} + C\log(\mathrm{T}) + DT^{-3}$ from ref. 65, with the tabulated empirical parameters A, B, C & D.

much smaller than the binding energy released upon cluster formation, so that E_X can be approximated by the latter.

2.3 Nanoparticle deposition and analysis

The present thesis is based on results obtained from the evaluation of deposited nanoclusters or nanowires. The used He_N-beam machine also comprises a time of flight mass spectrometer (TOFMS) for in-beam analysis. For more information on this topic, the reader is referred to the works of Johannes Steurer[62] and Philipp Thaler[61] as well as to ref. 18.
Surface deposition of the nanoparticles contained in He_N can be achieved by terminating the beam on any suitable substrate. For the experiments presented in this work, the nanoparticles are either deposited on gold-coated quartz crystals (Inficon, 64140-0930) for the measurement of deposition rates, or on amorphous carbon transmission electron microscopy (TEM) grids (Ted Pella, Inc., Prod. No. 01824) for subsequent TEM analysis.

2.3.1 Measuring deposition rates

Deposition rates of nanoparticles synthesized in He_N have been measured using a quartz crystal monitor (QCM, Inficon Qpod, S/N 1485). The measuring principle relies on a change in the eigenfrequency of a quartz crystal's shear vibration as a result of mass deposition on the crystal surface, as described by Sauerbrey.[66] In the used QCM, a 6 MHz gold-coated quartz crystal is the frequency determining element of a harmonic oscillator. The nanoparticles are deposited on the crystal by terminating the He_N on the surface and frequency changes or deposition rates can be directly monitored on a computer.
Fig. 2.4 exemplarily depicts the dependence of the deposited mass of Ag_n per area for different droplet sizes as obtained with the setup described in Chap. 4. The slopes in distinct time intervals correspond to the deposition rates. Different slopes result from a change in He_N size at constant dopant vapor pressure. Time intervals where deposition is achieved are highlighted in gray. It can be seen that the deposition has been interrupted several times, which has been achieved by closing the valves between source chamber and pickup chamber as well as between pickup chamber and measurement chamber. Due to the temperature dependence of the shear vibration eigenfrequency, temperature stabilization of the QCM to $\pm 0.02\,\mathrm{K}$ has been necessary for the reliable measurement of deposition rates as low as $10^{-5}\,\mu\mathrm{g\,cm^{-2}\,s^{-1}}$. The high reproducibility of lines with nearly zero slope for halted deposition as seen in Fig. 2.4 is a good indicator for the effective elimination of temperature influences.
During the time interval labeled "e.b." only the valve between the source chamber and

the pickup chamber has been closed and the valve between pickup chamber and measurement chamber was left open. The measured mass increase can be associated with a beam of silver atoms effusing out of the pickup cell, i.e. nanoparticle deposition is accompanied by the deposition of metal atoms.

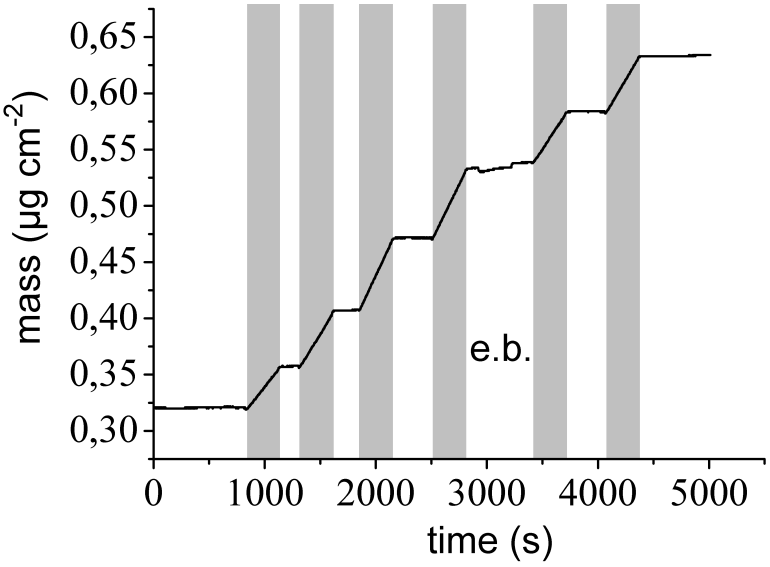

Figure 2.4: Deposited Ag_n mass per area over time for different He_N sizes. Time intervals highlighted in gray correspond to nanoparticle deposition. Different slopes/ deposition rates result from a change in He_N size, while keeping the dopant vapor pressure constant. The slope in the interval labeled "e.b." is determined by mass deposition *via* an effusive beam of Ag atoms.

2.3.2 Measuring particle sizes

The sizes of deposited nanoparticles can be obtained from the evaluation of TEM images. The image processing package Fiji[67] has been used for all image analysis in the course of this thesis. With this software, a threshold for gray scale values is set to distinguish between nanoparticles and background. Subsequently, a binary image with black nanoparticle areas and white background is generated.
Naturally, such a method is sensitive to illumination gradients, which have to be removed before setting the threshold. Fig. 2.5 shows the steps from the raw (Fig. 2.5 (a)) to the binary (Fig. 2.5 (c)) image. The illumination gradient is removed from Fig. 2.5 (a) to (b) by performing a fast Fourier transformation (FFT) of the image, cutting the low frequencies and subsequent execution of the inverse FFT. To exclude any alteration of the particle sizes due to the image manipulations, the binary and corresponding raw images are overlaid before starting the particle evaluation. Fiji is capable of directly

measuring properties related to particle shape and size (*e.g.* diameter, area, perimeter, circularity) from the scaled binary images. The obtained data is stored in a suitable file format and further evaluation is carried out in Matlab.
It is an important fact, that TEM micrographs are 2D projections of the 3D nanoparticles. It is therefore necessary to have some additional information for the determination

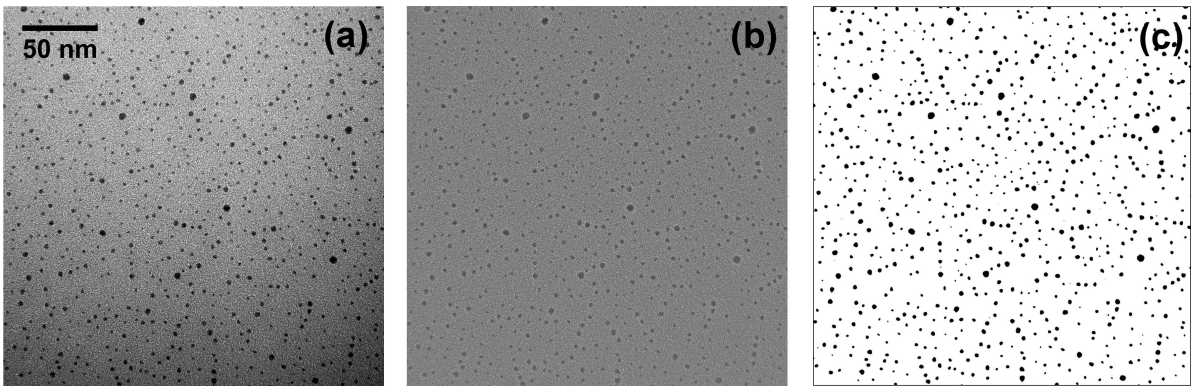

Figure 2.5: Image manipulation for particle size evaluation. Illumination gradients in the original image (a) are removed by FFT frequency splitting. Only the image containing the high frequencies (b) is used to generate a binary black and white image (c) by setting the corresponding gray value threshold in Fiji.

of the 3D shape. One possibility is to assume a certain shape of the particles (*e.g.* spheres) to calculate the deposited mass from the TEM image. Subsequently, the assumption is checked by comparison with the deposition rates which have been measured with the QCM. Another approach to overcome this problem is to record several TEM images while tilting the substrate with respect to the electron beam.[17] Both methods led to the insight that the deposited nanoparticles are only slightly flattened, meaning that it is reasonable to assume spherical cluster shape and cylindrical shape for nanowires. Therefore, in case of clusters, the diameters can be directly measured using Fiji. For nanowires it turned out to be best practice to first evaluate the perimeter and to additionally measure the length of the wire *via* a manually set path. The mean wire diameter is then calculated under the assumption of a cylindrical wire shape.

2.3.3 Determination of nanoparticle morphologies

The morphologies of deposited nanoparticles have been determined by evaluation of high resolution transmission electron microscopy (HRTEM) images. Contrast in HRTEM micrographs of crystalline samples is an interference phenomenon. The charge distributions of electrons and nuclei in a sample cause the crystal potential. Electrons passing the sample interact with this potential and experience an according phase shift. This phase

shift is more prominent for electrons which pass the sample near the nuclei of a crystal plane than for those which do not feel such a strong attractive potential. The transmitted electron waves interfere in the image plane of the TEM, which leads to contrast in the recorded images.[68]

This mechanism is different from our daily experience, where contrast emerges mainly from the different reflectance and absorbances of objects. In most cases it is therefore impossible to directly deduce the 3D morphology of the observed nanoparticles from the micrographs. This is especially true when the nanoparticles are not present in highly symmetric orientations with respect to the incoming electron beam. It is an established routine in the TEM community to use the so called multi slice method as a reverse engineering approach to solve this problem (see Chap. 9.6 of ref. 68). In this technique, a model structure is generated to calculate the expected TEM image. The model is cut into thin slices and successively, the interaction of the electron plane waves with the effective potential of every single slice is evaluated to obtain the total phase shift. Subsequently, the model structure is adapted until the calculated and the experimentally obtained images match.

Due to the nature of the deposition process, clusters produced with the He_N technique exhibit random orientations on the substrate. Only a few of the particles are oriented with an axis of high symmetry parallel to the incoming e^--beam. For a statistical evaluation of cluster morphologies as performed in Chap. 4, it is therefore important to also evaluate the morphologies of tilted clusters. This can only be achieved by comparison with calculated images like those provided by Koga *et al.*.[69] The authors of the respective study performed multi slice simulations for perfect icosahedral and decahedral Au clusters under different tilting angles and proved the validity of the obtained results by comparison with experimentally recorded HR-micrographs. The results of this work can also be applied for Ag clusters, as the lattice constant between Au and Ag differ by only 0.01 Å.[57] Of course the crystal potential is different for the two metals, however this does not affect the interference patterns itself but only contrast, *i.e.* the gray values of specific points of the clusters.

Fig. 2.6 exemplarily depicts two clusters with the same morphology, but different orientations towards the e^--beam. Their correct assignment is only possible by comparison with the simulated images of the respective morphologies under various tilting angles (Fig. 2.6 (c)). It can be seen that Fig. 2.6 (a) corresponds to "a" of Fig. 2.6 (c), while the pattern in Fig. 2.6 (b) matches the one in "f" of Fig. 2.6 (c).

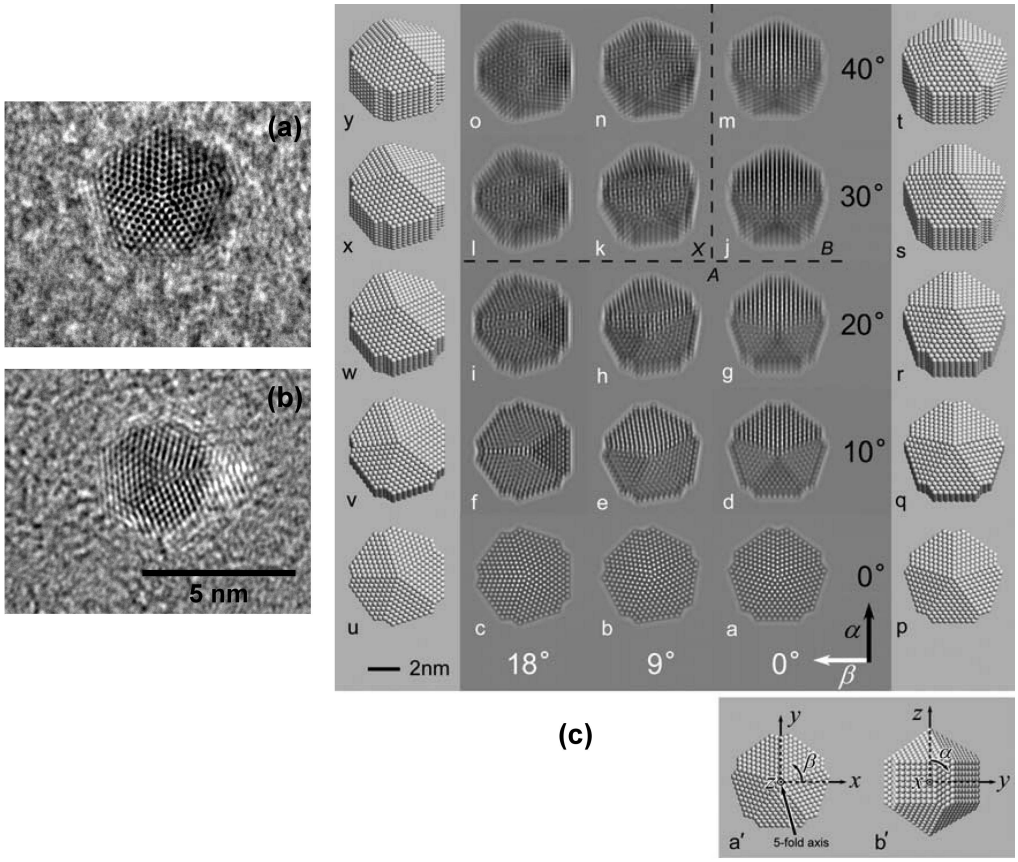

Figure 2.6: Morphology assignment of clusters with different orientations with respect to the TEM electron beam. Comparison with the results of multi slice simulations (c) shows, that both clusters in (a) and (b) are decahedra. The situation in (a) is equal to (c)-"a", while (b) agrees best with (c)-"f". Scale is the same for (a) and (b). (c) is reprinted from ref. 69 with permission from Elsevier.

3 Computational Methods

The following is a summary of the most important computer simulations conducted in the course of this thesis. It is intended to give a more detailed insight in the structure of the code and describes selected problems which arise during programming.

3.1 Breakup of deposited nanowires

The recurring observation of well aligned cluster segments instead of continuous nanowires in case of doping He_N with silver, has been explained in the course of this thesis.[12] The corresponding publication is reprinted in Chap. 5. It shows, that the observed chains of clusters are the result of a breakup of continuous nanowires after their deposition on a warm substrate. Due to a gradient in the chemical potential, silver atoms diffuse along the wire surface towards places of larger wire diameter. This surface self-diffusion process further constricts initially thin parts of the wire, which finally leads to the breakup. Due to a lack of 3D information in the experimentally recorded TEM images, the simulations are conducted in 2D. The behavior can be simulated in the framework of the Mullins equations,[70,71] as explained in Sec. 5.3. In this model, the gradient of the chemical potential is replaced by the surface curvature, so that the local transversal displacement z of the contour line is described by

$$\frac{\partial z}{\partial t} = B\frac{\partial^2 z}{\partial s^2} \tag{3.1}$$

with s the curvilinear abscissa. B absorbs several material constants (see Sec. 5.3). Since B only affects the size of a timestep it can be set to 1 in the simulations without qualitatively influencing the outcome.
The contour lines of observed nanowires are extracted from the TEM images using Fiji.[67] The result of the extraction is a set of N (x, y) coordinates which resemble the initial contour line. The resolution of details in the curvature of such a line is proportional to the point resolution of the initial image. All N coordinates are saved in a suitable file format and further calculations are conducted in Matlab.
The distance between the points (x_n, y_n) and (x_{n+1}, y_{n+1}) is denoted by Δ_n with $n = 1, 2, ...N$ and $\Delta_{N+1} = \Delta_1$. The curvature at point (x_n, y_n) can be approximated by[71]

$$K_n = \frac{2h}{\Delta_{n-1}\Delta_n}, \tag{3.2}$$

where h is the distance between (x_n, y_n) and $\overline{(x_{n-1}, y_{n-1})(x_{n+1}, y_{n+1})}$. The first and second derivatives of K_n can be calculated by

$$\frac{\partial K_n}{\partial s} = \frac{K_{n+1} - K_n}{\Delta_n}, \tag{3.3}$$

$$\frac{\partial^2 K_n}{\partial s^2} = 2\frac{\frac{\partial K_n}{\partial s} - \frac{\partial K_{n-1}}{\partial s}}{\Delta_{n-1} + \Delta_n}. \tag{3.4}$$

The displacement of (x_n, y_n) during one time-step of length τ, is calculated according to

$$h' = h + \tau \frac{\partial^2 K_n}{\partial s^2}. \tag{3.5}$$

The new position of (x_n, y_n) is then evaluated using h' and assuming equal distances to (x_{n-1}, y_{n-1}) and (x_{n+1}, y_{n+1}). The time dependent alteration of the contour line can then be calculated *via* the following scheme:

a) Load (x, y) coordinates of the initial contour line.

b) Determine the suitable length for τ.

c) Determine point indices for points lying opposite to each other on the contour line (*e.g.* (x_n, y_n) and (x_{n+i}, y_{n+i})).
→ Has to be done every k time-steps (k depending on τ).

d) Evaluate the second derivative of the curvature at each point of the contour line (see eqn. 3.2-3.4) and displace each point according to eqn. 3.5.

e) Check if any of the opposite lying line segments $\overline{(x_n, y_n)(x_{n\pm1}, y_{n\pm1})}$, $\overline{(x_{i+n}, y_{i+n})(x_{n+i\pm1}, y_{n+i\pm1})}$ cross.

IF $\begin{cases} NO & \rightarrow \text{go to c)} \\ YES & \rightarrow \text{split contour lines at point of intersection} \end{cases}$

In case of a split, all points from (x_1, y_1) to $(x_{\mathrm{intersec}}, y_{\mathrm{intersec}})$ are treated as one new contour line and all remaining points are combined to another new contour line. Subsequently, both new lines have to be propagated in time separately starting at b).
τ can be obtained from[71] $\tau \approx C\Delta_{\mathrm{m}}$ with Δ_{m} denoting the mean value over all Δ_{n}'s and C a constant for controlling the errors.
It turns out, that a common problem of this code are numerical instabilities after a breakup event, *i.e.* after a split of contour lines induced by their crossing. Due to constrictions of a contour in the vicinity of the crossing point, opposite lying points can exhibit much closer distances to each other than the mean distance Δ_{m}. As a result

of the split, two initially opposite lying points are assigned to the same newly created contour line as now neighboring points. It is evident from the equations above, that in these cases the local curvature changes dramatically. This results in a displacement h' of the concerned points, which is much larger than the mean displacements of the other points, so that the contour line starts to loose its shape in the respective region.
This problem can be overcome by adjusting the point density for the whole contour line by generating new points, so that the local Δ_{n} does not noticeably deviate from Δ_{m}. Of course, this leads to longer calculation times, so that it is desirable to continuously reduce the point density again during the subsequent steps of the simulation. This has to be done under simultaneous consideration of the numerical stability.

3.2 Timescales of atomic collisions

Atomic collisions are the starting point of cluster growth inside of He_N. Therefore, a profound knowledge of the timescales of these collisions is essential in order to model the formation of larger particles. The respective collision times for different dopant metal atoms can be obtained *via* the following calculation scheme:

a) Determine the dopant solvation energy in helium droplets of different size and the corresponding confinement potential for each dopant element as a function of radial distance from the droplet center *via* DFT.

b) Calculate the undisturbed dopant-dopant potential curves with methods of electronic structure theory (coupled cluster with single and double excitations plus perturbative triples [RHF-RCCSD(T)][72,73]).

c) Estimate the influence of He_N on the dopant-dopant potential *via* He-DFT.

d) Correct the dopant-dopant potential curves for dopants immersed in He_N using the results obtained in step c).

e) Perform MD simulations of the collision process using the corrected dopant-dopant potential curves and the confinement potentials given by the He_N.

The realization of the required calculations for the dopants Ag, Au and Cu is discussed in detail in ref. 13, which is reprinted in Chap. 6 of the present thesis.
It shows that the correction for the dopant-dopant potential curves, as derived in step d), are negligible in case of the strongly bound metals. For droplet sizes of up to $N = 10000$ the MD calculations are performed by exact evaluation of the He_N-dopant and dopant-dopant potentials during each time-step. However, in large He_N the dopants travel long distances without any noticeable influence of the short ranging inter-particle potential.

Therefore, the dopant-dopant interaction is only evaluated for the calculation of trajectories in cases where the distance between the two atoms is smaller than 30 Å. Further, the confinement potential given by the droplet noticeably differs from zero only in a relatively small spatial region at the droplet boundary ($\approx$ 15 Å), which allows for an additional speedup of the calculations by the assumption of simple hard wall reflections. The most crucial point of the MD calculations is to find an appropriate size for the simulation time-steps Δt . If the chosen Δt is too long, the interaction of the dopants with the hard-wall confinement potential cannot be described properly, which may alter the collision times noticeably. On the other hand, the calculations can easily become too time consuming in the case of short time-steps. $\Delta t = 0.1$ ps has turned out to be a good compromise between accuracy and computational costs.
The obtained results enter the model presented in Chap. 7, which is used to describe the growth process of larger nanoparticles within a droplet.

3.3 Simulation of cluster growth inside of helium nanodroplets

Due to the large number of atoms involved, the growth process of larger clusters or nanowires cannot be treated in the framework of molecular dynamics simulations. Instead, it is feasible to use a rate-based model, as described in Sec. 7.4. The corresponding algorithm is described in detail in Chap. 4.2 of ref. 61.
In brief, the rate for the addition of new atoms to the He_N is derived from the velocity of the droplet beam, the length of the pickup cells and the total amount of atoms picked up by one droplet in the experiment. Further, the rate of collisions between atoms or clusters inside a single droplet is derived from the work reprinted in Chap. 6, but corrected for evaporative droplet shrinking and decreasing particle velocities due to conservation of momentum during multiple collisions.
Every particle is given an individual timer based on these considerations. When a timer has expired, the corresponding particle merges with another particle. The new particle shape depends on the temperature increase of the initial particles, which is determined by the binding energy released during coalescence and the constant cooling rate r_c provided by the surrounding helium. Whenever the energy is sufficient to melt at least one of the involved collision partners, the resulting particle is assumed to have spherical shape. In the non-melting case, the two particles are treated as sticking together, but retain their initial shape. The diameter of this short wire-like segment is then determined by the mean diameter of the individual particles.
In ref. 17, this algorithm is used to determine the He_N-size at which the transition from single- to multi-core structures takes place during sequential pickup of silver and gold

atoms. In Chap. 7 of the present work, the simulation is adapted to yield information on the impact of the metal atom doping rate on the growth process of clusters and nanowires inside He_N of a given size. The experimentally observed nanowire diameter is determined by the particle size at which the last melting occurs upon coagulation. In other words, after a coagulation event which yields a large elongated particle, it is very improbable that such a particle melts again in a subsequent collision process, due to the unfavorable ratio between released binding energy and heat capacity. The capture of these elongated particles by a vortex and their further coagulation while being pinned to the vortex core, lead to nanowires with a thickness corresponding to the mean diameter of all these building blocks. In order to obtain comparability with the experiment, r_c is adjusted such as to obtain the same nanowire diameters in the simulations as observed in the TEM images. The decision for adjusting the cooling rate is based on the fact, that it is the system's physical quantity with the largest uncertainty. The finally chosen value is within the region provided by literature.
With these modifications it is now possible to track the evolution of the number of metal particles as well as their size distribution inside a single He_N of given size for different metal atom doping rates. This yields the sizes at which the particles finally "freeze" for a given doping rate, which can be used to explain the occurrence of certain nanowire morphologies as explained in Chap. 7.

3.4 Capture of clusters by vortices

Dopant particles are captured by quantized vortices in large He_N due to an attractive force which is induced by a pressure gradient around the vortex cores.[35] A valid far-field expression for this force acting on a spherical particle is given by[74–76]

$$F_{\mathrm{far}} \approx \left(\frac{r}{s}\right)^3 \frac{\rho_{\mathrm{s}}\kappa^2}{3\pi} \tag{3.6}$$

with r the particle radius, s the distance between particle and vortex core and ρ the density of He II. $\kappa = h/m_{\mathrm{He}}$ denotes the quantum of circulation, with h the Planck constant and m_{He} the atomic mass of He. Expressing the particle's mass by

$$m = \frac{4}{3} r^3 \pi \rho_{\mathrm{p}} \tag{3.7}$$

and using Newton's equation of motion, gives the size-independent acceleration a_{far} of a particle with density ρ_{p} towards the vortex core:

$$a_{\mathrm{far}} \approx \frac{1}{4}\frac{\rho_{\mathrm{s}}}{\rho_{\mathrm{p}}}\frac{\kappa^2}{\pi^2}\frac{1}{s^3}. \tag{3.8}$$

As a_{far} diverges for $s \to 0$, the near-field expression for the attractive force[74–76]

$$F_{\mathrm{near}} \approx \rho_{\mathrm{s}}\kappa^2 \log\left(\frac{r}{\zeta}\right) \tag{3.9}$$

is used to determine

$$a_{\mathrm{near}} \approx \frac{3}{4}\frac{\rho_{\mathrm{s}}}{\rho_{\mathrm{p}}}\frac{\kappa^2}{\pi}\frac{\log\left(\frac{r}{\zeta}\right)}{r^3} \tag{3.10}$$

where $\zeta \approx 1\,\text{Å}$ denotes the vortex core diameter.
In order to obtain the time t_{trap} it takes for a particle to get trapped by a vortex, the mean distance between particle and vortex core for a given He_N size is calculated. Subsequently the particle's equation of motion is solved using the Velocity-Verlet algorithm[77] under the assumption of a continuous connection of F_{far} and F_{near}, which equals the constraint

$$a = \begin{cases} a_{\mathrm{far}} & \text{for } F_{\mathrm{far}} < F_{\mathrm{near}} \\ a_{\mathrm{near}} & \text{for } F_{\mathrm{far}} > F_{\mathrm{near}} \end{cases} \tag{3.11}$$

Under the assumptions made above, F_{far} determines the particle's acceleration down to particle-vortex distances smaller than 3 nm for the largest particle sizes observed in our experiments, so that the influence of F_{near} on t_{trap} turns out to be negligible. Results for t_{trap} are presented in Chap. 7.

4 Morphologies of small silver clusters grown in helium nanodroplets

The following corresponds to the publication
"High resolution electron microscopy of Ag-clusters in crystalline and non-crystalline morphologies grown inside superfluid helium nanodroplets" by **Alexander Volk**, Philipp Thaler, Markus Koch, Evelin Fisslthaler, Werner Grogger and Wolfgang E. Ernst in *The Journal of Chemical Physics* **138**, 214312 (2013).

The author of this thesis was responsible for

- the design and execution of the experiments,
- the evaluation of the obtained electron micrographs,
- the literature research and interpretation of the obtained data,
- and the authorship of the manuscript.

The contributions of the co-authors are listed below:

- Philipp Thaler: assistance in the experiments and in the evaluation of electron micrographs
- Markus Koch: assistance in the experiments, manuscript editing
- Evelin Fisslthaler: recording of electron micrographs
- Werner Grogger: supervision and funding (electron microscopy)
- Wolfgang E. Ernst: supervision, manuscript editing, funding

Abstract

We present a first investigation of structural properties of Ag clusters with a diameter of up to 5.5 nm grown inside superfluid helium nanodroplets (He_N) and deposited on an amorphous C surface. With high resolution transmission electron microscope images we are able to show that in addition to the crystalline face centered cubic (fcc) structure noncrystalline icosahedral (Ih) and decahedral (Dh) morphologies are grown. Relative abundances (56% fcc, 31% Dh and 13% Ih) as well as the size distribution of each morphology (mean diameters $\bar{d}_{fcc} = 2.62(5)$ nm, $\bar{d}_{Dh} = 3.34(7)$ nm and $\bar{d}_{Ih} = 3.93(2)$ nm) do not reflect the situation expected from pure energetic considerations, where small Ihs should be followed by medium sized Dhs and large fccs. Instead, kinetic factors seem to play an important role in the formation of these structures, as it appears to be the case for clusters formed by inert gas aggregation. Considering the low temperatures (0.37 K) and extremely high cooling rates, we discuss basic ideas that might lead to a qualitative picture of the cluster formation process inside He_N.

4.1 Introduction

Metal clusters of nanometer size have been subject to intense research during the past decades. Many of their properties, such as optical,[58] magnetic[59] and catalytic,[60] differ considerably from those of both their atomic constituents and bulk matter, which makes them interesting also for technical applications.

There are several physical production methods for metal nano clusters, which allow a subsequent mass selection and/or surface deposition and have repeatedly been reviewed.[55,78,79] Intense focus of experimental and theoretical studies has been put on the morphologies of small particles,[80–82] as they give information on the underlying growth process.

Noble metal clusters are found to adopt primarily three different morphologies. In addition to the bulk face centered cubic (fcc) structure appearing with multiple truncations, icosahedral (Ih) and decahedral (Dh) structures are found, both of which are non-crystalline, but highly symmetric arrangements exhibiting a fivefold symmetry.[83] The Mackay icosahedron is built from 20 regular tetrahedra around a common vertex, a structure with inherent strains which should be adopted by small clusters from an

energetical point of view.[81,84] Dhs consist of five tetrahedra sharing a common edge to form a pentagonal bipyramid; truncation schemes have been proposed by Ino and later by Marks.[85,86]
While pure energetic considerations lead to the expectation that small clusters are of Ih morphology, followed by Dh for intermediate sizes and fcc for large clusters,[81] experimental observations of Ag clusters produced by inert gas aggregation (IGA) actually reveal a completely different size dependence of observed structures.[87] This discrepancy leads the respective authors to the conclusion that the final atomic arrangement strongly depends on environmental conditions of the growth process rather than pure energetic considerations. Atoms added to a cluster tend to build on the existing structure and the energy required for full internal structure rearrangement increases steadily.[87]
Superfluid helium nanodroplets (He_N) provide an extraordinary environment for particle growth. They combine confinement at low temperatures (0.37 K) with versatile doping possibilities in a very advantageous way and have therefore been used extensively for spectroscopic studies of cold and isolated atoms, molecules and clusters.[21,29] The unique properties of this cryogenic quantum matrix have also been exploited for the formation and in-droplet investigation of clusters since the early days of He_N experiments.[88] Various different spectroscopic techniques have been used since then to study metal clusters in He_N, such as optical spectroscopy,[89,90] strong field laser physics,[33] and electron ionization mass spectroscopy.[91,92]
Despite this promising approach of cluster formation in a quantum fluid environment the first step towards potential technical applications, namely the deposition of the formed clusters onto a surface, was only taken very recently.[1–3,8] First deposition studies of Au and Ag clusters on a quartz microbalance found deposition rates that are comparable to or larger than those obtained with other deposition techniques.[1] In a second study, deposited Ag clusters (Ag_n) of $\langle n \rangle \sim 300$–$6000$ were imaged with a transmission electron microscope (TEM).[2] The authors investigate the size distribution and conclude that the metal clusters remain attached to the surface with a high probability upon impact of the cluster-loaded He_N. They furthermore discuss stability issues of the clusters during the deposition process, which we consider to be one of the key questions, as the ability to exploit tailored cluster properties achieved by cluster formation in a quantum fluid environment critically depends on the processes during deposition. In very recent experiments Ag/Au and Ni/Au core-shell structures were produced inside He_N and investigated by high resolution TEM (HRTEM) and X-ray photoelectron spectroscopy.[3] The absence of shifts in the Au 4f and Ni 2p photoelectron lines obtained from Ni/Au core-shell clusters as compared to pure Au and Ni clusters are taken as strong indication that no alloying takes place neither during formation nor upon deposition. Furthermore, an HRTEM image of an Ag/Au cluster showing an fcc structure is presented.
In this work we present a detailed structural study of the self assembling process of Ag clusters inside a He_N. First, we combine the sizes of a large amount of clusters

from TEM images with deposition rates measured with a microbalance to obtain information about size distribution and sphericity of the clusters. By comparing HRTEM images to simulated morphologies[69,93] we are able to identify the three different structures fcc, Ih and Dh and obtain their relative abundances and size distributions. Based on mechanisms obtained from molecular dynamics simulations of cluster formation in an IGA source[81,94–96] we finally try to present a qualitative picture of the cluster formation process inside He_N.

4.2 Experimental Setup

4.2.1 Setup for cluster production

For the deposition studies presented here, we modified one of our existing He_N setups for laser spectroscopic investigations,[64] to allow for high temperature metal pickup and surface deposition. A He_N beam is produced via a supersonic free jet expansion of highly purified (99.9999%) ^{4}He gas through a 5 μm nozzle into vacuum. The source conditions are given by the nozzle temperature $T_0 = 11.4\,\mathrm{K}$ and the stagnation pressure $p_0 = 50\,\mathrm{bar}$, resulting in an average number of helium atoms per droplet of $\bar{N} \approx 3 \times 10^6$ (This value is obtained by comparison to droplet sizes for $p_0 = 20\,\mathrm{bar}$[97] through extrapolation along isentropes in the ^{4}He phase diagram.[98])
The droplet beam passes through a skimmer (400 μm aperture, 13 mm after the nozzle) into the pickup chamber, where the He_N are doped with Ag atoms. We developed a crossed beam setup for the doping process, in order to minimize the effusive flux of bare atoms towards the deposition region. Silver (99.99% purity) is resistively heated in an alumina coated tungsten wire basket (Ted Pella, Inc., prod. no. 84-27) which is covered with a thin tantalum sheet with a 3 cm long and 3 mm broad slit, aligned parallel to the He_N beam. The droplet beam passes the slit at a distance of $\sim 4\,\mathrm{mm}$ and is doped with up to several hundreds of Ag atoms. The whole setup is surrounded by a water cooled radiation shield with entry and exit holes for the He_N beam.
After pickup, the droplet beam enters the measurement chamber, where the crystal holder (Inficon, SL-A0E47) of a quartz crystal monitor (QCM, Inficon Qpod, S/N 1485) is located at a distance of $\sim 40\,\mathrm{cm}$ to the nozzle. The helium spreads on impact,[2,54] leaving the Ag_n on the crystal surface. All measurements were taken using 6 MHz gold coated crystals (Inficon, 64140-0930). As the measured deposition rates are often as low as $10^{-5}\mu\mathrm{g\,cm^{-2}\,s^{-1}}$ temperature stabilization of the quartz crystal turned out to be very important. Using a home-built water chiller with a commercial proportional-integral-derivative temperature controller we were able to stabilize the quartz crystal temperature to 22.00(3)°C.
The QCM can be replaced by a substrate holder for up to five commercial TEM substrates (Ted Pella, Inc., Prod. No. 01824), which can be brought into the beam sepa-

rately. The TEM substrates consist of an ultra-thin amorphous carbon (a-C) film with a thickness smaller than 3 nm, backed with a holey carbon support film and a 400 mesh copper grid.
The measurement chamber is also equipped with an electron impact ionization quadrupole mass spectrometer (QMS; Balzers QMA 400 / QMH 400-5) with the rod system being perpendicular to the He_N beam direction. As the QMS is located behind the QCM/TEM grid holder the latter have to be removed from the beam path during QMS measurements.

4.2.2 TEM analysis

TEM substrates loaded with Ag clusters were taken out of the vacuum apparatus and immediately transported under ambient conditions (exposure time approx. 10 min) to the microscope. The deposited clusters were studied using TEM (for size distribution analysis) and HRTEM (for investigations on cluster morphology). The instrument we used was a Tecnai TF20 (FEI Company) equipped with a FEG source and featuring an acceleration voltage of 200 kV. This microscope is equipped with a High Resolution Gatan Imaging Filter including an UltraScan CCD camera (2048 pixels x 2048 pixels) that was used to capture the micrographs. The illumination conditions were configured so as to ascertain that the irradiation by the electron beam did not impair the structure of the Ag_n during image acquisition. The electron beam featuring a current of approximately 2 nA illuminated an area with a diameter of about 50 nm, resulting in a current density of $1\,\mathrm{pA\,nm^{-2}}$.

4.3 Experimental Results and Discussion

4.3.1 Microbalance and TEM measurements

For a first characterization of our cluster deposition system we determined the mass deposition rates of Ag transported by He_N to the QCM for different pickup cell heating powers. We found a maximum rate of $2.9(4) \times 10^{-4}\,\mu\mathrm{g\,cm^{-2}\,s^{-1}}$ at a heating power of 140 W, which has been used for all further measurements. With the QMS set to the mass of 8 amu, which we take as a measure of the He_N flux, we found a decrease of the signal by 33%, due to evaporative cooling processes upon doping with this optimized heating power. This is the same decrease in He_N flux as reported in ref. 1 (we have a higher deposition rate which we attribute to a shorter He_N beam path).
Despite the crossed setup for pickup, the QCM detects Ag atom deposition when the He_N beam is blocked. This has to be bare atom deposition with a rate of below 3% of the rate obtained with He_N, which is most probably due to Ag atoms being scattered towards the QCM in the high particle density region above the pickup cell. We point

out, however, that it is important to keep this bare atom flux as low as possible to minimize the amount of clusters formed by self-aggregation on the surface as opposed to deposited clusters.
A comparison of the deposited Ag mass with the cluster sizes observed in TEM images allows an estimation of the sphericity of the clusters. We deposited Ag_n grown in He_N on a TEM substrate for 10 min, as shown in Fig. 4.1. This deposition time was chosen as a good trade off between high surface coverage and low amount of coalesced clusters. According to the QCM deposition rate determined above, we assume the mass per unit area to be $0.17(2)\,\mu g\ cm^{-2}$.
The evaluation was performed with the image processing package Fiji.[67] Background gradients, as well as the noise arising from the amorphous substrate, were reduced with fast Fourier transform filters.
In total, 9139 clusters from 8 different substrate spots are evaluated in terms of diameter

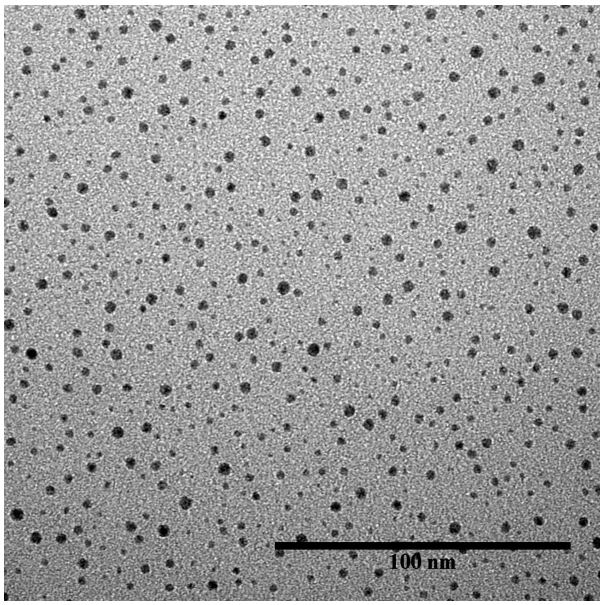

Figure 4.1: Typical TEM image obtained by 10 min deposition of Ag clusters grown in He_N and deposited on amorphous carbon.

and circularity. The surface coverage is 8.2% and the projections of the clusters appear to be mostly circular, as indicated by the mean circularity of 93%. We thus assume spherical clusters and calculate, based on the observed diameters, the mass per unit area to be $0.17(3)\,\mu g\,cm^{-2}$, which is in perfect agreement with the result obtained with the QCM. We note that, since the total deposition area does not cover the whole quartz crystal, the QCM sensitivity and thus the value obtained for the deposited mass might be slightly biased.[66] Based on optical inspection of the size and position of the covered region we expect this fact to have only a minor influence on the given result.
We therefore argue that most of the particles are quasi-spherical. This is to be expected

as the deposition of the Ag_n by the helium droplets is well in the so called soft-landing regime.[2,55] Theoretical calculations on the impact of He_N on a TiO_2 surface further indicate that the droplets might even cushion the deposition of an embedded species.[54] The distribution of Ag_n cluster diameters as extracted from the TEM images is depicted in Fig. 4.2. The data were fitted by a Gaussian distribution with the mean

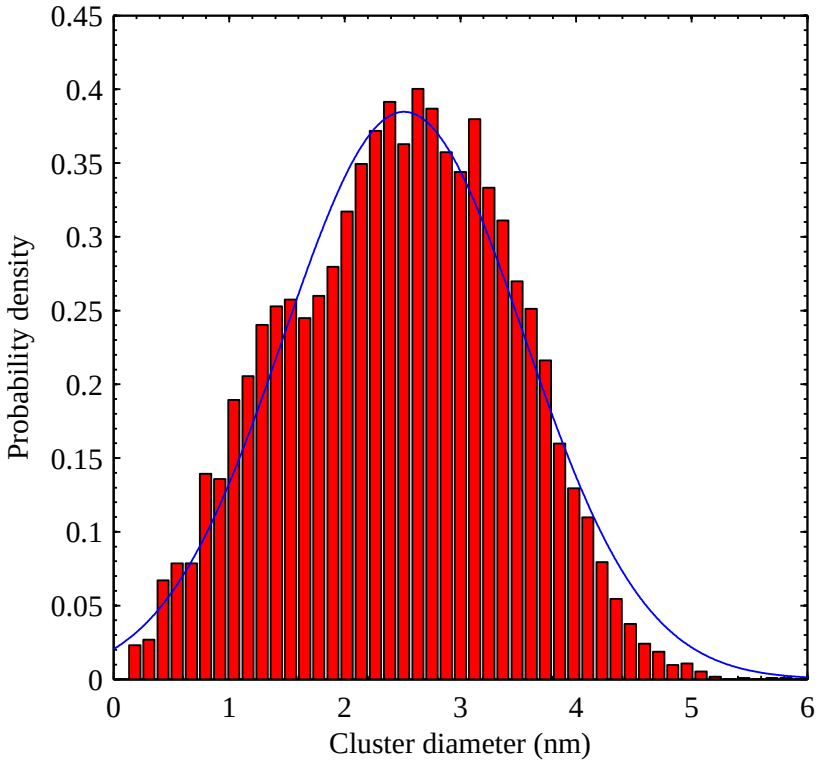

Figure 4.2: (Color online) Size distribution of deposited Ag clusters determined from TEM images. The plotted curve results from a Gaussian fit. The mean diameter $\bar{d}$ of the cluster has been determined to be $\bar{d} = 2.51(5)\,\mathrm{nm}$ ($n \approx 490$).

cluster diameter $\bar{d}$ and its standard deviation σ taken as free parameters. We obtained $\bar{d} = 2.51(5)\,\mathrm{nm}$ ($n \approx 490$ *) and $\sigma = 1.04(4)\,\mathrm{nm}$ (connected to the full half width by $\mathrm{FWHM} = 2\sqrt{2\ln 2}\,\sigma$). In order to evaluate the influence of the minute flux of bare Ag atoms ($\sim 3\%$, see above) on this distribution we exposed a TEM substrate to the pure Ag atom beam using the same conditions but with the He_N beam turned off. However, we were not able to find any Ag cluster in the resulting TEM images, which is contrary to previous experiments[2] and can be attributed to our crossed pickup geometry.

*Calculated assuming spherical particles and Ag bulk density $\rho_{Ag} = 10.50\,\mathrm{g\,cm^{-3}}$.[57] Note that the error of this approximation increases for small clusters

Fig. 4.2 also shows a slight asymmetry of the cluster size distribution, with a shoulder evolving at diameters below 1.5 nm ($n \approx 100$). Boatwright and coworkers observed a similar, although more pronounced feature[3] and proposed an interpretation based on multicenter aggregation as proposed by ref. 89. We think that this observation might be due to a bimodal droplet size distribution as observed in ref. 99, for $T_0 \leq 10\,\mathrm{K}$ at $p_0 = 20\,\mathrm{bar}$, which is comparable to the source conditions of this experiment.[98] While multicenter aggregation should lead to colloidal cluster-cluster aggregates inside the He_N[89] we did not find any of such aggregates nor a reasonable amount of coalesced particles on our substrate. On the other hand, multicenter aggregation seems to become noticeable for He_N as large as $\bar{N} \approx 1.4 \times 10^7$.[89] This may also relate to vortices inside the He_N, which seem to start forming at these droplet sizes and serve as traps for dopants and thereby as aggregation centers.[8] However, $\bar{N}$ is nearly one order of magnitude smaller in our experiment ($\bar{N} \approx 3 \times 10^6$), so that we do not consider such a behavior, in the present study.

4.3.2 HRTEM evaluation

To obtain structural properties of the deposited Ag clusters, HRTEM micrographs were recorded and analyzed at 94 different spots of the substrate. Multiple images with different defocus settings were collected at most spots.

Of a total of 737 clusters imaged with HRTEM, 319 showed a poor contrast, mostly because of their size being smaller than the thickness of the substrate. From the remaining 418 clusters, 88% could be assigned to one of the three different morphologies icosahedral (Ih), decahedral (Dh) and face centered cubic (fcc). The remaining 12% were left unassigned because they exhibit distorted morphologies, or were deposited with disadvantageous orientations with respect to the incoming electron beam, leading to indistinct images.

The assignment was achieved by comparison to simulated morphologies.[69,93,†] Taking the structures depicted in Fig. 4.3 as a simple example for the assignment procedure, the morphology of the particle in (a) can be easily identified as Dh, viewed along an axis of five-fold symmetry as shown in Fig. 2 of ref. 69. The Ih structure in (b), on the other hand, can be found in Fig. 6 of the same publication as both, a simulated HRTEM contrast and a corresponding TEM micrograph. Finally the very regular pattern in (c) can be assigned to a single-crystalline cuboctahedron (compare to *e.g.* Figs. 3 (b) and (c) of ref. 93) and therefore to be of fcc structure.

The resulting distribution of the observed morphologies is shown in Fig. 4.4. While for most clusters an unambiguous structural assignment could easily be achieved, about

[†] In ref. 69,93 the structures of different morphologies have been investigated for Au clusters. However, the resulting interference patterns can also be taken to classify Ag clusters, as the lattice constants a for Ag and Au are nearly the same ($\Delta a = 0.01\,\text{Å}$)[57]

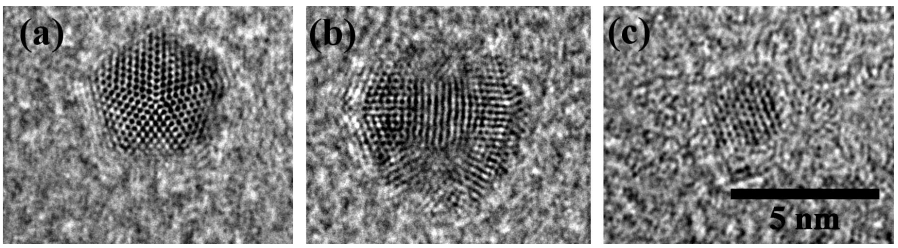

Figure 4.3: Examples for the three different cluster morphologies that can be clearly assigned to decahedral (a), icosahedral (b) and fcc structures (c). Scale for all images is the same as shown for (c). For the assignment compare (a) to Fig. 2 and (b) to Fig. 3 of ref. 69 as well as (c) to Figs. 3(b) and (c) of ref. 93.

25% needed a closer investigation. The corresponding fractions are labeled with c.i. in the figure legend. We take these percentages as a measure for the maximum uncertainty of the distribution which arises from the fact that for clusters viewed under high tilting angles with respect to a symmetry axis it becomes more difficult to interpret the resulting structure.[69]
An activation of a structural transition from Ih to Dh induced by the electron beam was only observed in one of 350 exposures. Otherwise the cluster structures were preserved even after several illuminations with the e-beam.
From a combination of structural information with Ag_n cluster sizes we obtain a size

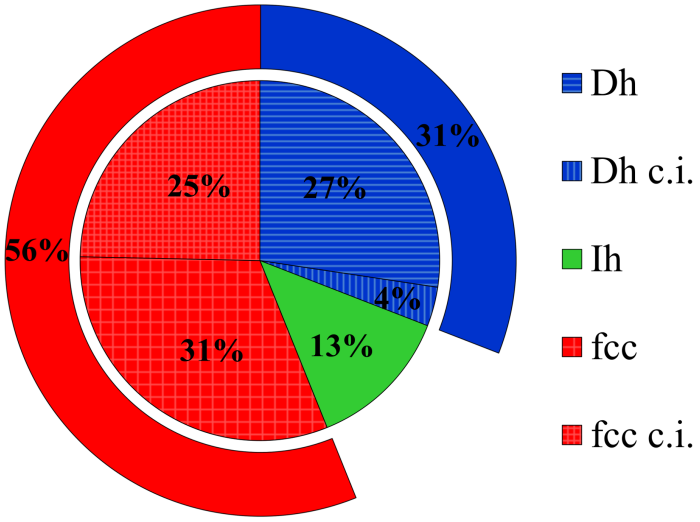

Figure 4.4: (Color online) Relative abundances of the observed cluster morphologies. Fractions labeled with c.i. in the legend belong to clusters which were subject to deeper investigation before being classified.

distribution for each of the three observed morphologies, as shown in Fig. 4.5. This result

reveals additional information about the growth process inside He_N and allows a comparison with other cluster formation methods. Each of the three resulting histograms is fitted with the same Gaussian distribution as used above, so that the free parameters (mean cluster diameter $\bar{d}$ and its standard deviation σ) can be compared with those of the over all size distribution shown in in Fig. 4.2. Here we find $\bar{d} = 3.34(7)\,\mathrm{nm}$ ($n \approx 1150$) and $\sigma = 0.61(5)\,\mathrm{nm}$ for Dh, $\bar{d} = 3.93(2)\,\mathrm{nm}$ ($n \approx 1870$) and $\sigma = 0.51(2)\,\mathrm{nm}$ for Ih and $\bar{d} = 2.62(5)\,\mathrm{nm}$ ($n \approx 550$) and $\sigma = 0.55(4)\,\mathrm{nm}$ for fcc clusters. $\bar{d}$ of the overall size distribution (Fig. 4.2) is much smaller because it was not possible to assign clusters below 1.5 nm diameter ($n \approx 100$).
From Figs. 4.4 and 4.5 it is immediately evident that fcc structures are the most abun-

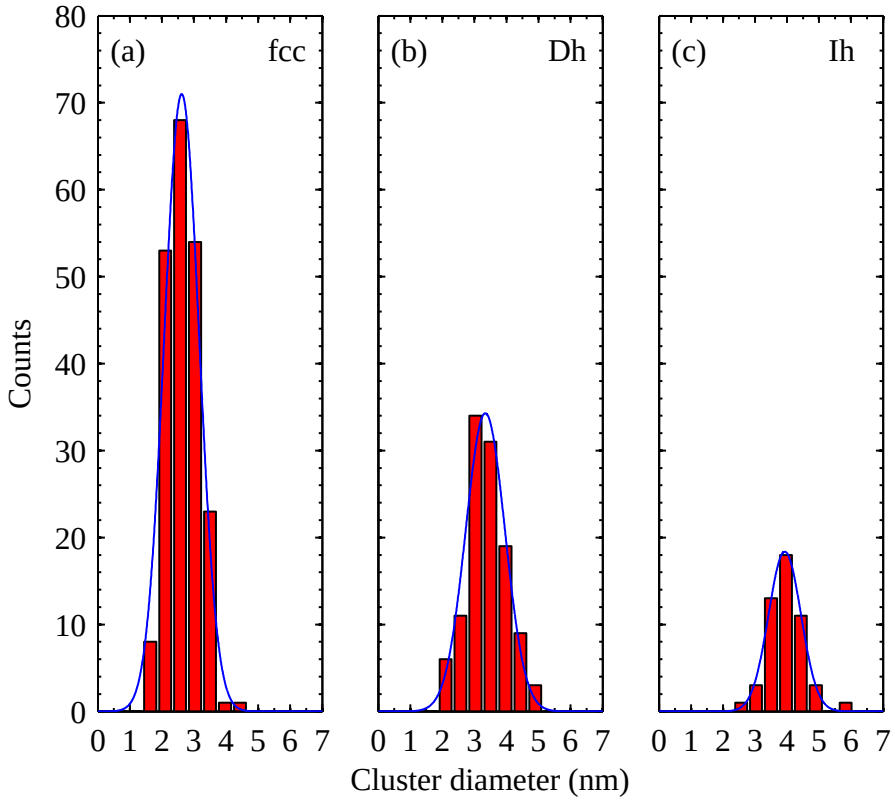

Figure 4.5: (Color online) Histograms of cluster diameters with fitted Gaussian curves for (a) fcc ($\bar{d} = 2.62(5)\,\mathrm{nm}$, $n \approx 550$), (b) Dh ($\bar{d} = 3.34(7)\,\mathrm{nm}$, $n \approx 1150$) and (c) Ih clusters ($\bar{d} = 3.93(2)\,\mathrm{nm}$, $n \approx 1870$).

dant ones, followed by Dh and Ih. The fcc morphology is also represented by the smallest clusters, again followed by Dh and Ih. This trend is emphasized by the fact that the mean fcc diameter (2.62(5) nm) is separated by more than a full half width ($2\sqrt{2\ln 2}\,\sigma = 1.2(1)\,\mathrm{nm}$) from the mean Ih diameter (3.93(2) nm). We do not expect that this significant difference is influenced by the uncertainty in assignment between

fcc and Dh (mentioned above) which mainly concerns the lower side of their size distributions. There was neither evidence for lots of large ($d > 4.5\,\mathrm{nm}$, $n \approx 2800$) fcc neither for small ($d < 2.5\,\mathrm{nm}$, $n \approx 480$) Ih particles, which look considerably different and can be clearly distinguished from each other in these size regions.

Figs. 4.2, 4.4 and 4.5 lead thus to the conclusion that small, intermediate and large Ag clusters formed in He_N are of fcc, Dh and Ih structure, respectively, and that their individual abundance is governed by the overall cluster size distribution.

This result is in clear contradiction to what would be expected from pure energetic considerations, where the Ih morphology should be the most stable configuration for small clusters, followed by Dh for intermediate and fcc for large clusters. The crossover sizes between the different morphologies have been calculated for transition and noble-metal clusters by MD simulations and can be found in Table III of ref. 100 (for more general information on the energetic effects in nanoclusters see ref. 81 and references therein).

Less surprising is our result, however, when compared to the structures observed in free Ag clusters produced by IGA,[87] although there are still major differences. There, small clusters were found mainly in Dh morphology with sizes of 2–3 nm ($n \approx 250$–830). Large clusters (6–10 nm, $n \approx 6640$–30720) were observed in Ih and fcc structure with Ih often dominating over fcc and an increase of fcc for increasing evaporation temperature (without significant change in cluster size). Recently, large (3.7–5.5 nm, $n \approx 1560$–5100) Ih morphologies were also observed in mass selected Ag_n from an IGA source.[101]

Baletto and coworkers were able to explain the occurrence of small ($n \leq 150$, $d \approx 1.7\,\mathrm{nm}$) decahedral and icosahedral Ag_n in IGA experiments by means of reentrant morphology transitions, which follow different transition paths depending on the ambient conditions.[94] They performed molecular dynamics simulations for different temperatures (350–650 K) and time intervals between subsequent depositions (2–21 ns). In a second study on larger Ag_n clusters ($n \leq 600$, $d \approx 2.7\,\mathrm{nm}$) they were also able to identify a mechanism that allows for the growth of large Ih clusters.[95] In the context of our results we consider the fact important, that higher cooling rates (5 and 20 K/ns) favor the formation of small fcc clusters.[96] All these studies clearly show that in addition to pure energetic considerations, kinetic factors play an important role in the formation of observed structures.

Cluster formation in He_N clearly takes place at much lower temperatures and much higher cooling rates than in other aggregation sources. In the following we discuss some basic considerations that might form a basis for a qualitative picture of the cluster formation process inside He_N. For IGA the environmental conditions and thus the obtained cluster structure depends not only on external parameters (evaporation temperature, pressure and type of the carrier gas) but also on the region within the IGA source where the formation takes place (hot inner zone, supersaturated intermediate zone or outer zone).[102,103] For He_N the situation seems to be simpler. Assuming the formation of one of the largest observed Ag clusters with 5.5 nm ($n \approx 5100$), the average time between

two successive Ag atom pickups is 20 ns (given by the He_N velocity of 300 m s^{-1} [98] and the 3 cm length of the pickup region). Comparing this value to observed cooling rates for neutral particles embedded into He_N of 10^5 K ns^{-1} [104,105] clearly shows that the cluster is always cooled to the droplet temperature of 0.37 K between two successive captures of dopants. Note that the cooling rate inside He_N is higher by a factor of $\sim 10^5$ compared to that of an IGA source.[96] We further assume that any kinetic energy of the Ag atoms due to elevated temperatures of the pickup source has been dissipated by the time the atoms reach the cluster so that only the released binding energy E_b has to be considered; an empirical form of which is given by[106]

$$E_\mathrm{b}(N) = E_\mathrm{b,bulk} + 2^{\frac{1}{3}} \left(\frac{1}{2} D_\mathrm{e} - E_\mathrm{b,bulk} \right) N^{-\frac{1}{3}} \tag{4.1}$$

with the binding energy per atom in bulk Ag $E_\mathrm{b,bulk} \approx 3$ eV [57] and the binding energy of the Ag dimer $D_\mathrm{e} = 1.65$ eV.[107] For a simplified estimation we assume that E_b is transferred to the Ag_n cluster and equally distributed among the n Ag atoms, resulting in a momentary increase of the cluster temperature $T_\mathrm{Ag}(n)$. Clearly, the rise in temperature for the addition of an extra atom is more prominent for small clusters, so that $T_\mathrm{Ag}(n)$ fluctuates between 0.37 K and rather high temperatures at the beginning of the growth process, while for larger Ag_n, the addition of a further Ag atom has a small impact. Based on these simple considerations we find that for $45 \leq n \leq 70$ ($1.1 \leq d \leq 1.3$ nm), T_Ag is between 600 K and 400 K, while it drops to $T_\mathrm{Ag} \approx 200$ K for $n = 150$ ($d \approx 1.7$ nm). In summary, we think that the observed structures can be explained by the fact that every cluster undergoes multiple growth modes. For small n, the addition of an extra atom leads to a significant internal temperature increase of the Ag_n cluster, which may oscillate between a liquid and a solid phase. In this size regime ($n < 70$, $d \approx 1.3$ nm), the most stable Ag_n configuration has been determined to be icosahedral, while around $n = 75$ preferentially Dhs are formed.[108] Subsequently, a solid state growth process follows, including morphology transitions or a shell by shell growth as proposed by the group of Ferrando for the IGA method,[94,95] to form the final structures, which we find for cluster diameters of 3 nm or larger as Ih or Dh in the electron microscope analysis. In other words, for cluster sizes of $n > 1000$ ($d \approx 3.2$ nm) the morphology seems to be preserved upon deposition on the carbon substrate. As one can see from the graphs in Fig. 4.5, particles with fcc structure exhibit the smallest of all mean diameters $\bar{d} = 2.62(5)$ nm, which corresponds to approximately 550 atoms per cluster. First results of molecular dynamics (MD) simulations indicate, that the smaller clusters may rearrange into the fcc structures due to an attractive interaction potential towards the surface, which is ≈ 0.75 eV for Ag atoms.[109] We note that this may lead to the fact that the size distributions for different morphologies on a surface as depicted in Fig. 4.5 may not exactly reflect their counterparts inside the He_N. On the other hand, there is no evidence for a structural transformation of large particles, and especially large fcc clusters have

not been observed. We therefore expect that the general trends resulting from the study of larger clusters reflect the growth processes inside the He_N.
A detailed analysis of these processes is currently the subject of an MD simulation study in our group.

4.4 Conclusions

Ag clusters were grown in He nanodroplets and deposited on either a microbalance or amorphous carbon TEM substrates. Comparison of the monitored mass rates with the substrate coverage confirms that the particles can be viewed as quasi-spherical. The cluster size distribution shows a slight asymmetry, which we attribute to a bimodal He_N size distribution.[99]
We provide a detailed study of the morphologies evolving from cluster growth inside superfluid helium droplets. Large icosahedra ($\bar{d} = 3.93(2)$ nm, $n \approx 1870$) and medium sized decahedra ($\bar{d} = 3.34(7)$ nm, $n \approx 1150$) are found as well as a large fraction of small ($\bar{d} = 2.62(5)$ nm, $n \approx 550$) fcc particles. This equals the results of former experiments conducted with inert gas aggregation sources.[87,101] An estimation for the evolvement of the cluster temperature leads us to the conclusion that Ag_n solidify at an early stage of the growth process. Subsequently the particles may undergo morphology transitions and shell by shell growth as proposed for clusters produced by the IGA method.[94,95] On the other hand, the finding of a large amount of small fcc particles on the substrate may result from reconstruction processes for smaller clusters due to the surface potential as indicated by performed MD simulations. We currently pursue an extended study on this behavior.
Finally, we point out that it is desirable to not only engineer nanoparticles in this sophisticated environment, but to be also capable of tuning their specific properties. The underlying growth process in helium nanodroplets must therefore be subject of deeper investigations and the determination of the dopant cluster structures plays a key role to achieve this goal.

5 Thermally induced breakup of deposited silver nanowires

The following corresponds to the publication
"Thermal instabilities and Rayleigh breakup of ultrathin silver nanowires grown in helium nanodroplets" by **Alexander Volk**, Daniel Knez, Philipp Thaler, Andreas W. Hauser, Werner Grogger, Ferdinand Hofer and Wolfgang E. Ernst in *Physical Chemistry Chemical Physics* **17**, 24570-24575 (2015).

The author of this thesis was responsible for

- the design and execution of the experiments,
- the evaluation of the obtained electron micrographs,
- contributions to the program code and execution of the performed simulations,
- the literature research and interpretation of the obtained data,
- the authorship of the manuscript,
- and assisted in recording the electron micrographs.

The contributions of the co-authors are listed below:

- Daniel Knez: recording of electron micrographs
- Philipp Thaler: assistance in the experiments, contributions to the program code
- Andreas W. Hauser: contributions to the program code, assistance in interpretation of results, manuscript editing
- Werner Grogger: supervision and funding (electron microscopy)
- Ferdinand Hofer: supervision and funding (electron microscopy)
- Wolfgang E. Ernst: supervision, manuscript editing, funding

Reproduced from "Thermal instabilities and Rayleigh breakup of ultrathin silver nanowires grown in helium nanodroplets" by Alexander Volk, Daniel Knez, Philipp Thaler, Andreas W. Hauser, Werner Grogger, Ferdinand Hofer and Wolfgang E. Ernst *Physical Chemistry Chemical Physics* **17**, 24570-24575 (2015)- Published by the PCCP Owner Societies.

Abstract

Ag nanowires with diameters below 6 nm are grown within vortex containing superfluid helium nanodroplets and deposited onto a heatable substrate at cryogenic temperatures. The experimental setup allows an unbiased investigation of the inherent stability of pristine silver nanowires, which is virtually impossible with other methods due to chemical processes or templates involved in standard production routes. We demonstrate by experiment and by adaption of a theoretical model that initially continuous wires disintegrate into chains of spheres. This phenomenon is well described by a Rayleigh–like breakup mechanism when the substrate is heated to room temperature. Our findings clarify the recent discussions on the cause of the observed segmented patterns, where a breakup during deposition [Gomez *et al.*, *Phys. Rev. Lett.*, 2012, **108**, 155302] or mechanisms intrinsic to the helium droplet mediated growth process [Spence *et al.*, *Phys. Chem. Chem. Phys.*, 2014, **16**, 6903] have been proposed. The experimental setup confirms the validity of previous suggestions derived from bulk superfluid helium experiments [Gordon *et al.*, *Phys. Chem. Chem. Phys.*, 2014, **16**, 25229] for the helium droplet system, and further allows a much more accurate determination of the breakup temperature.

5.1 Introduction

One-dimensional nanostructures such as wires, rods and tubes, have attracted considerable attention due to their potential usage as building blocks in nanodevices,[110,111] membranes,[112] biosensors[113–115] or waveguides[116]. Ultrathin nanowires with diameters of less than 10 nm show a whole series of unusual properties such as ferromagnetism,[117] negative magnetoresistance[118] or quantum conductance,[119] and have been suggested as components for miniature electronic circuits.[120]

Superfluid helium nanodroplets (He_N) can be exploited as nanolabs for the production of 1D-structures without any chemical solvent, external field or template. Their applicability to studies of nanowire growth has been demonstrated recently.[9,16] Doping of He_N with atoms, molecules or clusters is well established in spectroscopy,[21,29,33] and has recently been adapted for the controlled production and structure preserving soft

deposition of metal clusters.[1,2,11,15,56] Helium droplets with diameters of about 1 μm, as used in this work, contain quantized vortices,[8,53] a phenomenon attributed to superfluidity.[121,122] As observed in bulk superfluid helium (He II),[36–38] these vortices exhibit an attractive force on dopants immersed in the helium due to a pressure gradient around the vortex core,[35,76] ultimately causing their agglomeration into nanowires.[39,40,42]
While continuous wires from Au, Ni, Cr and Si were formed with the He_N technique,[9] only segmented chains of clusters were found in the case of Ag.[8,10] Several attempts were made to explain this observation, including the breakup of wires during surface deposition or the existence of forces intrinsic to the He_N–vortex–Ag system hindering the agglomeration process.[8,10] However, none of these suggestions could be either confirmed or falsified by experiment due to the complicated setup which is necessary to synthesise metal wires in He_N. The droplets, moving at $\approx 200\,m/s$, do not allow a direct observation of cluster growth and wire formation. Theory, on the other hand, is only beginning to understand the nature of vortices in superfluid helium, and therefore not able to deliver quantitative answers yet. Fortunately, the solution to the phenomenon of wire breakup is much simpler than was assumed in the literature.
In this article, we show by experiment and computer simulations that the degradation of 'ultrathin', He droplet-grown silver wires with diameters below 6 nm appears only after deposition to a surface and is strongly dependent on the substrate temperature. Although similar problems are well documented in the literature on the miniaturisation of optical or electronic devices, the breakup of He-mediated nanowires due to thermal instabilities had not been taken into consideration. This might be due to the fact that the crucial temperatures for wire breakup in this size regime, as will be shown, are so surprisingly low that even standard conditions are sufficient to initiate the degradation process. Typically, such a breakup mechanism can be associated to thermally activated surface diffusion effects, and the final structures can be explained by adapting Rayleigh's model for the breakup of a fluid jet[123]as proposed by Nichols and Mullins.[124–126] Experiments on larger structures were carried out on nanowires made from *e.g.* Ag,[127] Cu,[128,129] Au,[130,131] Sn[132] and Pt,[133] all with diameters above 20 nm. Breakup temperatures well below the bulk melting temperature were reported in all cases, but still far above room temperature. Only for Ag nanofractals, with initial branch diameters of $\approx$16 nm structural changes near room temperature could be observed.[134,135] We note that a breakup of the Ag nanowires synthesised in He_N on the surface had been suggested by Gordon et al. based on observations made in bulk He II. However, due to the nature of their experimental setup the direct observation of isolated ultrathin Ag nanowires and a temperature-dependent monitoring of the breakup process were not possible,[46,47] which motivated us to conduct the present study. Due to the challenging nature of nanowire production in the sub 10 nm diameter range, Ag nanowires in this size range are typically stabilised by templates,[136–138] which introduces a large bias in stability measurements at smallest diameters. Our study can therefore be taken as the first investigation of the

thermal stability of ultrathin pristine Ag wires, thereby demonstrating the ability of the He_N technique to gain new insights into fundamental questions of material science.

5.2 Experimental

A detailed description of the used helium droplet apparatus will be given elsewhere.[18] In brief, gaseous helium (99.9999% purity) is cooled to temperatures $< 10\,K$ by a closed-cycle refrigerator (Sumitomo, RDK-408D2) and expanded into a high vacuum region through a $5\,\mu m$ nozzle. For all experiments discussed in this work, the helium stagnation pressure is 20 bar, and the nozzle temperature is kept at 5.4 K. The resulting beam of helium droplets (mean droplet diameter $D \approx 1\,\mu m$) is collimated by a 0.4 mm skimmer and directed into a separate vacuum chamber with a base pressure $\approx 10^{-7}$ mbar. There the He_N incorporate multiple Ag atoms while crossing a region of silver vapor emanating from the evaporation of high purity (99.99%) silver, which leads to the formation of Ag clusters and ultimately to Ag nanowires inside the droplets. The Ag doping rate, and hence, the wire diameter, are controlled by the adjustment of the oven temperature while monitoring the attenuation of the total He flux into the adjacent deposition chamber (base pressure 10^{-10} mbar). Nanowire deposition is achieved by terminating the droplet beam on 3 nm amorphous carbon TEM grids (Ted Pella, Inc., Prod. No. 01824) cooled to LN_2 temperature. After the deposition process the vacuum chamber is vented with N_2 (99.999% purity), thereby preventing the substrate's exposure to ambient conditions. Before opening the vacuum chamber a glove bag is attached to the respective flange and filled with N_2 as to prevent contact of the substrate with air. The substrate holder is removed from its LN_2 cooled mount inside the vacuum chamber and totally immersed into LN_2 within 5 s. All further substrate manipulations, such as the transfer from the substrate holder to a cryo-TEM holder (Gatan, Model 626) are performed in LN_2, so that an inert environment is guaranteed at all times.
For the nanowire stability investigations, TEM images are recorded with a 120 kV LaB_6 FEI Tecnai 12 transmission electron microscope, equipped with a Bio Scan Camera (Gatan, Model 792). The substrate temperature can be controlled from 77 K to 363 K *via* the cryo-TEM holder. Temperature is increased from 243 K to 293 K in steps of 5 K every 15 min and finally set to the maximum of 363 K for 30 min. Multiple substrate spots are imaged for each temperature step.

5.3 Computational details

To verify that the Ag nanowire breakup originates from surface diffusion and not *e.g.* from an unexpected interaction with the substrate, we also performed model calculations, taking the initial nanowire contours as observed in the experiment as starting point. The

gradient of the chemical potential for a surface atom can be related to the gradient of the surface curvature, and subsequently, to a force on the respective surface element.[70] As with the cryo-TEM setup an accurate quantification of the wire thickness in three dimensions is impossible, we restrict ourselves to a 2D model.[71] The contourlines of the nanowires are discretised and propagated in time based on the Mullins equation, originally introduced to describe the thermal grooving at metallic grain boundaries.[70] Two mechanisms of mass transport along the surface can be distinguished: evaporation-condensation and surface diffusion. For silver, the latter is known to dominate the process. A partial differential equation can be derived, which relates $\mathbf{J}$, the flux of surface atoms, to $\nabla\mathbf{K}$, the gradient of the local surface curvature, via[71]

$$\mathbf{J} \propto -\frac{1}{T}\nabla\mathbf{K}. \tag{5.1}$$

Making the assumption of a monometallic structure of constant thickness, the gradient in eqn. (5.1) can be replaced by the derivative with respect to the curvilinear abscissa s. Furthermore, in this simplified 2D picture, mass conservation equals surface conservation, and the flux $J(s)$ must obey the relation

$$[J(s) - J(s+ds)]\Omega dt = dz\, ds, \tag{5.2}$$

where z describes the local transversal displacement of the contour line of the structure and Ω the volume of a diffusing particle. Together with eqn. (5.1) we obtain the equation

$$\frac{\partial z}{\partial t} = B\frac{\partial^2 z}{\partial s^2}, \tag{5.3}$$

with

$$B = \frac{D_\mathrm{s}\gamma\Omega^{4/3}}{k_\mathrm{B}T} \tag{5.4}$$

where D_s is the surface self-diffusion constant of a diffusing particle, γ denotes the surface tension, T is the temperature and k_B the Boltzmann constant. Since we are only interested in a qualitative description of the degradation of the silver structures, B is set to 1 in our simulation. The discretisation in s is determined by the resolution of the TEM images. This leaves arbitrary units for the discretisation in time, which has to be sufficiently fine to avoid instabilities during time propagation. As can be seen from eqn. (5.3), each point of the discretised contour line is shifted according to the second derivative of the surface curvature during a timestep. In other words, the diameter perturbations of the initial nanowire contours are propagating in time. This behaviour is analogous to the Rayleigh breakup of fluids, where the growth of initial diameter perturbations leads to the disintegration of the respective jet.[123]
Breakup events occur as soon as local constrictions of a wire lead to crossings of contour lines. In this case, the initial contour splits into two segments at the crossing point,

and the contour lines of the new segments are propagated separately in the following timesteps. Numerical instabilities, which are intrinsic to this technique, evolve from inhomogeneous point distributions along a contour line after a breakup event. In contrast to ref. 71, where this problem is overcome by pruning the constricted parts of the corresponding contour line, we increase the point density after each breakup. Although computationally more costly, this approach reflects our experimental results in greater detail. The accuracy of the simulation can be judged by monitoring of the total surface area, which has to stay constant throughout propagation.[71] For the initial contour lines taken from experiment, several million steps are necessary to obtain fully equilibrated structures (i.e., perfect circles in the 2D case). The surface is reduced by less than 4 %.

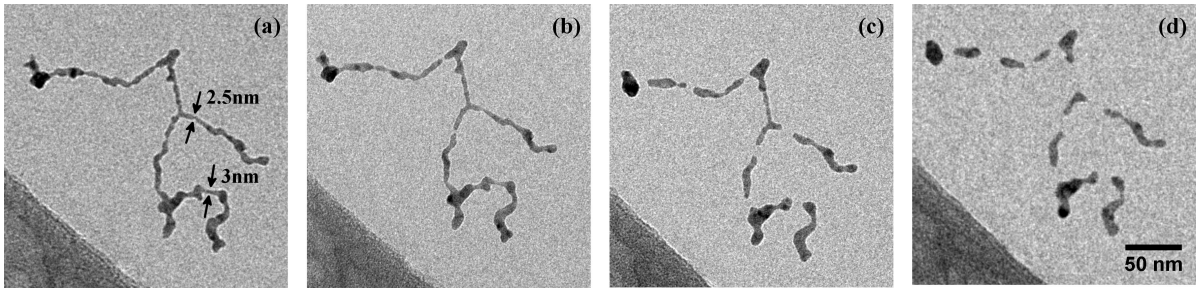

Figure 5.1: Structure evolution of a Ag nanowire at increasing temperatures of 253 K (a), 268 K (b), 293 K (c), 363 K (d). Structure as deposited (no change to situation at 77 K) is shown in (a). (b) marks the begin of wire breakup after surface smoothing, while (c) shows the fully segmented wire at ambient conditions. At higher temperatures the relaxation into spheres is suppressed by a carbonaceous capping layer (d). Scale is the same for all images.

5.4 Results and Discussion

5.4.1 Nanowire growth, deposition and stability measurements

We use He_N to produce Ag nanowires with a mean length of 500 nm and mean diameter $\bar{d}_{\mathrm{nw}} = 5\,\mathrm{nm}$. Fig. 5.1 (a) shows a typical deposited Ag nanowire structure with some constrictions marked by arrows. No evidence of wire breakup could be found on the cooled substrate. During heatup of the sample, a smoothing of the wire surface as well as a further decrease of the diameter in the vicinity of initial constrictions can be observed already at 268 K (Fig. 5.1 (b)), ultimately causing the breakup of the wire at temperatures below 293 K (Fig. 5.1 (c)).
Interestingly, for the investigated wires we are not able to observe a total relaxation into the equilibrium state, which corresponds to chains of spherical particles according to the Rayleigh model. An increase of the substrate temperature to 363 K leads to

further segmentation (Fig. 5.1 (d)), but the resulting segments stay well elongated. We can attribute this behaviour to a measurement artifact resulting from the deposition of a stabilising carbonaceous capping layer by ionisation and subsequent condensation of hydrocarbons present in the TEM vacuum. It is known that layers with a thickness of several nanometers can accumulate within minutes of specimen irradiation.[68,139,140] We note that during the heating process the same substrate spots were repeatedly imaged in order to track any structural changes. Therefore, the imaged nanowires were exposed to the electron beam for times longer than 30 min. Comparative images taken from specimen areas which were not exposed to the electron beam at any stage of the prior investigation all show a complete decay of the nanowires into chains of spheres, as depicted in Fig. 5.2 (a). Nanowires on a reference specimen, which was stored under ambient conditions for 1 week, show the same breakup patterns (Fig. 5.2 (b)), indicating that at 293 K the equilibrium state is also reached.
We measured the distances λ between the centers of neighbouring spheres, as well as

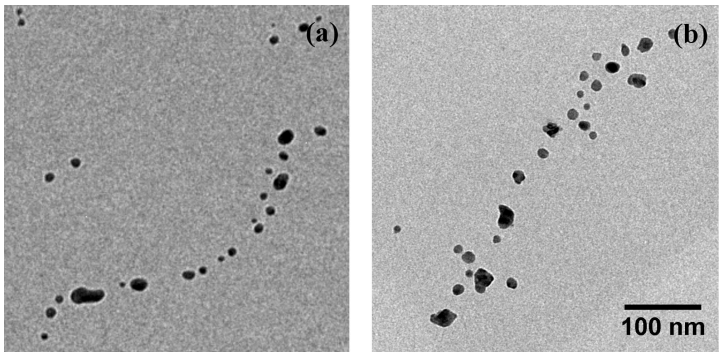

Figure 5.2: Undisturbed breakup patterns of Ag nanowires on substrate spots unimpaired by the electron beam. (a) shows sample from Fig. 5.1 heated to 363 K, (b) a reference substrate stored under ambient conditions for 1 week. Scale is the same for both images.

their diameters d_{sp} for several chains of segments, using the image processing package FIJI.[67] From the fits to the obtained histograms we can extract the ratios

$$\frac{\lambda}{R_0} \approx 15 \quad \text{and} \quad \frac{d_{\mathrm{sp}}}{R_0} \approx 5$$

with $R_0 = \bar{d}_{\mathrm{nw}}/2$ and variances of $\pm 20\,\%$.
The observed behaviour is in good agreement with the model of a Rayleigh breakup, i.e. the growth of initial diameter perturbations caused by the diffusion of Ag atoms along the wire surface. This diffusion is driven by a gradient of the chemical potential which can be associated to the gradient of surface curvature.[70,124,125]
Nichols and Mullins predicted the ratio $\lambda/R_0 = 8.89$ for surface diffusion dominated breakup of a cylindrical wire as result of harmonic surface perturbations.[124] Assuming

constant volume, one can estimate $d_{sp}/R_0 = 3.76$. The ratios observed in the present work exceed those obtained from theory. However, most investigated wires in literature are far from the ideal shape and isotropy which is assumed in this model calculation, thus the observed patterns deviate from the prediction.[131,141,142] Additionally the presence of a substrate generally tends to stabilise the nanowires.[143] The larger values of λ and d_{sp} indeed reflect a slightly larger stability of the wires compared to the model and are in good agreement with other experimental findings.[130,144]

5.4.2 Simulation of the degradation process

The initial contourlines of nanowires after deposition are taken as starting point for a computational study, using the 2D model described in Sec. 5.3. Exemplary results of the simulation are presented in Fig. 5.3 for the contourline taken from the nanowire depicted in Fig. 5.1 after 9×10^5 and 9.6×10^5 simulation timesteps respectively. The

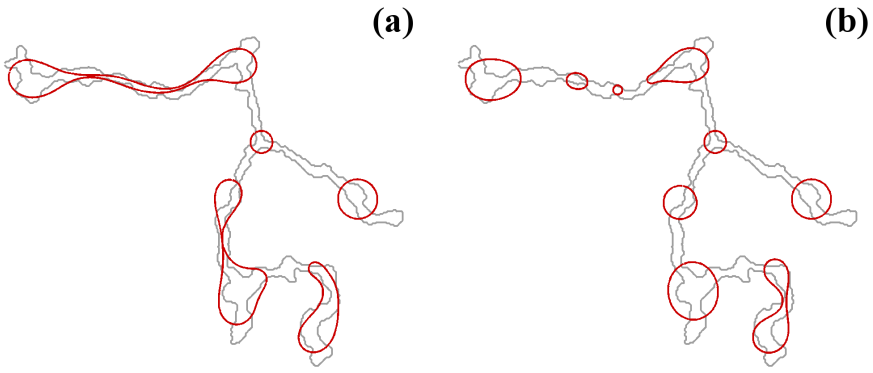

Figure 5.3: Evolution of the nanowire contourline (red) as simulated using a 2D model. The upper part of the wire is still intact in (a) after 9×10^5 timesteps, although considerably constricted at some points. After 9.6×10^5 timesteps (b) most segments have reached their final circular shape. The initial contourline of the simulation (light grey) is taken from Fig. 5.1 (a). The points of breakup coincide well with those observed in the experiment.

points of wire breakup are in excellent agreement with the experimental data (compare Fig. 5.1 (c) & (d) and Fig. 5.3). The reduced stability of the upper wire branch in the experiment compared to the simulation is related to a mass accumulation at the left upper end of the wire. While this is apparent from the higher contrast (i.e. a dark spot) in the TEM image, it is not accounted for in the 2D simulation. The model contours clearly propagate towards the spherical equilibrium state. The same tendency is seen in the experiment, but hindered due to the growth of carbon layers mentioned above.

Nevertheless, the degradation process is very well captured by our simulations, which shows that thermally activated surface diffusion is the main reason for the breakup of the nanowires. According to the experiment, the onset of this process becomes noticeable at $\approx 260\,\mathrm{K}$.

In experiments on Ag nanofractals, a breakup of fractal arms (diameter $\approx 16\,\mathrm{nm}$) was observed near room temperature.[134] Relaxation into spherical particles has not been observed for fractals of pure Ag due to slow fragmentation kinetics. Interestingly, the doping of the fractals with oxygen impurities during the growth process led to a full decay into spheres. This behaviour was also confirmed in a follow-up study[135] and was interpreted as a result of a strongly enhanced surface mobility near the oxygen atoms. Total spherodisation of the pure Ag nanofractal branches, on the other hand, was obtained only after annealing at 573 K.

In our study, the substrate is kept in an inert environment at all times. Therefore, a structure degeneration as a result of chemical processes can be fully excluded. This also rules out a possible Ag sulfidation by atmospheric gases as the origin of the degradation, which has been proposed in other cases.[145–147] Breakup occurs within minutes after the sample was heated to $\approx 260\,\mathrm{K}$. The observed timescale is in good agreement with the estimations derived for nanofractals.[134] Furthermore, no alteration of the initial wire structures can be found for an identically prepared reference specimen which had been stored in LN_2 for 48 hrs. This indicates a full suppression of the diffusion process at a temperature of 77 Kelvin. The advantage of our approach lies in the possibility to track structural changes in the TEM during the heatup. This also enables us to repeatedly image the same substrate spot and thereby track the structural changes of a single wire, which, in turn, facilitates a direct comparison to a simulation of exactly the same structure. The experimental approach allows a much more accurate determination of the decomposition temperature than in previous works.[46,47]

Our study confirms that the breakup of Ag nanowires synthesised in He_N occurs on the surface after deposition, as it had been proposed by Gordon et al. from results obtained in bulk He II.[46,47] The authors of the respective studies exploited vortices to grow nanowires of different metals and also found instabilities in the case of Ag. While for Pt, In, and Au nanowires spanned across the holes of a porous carbon TEM grid were found to be stable at ambient conditions, no such wires could be observed in case of Ag. Only a Ag nanoweb consisting of considerably thicker wires was found to be stable long enough for recording TEM images. The breakup of the thin Ag wires was explained by a change in the surface tension at small wire diameters.[47] In the framework of the Rayleigh breakup the surface tension γ enters the calculations as described in eqn. (5.4). Therefore, an increase in γ influences the breakup of nanostructures. However, also the surface self-diffusion constant plays an important role, as it is not only strongly dependent on temperature, but also exhibits large values for Ag compared to Au, Cu or Ni.[148] The suppression of the diffusion process at LN_2 temperature as described in

this work is in good agreement with this concept. It was found that a doping of the Ag nanowires with Cu atoms can increase their thermal stability by decreasing the surface atom mobility.[46] This is a further indicator that D_s governs the differences between nanowires of the same diameter made from different metals, while a general onset of the breakup is only observable at small diameters in accordance to the suggestions made previously.[47]

5.5 Conclusions

Our results prove that the experimentally observed segmented lines or 'chains' of He_N-grown Ag clusters[8–10] are neither an intrinsic feature of growth within the nanodroplets nor a consequence of the surface impact. Instead, the breakup is a consequence of diffusion processes caused by a 'warm' substrate. This confirms the suggestions of Gordon et al. of a nanowire breakup on the surface derived from bulk He II experiments.[46,47] We further investigate the structural degradation of the nanowires as a function of temperature. Due to the possibility of directly tracking the breakup process of a single wire, our experiment delivers an accurate measure of the breakup temperature $T_b \approx 260\,\mathrm{K}$ of the nanowires. The large experimental effort of a wire synthesis within He_N is rewarded by the complete inertness of the production and measurement process. The total absence of any solvents or templates enables an unbiased view on the thermal stability of pristine ultrathin Ag nanowires. We believe these findings will be useful in the context of further miniaturisation attempts regarding electronic or optical devices.

6 Timescales of atomic collisions in helium nanodroplets

The following corresponds to the publication
"Atomic collisions in suprafluid helium-nanodroplets: timescales for metal-cluster formation derived from He-density functional theory" by Andreas W. Hauser, **Alexander Volk**, Philipp Thaler, and Wolfgang E. Ernst in *Physical Chemistry Chemical Physics* **17**, 10805-10812 (2015).

The author of this thesis was responsible for

- the development of the simulation concept together with A.W.H.,
- the characterization of the He-dopant system by assumptions derived from literature,
- the assistance in the interpretation of results, comparison to alternative methods, data acquisition, coding and scripting
- manuscript editing, and the authorship of Sec. 6.4.4 including Fig. 6.8, as well as assisted authorship of Sec. 6.2.

The contributions of the co-authors are listed below:

- Andreas W. Hauser: He-DFT calculations, MD coding and simulations, interpretation of the results, authorship of the manuscript except from the parts disclosed above
- Philipp Thaler: preliminary discussions
- Wolfgang E. Ernst: supervision, funding

Reproduced from "Atomic collisions in suprafluid helium-nanodroplets: timescales for metal-cluster formation derived from He-density functional theory" by Andreas W. Hauser, Alexander Volk, Philipp Thaler, and Wolfgang E. Ernst in *Physical Chemistry Chemical Physics* **17**, 10805-10812 (2015)- Published by the PCCP Owner Societies.

6.1 Abstract

Collision times for the coinage metal atoms Cu, Ag and Au in He-droplets are derived from helium density functional theory and molecular dynamics simulations. The strength of the attractive interaction between the metal atoms turns out to be less important than the mass of the propagating metal atoms. Even for small droplets consisting of a few thousand helium atoms, the collision times are shortest for Cu, followed by Ag and Au, despite the higher binding energy of Au_2 compared to Cu_2.

6.2 Introduction

Metal clusters containing a few hundred or thousand atoms have experienced a tremendous interest in recent years due to their numerous potential applications in catalysis,[60] optics[58] and magnetics[59] industries. However, bridging between isolated, single atoms and the bulk material, their properties are heavily dependent on particle size and structure,[78,81] which leads to high demands on current synthesis techniques. In this context, superfluid helium droplets (He_N) provide a novel, extraordinary tool for controlled particle growth, combining the advantage of a minimally interactive confinement at 0.37 K with versatile doping techniques that allow for a fine-tuned synthesis of pure or mixed metal clusters.[21,29,33,88] First steps towards industrial applications such as the deposition of He_N-grown clusters, cluster films or nano wires onto surfaces, were taken recently.[1–3,5,8,11,16,149]

Despite several theoretical studies of the interaction between a coinage metal dopant and the He environment,[150,151] information on He-mediated cluster formation processes for coinage metals is yet very scarce. Of particular interest to the community is the knowledge about timescales for cluster formation, since it is crucial for a controlled growth of nanoparticles in helium droplets. Related studies of cluster formation in bulk helium describe a different growth mechanism, which is initiated by laser ablation of immersed metal targets and accompanied by the creation of vortices.[40,44,152]

As a first step towards this goal it will be necessary to investigate the motion of two dopants within a droplet of a given size. In this article, we apply He density functional theory to describe the initial mechanism of any cluster formation, namely the collision of two metal atoms. We pick the coinage metals Cu, Ag and Au (denoted as X through-

out the article) for our study, since several experiments have been performed with these elements in our group recently.[11,15] The necessary interaction potentials are taken from previous studies in the case of He-X or are generated by ourselves via high-level ab initio calculations in the case of the X-X potential curves. This manuscript is structured as follows. Section 6.3 is dedicated to technicalities of our approach. We discuss the diatomic potentials, the DFT approach and the molecular dynamics simulation. A correction for the X-X interaction potential is suggested, which takes the He-environment into consideration. In section 6.4, we present results for the confinement potentials and use them together with the corrected intermetallic potentials for the simulation of atomic collision processes. A statistical analysis is given, including predictions for average collision times in case of Cu, Ag and Au capture. The results are compared to previous studies and experiments where possible.

6.3 Theory

Our computational approach can be divided into three steps, which will be discussed in separate sections: The ab initio calculation of the necessary diatomic potentials, the creation of density profiles and solvation energies for doped He droplets of various size, and the simulation of dopant movements within a droplet via molecular dynamics (MD).

6.3.1 He-X and X-X interactions

A first ingredient are the pair potentials for He-Cu, He-Ag and He-Au, which are needed as input for a He-DFT code that generates relaxed He density distributions for larger droplets. Fortunately, the corresponding potential energy curves are available at high accuracy from ref. 153 and do not need to be calculated here. The corresponding binding energies are 6, 7 and 15 cm^{-1} for He-Cu, He-Ag and He-Au, respectively. Potential energy curves for the Cu_2, Ag_2 and Au_2 metal dimers, on the other hand, are calculated by us at the coupled-cluster level of theory. They do not enter the DFT calculation, but are needed later for the MD simulation. A single-reference, partially spin-restricted open-shell variant of the coupled-cluster method with single and double excitations plus perturbative triples [RHF-RCCSD(T)] is employed,[72,73]as it is implemented in the Molpro program package.[154] The aug-cc-pVQZ-PP basis sets of Peterson *et al.*[155] are used together with their corresponding effective core potentials, which replace all but the outmost 19 electrons of each metal atom.[156] All calculations are corrected for basis set superposition errors (BSSE) via the counterpoise method of Boys and Bernardi.[157]. The resulting dimer potential curves are plotted in Fig. 6.1. Accuracy at long interatomic distances is granted via $1/r^6$ fits to the atomic asymptotes. Binding energies D_e, equilibrium bond lengths r_e and harmonic frequencies ω are summarized in Table 6.1 and

compared to experimental data. The frequencies are derived from the first few vibrational levels of the ab initio potential curves. A symmetric three-point finite difference method has been used to solve the one-dimensional Schrödinger equation for the nuclear motion. All parameters are in good agreement with previous theoretical[158] and experimental studies.[159]

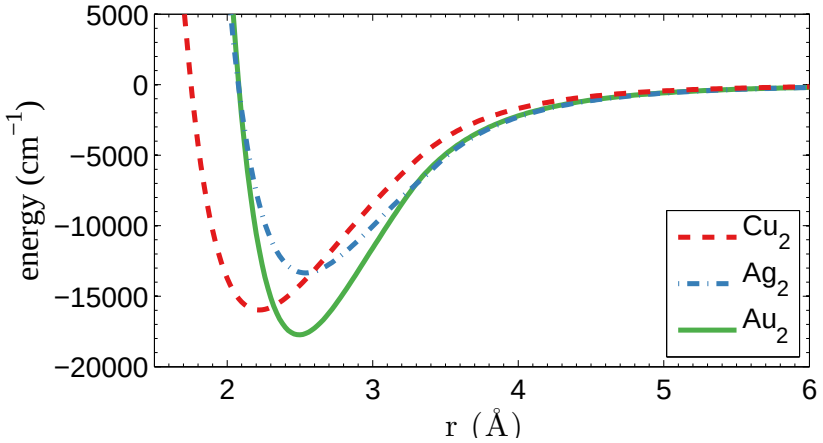

Figure 6.1: Potential energy curves for Cu_2, Ag_2 and Au_2, calculated at the CCSD(T) level of theory. All curves are corrected for BSSE and have been fitted with an r^{-6} dependence at long range.

Table 6.1: Parameters of the X-X potential energy curves. Results of the present work (pw) are compared to experimental data taken from ref. 159.

PES	r_e (Å)	D_e (cm^{-1})	ω (cm^{-1})	Ref.
Cu-Cu	2.22	15974	264	pw
Cu-Cu	2.22	16534	265	exp.
Ag-Ag	2.54	13345	188	pw
Ag-Ag	2.53	13389	192	exp.
Au-Au	2.50	17737	182	pw
Au-Au	2.50	18551	191	exp.

6.3.2 Dopant solvation in He_N

Single atom solvation

Free energies and density distributions for doped droplets of varying size are obtained from a He density functional approach, which accounts for a one-sided interaction be-

tween dopant and He droplet. We apply the Orsay-Trento-density functional[160] to map the He density onto the energy, using the FORTRAN code of F. Dalfovo with modifications of K.K. Lehmann and R. Schmied.[161] $F[\rho]$, the free energy of a doped He droplet, is minimized with respect to a fixed dopant position by evaluation of the He density distribution on a cylinder symmetric grid of cylinder coordinates $z \times r$, spanning over 601×300 points with a spacing of 0.238 Å. It can be written as a functional of the He density ρ, according to the formula[162]

$$F[\rho] = E[\rho] + U_{\text{ext}}[\rho] - \mu N[\rho], \tag{6.1}$$

with $E[\rho]$ denoting the Orsay-Trento functional and U_{ext} as the external potential. The latter introduces the interaction between He and the dopant, and is generated by a summation over energy contributions from the corresponding He-X pair potential of the previous subsection at the various distances between dopant and the He density distribution on the given grid. The third term in Equation 6.1 accounts for the conservation of the total helium amount, and consists of $N[\rho]$, the number of He atoms, multiplied by its corresponding Lagrange parameter, the chemical potential μ.

Solvation effects on X-X interactions

We further use the DFT approach of above to study effects of the superfluid helium environment on interatomic interactions by immersing two metal atoms into the droplet, followed by a re-evaluation of their dimer potential energy curve as a function of distance. Note, however, that the DFT code does not account for any direct interaction between two metal atoms. Therefore, the only energy dependence that can be derived from this computational experiment is a description of how the He_N droplet energy is affected by the helium density disturbance (i.e. the two 'density holes') caused by the immersion of X-X). If we remain with the assumption of negligible three-body-interactions in the given study (which is the fundamental assumption behind the well-established pair summation technique of He-X interactions anyway), this allows us to correct the X-X potential curves in a simple manner: We put two dopants into the middle of a He_N droplet and calculate the energy of the doped droplet as a function of the interatomic distance between the two dopants with the asymptotic value set to zero. The ab initio-derived X-X curves are then corrected by this extra energy contribution that stems only from the He density rearrangement caused by the X-X bond length variation:

$$\Delta E^{\text{He}_N}_{X-X}(r) = \Delta E^{\text{free}}_{X-X}(r) + \Delta E^{\text{He}_N}_{*-*}(r) \tag{6.2}$$

The stars in the last term represent the density holes caused by the He-X interactions. Note that for droplets of 1000 He atoms and larger the potential energy of a single dopant X with respect to its absolute position within the droplet is almost constant (as will be shown in the results section) except for near-surface positions, and can therefore be neglected here.

6.3.3 MD simulation of dopant motions

In the final step we combine the He-X and X-X interactions of the previous sections to calculate trajectories for the metal atoms immersed in He_N by solving Newton's equations of motion in a classic picture. We apply the Velocity-Verlet algorithm with a fixed time step of 0.1 picoseconds. The He-X interactions create a spherically symmetric confinement potential which keeps the dopants within the droplet. This potential has its minimum at the center of the droplet. Additionally, the metal atoms themselves interact as described by the corrected X-X potential. The actual motion of the dopants through liquid helium is accounted for in a simple manner: Their velocity can not overcome the Landau limit $v_\lambda \approx 56$ m/s at any time during the simulation. Recently, it has been shown that such a critical velocity is existent even for droplets consisting of only a thousand He atoms.[32] Such a limitation of the velocity during the simulation addresses the fact that friction, appearing for velocities $v > v_\lambda$, leads to the immediate dissipation of the excess kinetic energy by the creation of roton pairs. The generation of these quasiparticles, which correspond to local excitations of the He density, reduces the dopant velocity until it drops below the Landau level.[35,163]
Initial positions are randomly distributed within the droplet, and the particle velocities are chosen from a uniform distribution in the interval from 0 to v_λ. This grants an unbiased sampling, but also allows for some particles to leave the droplet, which we dismiss from the statistics since they can not be considered 'captured'. A particle is considered as lost if it shows a trajectory that leads out of the He droplet environment. We define the latter as the volume inside a sphere of radius $R+r_{eq}$, with R chosen as the distance where the He density drops below 1/e of its bulk value, and $r_{eq} = 4.5$ Å as an average value for the He-X equilibrium distances. For the larger droplets this restriction leads to a sampling loss of less than one percent.

6.4 Results and discussion

6.4.1 Interaction potentials and solvation effects

We start with a comparison of confinement potentials obtained for Cu, Ag and Au, as a function of the distance to the center of mass of the total helium density. They are given in Figure 6.2. If we assume a maximum velocity of v_λ for the dopant atoms, their kinetic energies are always below 8, 14 and 26 cm^{-1} for Cu, Ag and Au, respectively. Note that the reflection points for silver atoms with velocities near v_λ lie very close at the droplet surface, and for gold atoms they are even outside of the valid sampling range defined above. These heavy atoms are able to leave the region of high He density behind and move beyond the droplet radius even if their trajectory goes through the droplet center. However, from the same table it can be seen that even in these cases the dopant energies

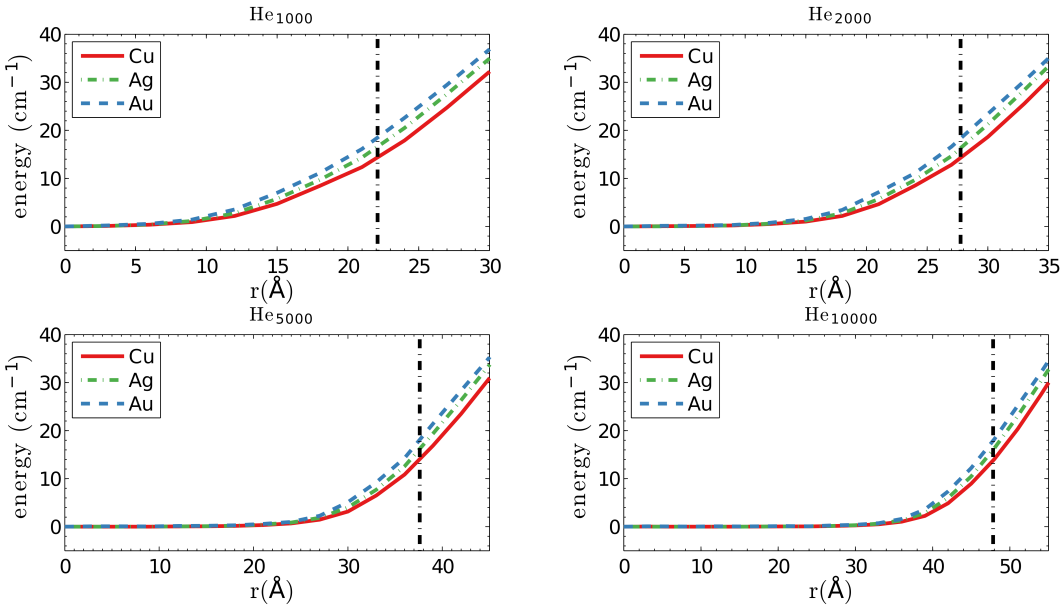

Figure 6.2: Confinement potentials for Cu, Ag and Au in helium droplets consisting of 1000, 2000, 5000 and 10000 atoms. The estimated droplet radius is indicated by a straight, dash-dotted line.

are well below the corresponding solvation energies, meaning that the atoms are still not able to fully detach from the helium droplet. They are dragged back via long-ranging van der Waals interactions, and get fully immersed into the droplet again. These interesting cases are probably worth a study on their own, but will be skipped here for two reasons. One argument is that such a surface-interacting or 'diving' trajectory might be poorly described with classical methods, as is necessitates a dynamic description of the He density distortion created on the droplet surface. The other one is that droplets of a size where the sampling loss is not marginal are barely able to capture such a heavy atom in the first place. Recently, a closely related type of translational dynamics was investigated for photoexcited Ag atoms on small He droplets ($N = 1000$) via time-dependent density functional theory.[164]

Solvation energies, defined as the energy difference between the doped and the undoped droplet via the equation

$$S(M) = E(\mathrm{He}_N + M) - E(\mathrm{He}), \tag{6.3}$$

are listed in Table 6.2. Absolute values of the solvation energies increase with the size of the droplet. As expected from the pair potential depths, He_N-Au gives the largest absolute value, followed by Ag and Cu.

In the next step we discuss corrections to the X-X potentials. The correction functions $\Delta E_{*-*}^{\mathrm{He}_N}(\mathrm{r})$ are plotted in Figure 6.3 for doped droplets consisting of 5000 He atoms.

Table 6.2: Solvation energies (cm^{-1}) of Cu, Ag and Au in helium droplets of various size. Droplet radii are given in Å.

dopant	He_{1000}	He_{2000}	He_{5000}	He_{10000}
Cu	63.2	64.0	64.3	64.6
Ag	85.2	85.9	86.3	86.5
Au	175.6	175.8	175.6	175.5
He_N radius[a]	22.11	27.76	37.61	47.83

[a] Radial distance from center of He_N mass where the density drops below 1/e of the bulk value $\rho = 0.02185$ Å^{-3}.

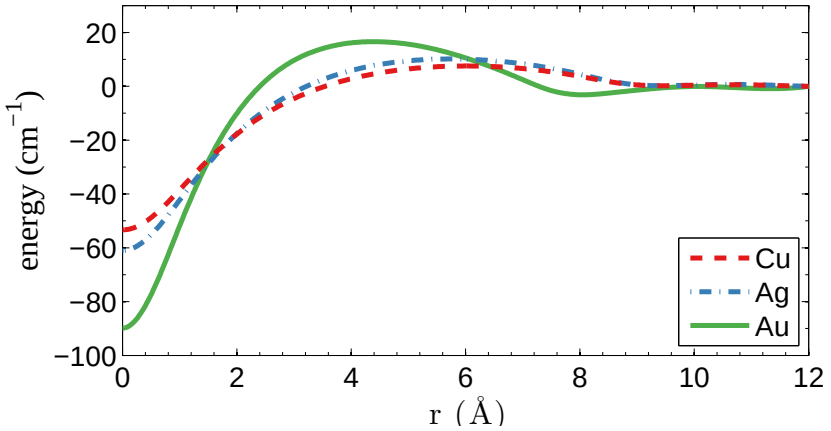

Figure 6.3: Correction energies for the PES of Cu_2, Ag_2 and Au_2 in He_{5000}, as a function of the dimer bond length.

The asymptotic value is set to zero for all curves. Energies were calculated at steps of 0.5 Å. All curves show minima for overlapping atoms, which seems counterintuitive at first sight, since such a geometry represents a minimum of the contact surface between the dopant atoms and the surrounding He density, while two dopants, embedded in separate bubbles, would correspond to a maximum of the contact surface area. From this finding we derive that the minimization of local distortions in the helium distribution overcompensates the loss of contact surface to the surrounding helium. Therefore, the X-X potential curves experience a slight contraction when corrected for the presence of helium. However, the corrections are very small compared to the overall dimer binding energies, and the geometry effects are completely negligible. We note that similar He density effects play a much bigger role in cases of weak diatomic interactions, *e.g.* for Rb-Xe in He_N.[165] Interestingly, the curves show a maximum at finite distances (6.0, 5.7, and 4.4 Å for Cu, Ag and Au) and a slight oscillation towards the asymptote, which

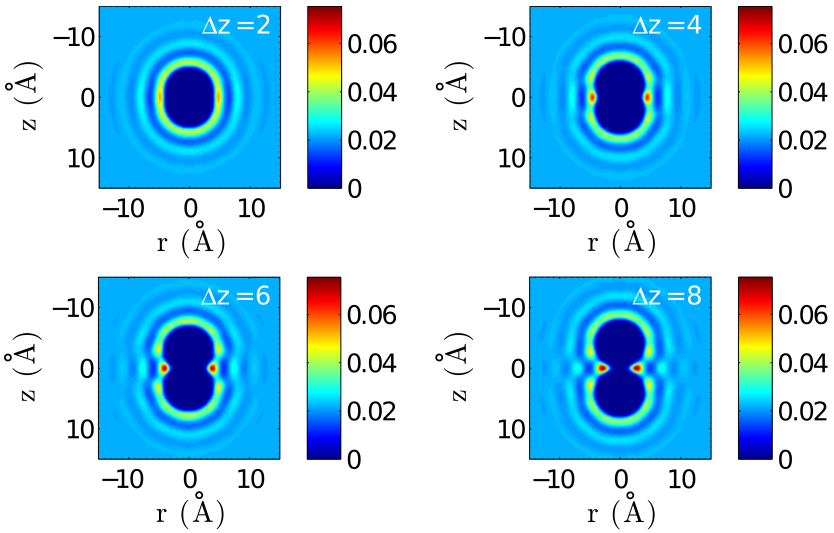

Figure 6.4: Helium density distribution of an Ag_2 doped droplet for various interatomic Ag-Ag distances (denoted as Δz). The local distortion causes a series of damped oscillations in the nearby He density. Note also the maxima of the He density in the mirror plane of the molecule, perpendicular to the internuclear axis (i.e., the z-axis). Densities are given in units of $Å^{-3}$.

we explain by the spherical density fluctuations around each dopant. These fluctuations are illustrated in Figure 6.4, which contains a series of density plots for Ag-Ag distances from 2 to 8 Å. An interesting feature besides the known oscillations of the He density in the nearby region is the formation of a donut-shaped ring of higher He density, which gets more pronounced for larger internuclear distances and appears as two separate maxima in the two-dimensional density cuts. Similar effects were reported recently for chains of atoms pinned to a vortex in superfluid He.[166] We note that this phenomenon of increased density at small internuclear distances and the related energy penalty could have an effect on collision probabilities of weakly interacting particles. If the correction energy as shown in Figure 6.3 is not overcompensated by the attractive interaction, a barrier will remain, and collision times obtained from the classical picture might have to be corrected for the effect of quantum tunneling.

6.4.2 Dopant trajectories and average collision times

In this section we present the results of the MD simulations. Example trajectories for Cu in He_{5000} are given in Figure 6.5, where the cases of single and double deposition are depicted. In the case of a single atom deposition, the angular momentum of the particle is conserved, and its trajectory is therefore always planar. This symmetry is removed as soon as a second atom is introduced to the system, and their trajectories are forced out

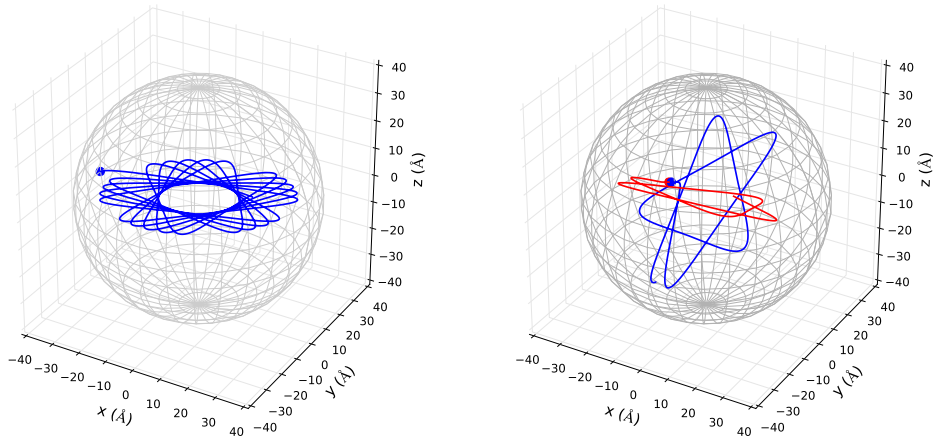

Figure 6.5: Typical trajectories for a single (left) or for two atoms (right), given the example of Cu dopants in He_{5000}. Note the conservation of the angular momentum in the case of a single atom deposition, which leads to a rosetta-like, planar trajectory. In the right picture, where the two atoms attract each other, only the total angular momentum is conserved. Both particles move independently in their planes until the internuclear distance is accidentally small enough for the attractive interaction to force them on a collision course.

of plane due to the interatomic Cu-Cu interaction.

10^4 collisions have been simulated for each metal dopant and each droplet size. The results for the average collision times are summarized in Table 6.3. The evaluation of Ag and Au in He_{1000} has been skipped due to the higher loss of particles during the simulation and a strong dependence of the collision times on our definition of the valid trajectory range. Collision times rank from about 0.3 to 4 nanoseconds in this size regime. We find that even for He_{2000} droplets, with radii of less than 28 Å, the collision times are not ranked according to the depth of the X-X interaction potential. The plausible assumption of higher binding energies leading to shorter collision times holds only for particles of similar mass. For the dopants chosen here, with mass ratios of roughly 2:3:6, the time ranking correlates with the particle mass for all droplet sizes. Copper collisions happen fastest, followed by silver and gold. The more energetic, heavier atoms propagate on average through a larger volume of the droplet, since they are reflected further outside by the confinement potential. As can be seen from Figure 6.2, the kinetic energy difference between Cu (8 cm^{-1}) and Au (26 cm^{-1}) translates into a difference of about 10 Å for their point of reflection.

Interestingly, the probability density for collision events over time shows a slight periodicity, as can be seen from the example histogram given in Fig. 6.6 for Cu_2 in He_{5000}. The peak-to-peak distance, in this case about 130 picoseconds, is the approximate time

needed for a particle at v_λ to traverse the droplet. This relationship also holds for larger and smaller droplets, leading to longer and shorter intervals, respectively.

Table 6.3: Collision times (picoseconds) for pairs of Cu, Ag and Au atoms in helium droplets of various size.

dopant	He_{1000}	He_{2000}	He_{5000}	He_{10000}
Cu	316	515	1274	2620
Ag[a]	-	928	1708	2843
Au[a]	-	1374	2266	3990

[a] The average collision times for gold and silver in He_{1000} have been skipped since they are strongly biased by the cutoff definition (see text).

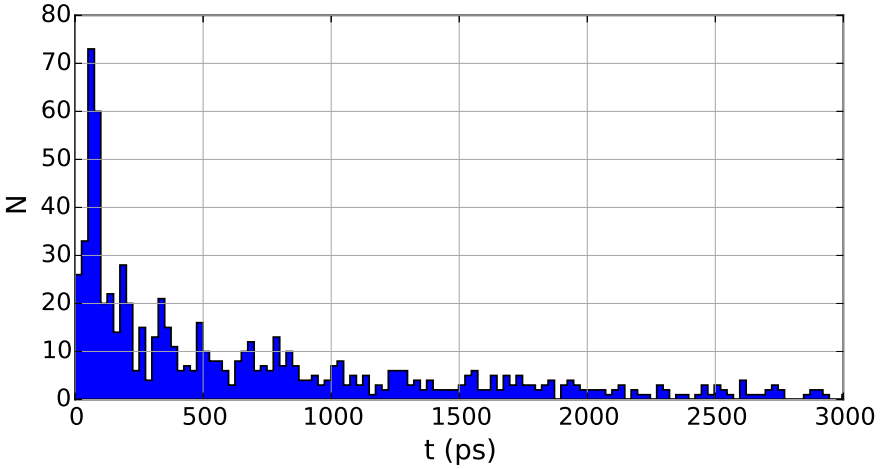

Figure 6.6: Collision times for Cu in He_{5000}. The long tail of the probability density has been cut to emphasize details. Note the periodicity of about 130 picoseconds between peaks.

6.4.3 Extrapolations to larger droplets

We extend our MD analysis to larger He droplets with radii up to 100 nm, which play a much bigger role in the ongoing experiments on metal cluster formation for the following reason: From our DFT simulations we obtain a chemical potential of about 4 cm^{-1} for He, which means that upon formation of our metal dimers about 3000 to 4000 He atoms have to be dissipated after the atomic collision. Therefore, cluster formation processes

can only take place in droplets with larger radii. DFT simulations are currently too expensive in this size regime, but we can take advantage of the fact that the curvatures of the confinement potentials for the same metal but different droplet sizes are almost identical in the relevant energy range. This is illustrated in Figure 6.7, where the confinement potentials for Cu in He_N are compared to each other. Following the definition of the droplet radius as given in Table 6.2, and setting this value to zero for each droplet, one finds almost overlapping confinement curves, as far as the curvature near the surface is concerned. From this we conclude that confinement potentials for larger droplets ($N > 10000$) can be easily obtained by simple shifts of the He_{10000} potential to larger distances r. We repeat our simulations for larger droplets with radii of 100, 200, 500 and 1000 Å, respectively.

In our MD simulation, the most time consuming step is the evaluation of the potential

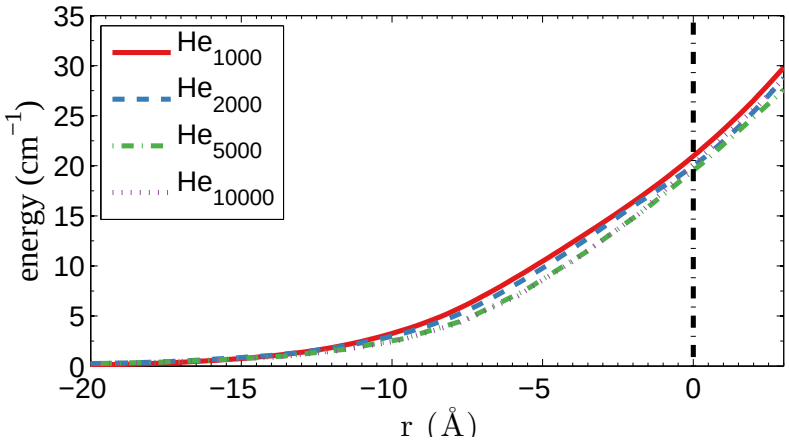

Figure 6.7: Confinement potentials for Cu in He droplets of various size. The zero position is set to the point where the He density drops below 1/e of the bulk value (vertical, dashed line). On this x-axis, the droplet centers lie at $-r$, with r taken from Table 6.2.

energy gradient at each timestep. In large droplets, this evaluation is not necessary most of the time, since the particles move on straight lines. This is taken into consideration in the code by reducing the evaluation to cases where the inter-particle distance drops below 30 Å or when they are closer than 15 Å to the droplet surface. However, a much more significant reduction of computational costs can be achieved by a complete avoidance of gradient evaluations for the confinement potential. Benchmark calculations for He droplets with a radius of 200 Å show that at this size the confinement potential can be replaced by a simple hard wall reflection, since the time spent in the areas with potential energy $U_{\mathrm{pot}} > 0$ is small compared to the free motion ($U_{\mathrm{pot}} = 0$) through the droplet. For better agreement with the more accurate model the actual position of the

hard wall is chosen with respect to the atom type as follows: Assuming a shifted soft potential as described in the text, we determine the point of reflection for atoms with velocity $v_\lambda/2$, and place the hard wall at this position. For droplets with a radius of 1000 Å, for example, the reflective wall is placed at 991, 993 and 995 Å for Cu, Ag and Au, respectively. This way, the simplified model also accounts for the larger accessible volume of heavier atoms.The difference in collision time predictions for droplets with a radius of 200 Å compared to results obtained with a the soft potential is less than 5 %. We therefore apply this simplified approach to the largest droplets with radii of 500 and 1000 Å. Our results for the average collision times in this size regime are summarized in Table 6.4. For the largest, and experimentally most relevant droplets with a radius of 1000 Å, we obtain collision times in the range of 0.01-0.014 ms.

Table 6.4: Collision times (nanoseconds) for pairs of Cu, Ag and Au atoms in larger helium droplets, sorted by their radius.

dopant	100 Å	200 Å	500 Å	1000 Å
Cu	16	114	1352	11031
Ag	18	121	1418	11401
Au	24	163	1790	14452

6.4.4 Comparison to other models

To our knowledge, this is the first evaluation of collision times t_{coll} for coinage metal atoms in He_N accounting for interactions between two dopants as well as between dopants and the helium droplet itself. However, knowledge about timescales of cluster formation are the key to a better understanding of complex growth processes observed in recent experiments, such as multicenter growth or the creation of nanowires.[1–3,8,11,16] Therefore, several model descriptions have been used in the past, which can be compared to our calculations.
In ref. 167, multiple dopant pickup and successive coagulation of gas atoms and molecules were investigated by mass spectroscopy and Monte Carlo simulations. Assuming that two successively collected dopants come to rest at random positions within a droplet, t_{coll} is calculated as being only dependent on the inter-particle van der Waals forces, thereby neglecting remaining kinetic energies and the influence of the He environment. Another approach to estimate the onset of multicenter aggregation is given in ref. 89, where the coagulation time for two particles is approximated as the time it takes to sweep the collision cross section of the particles through the total volume of the droplet at constant velocity. Both aforementioned formalisms were applied to droplet sizes and

dopants considered in this work. For the first model, the corresponding C_6 coefficients of the $-C_6/r^6$ van der Waals potentials are derived from the dimer curves given in Fig. 6.1. We average over several simulation runs with initial distances randomly chosen within the droplet diameter. For the second model, we assume an average velocity of $v_\lambda/2$. The results are comparatively depicted in Fig. 6.8. One finds that the values

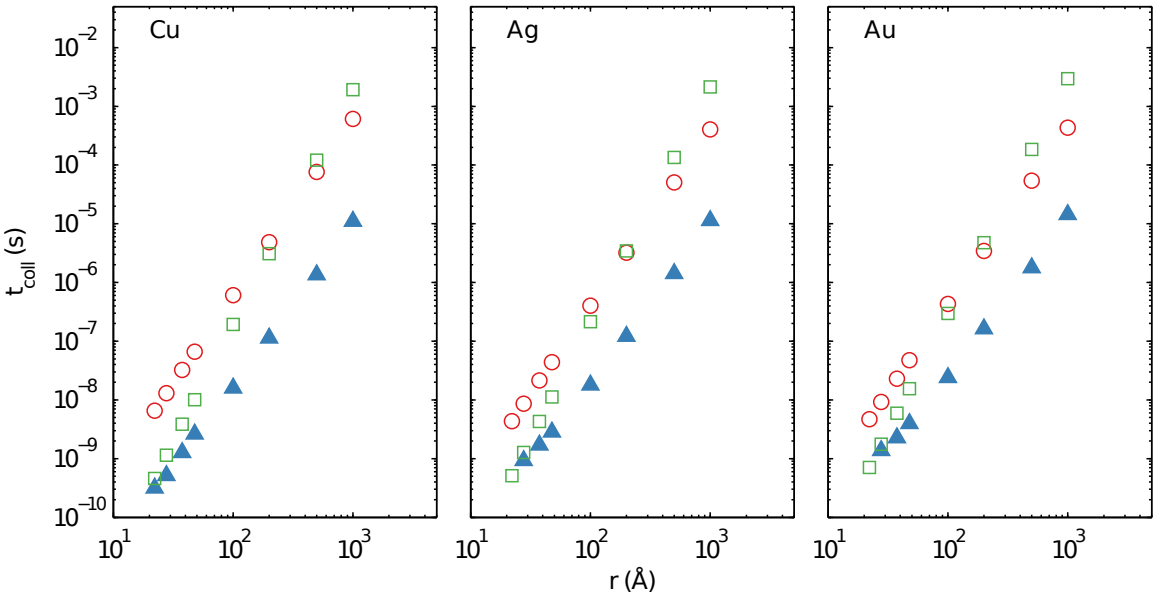

Figure 6.8: Collision times of coinage metals in He_N as obtained with different models, either by dividing the total He_N volume by the product of particle velocity and cross section as proposed in ref. 89 (open circles), by assuming pure van der Waals attraction as proposed in ref. 167 (open squares), and from the calculations in this work (full triangles). See text for further discussion.

for t_{coll} in the present work are generally lower and the agreement with the simpler models seems to get worse with increasing droplet size. Considering only van der Waals interaction, this seems to be intuitive as the attractive potential between the dopants is proportional to r^{-6}. Still, there is a good agreement between the van der Waals-only model and our calculation for small He_N sizes. Collision times obtained from the static volume model are more than one order of magnitude larger and show practically no dependence on the atom type. In the latter feature the simple model agrees with our calculations for large droplets, where the X-X interactions become less relevant. The slopes of the volume model and our calculation are almost parallel. Obviously, one reason for the overestimation of collision times lies in the complete neglect of interatomic attractive interactions. However, this argument does not explain the still significant discrepancy for larger droplets. The additional, and apparently more relevant deviation

that remains in the case of larger volumes stems from the fact that the trajectory of an essentially unaffected, confined particle is planar due to the conservation of the angular momentum. Therefore, the assumption of the whole volume being accessible must lead to an overestimation of collision times.

6.5 Conclusion

We simulated the motion of Cu, Ag and Au atoms in droplets of superfluid helium via a combination of He-density functional theory and classical molecular dynamics. The necessary two-particle interaction potentials were either taken from literature or derived from quantum chemistry calculations at the CCSD(T) level of theory. The metal dimer potentials were corrected for energy penalties which arise due to local distortions of the helium density. However, these corrections turn out to be fully negligible (less than 100 cm^{-1}) for the strongly bound metal dimers and do not affect their equilibrium geometries, but could become relevant for weakly bound species such as Mg_2. The confinement potentials were calculated with our DFT code for He droplets consisting of up to 10000 atoms. We found that the shapes of these potentials are minimally affected by the droplet size, which allowed the simulation of larger droplets with radii of up to 100 nm by simple shifts of the curves.
In a series of molecular dynamics simulations for helium droplets with radii from 23 to 1000 Å we calculated the trajectories of two metal atoms in a symmetric confinement via a Velocity-Verlet integration upon collision. A statistical analysis of collision times for the various helium droplet sizes after the pickup of a second metal atom shows that the strength of the metal-metal interaction is overcompensated by particle mass effects even in small droplets consisting of a few thousand helium droplets (radii below 30 Å). On average, Cu collisions are slightly faster than Ag and Au collisions.
Our findings should be useful to experimentalists for basic estimates of more complex cluster growth scenarios in helium droplets of various size, where collision events, pickup processes and other phenomena such as vortex-induced nanowire formation have to be taken into consideration. An extension of our theoretical studies towards the simulation of actual growth mechanisms in combination with experiments on coinage-metal-doped He droplets is in preparation.

7 Doping rate dependence of nanowire growth in helium nanodroplets

The following corresponds to the manuscript
"The impact of doping rates on the morphologies of silver and gold nanowires grown in helium nanodroplets" by **Alexander Volk**, Philipp Thaler, Daniel Knez, Andreas W. Hauser, Johannes Steuer, Werner Grogger, Ferdinand Hofer and Wolfgang E. Ernst, in *Physical Chemistry Chemical Physics* **18**, 1451-1459 (2016)

The author of this thesis was responsible for

- the design and execution of the experiments,
- the evaluation of the obtained electron micrographs,
- the adaption of the program code from P.T. and application to the current system,
- the literature research and interpretation of the obtained data,
- and the authorship of the manuscript.

The contributions of the co-authors are listed below:

- Philipp Thaler: development of the program code and assistance in the experiments
- Daniel Knez: recording of electron micrographs
- Andreas W. Hauser: manuscript editing
- Johannes Steuer: assistance in the experiments
- Werner Grogger: supervision and funding (electron microscopy)
- Ferdinand Hofer: supervision and funding (electron microscopy)
- Wolfgang E. Ernst: supervision, funding, manuscript editing

Remark: Due to a unit conversion error, the values for t_{trap} given in Table 7.2 are not correct. Please find an erratum in Sec. 7.7, which addresses this fact and has been submitted to *Phys. Chem. Chem. Phys.*.

Reproduced from "The impact of doping rates on the morphologies of silver and gold nanowires grown in helium nanodroplets" by **Alexander Volk**, Philipp Thaler, Daniel Knez, Andreas W. Hauser, Johannes Steuer, Werner Grogger, Ferdinand Hofer and Wolfgang E. Ernst, in *Physical Chemistry Chemical Physics* **18**, 1451-1459 (2016)- Published by the PCCP Owner Societies.

7.1 Abstract

Silver and gold nanowires are grown within superfluid helium nanodroplets and investigated by high resolution electron microscopy after surface deposition. The wire morphologies depend on the rate of metal atom doping in the pickup sequence. While high doping rates result in a polycrystalline face-centered cubic nanowire structure, at lower doping rates the initial fivefold-symmetry seems to be preserved. An explanation for this observation is given by computer simulations, which allow the derivation of timescales for the nanowire growth process inside helium nanodroplets.

7.2 Introduction

Quantized vortices, accessory phenomena of superfluidity, have been predicted by Onsager and Feynman around 1950.[121,122] Despite earlier experimental evidence for their existence,[36,37] it took until 2006 to finally image them in bulk superfluid helium (He II) using hydrogen particles as tracers.[38] The fact that impurities get pinned to the vortices as the consequence of a pressure gradient around the vortex cores,[35] can be exploited to investigate processes such as vortex reconnection and quantum turbulence in He II.[168–170]
In a more applied approach, the use of the directed growth of nanoparticles in the presence of vortices in He II was proposed for the production of nanowires.[171] Single and bundled metal nanowires were obtained from laser ablation of metal targets immersed in He II and subsequently characterized in terms of structure, electrical properties and thermal stability.[39–48]
Helium nanodroplets (He_N), on the other hand, were extensively used as weakly perturbing cryogenic matrices for the spectroscopy of atoms, molecules and small clusters in molecular beam experiments (see ref. 21,29,33,34 for detailed reviews). The possibility of sequential doping and local confinement of different species at 0.37 K makes He_N also a unique environment for cluster growth.[21,29,33,90,92] The first surface deposition of

He_N-grown metal clusters,[1,2] triggered a series of experimental studies on cluster growth and follow-up surface deposition.[3–6,11] Gomez *et al.* found that Ag nanoparticles (Ag_n), synthesized in single helium droplets and subsequently deposited on a substrate, tend to agglomerate equidistantly along distinct lines.[8] In the absence of external guiding forces, this can be taken as the first experimental evidence for the existence of vortices inside of He_N. This confirms several preceding computational studies on this issue (see ref. 49–52 and references therein). Further proof for the presence of vortices or even vortex lattices in the droplets was given by recent X-ray diffraction experiments on a Xe-doped He_N-beam and complementary density functional theory (DFT) calculations.[53,172] Utilizing these vortices as inert templates, continuous monometallic nanowires with lengths of several hundred nanometers were synthesized inside He_N,[9] as well as bimetallic core-shell nanowires.[16] As an intrinsic property of the growth process, the diameter of these wires is $\approx 3 - 10\,\mathrm{nm}$. In a recent study on the stability of He_N-grown Ag nanowires we could show that these thin structures segment due to thermally induced Ag atom diffusion after their deposition on a surface.[12]

Despite these experimental achievements, little is known about the actual growth process of nanowires inside the droplets.[9,10] Our group was able to deduce a possible growth mechanism for pure Ag_n inside of vortex-free He_N by analyzing high resolution transmission electron microscopy (HRTEM) images of the deposited clusters.[11] A computational survey of the landing process revealed that small Ag_n (diameter $d_{Ag} < 3\,\mathrm{nm}$) presumably undergo reconstruction upon deposition, while for larger clusters the pronounced soft landing conditions[2,55,56] favour the conservation of the initial morphology.[15] Only recently we modeled the collision process between two coinage metal dopants in small He_N with a molecular dynamics (MD) simulation.[13] The obtained timescales for dimer collisions were subsequently used in a model suitable for larger droplet sizes. It shows that for large He_N, multicenter aggregation leads to well separated clusters in one droplet for long timescales.[17]

In the present study we extend our previous work by investigating the influence of the doping conditions on the cluster growth and aggregation inside of large He_N. We further give timescales for the pinning of clusters due to attractive forces exerted by vortices present in the droplets, which causes the nanowire-growth. The obtained results are compared to HRTEM images of bare Ag and Au clusters and nanowires. Experiment and calculations indicate that an alteration in the amount of metal dopants induces different growth scenarios, which finally influences the morphology of the produced nanowires. To our belief a good understanding of the underlying growth process of nanowires in He_N is one of the key questions to be addressed in order to be able to synthesize more elaborate structures with this technique.

7.3 Experimental

The experimental setup is described in detail elsewhere.[18] In brief, He_N are produced by the supersonic jet expansion of gaseous He (99.9999 % purity) through a precooled nozzle with a 5 μm orifice into high vacuum. The helium stagnation pressure (p_0) was kept at 20 bar for all experiments discussed in this work. By variation of the nozzle temperature (T_0) it is possible to alter the mean droplet size ($\bar{N}$).[21] In our experiments, vortices have exclusively been observed for $T_0 \leq 6.5\,\mathrm{K}$ at $p_0 = 20\,\mathrm{bar}$. Therefore, it can be assumed that they are efficiently created and preserved only when large He_N ($\bar{N} > 10^8$ atoms) are formed *via* breakup of liquid He during the expansion process.[8,97,98] For experiments on vortex-free He_N we therefore keep T_0 at 8 K. In all other cases, T_0 is set to 5.4 K. This corresponds to $\bar{N} \approx 7 \times 10^6$ atoms (droplet diameter $\bar{d_\mathrm{D}} \approx 85\,\mathrm{nm}$) and $\bar{N} \approx 1.7 \times 10^{10}$ atoms ($\bar{d_\mathrm{D}} \approx 1100\,\mathrm{nm}$) respectively.[21,26,97] We note that recent calculations also suggest vortex nucleation in small He_N ($N = 1000$) by ionization of attached dopants[173,174] or during the doping process with neutral atoms.[175] However, in the latter case theory suggests limited vortex-lifetimes in the picosecond range.

The He_N-beam passes a 400 μm skimmer into a separate vacuum chamber where the droplets are doped with the desired metal. Ag or Au atoms are evaporated from separate resistively heated alumina ovens of 2.3 cm length. They are captured by the passing droplets, in which they subsequently agglomerate to clusters. After the pickup, the droplet beam enters a UHV chamber (base pressure $< 6 \times 10^{-10}$ mbar) and is terminated on commercial TEM grids (Ted Pella, Inc., Prod. No. 01824). This leads to the disintegration of the droplet and a soft deposition of the contained aggregates on the amorphous carbon (a-c) surface.[2,15,55,56]

The disintegration of the He_N causes a rise in the He background pressure p_He, which can be monitored with an ionization pressure gauge (Leybold Heraeus IM 220) and a quadrupole residual gas analyzer (Balzers QMA 200/QME 200), both mounted off the beam axis. Due to evaporative cooling,[26] the He_N size and accordingly the total He flux Φ_He into the last chamber are reduced with increasing Ag/Au doping rate. Following ref. 2, we calculate the mean number of metal dopant atoms $\bar{n}_X$ per He_N as

$$\bar{n}_X = \frac{(\Phi_\mathrm{He,undoped} - \Phi_\mathrm{He,doped}) \times \bar{N}}{\Phi_\mathrm{He,undoped}} \times \frac{E_\mathrm{He}}{E_X} = \alpha \times \frac{\bar{N} \times E_\mathrm{He}}{E_X}, \tag{7.1}$$

where the index X denotes either Ag or Au. The attenuation of the He_N beam due to doping is denoted as α and $E_\mathrm{He} = 0.6\,\mathrm{meV}$ is the binding energy of 1 He atom to the droplet.[26] $E_\mathrm{Ag} = 3\,\mathrm{eV}$ and $E_\mathrm{Au} = 3.8\,\mathrm{eV}$ are the bulk binding energies for Ag and Au, respectively.[57] This approach neglects the kinetic energy transfer to the droplet by the dopant atoms, which is two orders of magnitude smaller than the binding energy. Table 7.1 contains the values for $\bar{n}_X$ as obtained for the attenuations used in this work. We note that E_X is dependent on the cluster size and considerably smaller at the beginning

of cluster growth.[107] This is taken into account for the small He_N ($\bar{N} \approx 7 \times 10^6$) in Table 7.1.

Table 7.1: Number of dopant atoms $\bar{n}_X$ per He_N for different droplet sizes $\bar{N}$ and attenuations α as calculated with eqn (7.1).

α	$\bar{N}$	n_{Ag}	n_{Au}
0.75	1.7×10^{10}	2.6×10^6	2.0×10^6
0.5	7×10^6	–	650
0.2	1.7×10^{10}	6.8×10^5	5.4×10^5
0.04	1.7×10^{10}	–	1.1×10^5

For the given average droplet speed $v_D \approx 173\,m/s$ at $T_0 = 5.4\,K$[97] the pickup rates reach up to 2×10^{10} atoms per second. The energy transferred to the droplet this way, leads to an estimated increase of the droplet temperature from 0.37 K [25] to $\approx 1.05\,K$.[26,176] Since this temperature is still below the He superfluid transition temperature of 2.17 K, quantized vortices are preserved during the pickup.
As for a previous study,[11] we use a Tecnai TF20 from FEI Company for TEM and HRTEM measurements on the deposited clusters and nanowires. The microscope is equipped with an FEG source and a high resolution Gatan imaging filter with an UltraScan CCD camera (2048 px x 2048 px). All images are recorded with 200 kV acceleration voltage and a current density as low as $1\,pA\,nm^{-2}$ to prevent morphology changes of the particles during the imaging process.
Since the breakup of Ag nanowires becomes noticeable already at $\approx 260\,K$,[12] some substrates are cooled *via* the substrate holder to liquid nitrogen (LN_2) temperature for the investigation of continuous wires. After nanowire deposition, cooled substrates are immersed into LN_2 within 5 s after the substrate holder has been detached from its mount in the chamber. These substrates are subsequently transferred to a suited cryo-TEM holder (Gatan, Model 792) without being removed from the LN_2 bath. Other substrates are exposed to ambient conditions for times shorter than 5 min when transferred to the TEM. In all cases, the chamber is vented with gaseous N_2 (grade 5).

7.4 Computational details

7.4.1 Cluster growth and aggregation

Recently, we investigated the time dependence of two-particle-collisions in He_N via a combination of helium density functional theory and molecular dynamics simulations.[13] While it is computationally feasible to simulate the collision of just two dopants within a droplet on quantum-chemistry level, a similar description of the actual particle growth

process is not possible due to the large time-scale (milliseconds) and the system size (up to 10^6 metal atoms). Instead, we use the collision times calculated in ref. 13 as input for a simplified, global model of multiple cluster growth in large helium droplets. We study the number and mass of all metal particles as a function of time without keeping track of actual particle positions. Qualitatively, the model is the same for simulations of Au and Ag dopants. Therefore, only the Ag case shall be described here in greater detail.
According to the real experiment, cluster growth in He_N starts by the pickup of single atoms in a locally defined region. In the computer simulation we therefore add $\bar{n}_{Ag}$ (see Table 7.1) atoms with a fixed doping frequency. The latter is determined by the length of the pickup region and the velocity of the droplets in the He_N beam. Benchmark calculations show that the shrinking of the droplet due to evaporative cooling has a negligible impact on the doping cross-section for a fixed dopant vapor pressure. Therefore a constant doping frequency can be assumed. The dopants are spawned within the He_N volume at Landau velocity $v_\lambda \approx 56\,\mathrm{m/s}$.[32] The time it takes for two atoms to aggregate $\Delta t_a(2)$ is taken from ref. 13 and adjusted as follows: As more dopant-atoms are added to the droplet, the nucleation rate will increase until equilibrium conditions are reached. In our model, the nucleation frequency ($\frac{1}{\Delta t_a(j)}$) increases with the number of pairs that can be formed by j particles, hence

$$\Delta t_a(j) = \frac{2 \times \Delta t_a(2)}{j^2 - j}. \tag{7.2}$$

The shrinking of He_N due to evaporative cooling leads to a decrease of $\Delta t_a(2)$ according to ref. 13, which is considered in the simulation. On the other hand, assuming inelastic collisions and conservation of momentum, the velocity of metal clusters consisting of n atoms must decrease with increasing n ($n > 1$),

$$v(n) = v_\lambda \times \sqrt{\frac{8}{3\pi n}} \tag{7.3}$$

causing a growth of $\Delta t_a(2)$ proportional to $\frac{v_\lambda}{v(n)}$.
An individual "aggregation timer" is defined for every particle enclosed in the droplet, which reflects the actual droplet size and its current loading with dopants, *i.e.* the size-dependent velocities of all clusters which are currently present in the droplet. For the first two atoms picked up by the droplet this timer is set to $\Delta t_a(2)$, but it is reevaluated after every additional pickup following eqn. (7.2) & (7.3). Whenever an aggregation timer expires, the corresponding particle merges with another particle randomly chosen from the current set, but with a probability proportional to the velocity of the second particle (*i.e.* mergers with smaller particles are preferred). The merging leads to the growth of the first particle and to a reevaluation of its aggregation timer according to eqn. (7.3), while the second particle is removed from the set.
In order to study structural changes in our set of metal particles over time, we further

keep track of the shape of each resulting particle, which is determined by the amount of binding energy released during the coalescence. While the addition of single atoms to a preexisting cluster is treated in a way that yields a new spherical particle, two clusters only coalesce into a spherical particle if the released energy is large enough to completely melt at least one of the involved clusters. This treatment is based on the findings in ref. 42 & 44. The authors of the respective studies showed, that the surface energy released upon coagulation of two small metal clusters in He II can lead to melting and a subsequent merging of the individual particles into a single sphere. For larger clusters the released energy may not be sufficient for a complete melting, so that the clusters stick together and form nanowires.
We use a slightly different approach to calculate the energy release upon coagulation, as this allows us a better implementation of coagulation events between different sized clusters. To start, we calculate the binding energy per atom $E_\mathrm{b}(n)$ in a cluster consisting of n atoms using the empirical relation[106]

$$E_\mathrm{b}(n) = E_\mathrm{Ag} + 2^{\frac{1}{3}} \left(\frac{1}{2} D_\mathrm{e} - E_\mathrm{Ag} \right) n^{-\frac{1}{3}} \tag{7.4}$$

to estimate the released binding energy during the coalescence of two clusters consisting of n_1 and n_2 atoms respectively, as

$$\Delta E_\mathrm{b} = (n_1 + n_2) \times E_\mathrm{b}(n_1 + n_2) - (n_1 \times E_\mathrm{b}(n_1) + n_2 \times E_\mathrm{b}(n_2)). \tag{7.5}$$

$E_\mathrm{Ag} \approx 3\,\mathrm{eV}$ [57] denotes the Ag bulk binding energy and $D_\mathrm{e} = 1.65\,\mathrm{eV}$ [107] the binding energy of the Ag dimer. Both collision partners receive half of the released energy ΔE_b and the accompanying increase of the temperature of the clusters is evaluated by the simple approximation of the Dulong-Petit law. Clusters are considered as melted if their temperature exceeds the bulk melting temperature. Melting point depressions and latent heat are counteracting effects which are neglected due to their computationally difficult implementation for the given case of a time-dependent, broad cluster size distribution. Clusters which do not melt during coalescence are treated as one elongated particle. The particle size gets extended in only one dimension upon collision in order to simulate the process of nanowire formation. The new diameter is calculated as the mean diameter of the individual building blocks. The total number of individual particles (atoms, clusters and nanowires) contained in a single droplet (j), and the number of atoms (n_sp) within each spherical metal clusters (partially coalesced to wires) are tracked in the course of the computations. In the simulations, the clusters are cooled by their helium environment at a constant cooling rate r_c which depends on the particle surface area. This rate is adjusted to reflect the experimental results, meaning that the mean cluster diameters obtained from n_sp at the end of the simulation time should be comparable to the nanowire diameters observed in the experiment. We find that $r_\mathrm{c} \approx 190\,\mathrm{W/cm^2}$ reflects the experimental findings best. A change in r_c of $+20\,\%$ decreases the mean

cluster diameters obtained at the end of the growth process by $\approx 25\%$, while a decrease in r_c of 20 % increases the observed diameters by up to 50%. Gordon *et al.* derived the maximum diameter for which two equally sized metal spheres coagulate into a finally spherical particle inside of He II, for several different metals by considering the release in surface energy during the coalescence.[42] The values for r_c used in this work are considerably higher than those assumed in ref. 42, but still lower than the maximum cooling rates observed for small molecules in other He_N experiments.[104,105]
It is evident that without additional effects, given sufficient time, such an algorithm inevitably leads to one single final particle. In the real experiment the growth rates are damped due to the presence of vortices in large He_N. Particles caught by vortices are pinned to the vortex core and their motion is subsequently restricted to the direction along the vortex line.[38,152] The coalescence of captured particles along the vortex core is the reason for the formation of continuous nanowires, but is not directly captured in the presented model. However, we can choose the maximum simulation time to be equal to the mean time it takes for a particle to get trapped by a vortex contained in the He_N, which will be derived in the next section. This enables us to follow the growth of the building blocks of the final nanowires.

7.4.2 Cluster capture by vortices

Due to a pressure gradient around the vortex core,[35] a vortex exhibits an attractive force on particles in the droplet, whose magnitude is given by[74–76]

$$F_{\text{far}} \approx \left(\frac{a}{s}\right)^3 \frac{\rho_s \kappa^2}{3\pi} \tag{7.6}$$

for spherical particles in the far field and by

$$F_{\text{near}} \approx \rho_s \kappa^2 \log\left(\frac{a}{\zeta}\right) \tag{7.7}$$

near the vortex core, with the radius of the particle a, s the particle's normal distance to the vortex center, ζ the vortex core diameter, ρ_s the density of He II and $\kappa = h/m_{\text{He}}$ the quantum of circulation with h the Planck constant and m_{He} the atomic mass of He. In the simplest case where only one vortex is spanned across the droplet along the z-axis, $\bar{s}$ can be given analytically as

$$\bar{s} = \frac{3\pi}{16}\frac{d_D}{2} \tag{7.8}$$

We assume only one vortex per droplet for the following calculations. This assumption does not affect any of our arguments substantially. As estimated in the experimental section, the maximum He_N temperature does not exceed 1.05 K, resulting in a maximum fraction of normal fluid in the superfluid droplets of $\approx 1\,\%$.[35] After the pickup process, the droplet temperature will rapidly decrease to 0.37 K, so that the non-superfluid part

will become negligibly small. Together with the low velocities of clusters within the droplets, this justifies the neglect of the Stokes drag on the particles. The acceleration of particles towards the vortex due to the attractive forces given above can then be calculated simply by the application of Newton's equation of motion. The far-field and near-field forces of eqn. (7.6) & (7.7) are continuously connected to a resulting attractive force, and the equation of motion is numerically solved for the time t_{trap} it takes to get a particle trapped by a vortex core. We note that t_{trap} is nearly unaffected by an alteration of the particle radius a, since the corresponding increase of F_{far} is compensated by an equivalent increase of the particle's mass, while the influence of the short ranging F_{near} on t_{trap} is negligible. t_{trap} is chosen as the maximum simulation time for the cluster aggregation process, as for later times a significant amount of particles is restricted in the direction of motion.

7.5 Results and discussion

7.5.1 HRTEM images

In order to ensure that the fundamental growth process for different coinage metal clusters in vortex-free He_N ($\bar{N} \approx 7 \times 10^6$ atoms) is the same, we repeat our previous experiment,[11] but dope the droplets with Au instead of Ag. The TEM substrate is exposed to the Au-doped ($\alpha = 0.5$) He_N-beam for 480 s. Following the routine of ref. 11, the mean diameter of deposited Au_n is measured using the image processing package FIJI.[67] The obtained diameter $\bar{d}_{\mathrm{Au}} \approx 2.9(1)$ nm corresponds to $\bar{n}_{\mathrm{Au}} \approx 750$ assuming a spherical cluster shape and bulk density of the metal.[11] The discrepancy between this value and the one given in Table 7.1 lies within the measurement uncertainties. We note that even small deviations in either of the variables in eqn. (7.1) lead to a reasonable change in the estimated absolute number of dopants. Fortunately, this becomes less crucial for the larger droplets investigated.
HRTEM images are recorded and compared to corresponding simulations[11,69] in order to determine the morphologies of the clusters. While a complete analysis of the Au_n morphology distribution lies beyond the scope of this article, we report that the findings are in good agreement with the measurements on Ag_n.[11] Above all, we can clearly identify icosahedral (Ih) and decahedral (Dh) clusters for large cluster diameters ($d_{\mathrm{Au}} > 3$ nm) in numerous cases, two of which are exemplary depicted in Fig. 7.1. As will be shown later, these structures can be identified as building blocks in conglomerated nanowires.

In order to investigate the aggregation process in the presence of vortices, large He_N ($\bar{N} \approx 1.7 \times 10^{10}$ atoms) are doped with Ag or Au atoms, respectively. In both cases, the doping rate was adjusted such as to obtain either heavy ($\alpha = 0.75$) or weak ($\alpha = 0.2$) loading of the droplets. Subsequently, the TEM substrates are exposed to the droplet

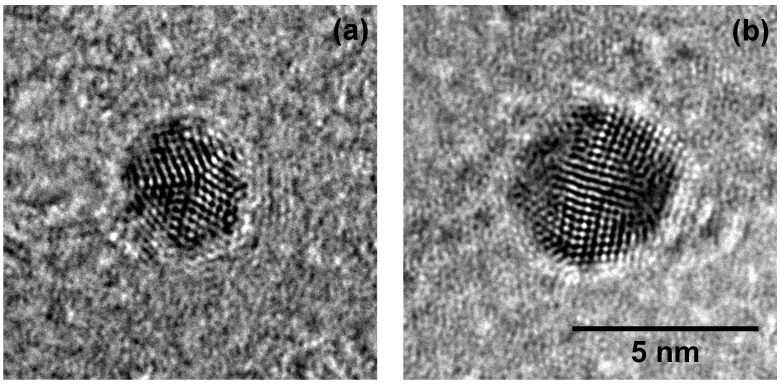

Figure 7.1: Decahedral (a) and icosahedral (b) Au_n synthesized in He_N free from vortices ($\bar{N} \approx 7 \times 10^6$ atoms), observed after deposition on a TEM substrate. The morphologies found agree well with those of Ag_n produced under comparable conditions.[11] Scale is the same for both images.

beam for 5 s. This time is chosen in order to obtain a decent surface coverage on one hand and to ensure an insignificant overlap between nanowires carried by different droplets. Fig. 7.2 (a) shows continuous Ag nanowires with a total length of several hundred nanometers and a mean diameter $\bar{d}_{\mathrm{nw}} \approx 5\,\mathrm{nm}$ (as obtained with $\alpha = 0.75$). Cryo-HRTEM measurements on these wires reveal multiple domains of face centered cubic (fcc) morphology (Fig. 7.2 (b)). Blurred parts along the wire are due to thickness oscillations, *i.e.* the structure is visible in the HRTEM measurements only for areas with similar thickness for a chosen defocus. Due to these perturbations in diameter, the wires break up *via* a surface diffusion process already below room temperature, as shown recently.[12] The outcome of this so-called Rayleigh breakup is the occurrence of chains of Ag segments as depicted in Fig. 7.3 (a) & (d), and previously found in other He_N [8–10] and He II bulk experiments.[46] HRTEM images reveal that in the case of heavy doping ($\alpha = 0.75$, left column of Fig. 7.3) these segments can either adopt polycrystalline fcc morphologies (Fig. 7.3 (b)) or exhibit large monocrystalline fcc domains (Fig. 7.3 (c)). No clusters with Ih or Dh morphology were found under these doping conditions.
This is completely different from the findings obtained with Ag and $\alpha = 0.2$ as depicted in the right column of Fig. 7.3. The existence of large Ihs (Fig. 7.3 (e) and top of (f)) and Dhs (bottom of Fig. 7.3 (f)) is dominating, being followed by particles with large monocrystalline domains. In contrast to the observations made for $\alpha = 0.75$ we find only a very small amount of polycrystalline particles for weak loading of the droplets.

For large Au nanowires ($\alpha = 0.75$) at LN_2 temperature, we find the same branched structures as depicted in Fig. 7.2 (a) for Ag. During the heat-up to room temperature Au nanowires undergo a surface smoothing but do not break into multiple segments (see Fig. 7.4 (a)). The inner morphology (Fig. 7.4 (b)) resembles that of continuous Ag wires, *i.e.* multiple fcc domains can be found. The wires resemble those found in bulk

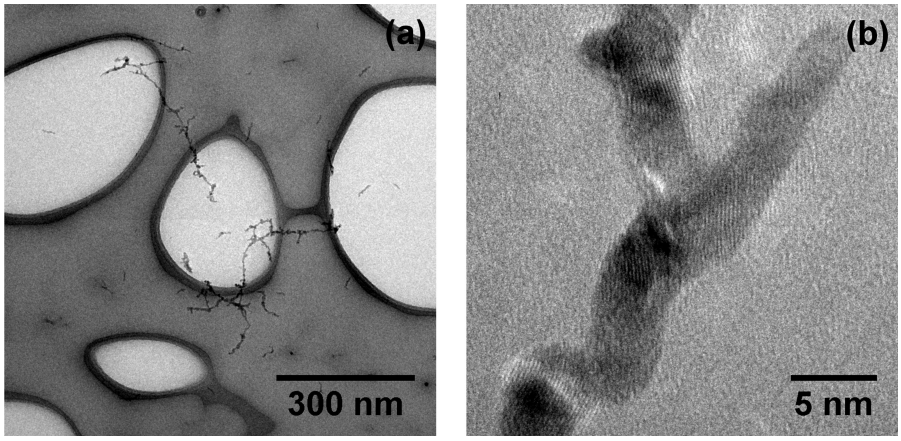

Figure 7.2: Ag nanowires synthesized in He_N ($\bar{N} \approx 1.7 \times 10^{10}$), deposited and imaged on a LN_2 cooled a-c TEM grid. Continuous branched wires (a) show polycrystalline domains in HRTEM mode (b).

He II experiments in diameter, shape and morphology.[40,41,45,47] Under low doping conditions ($\alpha = 0.2$) we find short but continuous Au wires of slightly smaller diameter (Fig. 7.4 (c)). In numerous cases, these wires contain spherical enclosures of ambiguous morphology, while the rest of the wire consists of multiple fcc domains (Fig. 7.4 (d)).

Further reduction of the amount of doped Au atoms ($\alpha = 0.04$) leads to the observation of segmented Au nanowires (Fig. 7.5). Assuming conserved volumes, we calculate the mean diameter of the initial wires as $\bar{d}_{\mathrm{nw}} \approx 3.0(1)\,\mathrm{nm}$. The distance between centers of neighboring segments $\lambda \approx (13 \pm 4)\,\mathrm{nm}$ is in very good agreement with the theoretically derived relationship $2\lambda/d = 8.89$ for the Rayleigh breakup of an ideal cylinder.[124] The HRTEM image in Fig. 7.5 shows a small decahedral cluster (marked by arrow) between two clusters of indistinct morphology.

As shown in our previous work,[12] the breakup of Ag nanowires can be explained by the diffusion of wire surface atoms from thinner to thicker parts of the wire due to a gradient of the chemical potential. It is therefore convenient to assume that the observed morphologies are present already inside the initially continuous wires, and that they become clearly visible in the course of the breakup. It has been shown in several theoretical studies that the icosahedral shape is energetically preferred for small metal clusters, while intermediate and large clusters seem to be more stable in Dh and fcc morphologies, respectively (see ref. 81,96,100 and references therein). Further, it has been determined by MD simulations that the fcc morphology is preferred over the icosahedral morphology for Ag clusters with sizes larger than 1590 atoms ($d_{\mathrm{Ag}} \approx 3.7\,\mathrm{nm}$).[177] The Ihs depicted in Fig. 7.3 (e) & (f) both exhibit diameters larger than 5 nm ($n > 3900$ atoms). Therefore, it can be excluded that they were formed from fcc particles *via* a restructuring process. Such a growth sequence would further strongly contradict MD simulations

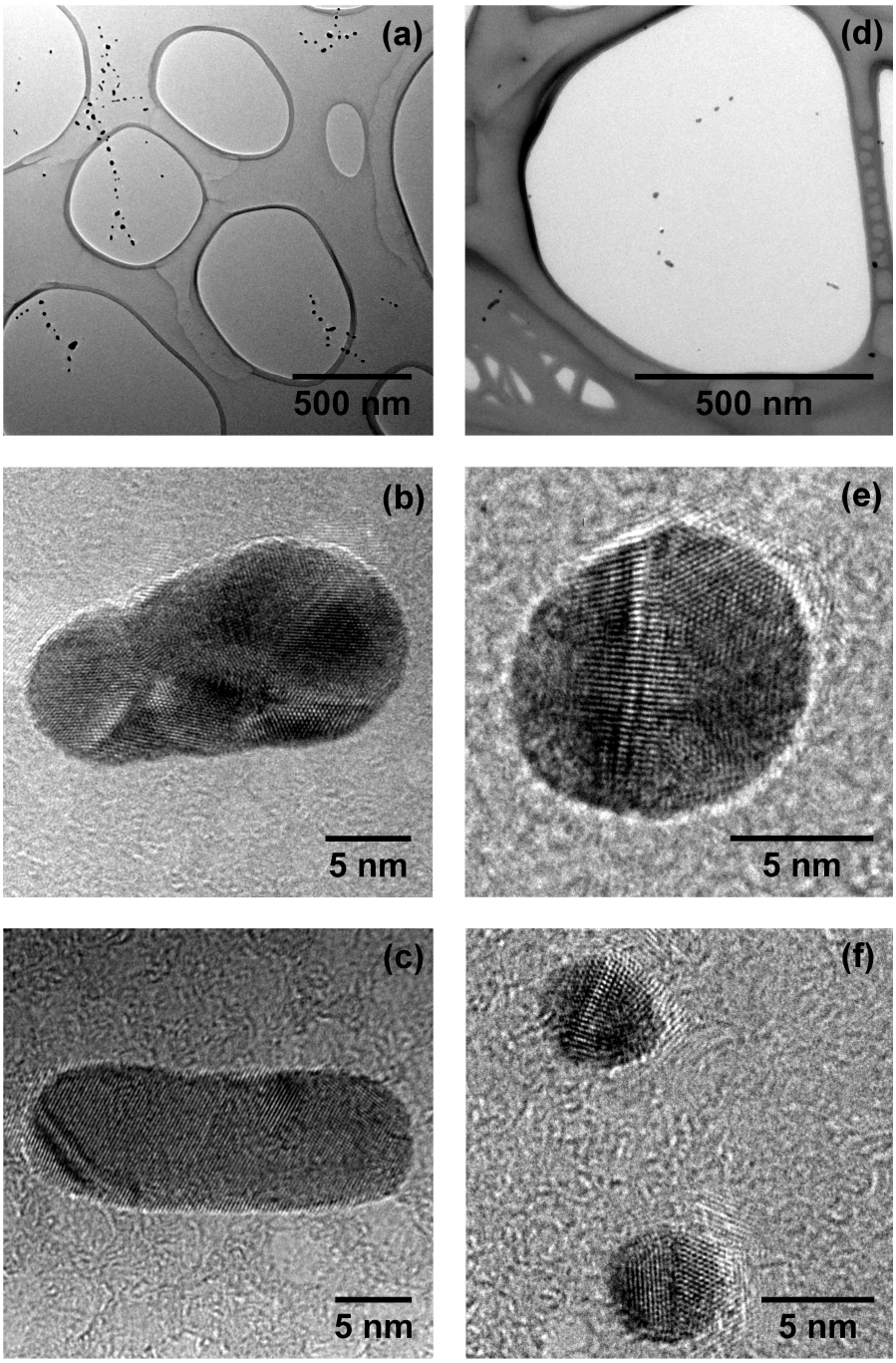

Figure 7.3: Chains of Ag segments resulting from the breakup of nanowires as depicted in Fig. 7.2. *Left column:* (a) heavy doping of the droplet ($\alpha = 0.75$). HRTEM measurements reveal either polycrystalline morphology (b) or large monocrystalline domains (c). *Right column:* (d) weak doping ($\alpha = 0.2$). Silver segments resulting from the breakup of small nanowires often exhibit fivefold symmetries, *i.e.* icosahedral ((e), top of (f)) or decahedral (bottom of (f)) morphologies.

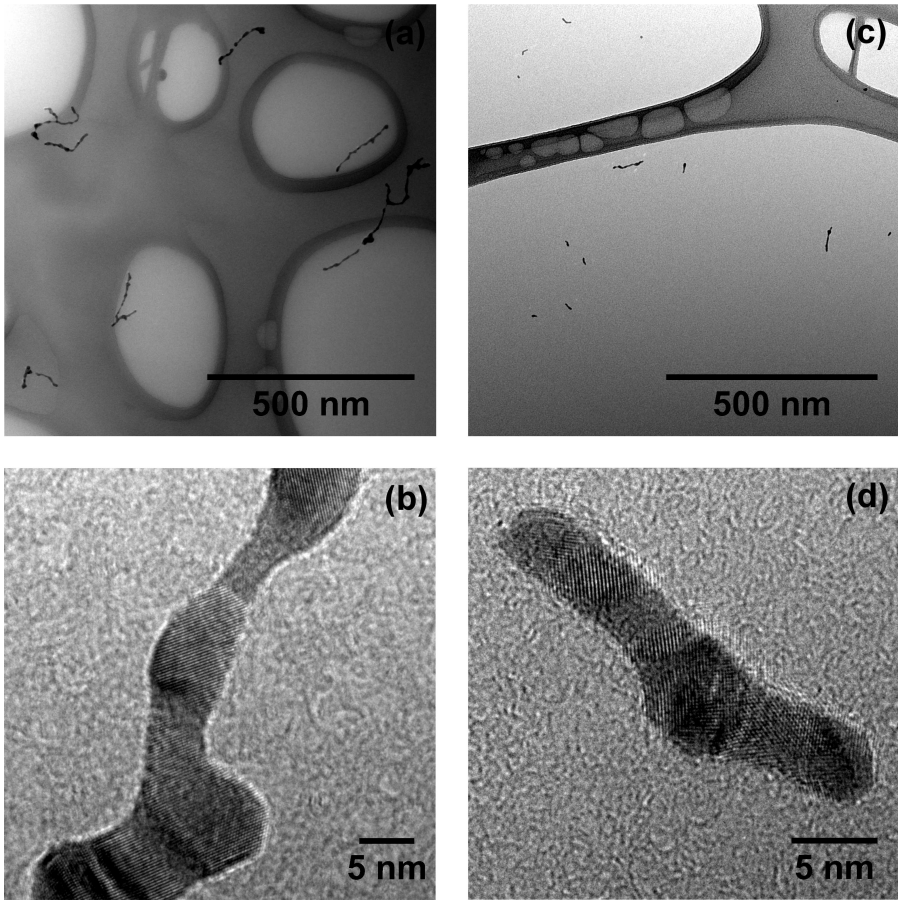

Figure 7.4: Au nanowires at room temperature. *Left column:* heavy doping of the droplet ($\alpha = 0.75$). Nanowires exhibit a smoothed surface and are continuous over several hundred nanometers (a). Multiple fcc domains are observed along a single wire in HRTEM measurements (b). *Right column:* weak doping ($\alpha = 0.2$) leads to short continuous nanowires of about the same diameter (c). HRTEM images (d) reveal spherical enclosures with ambiguous morphology in a wire consisting of several fcc domains.

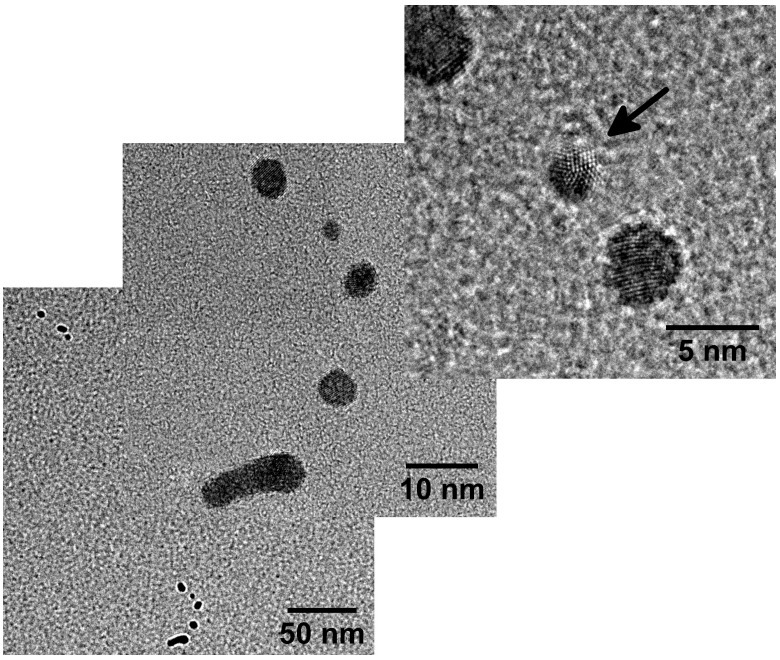

Figure 7.5: Segmented Au nanowire as resulting from very weak doping ($\alpha = 0.04$). The arrow marks a small decahedral cluster in the HRTEM image.

recently performed by our own group.[15] In simulations of silver clusters we could observe the conversion of Ihs and Dhs into fcc particles during surface deposition due to a recrystallization, but not a single event of an inverse transformation from fcc into a particle of fivefold symmetry.

7.5.2 Simulation of the growth process

In order to explain the different morphologies observed we simulate the cluster growth process for different doping rates, *i.e.* different attenuation coefficients α. The maximum simulation time is chosen to equal the mean time it takes for a particle to get trapped by a vortex (t_{trap}). The pickup of atoms and their coagulation into clusters lead to a shrinking of the droplets, which influences $\bar{s}$ given in eqn. (7.8). It turns out that t_{trap} is long compared to the timescale of cluster growth, which equals the timescale of the doping process ($\approx 130\,\mu$s) determined by the flight time of the He_N through the pickup region. It is therefore convenient to calculate $\bar{s}$ and subsequently t_{trap} using the droplet diameters of the attenuated droplet beam $d_{\mathrm{D},\alpha}$. The results for t_{trap} are summarized in Table 7.2.

Table 7.2: Time t_{trap} until particles get trapped by a vortex due to the attractive force given by eqn. (7.6) & (7.7). $d_{\mathrm{D},\alpha}$ is calculated assuming an initial He_N size of $\bar{N} = 1.7 \times 10^{10}$ atoms. $\bar{s}$ is calculated using eqn. (7.8) and $d_{\mathrm{D},\alpha}$.

element	α	d_{D} / nm	t_{trap} / ms
Ag	0.75	720	1.4
	0.2	1060	3.0
Au	0.75	720	1.8
	0.2	1060	4.0
	0.04	1130	4.6

The time evolution of the total number of particles j present in one helium droplet is depicted in Fig. 7.6 for the attenuations realized in the experiment. It can be seen that in both cases the number of individual particles quickly drops after the pickup of new atoms has ended and that the following agglomeration takes place on a much longer timescale. The reason for this behaviour lies in the slow velocities of large clusters (see

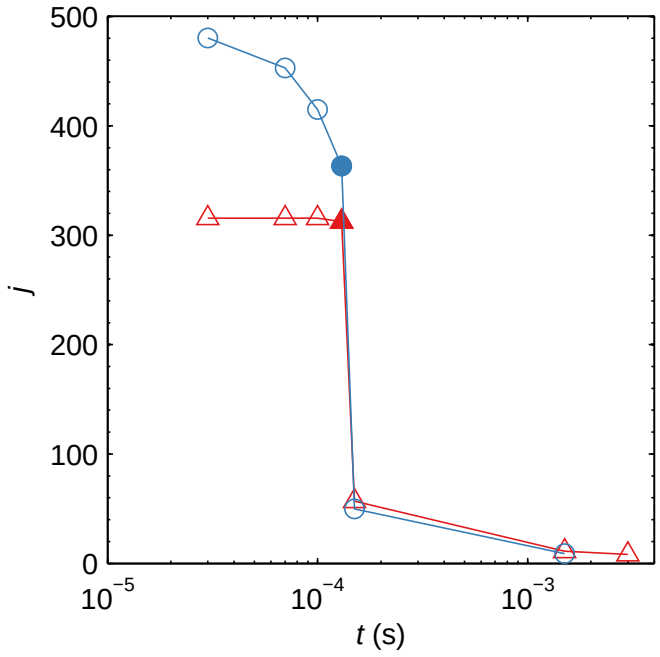

Figure 7.6: Time evolution of the number of particles j present in one He_N for $\alpha = 0.2$ (red triangles) and $\alpha = 0.75$ (blue circles). The pickup process ends after $\approx 130\,\mu$s, marked by full symbols. Lines are drawn to guide the eye.

eqn. (7.3)) compared to the Landau velocity assumed for freshly spawned metal atoms in the simulation. This finding has also been verified experimentally by the observation of bimetallic core-shell clusters with single or double cores.[17] In order to realize the

latter case two clusters have to grow in the droplet in the first of two consecutive pickup regions and have to stay separated until the droplets reach the second pickup cell. The corresponding He_N flight time can be estimated as ≈ 1 ms in our apparatus.[18]
Fig. 7.6 also reveals a decrease of j during the pickup process for larger attenuations, while j seems to stay nearly constant for $\alpha = 0.2$. This behaviour can be explained by the shrinking of He_N which is much more prominent for $\alpha = 0.75$ as can be seen from Table 7.2. The He_N flight time between the pickup cell and the TEM substrate is ≈ 6 ms. Comparing this to the timescale of cluster growth and to t_{trap}, it is evident that most clusters have to grow outside the vortex in a multicenter aggregation process, and that nearly all clusters will be captured by the vortex before substrate deposition.
The monitoring of the number of particles contained in spherical clusters n_{sp} can give us a further important insight into the agglomeration process. Fig. 7.7 depicts the absolute occurrence of a certain value of n_{sp} for all spherical particles contained in a single He_N. The lines shown correspond to the smoothed envelopes of histograms. Every histogram is calculated from several simulation runs for every depicted time of the aggregation process. Snapshots are taken during the pickup process at 30, 70, 130 (end of the pickup) and at 150 μs. As explained in the computational details, spherical clusters which do not melt during agglomeration are treated as elongated particles, built from the initially spherical collision partners. n_{sp} includes all spherical clusters, regardless whether they are present as building blocks of elongated structures or as individual spheres. From this, it follows that Fig. 7.7 directly reflects the sizes of the last complete melting of the clusters. A merging event which does not lead to molten clusters does affect j, but not the depicted histograms of n_{sp}.
The large amount of small clusters present in the droplets during the pickup process is efficiently reduced after the addition of new atoms has ended, which is in good agreement with the behaviour depicted in Fig. 7.6. In fact, the final distribution of spherical building blocks is reached after 150 μs. This means that melting processes are practically limited to the pickup time, and that 20 μs after the end of pickup melting is negligible. After 150 μs, the spherical clusters still coagulate to form the final nanoparticles. This process takes the time which we calculated as t_{trap} earlier.
The most striking feature in Fig. 7.7 is that the positions of the histogram maxima are determined by the attenuation, *i.e.* the doping rate. A high doping rate in case of $\alpha = 0.75$ leads to a stronger heating of the clusters as more atoms impinge within a given time while the cooling rate r_{c} is the same as for weaker doping. The effect is further enhanced by the pronounced shrinking of the droplet under heavy doping conditions, and leads to a slight shift of the histogram maxima towards higher values of n_{sp} in Fig. 7.7. We can extract from the histograms $\bar{n}_{\mathrm{sp}} \approx 600$ ($\bar{d}_{\mathrm{Ag}} \approx 2.7$ nm) for $\alpha = 0.2$ and $\bar{n}_{\mathrm{sp}} \approx 3000$ ($\bar{d}_{\mathrm{Ag}} \approx 4.6$ nm) for $\alpha = 0.75$, which is also in good agreement with the diameters observed for deposited nanowires in the cryo-TEM images. As explained above, the fcc structure is energetically preferred over the Ih morphology for cluster sizes

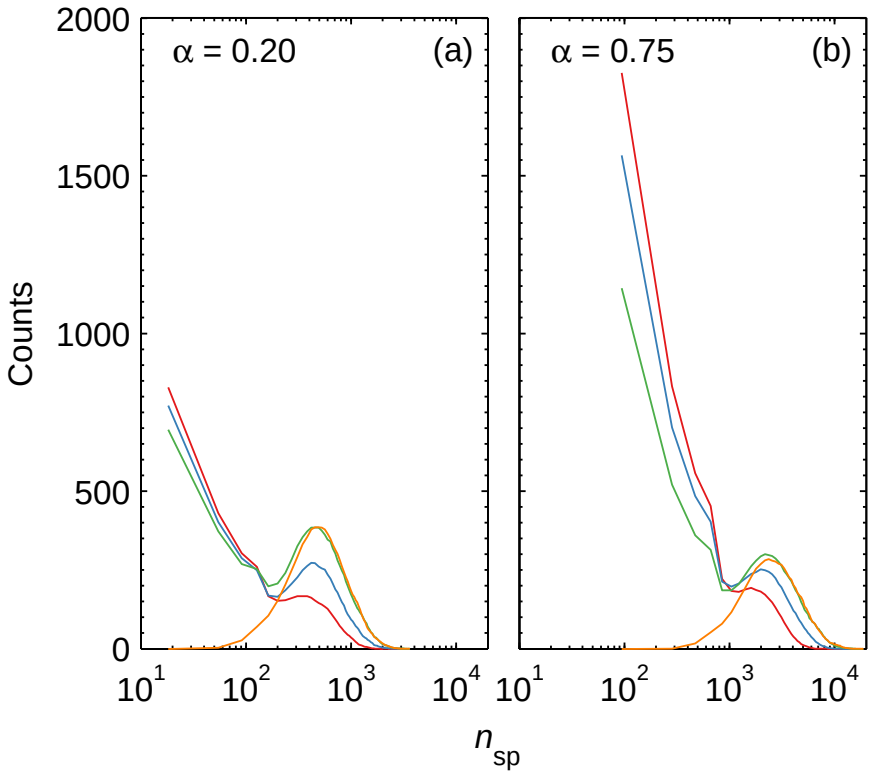

Figure 7.7: Number of atoms n_{sp} building up the spherical clusters contained in a single He_N for $\alpha = 0.2$ (a) and $\alpha = 0.75$ (b). Lines are envelopes of histograms taken at different times of the aggregation process: 30 μs (red), 70 μs (blue), 130 μs (green), 150 μs (orange).

larger than 1590 atoms ($d_{\mathrm{Ag}} \approx 3.7\,\mathrm{nm}$).[177] Since the clusters solidify from a molten state, it is justified to assume that the formation of Ihs is much more probable at $\alpha = 0.2$ than it is for $\alpha = 0.75$. This explains the exclusive findings of particles of fivefold symmetry under weak doping conditions in the experiment.

7.6 Conclusions

Experimentally observed morphologies of He_N-grown Au and Ag nanowires depend on the rate of doping with metal atoms during the pickup process. In the first step of the growth process, multiple clusters are formed within a droplet in a multicenter aggregation process. At low doping rates, a large portion of these clusters exhibits fivefold symmetries, while at high rates the presence of the fcc structure is dominating. In the second step of the growth process these clusters are captured by vortices and coagulate into nanowires. According to our simulations, their coagulation does not result in a complete melting of the single clusters. This is related to the large cluster sizes and the relatively low collision rates at this stage of the nanowire growth. Therefore, the morphologies of the initial building blocks, *i.e.* the coagulating clusters, are preserved within the nanowires.
We believe that our experimental findings and the computational model presented will be of use in future attempts of gaining better control over the synthesis and the design of nanostructures within He_N. It would also be desirable to determine the morphologies of clusters enclosed in the He_N before substrate deposition, *e.g.* by X-ray scattering, a technique which has been exploited recently to investigate the morphologies of large free Ag nanoparticles.[178]

The following is reproduced from:
"Correction: The impact of doping rates on the morphologies of silver and gold nanowires grown in helium nanodroplets" by **Alexander Volk**, Philipp Thaler, Daniel Knez, Andreas W. Hauser, Johannes Steuer, Werner Grogger, Ferdinand Hofer and Wolfgang E. Ernst, in *Physical Chemistry Chemical Physics* **18**, 3359 (2016)- Published by the PCCP Owner Societies.

7.7 Correction

Due to a unit conversion error, the authors would like to correct the values for t_{trap} given in Table 7.2 of the published article, as seen in the amended Table below.

Table 7.2.1: Time t_{trap} until particles get trapped by a vortex due to the attractive force given by eqn. (7.6) & (7.7). $d_{\mathrm{D},\alpha}$ is calculated assuming an initial He_N size of $\bar{N} = 1.7 \times 10^{10}$ atoms. $\bar{s}$ is calculated using eqn. (7.8) and $d_{\mathrm{D},\alpha}$.

element	α	d_{D} / nm	t_{trap} / μs
Ag	0.75	720	24
	0.2	1060	52
Au	0.75	720	33
	0.2	1060	71
	0.04	1130	80

These changes of t_{trap} affect some of the statements in the published article. Most notably, t_{trap} is now shorter than the pickup process that takes place over the length of the pickup cell. The so-called pickup time just means that during 130 μs new atoms are added.
At first sight, one is tempted to assume a more complex growth process due to simultaneous effects of doping, cluster formation, and vortex trapping. However, this is not the case, since cluster formation times are still shorter than vortex trapping times t_{trap}. In our cluster growth model following eqn. 7.2 and 7.3 of the article, metal clusters of 100 atoms for light doping ($\alpha = 0.2$) and 1000 atoms for heavy doping ($\alpha = 0.75$) have formed already within $\approx 1\,\mu$s after pickup. The size distribution in Fig. 7.7 obtains its final shape very quickly and the changes between 30 μs (red curve) and 150 μs (orange curve) reflect only the subsequent growth due to atoms added over the 130 μs pickup time. Most of the 'newcomers' will become embedded into that stable cluster size distribution before they are getting trapped in a vortex (compare the envelopes at 130 μs (green curve) and 150 μs in Fig. 7.7 of the main article). A slight shift of the maximum in the distribution functions towards larger particles with increasing time stems from

the higher collision rates which occur due to the reduction of the droplet volume via He evaporation.
Due to this fact, the final morphology of most particles is still determined before they get captured by vortices. Our conclusions on the morphologies of the nanowires remain the same and are in agreement with the experimental results observed in the HRTEM pictures.

8 Summary

In the present work, the growth of nanoclusters and nanowires in superfluid helium droplets is investigated by means of experiments and computer simulations. It turns out that despite the ultracold environment offered by the droplets, the morphologies of the obtained nanoparticles seem to be determined by a particle heatup due to the release of binding energy during cluster growth.

In small He_N ($N \leq 10^7$ atoms), the moderate pickup rates ($\approx 8 \times 10^6$ atoms/s) enable the cooling of embedded clusters (Ag_n or Au_n) to the droplet temperature between successive pickup events. For the small cluster sizes ($n < 100$ atoms) present at the beginning of cluster growth, the binding energy released upon addition of a single metal atom is sufficient to melt the clusters. During their subsequent cooling to the droplet temperature, the clusters adopt morphologies which are energetically favorable at the respective size. In most cases this leads to fivefold particle symmetries (icosahedral or decahedral). In the later course of this single-center growth process, the released energies are not sufficient to melt the clusters. Hence, the initial morphologies are retained and atoms are attached to the preexisting clusters in a shell-by-shell growth.

For the further treatment of cluster growth processes in He_N, the dimer collision times of coinage metal atoms in the droplets are calculated by MD-simulations. The He_N influence on the diatomic dopant potential is evaluated by DFT calculations, but turns out to be negligibly small. The obtained dimer collision times in He_N with $1\,\mu$m diameter lie in the range of $10 - 15\,\mu$s.

These values enter a rate based model for the description of the cluster growth process in large He_N ($N \approx 2 \times 10^{10}$ atoms), but are corrected for the simultaneous presence of multiple nanoparticles in one droplet. The respective model calculations reveal that for the high pickup rates ($\approx 2 \times 10^{10}$ atoms/s) used in the experiments, cluster formation takes place simultaneously at different droplet sites in a multicenter aggregation process. Due to the higher collision rates and associated heating rates in this process, melting is still possible at larger cluster sizes. As shown by the respective simulations, the final morphology of the clusters is determined by the preset pickup rate. Smaller rates favor the formation of fivefold symmetries, while at higher rates the fcc structure is adopted. Large He_N contain quantized vortices, which capture the immersed nanoparticles and cause their directed growth into nanowires. It turns out, that the cluster formation time ($\approx 1\,\mu$s) is shorter than the time it takes for the particles to get trapped by the vortices ($\approx 20 - 80\,\mu$s). Therefore, the building blocks of the nanowires exhibit the morphologies

which have formed *prior* in the multicenter aggregation process.
The general validity of continuous metallic nanowire formation in vortex containing He_N is proven for the case of Ag. After nanowire deposition on a substrate cooled to cryogenic temperatures, the breakup of the wires is tracked *in situ* in a transmission electron microscope. Complementary simulations prove that the breakup process is related to thermally activated diffusion of silver atoms along the wire surface. The starting temperature of this process is determined as $\approx 260\,\mathrm{K}$. These experiments do not only resolve the ongoing discussion on the reason for the previously observed segmented lines of Ag_n in the He_N-community, but further represent the first investigation of thermal stability of ultrathin (diameter $\approx 5\,\mathrm{nm}$) Ag nanowires without the influence of a stabilising template. This is a typical example for the capability of the He_N technique to provide new important insights in material properties at the nanoscale.

9 Bibliography

[1] Mozhayskiy, V., Slipchenko, M. N., Adamchuk, V. K. & Vilesov, A. F. Use of helium nanodroplets for assembly, transport, and surface deposition of large molecular and atomic clusters. *J. Chem. Phys.* **127**, 094701 (2007).

[2] Loginov, E., Gomez, L. F. & Vilesov, A. F. Surface deposition and imaging of large Ag clusters formed in He droplets. *J. Phys. Chem. A* **115**, 7199–7204 (2011).

[3] Boatwright, A., Feng, C., Spence, D., Latimer, E., Binns, C., Ellis, A. M. & Yang, S. Helium droplets: a new route to nanoparticles. *Faraday Discuss.* **162**, 113–124 (2013).

[4] Yang, S., Ellis, A. M., Spence, D., Feng, C., Boatwright, A., Latimer, E. & Binns, C. Growing metal nanoparticles in superfluid helium. *Nanoscale* **5**, 11545–11553 (2013).

[5] Emery, S. B., Rider, K. B., Little, B. K., Schrand, A. M. & Lindsay, C. M. Magnesium cluster film synthesis by helium nanodroplets. *J. Chem. Phys.* **139**, 054307 (2013).

[6] Emery, S. B., Rider, K. B. & Lindsay, C. M. Stabilized magnesium/perfluoropolyether nanocomposite films by helium droplet cluster assembly. *Propellants Explos. Pyrotech.* **39**, 161–165 (2014).

[7] Emery, S. B., Xin, Y., Ridge, C. J., Buszek, R. J., Boatz, J. A., Boyle, J. M., Little, B. K. & Lindsay, C. M. Unusual behavior in magnesium-copper cluster matter produced by helium droplet mediated deposition. *J. Chem. Phys.* **142**, 084307 (2015).

[8] Gomez, L. F., Loginov, E. & Vilesov, A. F. Traces of vortices in superfluid helium droplets. *Phys. Rev. Lett.* **108**, 155302 (2012).

[9] Latimer, E., Spence, D., Feng, C., Boatwright, A., Ellis, A. M. & Yang, S. Preparation of ultrathin nanowires using superfluid helium droplets. *Nano Lett.* **14**, 2902–2906 (2014).

[10] Spence, D., Latimer, E., Feng, C., Boatwright, A., Ellis, A. M. & Yang, S. Vortex-induced aggregation in superfluid helium droplets. *Phys. Chem. Chem. Phys.* **16**, 6903–6906 (2014).

[11] Volk, A., Thaler, P., Koch, M., Fisslthaler, E., Grogger, W. & Ernst, W. E. High resolution electron microscopy of Ag-clusters in crystalline and non-crystalline morphologies grown inside superfluid helium nanodroplets. *J. Chem. Phys.* **138**, 214312 (2013).

[12] Volk, A., Knez, D., Thaler, P., Hauser, A. W., Grogger, W., Hofer, F. & Ernst, W. E. Thermal instabilities and Rayleigh breakup of ultrathin silver nanowires grown in helium nanodroplets. *Phys. Chem. Chem. Phys.* **17**, 24570–24575 (2015).

[13] Hauser, A. W., Volk, A., Thaler, P. & Ernst, W. E. Atomic collisions in suprafluid helium-nanodroplets: timescales for metal-cluster formation derived from He-density functional theory. *Phys. Chem. Chem. Phys.* **17**, 10805–10812 (2015).

[14] Volk, A., Thaler, P., Knez, D., Hauser, A. W., Steurer, J., Grogger, W., Hofer, F. & Ernst, W. E. The impact of doping rates on the morphologies of silver and gold nanowires grown in helium nanodroplets. *Phys. Chem. Chem. Phys.* **18**, 1451–1459 (2016).

[15] Thaler, P., Volk, A., Ratschek, M., Koch, M. & Ernst, W. E. Molecular dynamics simulation of the deposition process of cold Ag-clusters under different landing conditions. *J. Chem. Phys.* **140**, 044326 (2014).

[16] Thaler, P., Volk, A., Lackner, F., Steurer, J., Knez, D., Grogger, W., Hofer, F. & Ernst, W. E. Formation of bimetallic core-shell nanowires along vortices in superfluid He nanodroplets. *Phys. Rev. B* **90**, 155442 (2014).

[17] Haberfehlner, G., Thaler, P., Knez, D., Volk, A., Hofer, F., Ernst, W. E. & Kothleitner, G. Formation of bimetallic clusters in superfluid helium nanodroplets analysed by atomic resolution electron tomography. *Nat. Commun.* **6**, 8779 (2015).

[18] Thaler, P., Volk, A., Knez, D., Lackner, F., Haberfehlner, G., Steurer, J., Schnedlitz, M. & Ernst, W. E. Synthesis of nanoparticles in helium droplets- a characterization comparing mass-spectra and electron microscopy data. *J. Chem. Phys.* **143**, 134201 (2015).

[19] Lohr, L. L. & Blinder, S. M. The weakest link: Bonding between helium atoms. *J. Chem. Educ.* **84**, 860–863 (2007).

[20] Grisenti, R. E., Schöllkopf, W., Toennies, J. P., Hegerfeldt, G. C., Köhler, T. & Stoll, M. Determination of the bond length and binding energy of the helium

dimer by diffraction from a transmission grating. *Phys. Rev. Lett.* **85**, 2284–2287 (2000).

[21] Toennies, J. P. & Vilesov, A. F. Superfluid helium droplets: a uniquely cold nanomatrix for molecules and molecular complexes. *Angew. Chem. Int. Ed.* **43**, 2622–2648 (2004).

[22] Kapitza, P. Viscosity of liquid helium below the λ-point. *Nature* **141**, 74 (1938).

[23] Donnelly, R. J. & Barenghi, C. F. The observed properties of liquid helium at the saturated vapor pressure. *J. Phys. Chem. Ref. Data* **27**, 1217–1274 (1998).

[24] Becker, E. W., Klingelhöfer, R. & Lohse, R. Strahlen aus kondensiertem Helium im Hochvakuum. *Z. Naturforschg.* **16 a**, 1259 (1961).

[25] Hartmann, M., Miller, R. E., Toennies, J. P. & Vilesov, A. Rotationally resolved spectroscopy of SF_6 in liquid helium clusters: a molecular probe of cluster temperature. *Phys. Rev. Lett.* **75**, 1566–1569 (1995).

[26] Brink, D. M. & Stringari, S. Density of states and evaporation rate of helium clusters. *Z. Phys. D: Atoms, Molecules and Clusters* **15**, 257–263 (1990).

[27] Grebenev, S., Toennies, J. P. & Vilesov, A. F. Superfluidity within a small helium-4 cluster: the microscopic Andronikashvili experiment. *Science* **279**, 2083–2086 (1998).

[28] Gough, T. E., Mengel, M., Rowntree, P. A. & Scoles, G. Infrared spectroscopy at the surface of clusters: SF_6 on Ar. *J. Chem. Phys.* **83**, 4958–4961 (1985).

[29] Callegari, C. & Ernst, W. E. Helium droplets as nanocryostats for molecular spectroscopy - from the vacuum ultraviolet to the microwave regime. In Merkt, F. & Quack, M. (eds.) *Handbook of High Resolution Spectroscopy*, vol. 3, 1551–1594 (John Wiley & Sons, Chichester, 2011).

[30] Coccia, E. & Gianturco, F. A. Attachment energetics of quantum dopants in a weakly interacting quantum solvent: ^{1}H, ^{2}H and ^{3}H in small ^{4}He clusters. *J. Phys. Chem. A* **114**, 3221–3228 (2010).

[31] Ancilotto, F., Lerner, P. B. & Cole, M. W. Physics of solvation. *J. Low Temp. Phys.* **101**, 1123–1146 (1995).

[32] Brauer, N. B., Smolarek, S., Loginov, E., Mateo, D., Hernando, A., Pi, M., Barranco, M., Buma, W. J. & Drabbels, M. Critical Landau velocity in helium nanodroplets. *Phys. Rev. Lett.* **111**, 153002 (2013).

[33] Tiggesbäumker, J. & Stienkemeier, F. Formation and properties of metal clusters isolated in helium droplets. *Phys. Chem. Chem. Phys.* **9**, 4748–4770 (2007).

[34] Mudrich, M. & Stienkemeier, F. Photoionisaton of pure and doped helium nanodroplets. *Int. Rev. Phys. Chem.* **33**, 301–339 (2014).

[35] Donelly, R. J. *Quantized Vortices in Helium II* (Cambridge University Press, Cambridge, 1991).

[36] Williams, G. A. & Packard, R. E. Photographs of quantized vortex lines in rotating He II. *Phys. Rev. Lett.* **33**, 280–283 (1974).

[37] Yarmchuk, E. J., Gordon, M. J. V. & Packard, R. E. Observation of stationary vortex arrays in rotating superfluid helium. *Phys. Rev. Lett.* **43**, 214–217 (1979).

[38] Bewley, G. P., Lathrop, D. P. & Sreenivasan, K. R. Superfluid helium: Visualization of quantized vortices. *Nature* **441**, 588 (2006).

[39] Gordon, E. B., Karabulin, A. V., Matyushenko, V. I., Sizov, V. D. & Khodos, I. I. Electric properties of metallic nanowires obtained in quantum vortices of superfluid helium. *Low Temp. Phys.* **36**, 590–595 (2010).

[40] Moroshkin, P., Lebedev, V., Grobety, B., Neururer, C., Gordon, E. B. & Weis, A. Nanowire formation by gold nano-fragment coalescence on quantized vortices in He II. *EPL* **90**, 34002 (2010).

[41] Lebedev, V., Moroshkin, P., Grobety, B., Gordon, E. & Weis, A. Formation of metallic nanowires by laser ablation in liquid helium. *J. Low Temp. Phys.* **165**, 166–176 (2011).

[42] Gordon, E. B., Karabulin, A. V., Matyushenko, V. I., Sizov, V. D. & Khodos, I. I. Structure of metallic nanowires and nanoclusters formed in superfluid helium. *J. Exp. Theor. Phys.* **112**, 1061–1070 (2011).

[43] Gordon, E. B., Karabulin, A. V., Matyushenko, V. I., Sizov, V. D. & Khodos, I. I. The electrical conductivity of bundles of superconducting nanowires produced by laser ablation of metals in superfluid helium. *Appl. Phys. Lett.* **101**, 052605 (2012).

[44] Gordon, E. B., Karabulin, A. V., Matyushenko, V. I., Sizov, V. D. & Khodos, I. I. The role of vortices in the process of impurity nanoparticles coalescence in liquid helium. *Chem. Phys. Lett.* **519-520**, 64–68 (2012).

[45] Gordon, E. B., Karabulin, A. V., Morozov, A. A., Matyushenko, V. I., Sizov, V. D. & Khodos, I. I. Structure and properties of platinum, gold and mercury nanowires grown in superfluid helium. *Phys. Chem. Lett.* **5**, 1072–1076 (2014).

[46] Gordon, E., Karabulin, A., Matyushenko, V., Sizov, V. & Khodos, I. Stability and structure of nanowires grown from silver, copper and their alloys by laser ablation into superfluid helium. *Phys. Chem. Chem. Phys.* **16**, 25229–25233 (2014).

[47] Gordon, E. B., Karabulin, A. V., Matyushenko, V. I. & Khodos, I. I. Experimental study of thermal stability of thin nanowires. *J. Phys. Chem. A* **119**, 2490–2501 (2015).

[48] Gordon, E. B., Karabulin, A. V., Matyushenko, V. I., Sizov, V. D. & Khodos, I. I. Production of ultrathin nanowires from refractory metals (Nb, Re, W, Mo) by laser ablation in superfluid helium. *Laser Phys. Lett.* **12**, 096002 (2015).

[49] Dalfovo, F., Mayol, R., Pi, M. & Barranco, M. Pinning of quantized vortices in helium drops by dopant atoms and molecules. *Phys. Rev. Lett.* **85**, 1028–1031 (2000).

[50] Lehmann, K. K. & Schmied, R. Energetics and possible formation and decay mechanisms of vortices in helium nanodroplets. *Phys. Rev. B* **68**, 224520 (2003).

[51] Ancilotto, F., Barranco, M. & Pi, M. Probing vortices in ^{4}He nanodroplets. *Phys. Rev. Lett.* **91**, 105302 (2003).

[52] Sola, E., Casulleras, J. & Boronat, J. Quantized vortices in ^{4}He droplets: a quantum monte carlo study. *Phys. Rev. B* **76**, 052507 (2007).

[53] Gomez, L. F., Ferguson, K. R., Cryan, J. P., Bacellar, C., Tanyag, R. M. P., Jones, C., Schorb, S., Anielski, D., Belkacem, A., Bernando, C., Boll, R., Bozek, J., Carron, S., Chen, G., Delmas, T., Englert, L., Epp, S. W., Erk, B., Foucar, L., Hartmann, R., Hexemer, A., Huth, M., Kwok, J., Leone, S. R., Ma, J. H. S., Maia, F. R. N. C., Malmerberg, E., Marchesini, S., Neumark, D. M., Poon, B., Prell, J., Rolles, D., Rudek, B., Rudenko, A., Seifrid, M., Siefermann, K. R., Sturm, F. P., Swiggers, M., Ullrich, J., Weise, F., Zwart, P., Bostedt, C., Gessner, O. & Vilesov, A. F. Shapes and vorticities of superfluid helium nanodroplets. *Science* **345**, 906–909 (2014).

[54] Aguirre, N. F., Mateo, D., Mitrushchenkov, A. O., Pi, M. & De Lara-Castells, M. P. Helium mediated deposition: modeling the He-$TiO_2(110) - (1 \times 1)$ interaction potential and application to the collision of a helium droplet from density functional calculations. *J. Chem. Phys.* **136**, 124703 (2012).

[55] Popok, V. N., Barke, I., Campbell, E. E. B. & Meiwes-Broer, K.-H. Cluster-surface interaction: from soft landing to implantation. *Surf. Sci. Rep.* **66**, 347–377 (2011).

[56] de Lara-Castells, M. P., Aguirre, N. F., Stoll, H., Mitrushchenkov, A. O., Mateo, D. & Pi, M. Communication: Unraveling the ^{4}He droplet-mediated soft-landing from *ab initio*-assisted and time-resolved density functional simulations: Au@^{4}He$_{300}$/TiO$_2$(110). *J. Chem. Phys.* **142**, 131101 (2015).

[57] Kittel, C. *Introduction to Solid State Physics* (John Wiley & Sons, Hoboken, 2005).

[58] Link, S. & El-Sayed, M. A. Optical properties and ultrafast dynamics of metallic nanocrystals. *Annu. Rev. Phys. Chem.* **54**, 331–366 (2003).

[59] Bansmann, J., Baker, S. H., Binns, C., Blackman, J. A., Bucher, J.-P., Dorantes-Dávila, J., Dupuis, V., Favre, L., Kechrakos, D., Kleibert, A., Meiwes-Broer, K.-H., Pastor, G. M., Perez, A., Toulemonde, O., Trohidou, K. N., Tuaillon, J. & Xie, Y. Magnetic and structural properties of isolated and assembled clusters. *Surf. Sci. Rep.* **56**, 189–275 (2005).

[60] Heiz, U. & Landman, U. (eds.) *Nanocatalysis* (Springer-Verlag, Berlin Heidelberg New York, 2007).

[61] Thaler, P. *Buildup and Characterization of an Apparatus for the Synthesis of Metallic Nanoparticles Inside Helium Droplets.* Ph.D. thesis, Graz University of Technology (2015).

[62] Steurer, J. *Helium Droplet Mediated Fabrication and Analysis of Noble Metal Nanoparticles.* Master's thesis, Graz University of Technology (2014).

[63] Koch, M. *Magnetic Resonance Spectroscopy of Single Alkali-Metal Atoms Isolated in Superfluid Helium Nanodroplets.* Ph.D. thesis, Graz University of Technology (2009).

[64] Koch, M., Lanzersdorfer, J., Callegari, C., Muenter, J. S. & Ernst, W. E. Molecular beam magnetic resonance in doped helium nanodroplets. A setup for optically detected ESR/NMR in the presence of unresolved Zeeman splittings. *J. Phys. Chem. A* **113**, 13347–13356 (2009).

[65] Lide, D. R. (ed.) *CRC Handbook of Chemistry and Physics* (CRC Press, Boca Raton, FL, 1996), 77th edn.

[66] Sauerbrey, G. Verwendung von Schwingquarzen zur Wägung dünner Schichten und zur Mikrowägung. *Z. Phys.* **155**, 206–222 (1959).

[67] Schindelin, J., Arganda-Carreras, I., Frise, E., Kaynig, V., Longair, M., Pietzsch, T., Preibisch, S., Rueden, C., Saalfeld, S., Schmid, B., Tinevez, J.-Y., White, D. J.,

Hartenstein, V., Eliceiri, K., Tomancak, P. & Cardona, A. Fiji: an open-source platform for biological-image analysis. *Nat. Methods* **9**, 676–682 (2012).

[68] Reimer, L. & Kohl, H. *Transmission Electron Microscopy* (Springer-Verlag New York, 2008).

[69] Koga, K. & Sugawara, K. Population statistics of gold nanoparticle morphologies: direct determination by HREM observations. *Surf. Sci.* **529**, 23–35 (2003).

[70] Mullins, W. W. Theory of thermal grooving. *J. Appl. Phys.* **28**, 333–339 (1957).

[71] Thouy, R., Olivi-Tran, N. & Jullien, R. Fragmentation of two-dimensional mass fractals by surface-diffusion sintering. *Phys. Rev. B* **56**, 5321–5327 (1997).

[72] Watts, J. D., Gauss, J. & Bartlett, R. J. Coupled-cluster methods with noniterative triple excitations for restricted open-shell Hartree–Fock and other general single determinant reference functions. Energies and analytical gradients. *J. Chem. Phys.* **98**, 8718–8733 (1993).

[73] Urban, M., Neogrády, P. & Hubač, I. Spin adaptions in the open shell coupled cluster theory with a single determinant restricted Hartree-Fock reference. In Bartlett, R. J. (ed.) *Recent Advances in Coupled-Cluster Methods*, vol. 3 of *Recent Advances in Computational Chemistry*, 275–306 (World Scientific, 1997).

[74] Meichle, D. P. & Lathrop, D. P. Nanoparticle dispersion in superfluid helium. *Rev. Sci. Instrum.* **85**, 073705 (2014).

[75] Chagovets, T. V. & Van Sciver, S. W. A study of thermal counterflow using particle tracking velocimetry. *Phys. Fluids* **23**, 107102 (2011).

[76] Sergeev, Y. A. & Barenghi, C. F. Particles-vortex interactions and flow visualization in ^{4}He. *J. Low. Temp. Phys.* **157**, 429–475 (2009).

[77] Frenkel, D. & Smit, B. *Understanding Molecular Simulation- From Algorithms to Applications* (Academic Press, San Diego, California, 2001), 2 edn.

[78] de Heer, W. A. The physics of simple metal clusters: experimental aspects and simple models. *Rev. Mod. Phys.* **65**, 611–676 (1993).

[79] Binns, C. Nanoclusters deposited on surfaces. *Surf. Sci. Rep.* **44**, 1–49 (2001).

[80] Marks, L. D. Experimental studies of small particle structures. *Rep. Prog. Phys.* **57**, 603–649 (1994).

[81] Baletto, F. & Ferrando, R. Structural properties of nanoclusters: energetic, thermodynamic, and kinetic effects. *Rev. Mod. Phys.* **77**, 371–423 (2005).

[82] Barnard, A. S. Modelling of nanoparticles: approaches to morphology and evolution. *Rep. Prog. Phys.* **73**, 086502 (2010).

[83] Martin, T. P. Shells of atoms. *Phys. Rep.* **273**, 199–241 (1996).

[84] Mackay, A. L. A dense non-crystallographic packing of equal spheres. *Acta Crystallogr.* **15**, 916–918 (1962).

[85] Ino, S. Stability of multiply-twinned particles. *J. Phys. Soc. Jpn.* **27**, 941–953 (1969).

[86] Marks, L. D. Surface structure and energetics of multiply twinned particles. *Philos. Mag. A* **49**, 81–93 (1984).

[87] Reinhard, D., Hall, B. D., Ugarte, D. & Monot, R. Size-independent fcc-to-icosahedral structural transition in unsupported silver clusters: an electron diffraction study of clusters produced by inert-gas aggregation. *Phys. Rev. B* **55**, 7868–7881 (1997).

[88] Bartelt, A., Close, J. D., Federmann, F., Quaas, N. & Toennies, J. P. Cold metal clusters: helium droplets as a nanoscale cryostat. *Phys. Rev. Lett.* **77**, 3525–3528 (1996).

[89] Loginov, E., Gomez, L. F., Chiang, N., Halder, A., Guggemos, N., Kresin, V. V. & Vilesov, A. F. Photoabsorption of Ag_N ($N \sim 6 - 6000$) nanoclusters formed in helium droplets: transition from compact to multicenter aggregation. *Phys. Rev. Lett.* **106**, 233401 (2011).

[90] Theisen, M., Lackner, F. & Ernst, W. E. Rb and Cs oligomers in different spin configurations on helium nanodroplets. *J. Phys. Chem. A* **115**, 7005–7009 (2011).

[91] An der Lan, L., Bartl, P., Leidlmair, C., Schöbel, H., Jochum, R., Denifl, S., Märk, T. D., Ellis, A. M. & Scheier, P. The submersion of sodium clusters in helium nanodroplets: identification of the surface $\rightarrow$ interior transition. *J. Chem. Phys.* **135**, 044309 (2011).

[92] Ratschek, M., Koch, M. & Ernst, W. E. Doping helium nanodroplets with high temperature metals: formation of chromium clusters. *J. Chem. Phys.* **136**, 104201 (2012).

[93] Buffat, P.-A., Flüeli, M., Spycher, R., Stadelmann, P. & Borel, J.-P. Crystallographic structure of small gold particles studied by high-resolution electron microscopy. *Faraday Discuss.* **92**, 173–187 (1991).

[94] Baletto, F., Mottet, C. & Ferrando, R. Reentrant morphology transition in the growth of free silver nanoclusters. *Phys. Rev. Lett.* **84**, 5544–5547 (2000).

[95] Baletto, F., Mottet, C. & Ferrando, R. Microscopic mechanisms of the growth of metastable silver icosahedra. *Phys. Rev. B* **63**, 155408 (2001).

[96] Baletto, F., Mottet, C. & Ferrando, R. Freezing of silver nanodroplets. *Chem. Phys. Lett.* **354**, 82–87 (2002).

[97] Gomez, L. F., Loginov, E., Sliter, R. & Vilesov, A. F. Sizes of large He droplets. *J. Chem. Phys.* **135**, 154201 (2011).

[98] Buchenau, H., Knuth, E. L., Northby, J., Toennies, J. P. & Winkler, C. Mass spectra and time-of-flight distributions of helium cluster beams. *J. Chem. Phys.* **92**, 6875–6889 (1990).

[99] Henne, U. & Toennies, J. P. Electron capture by large helium droplets. *J. Chem. Phys.* **108**, 9327–9338 (1998).

[100] Baletto, F., Ferrando, R., Fortunelli, A., Montalenti, F. & Mottet, C. Crossover among structural motifs in transition and noble-metal clusters. *J. Chem. Phys.* **116**, 3856–3863 (2002).

[101] Gracia-Pinilla, M. Á., Ferrer, D., Mejía-Rosales, S. & Pérez-Tijerina, E. Size-selected Ag nanoparticles with five-fold symmetry. *Nanoscale Res. Lett.* **4**, 896–902 (2009).

[102] Wada, N. Preparation of fine metal particles by means of evaporation in helium gas. *Jpn. J. Appl. Phys.* **6**, 553–556 (1967).

[103] Hayashi, T., Ohno, T., Yatsuya, S. & Uyeda, R. Formation of ultrafine metal particles by gas-evaporation technique. IV. Crystal habits of iron and fcc metals, Al, Co, Ni, Cu, Pd, Ag, In, Au and Pb. *Jpn. J. Appl. Phys.* **16**, 705–717 (1977).

[104] Lindsay, C. M. & Miller, R. E. Rotational and vibrational dynamics of ethylene in helium nanodroplets. *J. Chem. Phys.* **122**, 104306 (2005).

[105] Scheele, I., Conjusteau, A., Callegari, C., Schmied, R., Lehmann, K. K. & Scoles, G. Near-infrared spectroscopy of ethylene and ethylene dimer in superfluid helium droplets. *J. Chem. Phys.* **122**, 104307 (2005).

[106] Müller, H., Fritsche, H.-G. & Skala, L. Analytic cluster models and interpolation formulae for cluster properties. In Haberland, H. (ed.) *Clusters of Atoms and Molecules I*, 116–140 (Springer-Verlag, Berlin Heidelberg, 1995).

[107] Morse, M. D. Clusters of transition-metal atoms. *Chem. Rev.* **86**, 1049–1109 (1986).

[108] Michaelian, K., Rendón, N. & Garzón, I. L. Structure and energetics of Ni, Ag, and Au nanoclusters. *Phys. Rev. B* **60**, 2000–2010 (1999).

[109] Poppa, H. Heterogeneous nucleation of Bi and Ag on amorphous substrates (in situ electron microscopy studies). *J. Appl. Phys.* **38**, 3883–3894 (1967).

[110] Tang, Z. K., Zhang, L., Wang, N., Zhang, X. X., Wen, G. H., Li, G. D., Wang, J. N., Chan, C. T. & Sheng, P. Superconductivity in 4 angstrom single-walled carbon nanotubes. *Science* **292**, 2462–2465 (2001).

[111] Huang, Y., Duan, X., Cui, Y. & Lieber, C. M. Gallium nitride nanowire nanodevices. *Nano Lett.* **2**, 101–104 (2002).

[112] Kohli, P., Harrell, C. C., Cao, Z., Gasparac, R., Tan, W. & Martin, C. R. DNA-functionalized nanotube membranes with single-base mismatch selectivity. *Science* **305**, 984–986 (2004).

[113] Ahn, J.-H., Choi, S.-J., Han, J.-W., Park, T. J., Lee, S. Y. & Choi, Y.-K. Double-gate nanowire field effect transistor for a biosensor. *Nano Lett.* **10**, 2934–2938 (2010).

[114] Claussen, J. C., Franklin, A. D., ul Haque, A., Porterfield, D. M. & Fisher, T. S. Electrochemical biosensor of nanocube-augmented carbon nanotube networks. *ACS Nano* **3**, 37–44 (2009).

[115] Wang, Q., Min, F. & Zhu, J. Preparation of gold nanowires and its application in glucose biosensing. *Mater. Lett.* **91**, 9–11 (2013).

[116] Yin, Y., Sun, Y., Yu, M., Liu, X., Jiang, T., Yang, B., Liu, D., Liu, S. & Cao, W. ZnO nanorod array grown on Ag layer: a highly efficient fluorescence enhancement platform. *Sci. Rep.* **5**, 8152 (2015).

[117] Zhu, G., Zhang, S., Xu, Z., Ma, J. & Shen, X. Ultrathin ZnS single crystal nanowires: controlled synthesis and room-temperature ferromagnetism properties. *J. Am. Chem. Soc.* **133**, 15605–15612 (2011).

[118] Arutyunov, K. Yu. Negative magnetoresistance of ultra-narrow superconducting nanowires in the resistive state. *Physica C* **468**, 272–275 (2008).

[119] Dreher, M., Pauly, F., Heurich, J., Cuevas, J. C., Scheer, E. & Nielaba, P. Structure and conductance histogram of atomic-sized Au contacts. *Phys. Rev. B* **72**, 075435 (2005).

[120] Lieber, C. M. Nanoscale science and technology: Building a big future from small things. *MRS Bull.* **28**, 486–491 (2003).

[121] Feynman, R. P. Application of quantum mechanics to liquid helium. In Gorter, C. J. (ed.) *Progress in Low Temperature Physics*, 17–53 (North-Holland, Amsterdam, 1955).

[122] Onsager, L. Introductory talk. In *Proc. Int. Conf. Theor. Phys.*, 877–880 (Science Council of Japan, Tokyo, 1953).

[123] Rayleigh, J. W. S. On the instability of jets. *Proc. London Math. Soc* **10**, 4–13 (1878).

[124] Nichols, F. A. & Mullins, W. W. Surface- (interface-) and volume diffusion contributions to morphological changes driven by capillarity. *Trans. Metal. Soc. AIME* **233**, 1840–1848 (1965).

[125] Nichols, F. A. & Mullins, W. W. Morphological changes of a surface of revolution due to capillarity-induced surface diffusion. *J. Appl. Phys.* **36**, 1826–1835 (1965).

[126] Nichols, F. A. On the spheroidization of rod-shaped particles of finite length. *J Mater Sci* **11**, 1077–1082 (1976).

[127] Marzbanrad, E., Rivers, G., Peng, P., Zhao, B. & Zhou, N. Y. How morphology and surface crystal texture affect thermal stability of a metallic nanoparticle: The case of silver nanobelts and pentagonal silver nanowires. *Phys. Chem. Chem. Phys.* **17**, 315–324 (2015).

[128] Toimil Molares, M. E., Balogh, A. G., Cornelius, T. W., Neumann, R. & Trautmann, C. Fragmentation of nanowires driven by Rayleigh instability. *Appl. Phys. Lett* **85**, 5337–5339 (2004).

[129] Li, H., Biser, J. M., Perkins, J. T., Dutta, S., Vinci, R. P. & Chan, H. M. Thermal stability of Cu nanowires on a sapphire substrate. *J. Appl. Phys.* **103**, 024315 (2008).

[130] Karim, S., Toimil-Molares, M. E., Balogh, A. G., Ensinger, W., Cornelius, T. W., Khan, E. U. & Neumann, R. Morphological evolution of Au nanowires controlled by Rayleigh instability. *Nanotechnology* **17**, 5954–5959 (2006).

[131] Karim, S., Toimil-Molares, M. E., Ensinger, W., Balogh, A. G., Cornelius, T. W., Khan, E. U. & Neumann, R. Influence of crystallinity on the Rayleigh instability of gold nanowires. *J. Phys. D Appl. Phys.* **40**, 3767–3770 (2007).

[132] Shin, H. S., Yu, J. & Song, J. Y. Size-dependent thermal instability and melting behavior of Sn nanowires. *Appl. Phys. Lett* **91**, 173106 (2007).

[133] Rauber, M., Muench, F., Toimil-Molares, M. E. & Ensinger, W. Thermal stability of electrodeposited platinum nanowires and morphological transformations at elevated temperatures. *Nanotechnology* **23**, 475710 (2012).

[134] Bréchignac, C., Cahuzac, Ph., Carlier, F., Colliex, C., Leroux, J., Masson, A., Yoon, B. & Landman, U. Instability driven fragmentation of nanoscale fractal islands. *Phys. Rev. Lett.* **88**, 196103 (2002).

[135] Lando, A., Kébaïli, N., Cahuzac, Ph., Masson, A. & Bréchignac, C. Coarsening and pearling instabilities in silver nanofractal aggregates. *Phys. Rev. Lett.* **97**, 133402 (2006).

[136] Hong, B. H., Bae, S. C., Lee, C.-W., Jeong, S. & Kim, K. S. Ultrathin single-crystalline silver nanowire arrays formed in an ambient solution phase. *Science* **294**, 348–351 (2001).

[137] Malisauskas, M., Meskys, R. & Morozova-Roche, L. A. Ultrathin silver nanowires produced by amyloid biotemplating. *Biotechnol. Progr.* **24**, 1166–1170 (2008).

[138] Eisele, D. M., von Berlepsch, H., Böttcher, C., Stevenson, K. J., Vanden Bout, D. A., Kirstein, S. & Rabe, J. P. Photoinitiated growth of sub-7 nm silver nanowires within a chemically active organic nanotubular template. *J. Am. Chem. Soc.* **132**, 2104–2105 (2010).

[139] Horiuchi, S., Hanada, T., Ebisawa, M., Matsuda, Y., Kobayashi, M. & Takahara, A. Contamination-free transmission electron microscopy for high-resolution carbon elemental mapping of polymers. *ACS Nano* **3**, 1297–1304 (2009).

[140] Kumao, A., Hashimoto, H. & Shiraishi, K. Studies on specimen contamination by transmission electron microscopy. *J. Electron Microsc.* **30**, 161–170 (1981).

[141] Powers, J. D. & Glaeser, A. M. Orientation effects on the high-temperature morphological evolution of pore channels in sapphire. *J. Am. Ceram. Soc.* **83**, 2297–2304 (2000).

[142] Gurski, K. F. & McFadden, G. B. The effect of anisotropic surface energy on the Rayleigh instability. *Proc. R. Soc. Lond. A* **459**, 2575–2598 (2003).

[143] Gurski, K. F., McFadden, G. B. & Miksis, M. J. The effect of contact lines on the Rayleigh instability with anisotropic surface energy. *SIAM J. Appl. Math.* **66**, 1163–1187 (2006).

[144] Raabe, D. & Ge, J. Experimental study on the thermal stability of Cr filaments in a Cu-Cr-Ag in situ composite. *Scr. Mater.* **51**, 915–920 (2004).

[145] Khaligh, H. H. & Goldthorpe, I. A. Failure of silver nanowire transparent electrodes under current flow. *Nanoscale Res. Lett.* **8**, 235 (2013).

[146] Franey, J. P., Kammlott, G. W. & Graedel, T. E. The corrosion of silver by atmospheric sulfurous gases. *Corros. Sci.* **25**, 133–143 (1985).

[147] Elechiguerra, J. L., Larios-Lopez, L., Liu, C., Garcia-Gutierrez, D., Camacho-Bragado, A. & Yacaman, M. J. Corrosion at the nanoscale: the case of silver nanowires and nanoparticles. *Chem. Mater.* **17**, 6042–6052 (2005).

[148] Liu, C. L., Cohen, J. M., Adams, J. B. & F., V. A. EAM study of surface self-diffusion of single adatoms of fcc metals Ni, Cu, Al, Ag, Au, Pd, and Pt. *Surf. Sci.* **253**, 334–344 (1991).

[149] Emery, S. B., Rider, K. B., Little, B. K. & Lindsay, C. M. Helium droplet assembled nanocluster films: cluster formation and deposition rates. *J. Phys. Chem. C* **117**, 2358–2368 (2013).

[150] Cargnoni, F., Ponti, A. & Mella, M. Coinage metal exciplexes with helium atoms: a theoretical study of M*(^{2}L)He$_n$ (M = Cu, Ag, Au; L = P,D). *Phys. Chem. Chem. Phys.* **15**, 18410–18423 (2013).

[151] Cargnoni, F. & Mella, M. Solubility of metal atoms in helium droplets: exploring the effect of the well depth using the coinage metals Cu and Ag. *J. Phys. Chem. A* **115**, 7141–7152 (2011).

[152] Popov, E., Mammetkuliyev, M. & Eloranta, J. Dynamics of vortex assisted metal condensation in superfluid helium. *J. Chem. Phys.* **138**, 204307 (2013).

[153] Cargnoni, F., Kuś, T., Mella, M. & Bartlett, R. J. Ground state potential energy surfaces and bound states of M–He dimers (M=Cu,Ag,Au): a theoretical investigation. *J. Chem. Phys.* **129**, 204307 (2008).

[154] Werner, H.-J., Knowles, P. J., Lindh, R., Manby, F. R., Schütz, M., Celani, P., Korona, T., Rauhut, G., Amos, R. D., Bernhardsson, A., Berning, A., Cooper, D. L., Deegan, M. J. O., Dobbyn, A. J., Eckert, F., Hampel, C., Hetzer, G., Lloyd, A. W., McNicholas, S. J., Meyer, W., Mura, M. E., Nicklass, A., Palmieri, P., Pitzer, R., Schumann, U., Stoll, H., Stone, A. J., Tarroni, R. & Thorsteinsson, T. Molpro, version 2012.1, a package of ab initio programs (2008). See http://www.molpro.net.

[155] Peterson, K. A. & Puzzarini, C. Systematically convergent basis sets for transition metals. II. Pseudopotential-based correlation consistent basis sets for the group 11 (Cu, Ag, Au) and 12 (Zn, Cd, Hg) elements. *Theor. Chem. Acc.* **114**, 283–296 (2005).

[156] Figgen, D., Rauhut, G., Dolg, M. & Stoll, H. Energy-consistent pseudopotentials for group 11 and 12 atoms: adjustment to multi-configuration Dirac–Hartree–Fock data. *Chem. Phys.* **311**, 227–244 (2005).

[157] Boys, S. F. & Bernardi, F. The calculation of small molecular interactions by the differences of separate total energies. Some procedures with reduced errors. *Mol. Phys.* **19**, 553–556 (1970).

[158] Varga, S., Engel, E., Sepp, W.-D. & Fricke, B. Systematic study of the Ib diatomic molecules Cu_2, Ag_2, and Au_2 using advanced relativistic density functionals. *Phys. Rev. A* **59**, 4288–4293 (1999).

[159] Huber, K.-P. & Herzberg, G. *Molecular Spectra and Molecular Structure: IV. Constants of diatomic molecules* (Van Nostrand Reinhold Company, New York, 1979).

[160] Dalfovo, F., Lastri, A., Pricaupenko, L., Stringari, S. & Treiner, J. Structural and dynamical properties of superfluid helium: a density-functional approach. *Phys. Rev. B* **52**, 1193–1209 (1995).

[161] Dalfovo F., Lehmann K.K. & Schmied R. Doped clusters of ^{4}He - density profiles and energy. Trento, Feb 1, 1999. Modified Jan/Jul/Aug 2000, written in FORTRAN, private communications.

[162] Douberly, G. E., Stiles, P. L., Miller, R. E., Schmied, R. & Lehmann, K. K. $(HCN)_m$-M_n (M = K, Ca, Sr): vibrational excitation induced solvation and desolvation of dopants in and on helium nanodroplets. *J. Phys. Chem. A* **114**, 3391–3402 (2010).

[163] Allum, D. R., McClintock, P. V. E., Phillips, A. & Bowley, R. M. The breakdown of superfluidity in liquid ^{4}He: an experimental test of Landau's theory. *Philos. T. R. Soc. A* **284**, 179–224 (1977).

[164] Mateo, D., Hernando, A., Barranco, M., Loginov, E., Drabbels, M. & Pi, M. Translational dynamics of photoexcited atoms in ^{4}He nanodroplets: the case of silver. *Phys. Chem. Chem. Phys.* **15**, 18388–18400 (2013).

[165] Poms, J., Hauser, A. W. & Ernst, W. E. Helium nanodroplets doped with xenon and rubidium atoms: a case study of van der Waals interactions between heliophilic and heliophobic dopants. *Phys. Chem. Chem. Phys.* **14**, 15158–15165 (2012).

[166] Ancilotto, F., Pi, M. & Barranco, M. Vortex arrays in a rotating superfluid ^{4}He nanocylinder. *Phys. Rev. B* **90**, 174512 (2014).

[167] Lewerenz, M., Schilling, B. & Toennies, J. P. Successive capture and coagulation of atoms and molecules to small clusters in large liquid helium clusters. *J. Chem. Phys.* **102**, 8191–8207 (1995).

[168] Bewley, G. P., Paoletti, M. S., Sreenivasan, K. R. & Lathrop, D. P. Characterization of reconnecting vortices in superfluid helium. *P. Natl. Acad. Sci. USA* **105**, 13707–13710 (2008).

[169] Paoletti, M. S., Fisher, M. E., Sreenivasan, K. R. & Lathrop, D. P. Velocity statistics distinguish quantum turbulence from classical turbulence. *Phys. Rev. Lett.* **101**, 154501 (2008).

[170] Paoletti, M. S., Fisher, M. E. & Lathrop, D. P. Reconnection dynamics for quantized vortices. *Physica D* **239**, 1367–1377 (2010).

[171] Gordon, E. B. & Okuda, Y. Catalysis of impurities coalescence by quantized vortices in superfluid helium with nanofilament formation. *Low Temp. Phys.* **35**, 209–213 (2009).

[172] Ancilotto, F., Pi, M. & Barranco, M. Vortex arrays in nanoscopic superfluid helium droplets. *Phys. Rev. B* **91**, 100503(R) (2015).

[173] Leal, A., Mateo, D., Hernando, A., Pi, M., Barranco, M., Ponti, A., Cargnoni, F. & Drabbels, M. Picosecond solvation dynamics of alkali cations in superfluid ^{4}He nanodroplets. *Phys. Rev. B* **90**, 224518 (2014).

[174] Mateo, D., Leal, A., Hernando, A., Barranco, M., Pi, M., Cargnoni, F., Mella, M., Zhang, X. & Drabbels, M. Communication: Nucleation of quantized vortex rings in ^{4}He nanodroplets. *J. Chem. Phys.* **140**, 131101 (2014).

[175] Leal, A., Mateo, D., Hernando, A., Pi, M. & Barranco, M. Capture of heliophobic atoms by ^{4}He nanodroplets: the case of cesium. *Phys. Chem. Chem. Phys.* **16**, 23206–23213 (2014).

[176] Hartmann, M., Pörtner, N., Sartakov, B., Toennies, J. P. & Vilesov, A. F. High resolution infrared spectroscopy of single SF_6 molecules in helium droplets. I. Size effects in ^{4}He droplets. *J. Chem. Phys.* **110**, 5109–5123 (1999).

[177] Amano, C., Niina, H. & Mikami, Y. Molecular dynamics on silver cluster structures along the icosahedral noncrystalline and the cuboctahedral c.c.p. growth sequence. *J. Mol. Struc.-Theochem.* **904**, 64–68 (2009).

[178] Barke, I., Hartmann, H., Rupp, D., Flückiger, L., Sauppe, M., Adolph, M., Schorb, S., Bostedt, C., Treusch, R., Peltz, C., Bartling, S., Fennel, T., Meiwes-Broer, K.-H. & Möller, T. The 3D-architecture of individual free silver nanoparticles captured by X-ray scattering. *Nat. Commun.* **6**, 6187 (2015).

10 Addendum: Manual

This manual was written by Alexander Volk and Philipp Thaler who designed and set up the lab infrastructure and the helium droplet beam machine in PHEG 056 (Cluster Lab III). It is addressed to future custodians of the machine. In order to serve as a general reference book, repeated explanations of the same issues in different situations are deliberately accepted.

Chapters 3, 4 and 5.3.3 were written by Alexander Volk, chapters 1, 2 and 5 - 7 were written by Philipp Thaler. Both authors were responsible for editing and obtaining the presented data and settings.

Besides instructions on how to operate and service the present machine, this manual includes explanations of the dimensioning and design of the apparatus. Furthermore, it includes typical settings for the adjustable parameters and provides experimental data as benchmark for future experiments.

The structure of the content is primarily defined by the tangible parts of the apparatus, rather than by didactics. It is not the aim of this manual to cover the theory in this field of expertise.

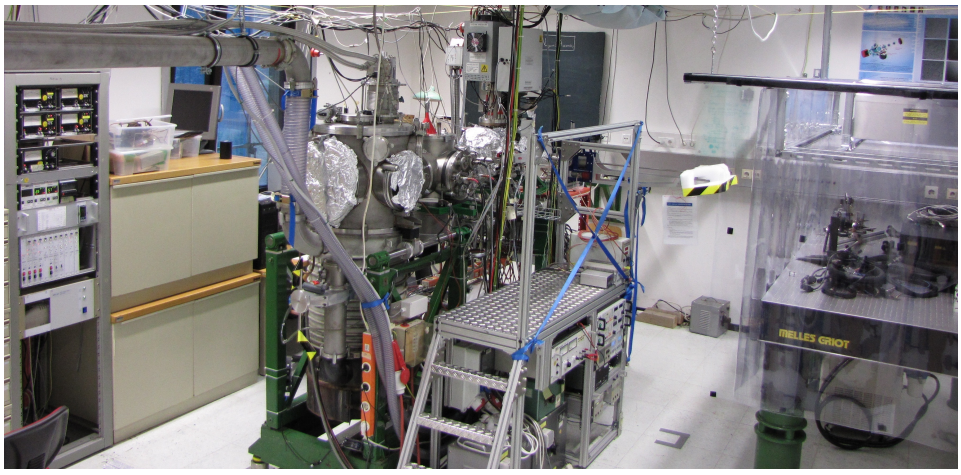

Figure A1: Foto: Cluster Lab III. Left: Control panel; Center: Helium droplet beam machine (HelENA); Right: Installation for the future laser setup.

Contents

List of Figures

List of Tables

1. History and Evolution

Helium droplet beam machines have been used at the TUG institute for experimental physics for some years. With these machines, ultra cold atoms and molecules were investigated spectroscopically on or in helium droplets. In 2011 an article reporting the formation of large silver clusters Ag_n (with n up to 6000) inside helium droplets caught the attention of the institute.[a] The decision was made to build a new machine, especially designed for the purpose of nanoparticle synthesis inside liquid helium droplets, using the knowledge emanating from the build-up and operation of the existing machines. The new apparatus was necessary, because the other machines on the institute are limited in terms of droplet size, and large helium droplets are essential for growing nanoparticles. An old helium atom beam machine, donated by Prof. Christof Wöll (Universität Bochum), was cannibalized in order to build up the new machine and was fitted with a new high-end cold head to reach the lower nozzle temperatures required for the formation of large helium droplets.

The motivation to build up this new machine was the promising prospect that the versatile doping possibilities of helium droplets combined with the cold temperatures provided by them would enable the controlled synthesis of nanoparticles with exotic material combinations exhibiting novel properties. Furthermore, for subsequent doping schemes with two different materials, the formation of core-shell structures was expected, with the low temperature preventing restructuring. Additionally, in 2012 first evidence for vortices inside liquid helium droplets was found.[b] While this phenomenon has been known in the bulk, vortices inside droplets eluded verification until that experiment, which exploits the fact that dopants prefer to reside along the vortex lines. The shape dictated by the vortices is stable upon deposition, which paves the way for a deliberate creation of one-dimensional structures with this technique.

The preparation of the infrastructure for the new laboratory started in September 2011, and the main setup was completed in September 2013 with the delivery of a time

[a] Loginov, E., Gomez, L. F., Chiang, N., Halder, A., Guggemos, N., Kresin, V. V., & Vilesov, A. F. Photoabsorption of Ag_N (N $\approx$ 6-6000) nanoclusters formed in helium droplets: transition from compact to multicenter aggregation. *Phys. Rev. Lett.* **106**, 233401 (2011).

[b] Gomez, L. F., Loginov, E. & Vilesov, A.F. Traces of vortices in superfluid helium droplets. *Phys. Rev. Lett.* **108**, 155302 (2012).

of flight mass spectrometer (TOFMS), which constitutes the main *in situ* measuring instrument of the apparatus. In the first setup, not all of the desired specifications were met, but after some modifications a nozzle temperature of $< 3.5\,\mathrm{K}$ and a background pressure of $< 5 \cdot 10^{-10}\,\mathrm{mbar}$ in the measurement chamber were reached in April 2014. Besides the *in situ* mass spectrometric investigations, using other (external) diagnostics, especially transmission electron microscopy (TEM), has always been part of the concept of this lab. Especially when experimenting with reactive elements, a transport of the samples to the external diagnostic facilities without breaking the vacuum is highly desired. A vacuum transfer system for sample exchange with the KFU was purchased and implemented in May 2015 and a system for the transport of samples to the FELMI was designed in fall 2015.

2. Introduction & Overview

The new apparatus described here is designed to produce a beam of large helium droplets, which subsequently serve as individual reactors for nanoparticle synthesis. Once the dopant-atoms or -molecules are added to a droplet they are cooled down to droplet temperature. The superfluid matrix enables the dopants to move inside the droplet which leads to their aggregation. The binding energy released upon aggregation is dissipated by the host, which guarantees efficient nanoparticle formation. After the doping process, the droplets carry the nanoparticles into the measurement chamber, where the nanoparticles can be analyzed *in-situ* or be deposited on various substrates for *ex-situ* analysis.

The main structure of the new apparatus comprises a system of vacuum chambers with decreasing base pressure along the beam axis. In our case, there are four chambers, which can be separated into three independent regions using two gate valves (see schematics in Fig. A.2). Helium droplets are formed if the nozzle is cooled down to temperatures lower than 20 K. Here, this low temperature can be reached using a closed cycle refrigerator whilst paying attention to a very good thermal insulation. For the doping of the helium droplets, the dopants have to be forced into the gas phase, which is realized by resistively heated ovens. In the current design, these ovens are equipped with water-cooled radiation shields and can reach a maximum temperature of 2000 K. For the analysis of the nanoparticles / the doped helium droplet beam, there are several measuring instruments installed at the measurement chamber, including a time of flight mass spectrometer (TOFMS), a quadrupole mass spectrometer (QMS), a quartz crystal micro-balance (QCM) as well as a sample holder for substrates for *ex-situ* analysis.

In the next chapters, the apparatus will be explained in more detail, starting with the infrastructure of the laboratory followed by a separate description of the individual vacuum chambers. Thereby, the sequence of the description matches the sequence in which the individual elements are passed by the helium droplet beam.

[a] Steurer, J. *Helium Droplet Mediated Fabrication and Analysis of Noble Metal Nanoparticles.* Master's thesis, Graz University of Technology (2014).

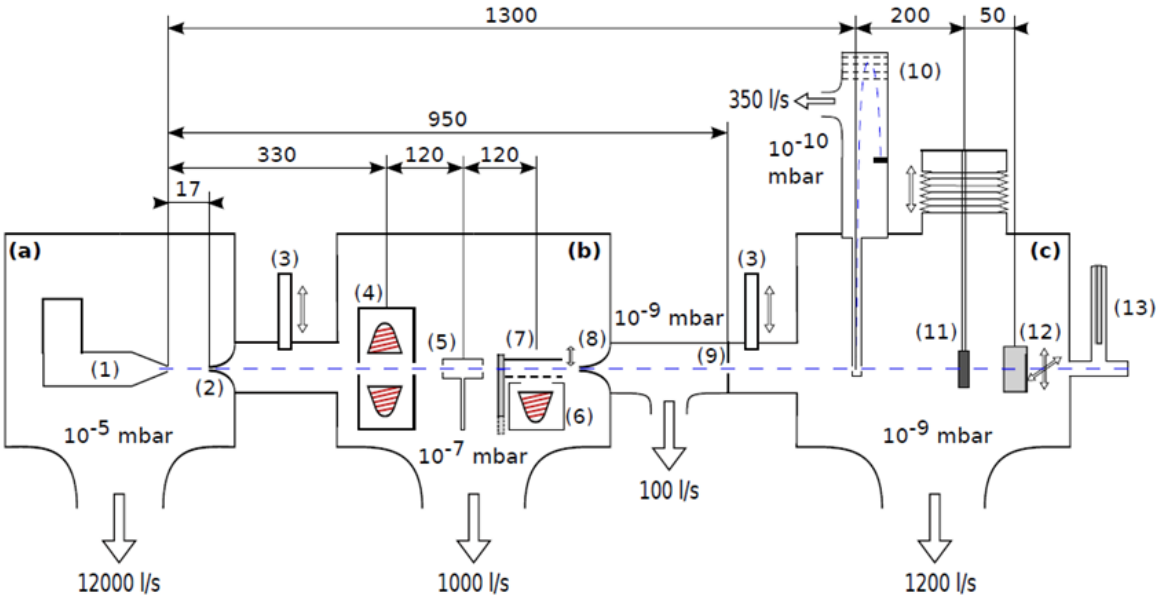

Figure A.2.: Schematic of the entire apparatus, taken from [a]

3. Laboratory Infrastructure

3.1. Layout

The whole laboratory facility consists of two rooms as depicted in Fig. A.3. While the main laboratory comprises the helium droplet apparatus, an optical table, a working area and several storage possibilities, the fore-vacuum pumps and the coldhead compressor are located in a separate room (hereafter referred to as the pump room) for noise reduction.

3.2. Electric Installations

The electrical power supply of the laboratory has been realized over an external distribution box. Every socket in the lab is labeled with an identifier distinct for the connected current circuit . Table A.1 lists the labels of all these sockets and the corresponding fuse labels in the distribution box. The over-current protective devices are customized for the intended application of the respective current circuits (see Tab. A.1). Some circuits are equipped with solid state relays, so that the current is switched on only if the interlock control wire with the corresponding number is connected with interlock control wire 1. This enables an efficient integration of the vacuum control system *via* relay connections. For example, the turbo vacuum pumps can only be switched on if the prevacuum pressure is below a certain threshold (see chapter 4). Fig. A.4 shows the location of the respective sockets in the lab.

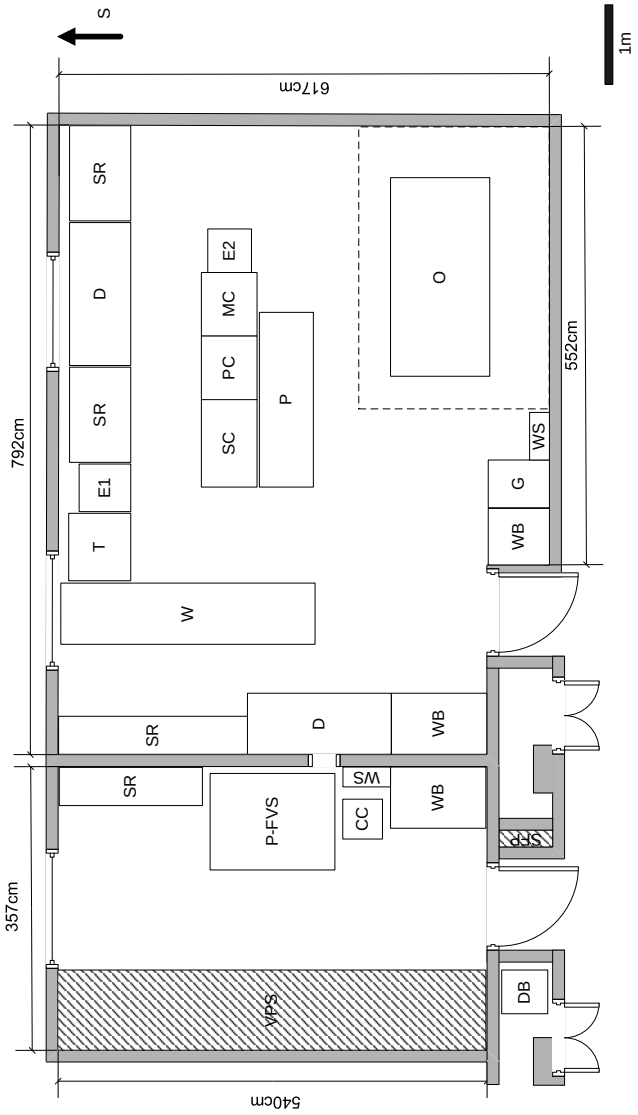

Figure A.3.: General layout of the laboratory and the pump room. CC... compressor for coldhead; D... desk; DB... distribution board; E1-2... rack for electronics; G... gas locker; MC... main chamber; O... optical table (dashed line shows borders of flow-box); P... platform; PC... pickup chamber; P-FVS... pumps of fore-vacuum system; SC... source chamber; SFP... structural fire protection; SR... storage room; T... tools; VPS... vacuum pump storage; W... working bench; WB... basin; WS... water supply (closed cooling cycle)

Table A.1.: Electric circuits of the laboratory. The electric circuits can be identified by their socket labels. The location of the respective sockets are depicted in Fig. A.4. The fuses in the distribution board are labeled according to the second column. Where an interlock is available, the number of the corresponding relay control wire is given.

socket label	fuse label	1~ / 3~	I_{max} / A	interlock control wire	assignment
CC	9Q2	3~	35	10	coldhead compressor
F	9Q1	3~	50	9	high current power supply
G	5F6	3~	16	n.a.	for general use
H	8F7	3~	16	n.a.	for general use
Laser	Laser	3~	200	2	for laser with high energy consumption
M	6Q3	1~	13	n.a.	computer
O/P/Q	6Q2/5Q5/5Q6	1~	13/16/16	n.a.	for general electronics
P1/P2/P3	8F2/8F3/8F4	3~	16/16/16	8	source chamber prevacuum pumps
P4	7Q2	3~	25	7	pickup chamber prevacuum pump
P5	7Q1	3~	35	6	source chamber diffusion pump
P6	6Q6	1~	13	5	pickup chamber turbo pumps
P7	6Q5	1~	13	4	main chamber turbo pumps
P8	6Q4	1~	13	3	TOF electronics
R1/R2	5Q1/5Q2	1~	16/16	n.a.	for general use
S1/S2	5Q3/5Q4	1~	16/16	n.a.	for general use
T	6Q1	1~	16	n.a.	main chamber prevacuum pumps

3.3. Gas Installations / Storage

The laboratory contains a fire-retarding gas locker suited for two 20 l gas bottles. In the present setup this locker contains a bottle of grade 6 helium for droplet generation, and a bottle of grade 5 N_2 for venting the vacuum chambers with dry air. The respective valves and connections for each gas line are depicted in Fig. A.5 & A.6. In order to prevent impurities from entering the gas system during a bottle exchange, it is possible to purge affected parts. To do so, the gate valve of the respective gas line has to be closed before the gas bottle is exchanged and the purge valve is used to flush the vented volume before re-opening the gate valve.
Gas controls for daily operations are located outside the gas locker for the purpose of easier monitoring. The pressure of the He gas can be regulated by a pressure regulator. All tubes of the He gas system are made of stainless steel and the setup has been tested to bear a pressure of 100 bar applied to the nozzle. There should always be a He flow through the 5 μm nozzle orifice to prevent a clogging, which means that the applied pressure should not fall below 10 bars, even if the nozzle is not in operation.
For the N_2 system fluorpolymer gas lines are used. When venting the vacuum chambers with N_2 one should act with caution in order to prevent the chambers from getting over pressurized. While the source chamber and the pickup chamber are equipped with pressure relief valves (releasing at $\approx$ 0.4 bar overpressure), a burst disc (releasing at $\approx 0.6 - 0.8$ bar overpressure) is attached to the main chamber. Further, an additional pressure relief valve is attached to the gas line right after the N_2 pressure regulator.
Although not in use, there are additional pressure regulators for H_2 available in the gas locker as well as outside. Bottles for other gases interesting for doping the He droplets may be directly placed and secured at the frame of the apparatus.

3.4. Air Conditioning

The air conditioning system comprises two convector fans in the main laboratory and one convector fan in the pump room. Every single of these air conditioners (Daikin, FWL10DATN6V3) exhibits a maximum cooling capacity of 8 kW. The cooling solvent is cooled *via* the heat exchanger of the building's central air conditioning system.
While the system proved to be effective in cooling the laboratory, the temperature stability is non-satisfying as exemplary depicted in Fig. A.7 for a preset temperature of 19°C. It can bee seen that the room temperature (black line) in Fig. A.7 oscillates around the preset value by more than $\pm$1°C in a time interval of $\approx$ 10 min. This behavior is the result of a simultaneous switching of the fan (see red line in Fig. A.7) and of the cooling-solvent flow regulating valve (see blue line in Fig. A.7).

It has to be noted that some measurement devices in the laboratory are sensitive to

temperature oscillations. This is especially the case for the quartz oscillator, so that extensive housing and thermal insulation of the respective device have been necessary. Another possibility to reduce the influence of the air conditioning on measurement results lies in the adaption of its regulation process. In preliminary tests the desired temperature has been preset to a very low value (e.g. 10°C) and the rotational speed of the fan monitor has been regulated by implementing a variable resistor. This setup allows to eliminate the influence of the cooling-solvent flow regulating valve, as the respective valve is opened all times and the preset temperature is never reached. On the other hand, the fan speed is maintained on a constant level. The tests showed good results as fast temperature oscillations were reduced, however long-term shifts in the temperature occurred due to changes in heat loads during full day operation. It would therefore be recommendable to imply a phase controlled modulator for the regulation of fan speed.

3.5. Aspiration System

In order to prevent the emission of oil mist inside the laboratory facility, the pump exhausts of all rotary vane vacuum pumps are connected to the central aspiration system. A suitable pipe is installed between the pump room and the laboratory, where it is connected to the aspiration system of the gas locker. It has to be noted that in case of a fire alarm the central aspiration system is shut down automatically. However, the volume of the pipes connecting the gas locker with the aspiration unit on the roof of the building is large, while the amount of air emitted by the pumps is small, so that proper functioning of the pumping system is still given.

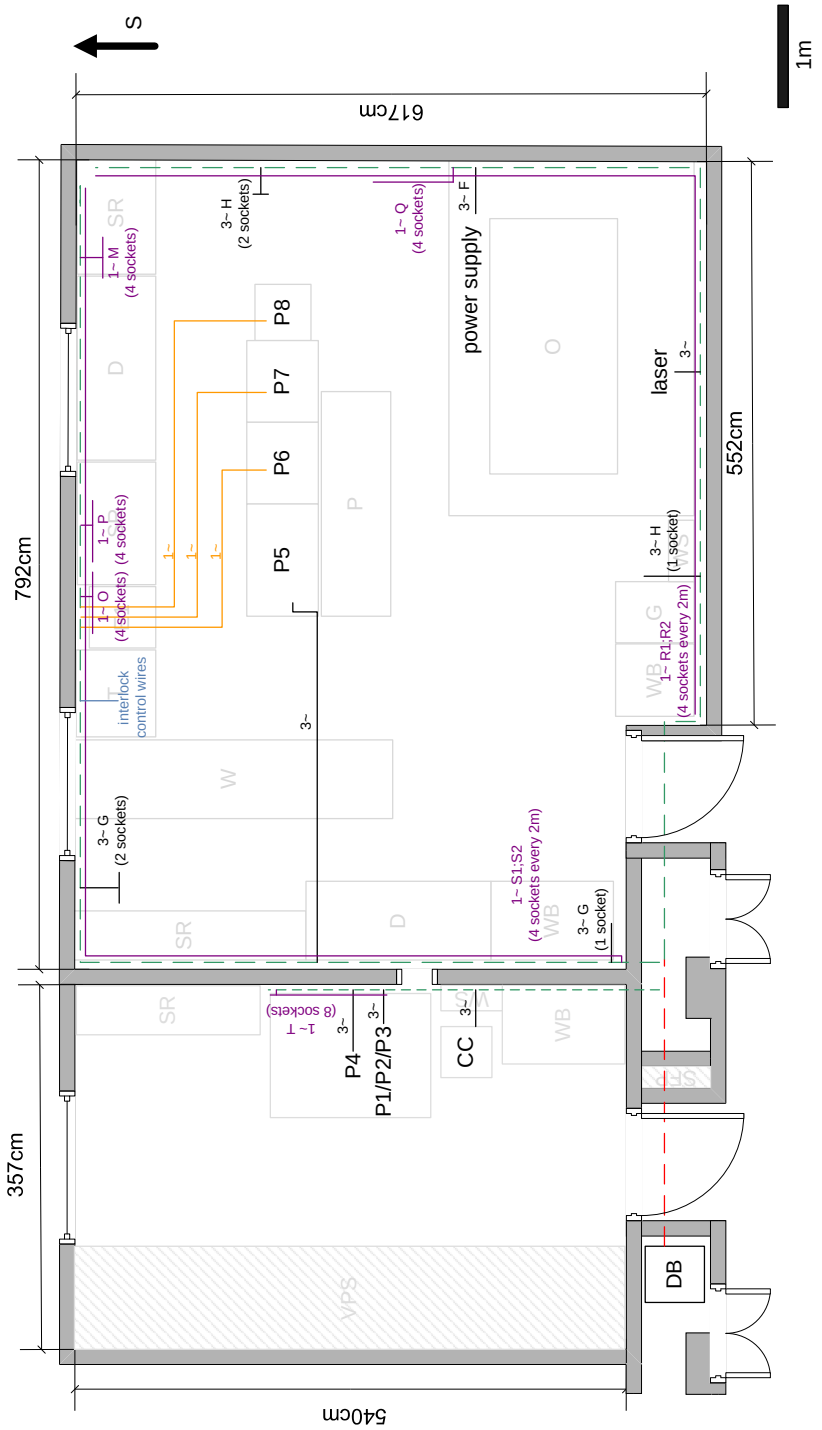

Figure A.4.: Electrical layout of the laboratory. See Tab. A.1 for a detailed description of the different electric circuits.

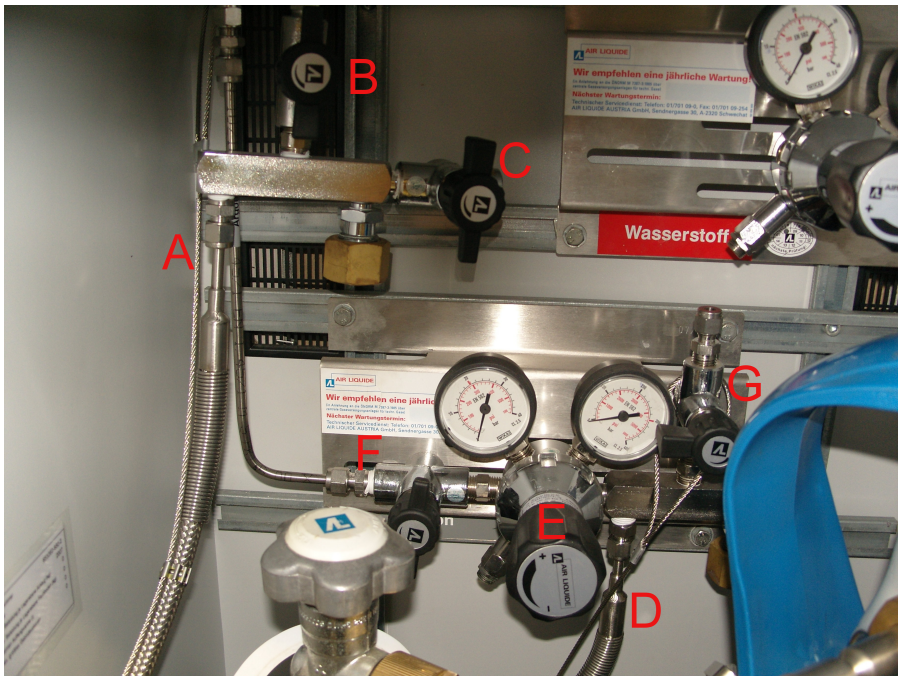

Figure A.5.: Connections and valves inside the gas locker. **A** He–gas connection; **B** He gate valve; **C** He purge valve; **D** N_2–gas connection; **E** N_2 pressure regulator; **F** N_2 gate valve; **G** N_2 purge valve.

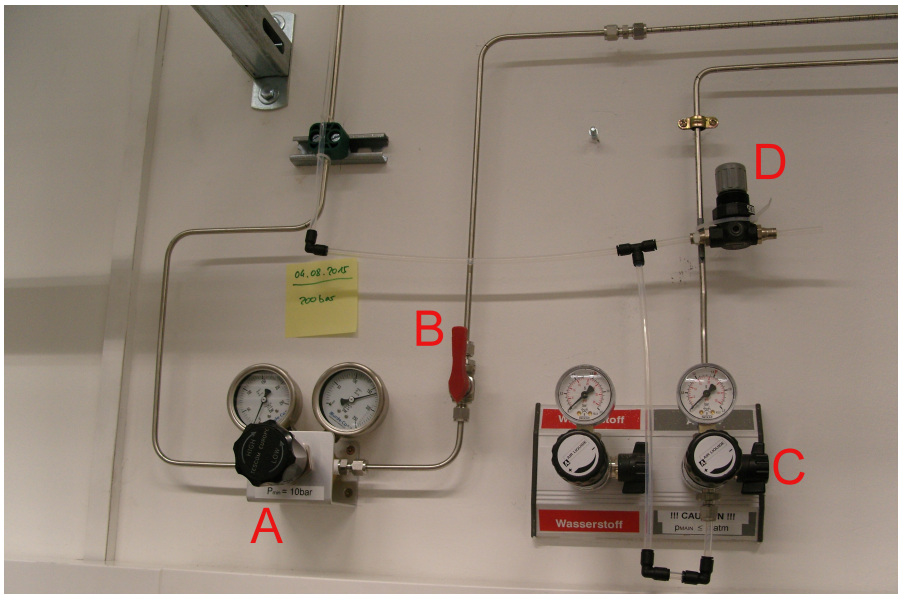

Figure A.6.: Gas controls for daily operation. **A** He pressure regulator; **B** He gate valve; **C** N_2 pressure regulator with included gate valve; **D** pressure relief valve for N_2 system.

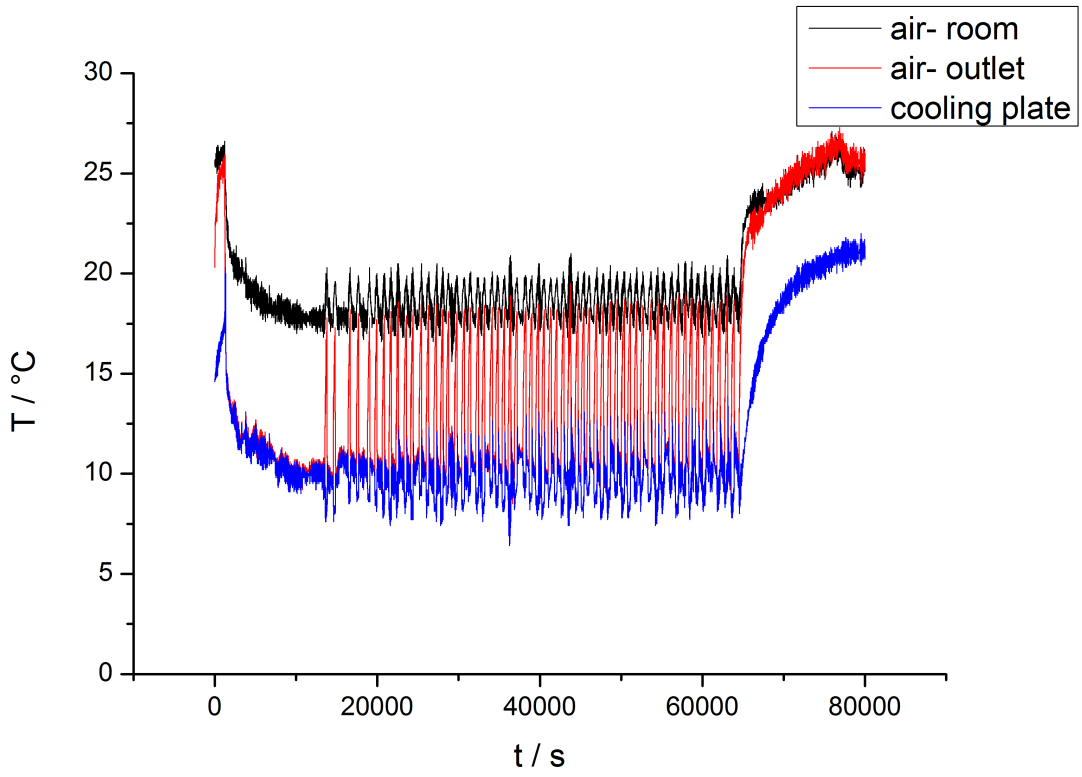

Figure A.7.: Temperature oscillation due to air conditioning. The temperature was measured away from direct air stream (black), in front of the fan (red) and on the cooling plate of the convector fan unit. The temperature was preset to 19°C

4. Vacuum and Water control system

For safety reasons as well as for easier monitoring and better handling, all vacuum pumps and coolant supplies are operated through a home-made central control system. This enables the linkage of the pressure monitoring system and the monitoring system for coolant flows in order to assure proper operating conditions for the vacuum pumps. Further, all pumps and solenoid valves can be switched on and off through a single control panel. Other devices which need a certain grade of vacuum during operation (e.g. the TOFMS) are directly linked to this system. The control panel is directly connected to the relay control wires of the respective current circuit (see Tab. A.1), i.e. the power supply of the connected devices is directly switched through the control panel. More detailed descriptions of single parts of the control system can be found in the following subsections.

4.1. Control Panel

The control panel (Fig. A.8) is the heart of the system. The state of every parameter monitored for proper operation of a certain device is indicated by LEDs. Devices can be switched between 3 different modes: "OFF", "Auto", or "Manual". The manual-mode is intended for the start up procedure and restricted by a timer, so that after 10 min in manual-mode the device is automatically switched off. If all monitored parameters meet the preset requirements (indicated by green LEDs) it is possible to switch the respective device to the auto-mode for continuous operation. In the following an exemplary description of the different parts of the control panel is given for the source chamber oil diffusion pump (marked as SOURCE in Fig. A.8). In case of the diffusion pump, 3 parameters are monitored, namely the vacuum pressure in the source chamber, the prevacuum pressure and the coolant flow. It can be seen that none of these parameters meets the requirements as indicated by red LEDs. While the coolant flow and the prevacuum pressure have to meet the diffusion pump manufacturer's requirements, the vacuum in the source chamber is additionally monitored. The corresponding set point is exceeded only in case of an ingress of air during operation. In order to switch the source pump to auto-mode, it would be necessary to first switch on the prevacuum pumps

(Prevac1) and the coolant flow. The solenoid valve of the cooling circuit can be opened by pressing the black start button. It is necessary to hold the button until sufficient flow is detected and the corresponding green LED turns on. All water circuits exhibit a programmable overrun, whose time can be set through the blue potentiometer from zero to a maximum of 15 min. In case of the oil diffusion pump this value is set to the maximum. When the prevacuum pressure and the coolant flow meet the requirements, the diffusion pump should be switched to the manual-mode.
For the turbo pumps of the pickup chamber and the main chamber it is possible to switch off the monitoring of the coolant flow because these pumps are sufficiently air cooled in normal operation (not during bake-out of the chamber!). However, the lifetime of the bearings increases with better cooling so that in the coolant flow should be switched on.

4.2. Pressure Monitoring

Several different vacuum gauges are used to monitor the pressures in the vacuum system. All vacuum gauges are connected to individual monitors which are mounted in the same electronic rack as the control panel (see Fig. A.9). These monitors usually feature a relay-output, and allow to define a pressure threshold. When the measured pressure falls below this threshold the output is switched from an open to a closed state or vice versa. These outputs are directly connected to the control panel.
Fore-vacuum pressures are measured with Pirani vacuum gauges (Leybold-Heraeus TR201) and corresponding monitors (L-H Thermovac TM 220 S 2). The pressure threshold can be adjusted *via* the potentiometer ("Threshold"), while pressing the "Test" button (Fig. A.9). For the source and the pickup chamber full range gauges (Pfeiffer PKR251; combination of pirani element and cold cathode) are used in combination with single gauge monitors (Pfeiffer TPG261). The main chamber is equipped with an ionization vacuum meter (L-H Ionivac IM220 / monitor: L-H IE220). Please consult the manual for questions on threshold settings in case of monitors with digital display.
The roots pumps are switched on only after a certain fore-vacuum pressure has been reached. The corresponding switch is directly connected to the pressure monitor labeled (PREVAC ROOTS) and can not be separately controlled *via* the control panel. Further, although not connected to the vacuum control system, there are also pressure gauges attached to the TOFMS (L-H IM210 / monitor: L-H IE211) and the differential pumping station (Pfeiffer PKR251 / monitor: TPG261).

4.3. Cooling Circuit

For some heat producing devices water cooling is necessary. The laboratory is connected to a central closed cooling circuit of the building. Several separated circuits are used

in the laboratory and in the pump room. Every circuit is equipped with a solenoid valve (Buerkert 138034) and a calorimetric flow monitor (IFM ST 1600) as depicted in Fig. A.10. The solenoid valves can be switched *via* the control panel. The flow monitor is attached in the return part of the system and connected to the control panel. For correct operation it is necessary to adjust the coolant flow as needed for the respective device by using the rotary ball valve, which is installed in front of the solenoid valve. The threshold of the flow monitor can then be adapted *via* a potentiometer. In current operation mode over-cooling of a device is impossible and as no water is lost in the closed cooling circuit the flow is set to higher values as needed. In case of a leak in the cooling circuit, the flow is stopped by closing the respective solenoid valve and the affected part of the vacuum system is shut down. In case of a power blackout the functioning of the cooling is ensured by an uninterruptible power supply (UPS) for $\approx 10 - 20\,\mathrm{min}$. This is especially important for the oil diffusion pump.

4.3.1. Maintenance

The proper functioning of the flow monitors has to be tested once a month by closing the lever valves mounted in front of the solenoid valves during operation. The solenoid valves should be tested by switching the flow on **and off** *via* the control panel. All connections should be checked on leak-tightness.

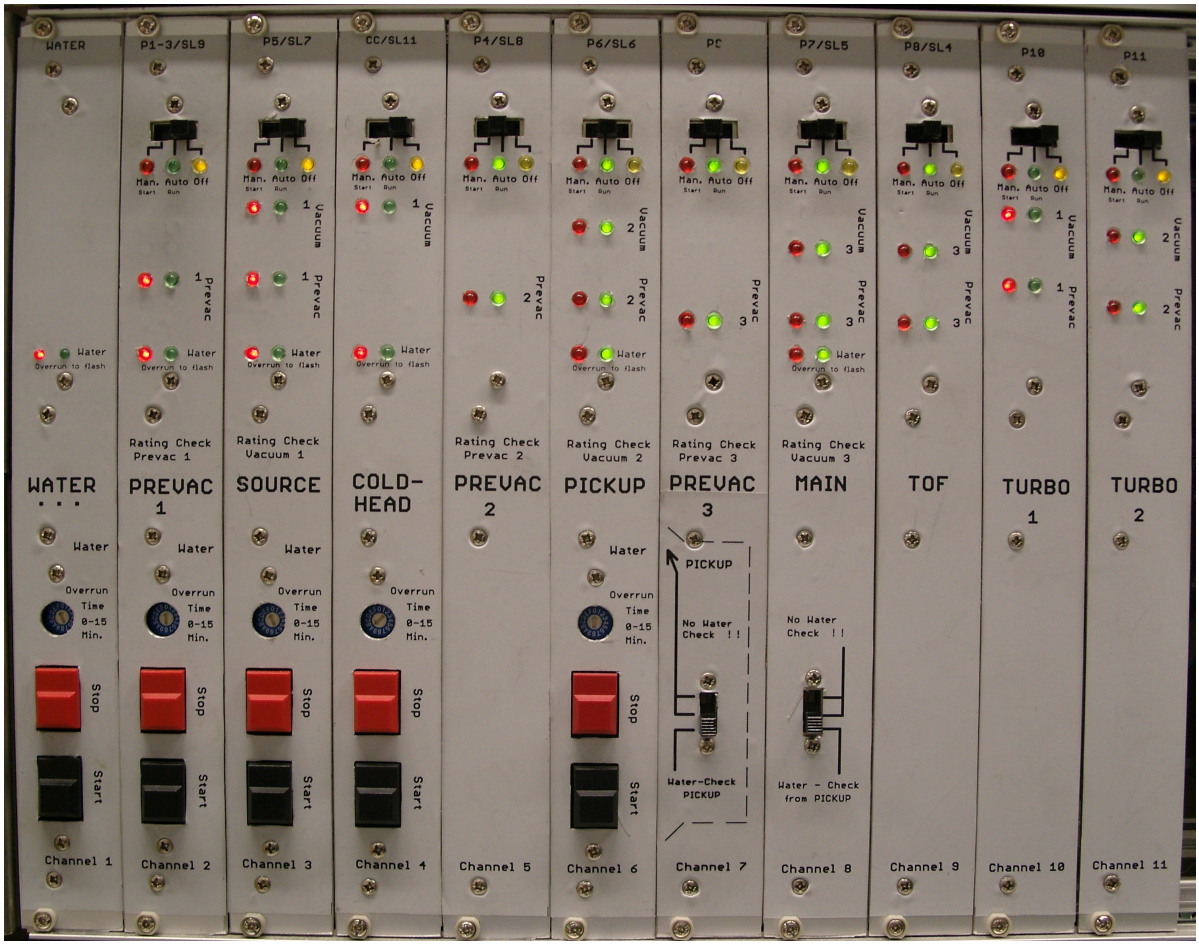

Figure A.8.: Vacuum and water control panel. Single segments control (from left to right): cooling of the pickup cells, prevacuum system of source chamber, source chamber oil diffusion pump, coldhead compressor, prevacuum system of pickup chamber, turbo pumps of pickup chamber, prevacuum system of main chamber, turbo pumps of main chamber, power supply of TOFMS. The two last panels are currently out of use.

Figure A.9.: Vacuum pressure monitors. Although the TM 220 S 2 model can control 2 pirani gauges, there is one separate monitor for every single prevacuum-line. Every monitor is labeled with respect to the position of its associated measurement gauge.

Figure A.10.: Connections of the cooling circuit. The black solenoid valves can be controlled *via* the control panel. The orange flow monitors in the return are adjustable *via* a potentiometer.

5. Helium Droplet Source (Source Chamber)

5.1. Abstract: Helium Droplet Beam Formation

Helium droplets can be created by expanding helium gas through a nozzle, cooled to cryogenic temperatures ($< 20\,\mathrm{K}$) by a closed cycle refrigerator (Sumitomo RDK-408D2). There are three basic formation mechanisms: Condensation of droplets out of the gas phase, fragmentation of the liquid phase and break-up of the liquid jet (illustration see Fig. A.11). Once droplets are formed, they cool themselves down to about 0.4 K by evaporative cooling. All three formation mechanisms can be realized with this machine, depending on the experimental conditions (*i.e.* nozzle-temperature and -pressure); the transition between the regimes is smooth. Typically this apparatus uses electron microscope apertures with $d_0 = 5\,\mu\mathrm{m}$ diameter as nozzle (Günther Frey GmbH) and operates at nozzle temperatures between $T_0 = 4$ and 25 K, and at pressures between $p_0 = 10$ and 50 bar. Tuning these parameters allows to control the droplet size distribution (dependency is shown below, in Fig. A.11) and, to some extent, the amount of He flux. The actual beam is formed by a skimmer (0.4 mm diameter), placed a few millimeters from the nozzle, which cuts out the center part of the emission profile of the nozzle. Details about the fluid mechanics involved in the beam-formation process as well as examples for dimensioning the nozzle-skimmer setup can be found in the literature.[a] [b] However, the calculations in these references do not target the situation where phase transitions become important, as in our case. Nevertheless, many of the concepts presented in these references still hold true and were used for the layout of the machine presented here.

[a] Pauly, H. *Atom, Molecule and Cluster Beams I: Basic Theory, Production and Detection of Thermal Energy Beams.* (Springer Series on Atomic, Optical and Plasma Physics, Springer-Verlag, Berlin Heidelberg, 2000.)

[b] Scoles, G. *Atomic and Molecular Beam Methods.*, Vol. 1. (Oxford University Press, New York, 1988.)

[c] Toennies, J.P. & Vilesov, A.F. Superfluid helium droplets: a uniquely cold nanomatrix for molecules and molecular complexes. *Angew. Chem. Int. Ed.* **43**, 2622-2648 (2004)

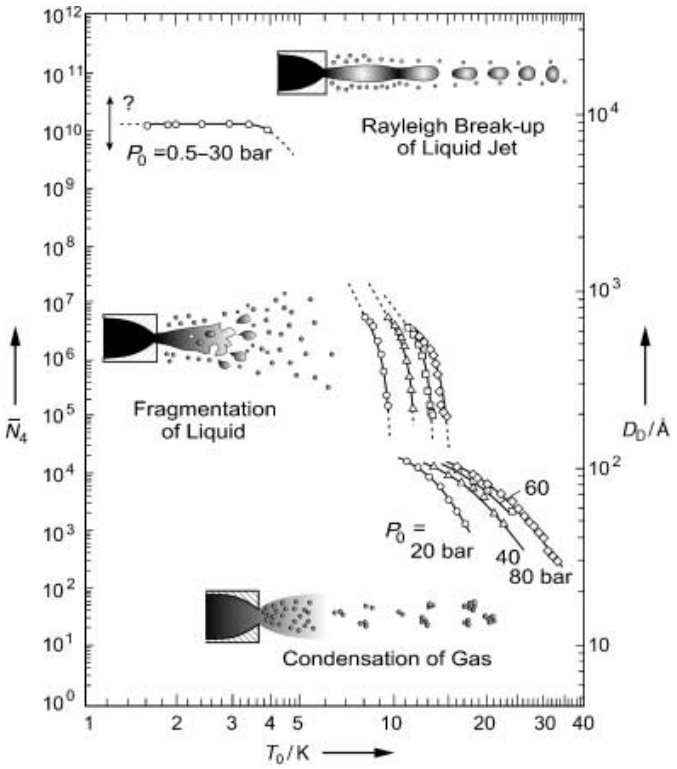

Figure A.11.: Dependency of the mean droplet size on the stagnation conditions. This graph is reprinted with permission from [c], Copyright (c) 2004 Wiley-VCH Verlag GmbH & CO. KGaA.

5.2. Vacuum System

5.2.1. Setup

The vacuum system of the source chamber is a 4-stage system: a large oil diffusion pump (Leybold DI12000, 12.000 l/s) is backed by 2 Roots-boosters (Edwards EH1200 and EH250, in series), which are backed by a rotary vane pump (Edwards E2M80). The exhaust port of the rotary vane pump is connected to the buildings aspiration system.

5.2.2. Dimensioning

The reason for this huge pumping system is the high He flux through the nozzle. At room temperature and ambient pressure the flow rate was measured by capturing the gas bubbled into a liquid.[a] At some point, the original nozzle plate clogged and was replaced

[a] Measurements from 10 to 50 bar in 10 bar steps, 2 measurements at every step (flow rate of 0.35 ml/s at 20 bar).

by a new plate with same nominal diameter.[a] The bubble measurement was repeated and the results corresponded reasonably well to the previous series.[b] Theoretical calculations [c] yield a flow rate which is about twice as high as measured. This means with our large pumping system (12.000 l/s), a pressure in the range of 10^{-5} mbar should be reached in the source chamber with the nozzle at room temperature and the helium beam on. This corresponds very well to the pressure measured in the experiments. As the nozzle is cooled down, the flow rate should increase. In principle, the used equations account for different nozzle temperatures, but it seems as if these equations are no longer valid at the cryogenic temperatures (< 20 K) are present in our experiments. The observed pressure at 10 K and 20 bar still lies in the 10^{-5} mbar range and only increases to a few times 10^{-4} mbar at the lowest nozzle temperature, in contrary to the theory, which predicts much higher values. This means that the provided base pressure is sufficiently low to ensure good beam characteristics and vanishing thermal conductivity of the residual gas in the chamber for all experimental settings.

5.2.3. Operating Instructions

While the other vacuum pumps used in this laboratory are usually working 24/7, the pumps of the source chamber are only switched on for the experiments. The diffusion pump needs some lead time until it starts working properly (heat up time ≈ 20 min), which is shorter than the cool-down time of the nozzle. The control system ensures that the diffusion pump can only be operated if the necessary fore-vacuum conditions are present and the pump is switched off in case of a malfunction. For special purposes (start-up, tests) the system can be overruled when switching to "manual", but the system will shut down automatically after 10 min in manual mode. The diffusion pump produces a large amount of heat; despite the water cooling, the air-conditioning of the laboratory should always be turned on when operating the pump. Since 2014, the water-cooling is realized *via* a closed cycle system, therefore there is no need for saving cooling-water and the water cooling should be used generously (long overrun time). Further the cooling water is treated so that no problems with calcification or formation of algae should occur. Nevertheless, the magnetic valves should be switched at least once a month to check their function (necessary in case of a pipe burst).

Start-up Procedure Before turning on the fore-vacuum pumps, check if the valve between the rotary vane pump and the Roots-boosters, as well as the gate valve in the

[a] Electron microscope images revealed diameters from 5 μm to 6.3 μm for nozzle plates with 5 μm nominal diameter.

[b] Measurements for 20 and 50 bar, only, flow rate of 0.29 ml/s at 20 bar.

[c] Scoles, G. *Atomic and Molecular Beam Methods.*, Vol. 1. (Oxford University Press, New York, 1988), p. 20, eqn. 2.10

vacuum line just before the diffusion pump are opened. It may be necessary to vent both sides of the gate valve (chamber and vacuum line) before opening it, as the valve should not be opened if there is a pressure difference between the two sides.
Check that the venting valves (chamber and pre-vacuum line) as well as the connecting gate valve between source-chamber and pickup-chamber are closed. Turn on the water-cooling of the Roots-pumps. Check that the nozzle pressure is ≤ 10 bar.
Set the "PREVAC 1" switch on the control panel to "manual" (auto is just for regular operation, not for the start-up) to start the rotary vane pump. In order to treat the Pirani-gauges gently, it is best practice to turn them on 2 min after starting the rotary vane pump. The employed control system turns on the Roots-boosters as soon as the lower pressure threshold of the first Pirani-gauge is reached. As the Roots-boosters start, it might happen that this pressure rises above the upper pressure threshold and the Roots-boosters are switched off again (possible on-off-oscillations). Very shortly after the Roots boosters are running constantly, the required fore-vacuum pressure (second Pirani-gauge) will be reached (all control lights on the "PREVAC 1" panel should be green) and the "PREVAC 1" switch can be set to "auto". If there are many on-off-oscillations as the control unit starts the Roots boosters, the pressure threshold should be adjusted.
Turn on the water-cooling of the oil diffusion pump and switch on the full range vacuum gauge "Source" which monitors the pressure in the chamber (now all control lights on the "SOURCE" panel should be green). Setting the "SOURCE" switch to "auto" turns on the diffusion pump (red light at the diffusion pump fuse box is on). Turn on the fan on the right hand side of the frame of the apparatus, next to the viewing glass of the diffusion pump. This helps to reduce the heat-up of the chamber walls. The diffusion pump takes a while (≈ 20 min) to reach its final pressure. During this time the pressure in the camber might rise and fall again a few times (*cf.* Fig. A.12). Final pressure with the nozzle at room temperature and 20 bar stagnation pressure should be $\leq 10^{-5}$ mbar. At the lowest nozzle temperatures it might rise up to a few 10^{-4} mbar.

Shut-down Procedure Make sure that the cryo-cooler (cold-head) is turned off, the valve between the pickup- and the source-chamber is closed and the nozzle pressure is set back to ≤ 10 bar.
Set the "SOURCE" switch to "off" (red light at the diffusion pump fuse box switches off). Turn on the second fan. Wait for $15 - 30$ minutes before turning off the water cooling (the timer on the panel allows a maximum water overrun time of 15 minutes, but the water overrun should be ≥ 30 min). The fore-vacuum pumps must be running and the gate valve in the fore vacuum line must not be closed as long as the diffusion pump is hot.
After the cool down of the diffusion pump and the warm up of the nozzle (otherwise danger of clogging the nozzle), the valves in the fore vacuum line can be closed and the

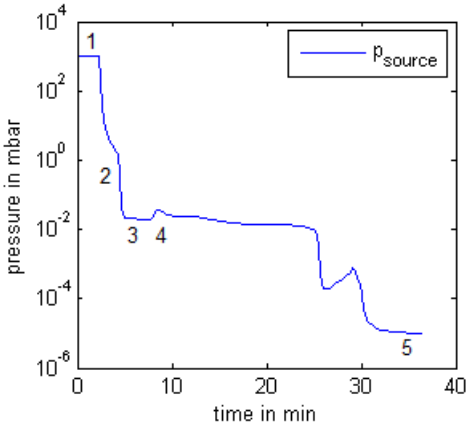

Figure A.12.: Pressure development during the start-up of the vacuum-system in the source-chamber. (1) pressure sensor in over-range, actual pressure decreasing; (2) pumping with rotary vane pump only; (3) auxiliary pumping with the Roots-boosters, plateau at $2 \cdot 10^{-2}$ mbar; (4) pressure variations during start-up phase of the oil diffusion pump; (5) oil diffusion pump in normal operation, final pressure $\approx 1 \cdot 10^{-5}$ mbar at 12 bar nozzle pressure

fore-pumps can be turned off (switch "PREVAC 1").

5.2.4. Maintenance

Cooling-Water System Since 2014, the water-cooling is realized via a closed cycle system where the cooling water is treated so that no problems with calcification or formation of algae should occur. Nevertheless, the function of the valves and flow-meters should be checked monthly to ensure the system is working in case of an emergency.

Fore-Vacuum System Depending on the operating hours of this system, the oil in the rotary vane pump as well as in the Roots boosters needs to be changed (aging process, leaks). Recommended oil-change intervals:
rotary vane pumps - semiannually (also clean the sieve filter at the filling inlet as well as the gas ballast valve and replace the oil filter; new blades are recommended after 3 years)
Roots boosters - annually
In our system the maintenance intervals maybe longer due to short on-time of the source-chamber vacuum system.

Oil Diffusion Pump If the oil-level drops below the threshold mark at the view-port, the reservoir needs to be filled up. In case the oil changes its color, it needs to be replaced and the pump needs to be cleaned. The oil diffusion pump is protected against

overheating by an external bimetal-temperature switch connected to the fuse box. In case of an unexpected switch-off of the pump, this switch should be checked for proper function.

5.3. Cooling System

5.3.1. Setup

In the current setup, the nozzle is directly connected to the second stage of the refrigerator (via a 40 mm diameter oxygen free copper block) and the whole assembly is placed onto a homemade manipulator (tripod consisting of three thread shafts separating the two flanges of a bellow) in order to be able to adjust the position of the nozzle relative to the skimmer (technical drawings for the whole setup: see appendix A). Further, a radiation shield is connected to the first stage of the refrigerator (cold-head), which completely surrounds the inner stage with the nozzle but is designed in a way that guarantees efficient pumping, *i.e.* good vacuum between the nozzle and the shield. The shield consists of just a single part of soldered copper tubes, is wrapped in highly reflective multi-layer foil and reaches a final temperature of 44 K in normal operation. The helium pipe (copper) coming from the vacuum feed-through (steel pipe for thermal isolation) is wrapped around and soldered to the radiation shield to pre-cool the helium gas. After the pre-cooling section, the gas is filtered by a sintered metal filter with 2 μm pore size and continues to flow through a long and thin steel capillary tube (thermal insulation) before it enters the another copper pipe wrapped around the second stage of the refrigerator for the final cooling. The already cool helium gas then moves on to the nozzle, where it expands through the clamped nozzle plate.
The temperature of the nozzle is measured by a temperature sensing diode (silicon diode, DT-670, Lakeshore Cryogenics), especially suited for this temperature range (steep characteristics between 0 K and 20 K). As the cold-head operates with constant cooling power, the temperature of the nozzle is controlled by a heating resistor (Arcol HS15), which is connected to a control-unit built on the institute. This control unit comprises a commercial PID-controller (Eurotherm 3500), a homemade constant current source (10 μA) to operate the diode and a pulse width modulated current source for the heater. The pin assignment can be found in the following figure (Fig. A.13).

In order to minimize the heat flow from the electrical feed-through to the parts at cryogenic temperatures, Manganin wires were used for the electrical connection of the heater and the diode. Furthermore, the wires coming from the electrical feed-through are thermally connected to the end plate of the cold-head before continuing to the heater and the diode ("thermal anchoring") in order to reduce the heat flow from the nozzle to the refrigerator (which leads to a temperature difference between the nozzle and the end plate of the cold-head).

Heater:

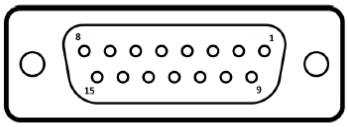

Pin #	Beschreibung
7	GND
14	GND
5	Pulse Width Modulation (+), 26V
12	Pulse Width Modulation (-), GND?

Sensor:

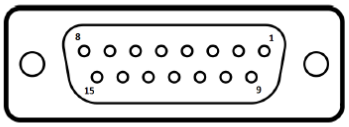

Pin #	Beschreibung
1	I_{out} (+), 10µA (4-wire-system)
9	I_{out} (-), GND (4--wire-system)
2	Shield (GND, galvanically separated)
3	Diode: Pin 1 (Anode (+), Connector closer to the edge of the diode, 4-wire-system)
11	Diode: Pin 2 (Cathode (-), Connector closer to the borehole of the diode, 4-wire-system)
6	PT100: Pin 2a (3-wire-system)
13	PT100: Pin 2b (3-wire-system)
8	PT100: Pin 1 (3-wire-system)

Figure A.13.: The pin assignment of the electrical feed-through

5.3.2. Dimensioning

To get towards big droplets (He_N with $N > 10^7$) it is important to get to very low temperatures ($T \leq 6\,K$). In order to reach these temperatures a cryo-cooler (Sumitomo RDK-408D2) with the following specifications is used:

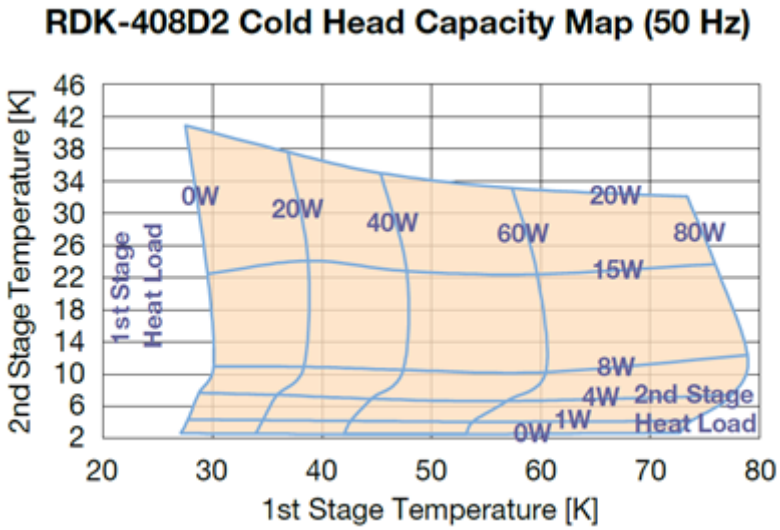

Figure A.14.: Cooling capacities of the 1st and 2nd stage of the refrigerator, depending on the stage temperature. Taken from [a].

The heat load applied to the first stage (shield) can be estimated by calculating the thermal radiation:

$$\dot{Q} = A_{\text{shield}} \cdot \sigma \cdot \epsilon \cdot \left(T^4_{\text{chamber}} - T^4_{\text{shield}}\right) \tag{5.1}$$

[a] SHI cryogenics group: http://www.shicryogenics.com

Where $A_{\text{shield}} \approx 0.2\,\text{m}^2$ is the surface area of the radiation shield, σ is the Stefan Boltzmann constant $\epsilon = 0.4$ (estimated) is the emission coefficient and T_{x} are the temperature of the wall of the vacuum chamber ($\approx 300\,\text{K}$) and the temperature of the radiation shield ($\approx 45\,\text{K}$). With these parameters the heat load yields about 40 W.

The same calculation can be applied to the 2nd stage:

$$\dot{Q} = A_{\text{nozzle}} \cdot \sigma \cdot \left(T_{\text{shield}}^4 - T_{\text{nozzle}}^4\right) \tag{5.2}$$

Where $A_{\text{nozzle}} \approx 0.03\,\text{m}^2$, $T_{\text{shield}} \approx 45\,\text{K}$ and $T_{\text{nozzle}} \approx 4\,\text{K}$ yields a heat load of 0.007 W. Clearly, the radiation can be neglected here and the heat flow through the wires of diode and heating resistor contributes the main part of the heat load. As the thermal conductivity of copper increases dramatically at temperatures around 25 K and can reach up to 15 times the value it has at room temperature, Manganin wires were used instead of copper. Manganin has a low thermal conductivity $\left(< 25\,\frac{\text{W}}{\text{m K}}\right)$ over the whole range from room temperature until cryogenic temperatures. (compare to copper: $400\,\frac{\text{W}}{\text{m K}}$ at room temperature and much higher at 25 K).

In this setup, temperatures as low as 3.7 K at 20 bar or 4.0 K at 50 bar were reached without additional alterations. Without gas flow (clogged nozzle) a minimum temperature of 2.5 K was reached. The cool down time from room temperature to temperatures below 10 K is ≈ 100 min.

5.3.3. Beam Dimensions

Sometimes it is important to know the approximate beam dimensions of the droplet beam at a specific location of the beam path, e.g. to prevent an unwanted simultaneous illumination of two separated substrates. Therefore we estimated the beam dimension by geometric considerations.
Fig. A.15 shows a compilation of possible beam limiting elements along the beam path. It turns out that the skimmer at the exit of the pickup chamber is the actual limiting element. From its relative position to the nozzle and its diameter one obtains a beam divergence of $\approx 0.271°$. However, we note that in some cases the helium nozzle is operated under conditions where the emerging beam is supposed to be even narrower. This will be the case especially when liquid helium is streaming out of the nozzle, *i.e.* at very cold nozzle temperatures (see Fig. A.11). On the quartz crystal of the microbalance one can see the area of pronounced deposition by naked eye. The diameter of this area is $\approx 6\,\mathrm{mm}$ which would correspond to a smaller beam divergence of $\approx 0.223°$ (indicated by red lines in Fig. A.15).

5.3.4. Operating Instructions

Following the code of best practice, there must always be a certain flow through the nozzle to avoid clogging. This is realized by keeping the nozzle pressure at $\geq 10\,\mathrm{bar}$ at all times. Once the nozzle is clogged (by a droplet of diffusion pump oil, dust, etc.) there is hardly any chance to get it working again - so far, clogged nozzles always had to be replaced.

Start-up Procedure As it takes about 100 min for the cold-head to cool down the nozzle, which is much longer than the diffusion pump needs to get started, one can begin with start-up procedure of the cold-head right after switching on the diffusion pump. To start the cold-head, turn on the water-cooling on the respective control panel and set the "COLD-HEAD" switch to "auto" (typical pumping noise of the cold-head). After a few minutes the nozzle temperature should start to decrease (monitor at the display of the temperature control unit or with iTools software on the computer). After about 100 min a temperature below 10 K should be reached. When the desired temperature is reached, the nozzle pressure can be increased to the required value.

Shut-down Procedure Set the nozzle temperature to $T_0 = 0\,\mathrm{K}$ and close iTools. Set the "COLD-HEAD" switch to "off" and turn off the water-cooling. After that, the cooling water will continue to run for another couple of minutes (as set on the panel), which is indicated by the flashing green light. The nozzle pressure can be reduced to the base-pressure of $\approx 10\,\mathrm{bar}$ which prevents the nozzle from clogging. As long as the

nozzle-structure is colder than $\approx 0\,^{\circ}\mathrm{C}$ the chamber should not be vented, otherwise the humidity in the air will immediately freeze on the cold parts, thereby possibly clogging the nozzle.

Maintenance, Troubleshooting

Compressor-Cold-Head Unit (Sumitomo RDK-408D2) Maintenance work that can be done by the user:

- Since 2014, the water-cooling is realized via a closed cycle system where the cooling water is treated so that no problems with calcification or formation of algae should occur. Nevertheless, the function of the valves and flow-meters should be checked monthly to ensure the system is working in case of an emergency.
- Replacement of the Compressor Adsorber (every 30.000 hrs $\rightarrow$ with the short run-time of our system, this will probably not apply to us), for instructions see manual of the compressor unit
- Recharging helium gas (as required $\rightarrow$ see pressure gauges on the compressor unit) , for instructions see manual of the cryocooler

Maintenance work that cannot be done by the user:

- Replacement of the cold-head mechanical parts (every 10.000 hrs), cold-head has to be shipped to the manufacturer

Adjusting the Nozzle-Setup Due to the cooling cycles of the nozzle-setup and the heating cycles of the oil diffusion pump it might happen that the position of the nozzle and/or the chamber gets distorted. If this is the case, the helium pressure in the source chamber does not change, but the helium flow through the skimmers is significantly reduced. If the droplet beam cannot pass the skimmers any longer, there will still be He-gas in the measurement chamber, but no droplets (distinguishable in the mass spectrum $\rightarrow$ no signal at the multiples of He_4). If the nozzle is clogged, on the other hand, not only the helium pressure in the down-stream chambers, but also in the source chamber is reduced. Once the nozzle is clogged (by a droplet of diffusion pump oil, dust, etc.) there is hardly any chance to get it working again - so far, clogged nozzle plates (electron microscope apertures, Günther Frey GmbH) always had to be replaced.
After replacing the nozzle or whenever the beam is poorly aligned, the alignment can be checked with a telescope, looking along the beam axis from the downstream end of the machine. In order to find the right position for the nozzle, the flange with the skimmer has to be removed from the source chamber. After this, the nozzle is visible in the telescope and the position as well as the tilt can be adjusted using the 3 screw

nuts on the tripod (gray in Fig. A.16). Keep in mind that the nozzle axis must be horizontal (check with a mason's level). The tilt around the vertical axis can be checked by controlling whether the nozzle and the flange-plane are parallel, using an indicating caliper. The tilt around the beam axis is used to change the nozzle position horizontally (left image in Fig. A.16). When putting the flange with the skimmer back on, its position must also be adjusted using the telescope (illuminate the skimmer from inside the source chamber). In the aligned setup, only minimal adjustments (less than a half turn on each of the 3 screw nuts of the tripod) are needed to optimize the helium flow through the chambers. If bigger adjustments are necessary, there is most likely something wrong with the nozzle plate. A more detailed description of the alignment procedure for the whole machine follows in section 8.1.

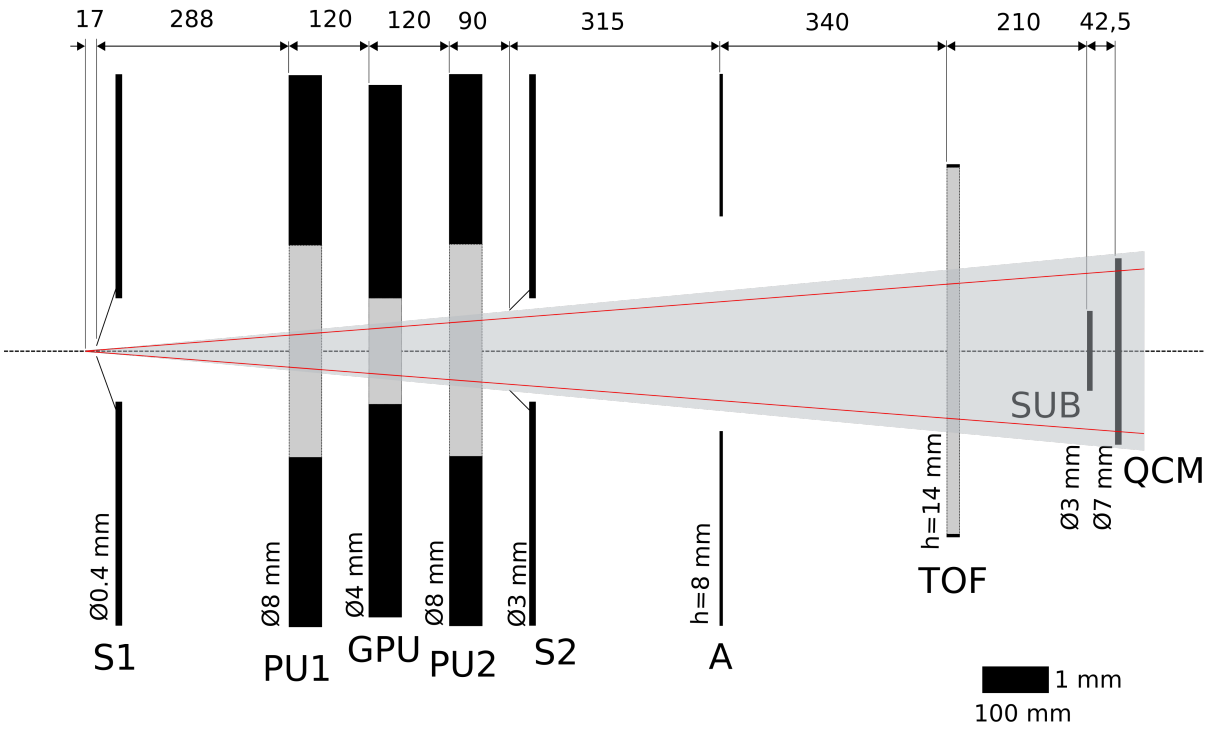

Figure A.15.: Dimensions of the droplet beam. **S1** skimmer in source chamber; **PU1/PU2** resistively heated pickup cells (length= 50 mm); **GPU** gas-pickup cell (length= 50 mm); **S2** skimmer at pickup chamber exit; **A** aperture separating differential pumping stage and main chamber (width= 3 mm); **TOF** time of flight mass spectrometer ionization zone (width= 20 mm, length= 20 mm); **SUB** substrate for cluster deposition; **QCM** quartz crystal monitor. The diameters/heights of the elements are indicated. Beam dimensions are plotted as obtained by geometrical considerations (grey area) and as visually determined (red lines). See text for further explanations. Scale is 1:10 in horizontal direction and 4:1 in vertical direction.

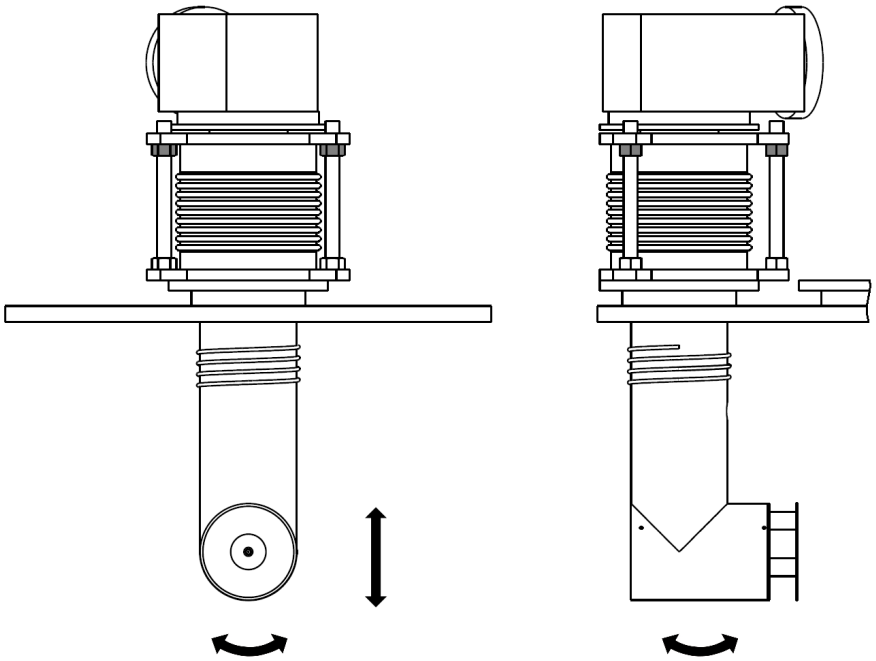

Figure A.16.: Schematics illustrating the adjustment of the nozzle. The left image shows the adjustment of the nozzle position. The tilt shown in the right image must be zero, *i.e.* the beam axis must be horizontal.

6. Droplet Doping (Pickup Chamber)

6.1. Abstract: Pickup and Cluster Formation Inside Helium Droplets

When a helium droplet collides with an atom or molecule, the probability that the particle gets picked up by the droplet is close to unity (for all dopant species). Therefore, the interaction cross section can be approximated by the geometrical cross section of the droplet. The amount residual gas pickup is defined by the droplet size and the base pressure in the pickup chamber. In order to keep the ratio between parasitic pickup of residual gas and the pickup of the desired dopant species low, base pressures lower than $\approx 1 \cdot 10^{-6}$ mbar have to be provided. Consequently, a certain pickup rate of a desired dopant can be adjusted by controlling its abundance (*i.e.* partial pressure / vapor pressure) along the beam line. For gaseous species, this is realized by dosing the dopant gas into a hollow cylinder through which the beam is guided. This way, the partial pressure of the dopant is elevated inside the pickup cell, while a low base pressure is maintained in the chamber (outside the cell). In order to pick up solid species, they have to be forced into the gas phase first, usually by heating the desired dopant to a temperature, at which the vapor pressure is sufficient to yield the necessary amount of collisions with helium droplets. For the synthesis of nanoparticles (*i.e.* the pickup of several thousand atoms) this temperature usually lies in the region of the melting point of the dopant material. The metal pickup cells used in this machine utilize resistively heated crucibles in a water-cooled housing, through which the beam is passed.
Once a dopant hits the droplet, it gets cooled down (slowed down), but afterwards the interactions with the superfluid environment are very weak and the dopant is able to move inside the droplet. If additional dopants are added to the same droplet, they will eventually meet and coagulate. Thereby, binding energy is released, which causes the evaporation of helium atoms from the droplet. Especially when producing larger clusters, this leads to a significant shrinking of the droplet. As a rule of thumb, about 1600 helium atoms are evaporated to dissipate 1 eV of binding energy. For most metals this means each atom added to the cluster leads to the evaporation of ≈ 5000 helium atoms.

The introduction of sequential pickup schemes as well as the low temperature of the droplet lead to interesting possibilities for cluster production in terms of exotic material combinations and core-shell systems.

6.2. Vacuum System

6.2.1. Setup

The vacuum system of the pickup chamber is a 2-stage system: a large turbo pump (Oerlikon Turbovac 1000C, nominal throughput = 1000 l/s) is backed by a rotary vane pump (Leybold Trivac D40B). The exhaust port of the rotary vane pump is connected to the buildings aspiration system. In order to reduce the noise level in the lab, the fore-pump is located in the adjacent room. During experiments, the vacuum in the pickup chamber can be improved by operating the installed liquid nitrogen cooling trap. At the end of the pickup chamber, there is a second skimmer (3 *mm* diameter), which shapes the beam before it runs through the differential pumping stage, which is pumped by a small turbo pump (Pfeiffer TPU 062, nominal throughput = 50 l/s). This turbo is backed by the same rotary vane pump as the pickup chamber. There are two valves in the fore-vacuum line, one right after the rotary vane pump and one just before the turbo pumps. The pickup chamber is sealed using rubber gaskets, which means that a minimum base line pressure of high 10^{-8} mbar or low 10^{-7} mbar can ultimately be reached. The differential pumping stage (sealed with copper gaskets) is necessary in order to maintain the very low pressures in the measurement chamber during operation (He_N-beam on). The copper gasket between the differential pumping stage and the measurement chamber is not ring-shaped as usual, but circular with a slit (height = 8 mm, width = 3 mm), which acts as another aperture for the beam, in order to increase the pressure gradient.

6.2.2. Dimensioning

Ideally, the helium beam created by the skimmer in the source chamber enters the pickup chamber on the front end and leaves it at the back end without any helium losses, as long as there is no doping. In practice, there will be losses due to self cooling and possibly the beam spread angle (skimmer at the exit of the pickup chamber). As soon as there is pickup, there will be additional evaporation losses. Furthermore, when heating up the crucibles, absorbed and adsorbed substances will desorb and add gas to the chamber. When dosing gas into the gas pickup chamber, only a fraction of the introduced atoms or molecules will be picked up, the rest has to be removed. In order to keep the base pressure in the pickup chamber low, especially when the pickup cells are turned on, the high throughput of the turbo pump is needed. Otherwise, there would be uncontrolled pickup of all residual gas species along the beam. In the current setup, only parasitic pickup of water molecules can be observed in the mass spectra, the abundance of all other gases is too low in order for them to be detected.
After the beam passes through the second skimmer (3 mm diameter) at the exit of the

pickup chamber, the beam enters the differential pumping stage with another aperture (rectangular, height = 8 mm, width = 3 mm), in order to get a larger pressure gradient between the pickup chamber and the last chamber. In a previous design, there were three apertures in the differential pumping stage, but it turned out that one is sufficient, which makes the alignment procedure (section 8.1) much easier. The rectangular shape of the aperture in the current setup was chosen in order to allow the beam to pass, even if it is deflected downwards by gravity (significant gravity effect can only occur at the lowest possible nozzle temperatures, where the beam velocity is low) or upwards by extensive doping.

6.2.3. Operating Instructions

Be aware that the vacuum systems of the pickup-chamber and the differential pumping stage are not separated and can only be operated together. Usually, the vacuum System of these 2 chambers is working 24/7 and maintains a base pressure in the low 10^{-7} mbar range in the pickup-chamber and a base pressure in the high 10^{-9} mbar range in the differential pumping stage.

Shut-down Procedure Before shutting down the system, make sure that the gate valves to the source- and measurement-chamber are closed and the crucibles are at room temperature. Close the valve in the fore-vacuum line and turn off the pumps at the control panel (switches "PREVAC 2" and "PICKUP" in position "off"). As a rule of best practice, one waits until the large turbo pump has slowed down to half its nominal speed (only half of the LEDs in the LED-bar on the controller Leybold TD20 are illuminated) before opening the venting valve. While opening the venting valve, monitor the chamber pressure. As soon as the pressure has risen by an order of magnitude, close the valve again and wait a minute for the turbo pump to slow down, then repeat the procedure. The chambers can either be vented with an inert gas (dry nitrogen or argon, which is recommended if the side flanges remain closed or are opened for only a few minutes) or with ambient air. Venting with an inert gas reduces the introduction of moisture to a minimum, therefore, good vacuum conditions can be reached very shortly after restarting the pumps. After venting with air or longer maintenance work, a bake-out of the chambers is needed in order to reach the before mentioned base pressures. When venting with inert gas, be aware that overpressure in the vacuum chamber should be avoided (may harm the gate valves, feed-throughs and windows). Unfortunately, the standard vacuum pressure gauges are very inaccurate above ≈ 10 mbar and cannot be used as indicators for reaching ambient pressure. Instead, the opening of the pressure relieve valve on the side flange can be taken as indicator to immediately close the venting valve (escaping of the gas can be heard and the button of the relieve valve can be moved).

As long as the system is at ambient pressure, the pressure gauges should be switched off.

Start-up Procedure Before starting the vacuum system, make sure that the gate valves to the source- and measurement-chamber are closed and the valves in the fore-vacuum line are opened. Start the fore-vacuum pump by setting the "PREVAC 2" switch on the control panel to "manual" and, after one minute, turn on the pressure gauge "PREVAC PICKUP". As soon as the backing pressure is sufficiently low, the "prevac" LED turns green and the "PREVAC 2" switch must be set to "auto" (otherwise, the system shuts down automatically after 10 min in "manual"-mode). Then, the "PICKUP" switch can be set to "manual". Turn on the cooling water (black button on the control panel) and the pressure gauge "PICKUP". As soon as $1 \cdot 10^{-3}$ mbar are reached in the pickup chamber all LEDs (prevac, vacuum, water) on the PICKUP control panel should be green and the PICKUP switch must be set to "auto". If the 10^{-5} mbar range is not reached within a short time, there will likely be a leak [a] [b]. When searching for a leak, start with the flanges that were open during the shutdown and control the Swagelok connections inside the chamber as well, if they were opened.

6.2.4. Maintenance

Since 2014, the water-cooling is realized via a closed cycle system where the cooling water is treated so that no problems with calcification or formation of algae should occur. Nevertheless, the function of the valves and flowmeters should be checked monthly to ensure the system is working in case of an emergency.
The oil in the rotary vane pump is recommended to be changed (aging process, leaks) semiannually (also clean the sieve filter at the filling inlet as well as the gas ballast valve and replace the oil filter), new blades are recommended after 3 years. The rotor of the Oerlikon turbo pump should be replaced after 9 years. The operating fluid of the Pfeiffer turbo pump should be changed every 4 years. Check manuals for further information.

6.3. Feed-Throughs

In order to operate the components inside the pickup chamber, several feed-throughs are required. Most importantly, for the two metal vapor pickup cells two high current (up to 185 A and 8 kV) 2-pole electrical feed-throughs (Vacom, W-HC8-CE-CV64) are installed. Be aware that these feed-throughs may become hot during operation (up

[a] In case of a leak: shutdown, find and seal the leak, start again.
[b] Exception: if the chamber has been opened for a day or longer, there will be a lot of water adsorbed, which takes some time to desorb and keeps the pressure in the 10^{-4} mbar range

to 200°C). Besides the power supply, these vapor cells need water-cooling, whereby the pipes are internally connected *via* Swagelok-connectors. The temperature inside the chamber can be monitored on several positions using a triple-feed-through of type K thermocouples (Vacom, W-TC3-CE-K) as well as a double-feed-through of type C thermocouples (Vacom W-TC2-CE-C). Furthermore, a gas-feed-though with a dosing valve on the outside of the chamber is installed in order to operate the gas-pickup cell.
For the operation of a chopper (as in other machines on the institute) a 15 pin SubD-feed-through (Vacom, W-SUBD-15-DE-CE-SSG, max. 500 V, 5 A/pin) is provided, however, was not used so far.
Other small loads can be connected via a multi-pole feed-through (Vacom, W-MPC2-19-SE-CE-SSG, max. 1 kV, 3 A/pin) which is fitted to a box with electrical sockets outside the chamber to enable fast and secure plugging. By the time this manual was written, only the light bulbs for the internal bake-out were connected, using sockets D and K (denomination adopted from the feed-through). In earlier experiments other pairs of sockets were used to operate lifting solenoids for blocking the droplet beam or blocking the dopant-atom beam (crossed beam setup).

6.4. Pickup Cells

6.4.1. Gas Pickup Cell

Using a regular gas dosing valve (Duniway VLVE-1000) gaseous (and some liquid substances) can be introduced into a vacuum chamber in finely adjustable amounts. Without any further action, the substance dosed into the vacuum chamber would spread in the whole chamber. In order to dope the helium droplets, a spatially confined pickup-region is desired. Only then, the sequence in which the different species are added to the droplet can be controlled by the position of the respective pickup-cells. The spatial confinement is realized by dosing the desired substance(s) into a tube with a hollow cylinder at the end, through which the beam is passed. Thereby, the gas volume inside the cylinder (12 mm diameter, 50 mm length) is larger than the interaction region with the beam, which enters and leaves the cylinder through a 4 mm borehole (see Fig. A.17).

Figure A.17.: Gas pickup cell

The option of dosing *e.g.* oxygen into the droplets opens the way to investigate chemical reactions inside the droplet. Furthermore, it allows a comparison between situation where *e.g.* oxygen is present already during cluster formation or not until after cluster formation.

6.4.2. Metal Pickup Cells

For the experiments conducted with this machine so far, magnetic fields inside the pickup chamber were not critical. Therefore, the simplest solution for evaporating the dopants are resistively heated crucibles (Ted Pella Aluminia Coated Tungsten Wire Basket, Style 6), which need high electrical currents (up to 40 A per crucible). With these, a maximum temperature of about 2000 K can be reached, which yields sufficient pickup conditions (vapor pressure) for a broad range of metals (so far, silver, gold, copper, chromium and nickel have been evaporated with this design). In order to avoid damage or excessive heating of other elements in the same chamber, the hot crucibles have to be housed in water-cooled radiation shields. Following, two different designs of the evaporation sources are described, technical drawings can be found in appendix A.

Crossed Beam Setup In this design the crucible is covered by a tantalum sheet with a 3 by 25 mm slit (see Fig. A.18a) in order to minimize the loss of Ag atoms and the heat flow to the cooling shield. The shield itself also has a slit, which is placed just below the helium beam (see Fig. A.18b). This way, the passing He droplet beam is hit by evaporated atoms from underneath, under an angle of about 90°.

(a) (b) (c)

Figure A.18.: Crossed beam setup. (a) crucible with tantalum cover (1), Cu columns as electrical contacts (2) and water-cooled base-plate (3); (b) assembly with water-cooled housing; (c) assembly with electromagnetic shutter. Figure taken from [a].

The main advantage of this design is the possibility to introduce a shutter (depicted in Fig. A.18 c), which allows to switch the source on and off within seconds, while in other

[a] Steurer, J. *Helium Droplet Mediated Fabrication and Analysis of Noble Metal Nanoparticles.* Master's thesis, Graz University of Technology (2014).

designs, the crucibles need to be heated up or cooled down in order to turn the pickup on and off. A disadvantage of this concept is the unidirectional doping, which deflects the helium droplet beam at high doping rates. Furthermore, this source requires frequent maintenance because the dopant material tends to condensate at the slits, making them narrower over time until they plug up completely.

Vapor Cell Setup Here, two crucibles are mounted on top of each other (mirrored) and the beam passes between the crucibles (see Fig. A.19). They are connected in

(a) (b)

Figure A.19.: Vapor cell setup with (a) and without (b) Cu cooling shield. Figure taken from [a].

parallel and consequently will have about the same temperature. The crucible at the bottom is filled with the metal to evaporate. Atoms that are evaporated at the bottom are either picked up by the He droplet beam or they arrive at the top crucible, where they will be reflected and thus can hit the droplet from the opposite direction. With this design the droplet beam is not deflected as in a crossed beam setup, which is crucial for experiments where heavy doping is desired.[a] Unlike the previous design, this setup does not allow turning the pickup on and off fast. Different pickup rates can only be adjusted by changing the temperature, which takes time.

[a] Steurer, J. *Helium Droplet Mediated Fabrication and Analysis of Noble Metal Nanoparticles.* Master's thesis, Graz University of Technology (2014).

Temperature Measurement Earlier designs were equipped with a Type C thermocouple, housed in a ceramic husk, which was placed inside the metal melt. During the first experiments it turned out, that it is practically impossible to avoid thermal contact of the husk with the cooling shield. Consequently, there is a significant heat-flow over the ceramic husk, which changes during melting and solidifying. Besides the varying heat flow, which leads to significantly different temperatures of the heated metals at identical heating power, also the temperature measurement itself is affected by the thermal contact to the shield. With this measuring principle, it was impossible to reproduce the same conditions in subsequent experiments. In order to get information about the dopant temperature after removing the thermocouple and husk, the electrical resistance of the wire basket was recorded and used as temperature sensor. Through this measure, reproducibility was guaranteed, however, this way of determining the dopant temperature is not accurate.

Computer Program: Temperature Control During the cluster synthesis process it is important that the vapor density in the pickup cells can be held at a constant level. As the vapor pressure depends exponentially on the temperature, temperature differences of 20 K or less do make a difference. Hence, setting a constant heating current and waiting for the temperature to stabilize is not a good strategy. An automated temperature control is needed.
After an attempt to realize the temperature control using LABVIEW, which always had stability issues, a MATLAB code was developed to communicate with the power supplies (EA-PS 9080-100). The communication with the power supplies (via UTA12-interface) is done with telegrams in hexadecimal form. A command cycle typically consists of a command transfer and a reply transfer. Hence, the interface works as a slave and waits for commands. Instructions on how to program the communication can be found as an attachment to the manual of the power supplies. For the communication to work it is important that the USB-Serial Ports are correctly configured in the hardware manager. Furthermore the ports have to be opened and closed properly in the computer program. If the power supplies are not responding to the MATLAB program, this is most likely related to a problem with the ports and can be resolved by restarting the MATLAB program.
The control program itself reads the voltage and current provided by the power supply and by calculating the resistance of the crucible gives a calculated temperature (eqn. 6.1).

$$T = \frac{\frac{R_T}{R_{20}} - 1}{\alpha} + 20°\mathrm{C} \qquad \text{with} \qquad \alpha = 0.0044\,°\mathrm{C}^{-1} \tag{6.1}$$

As the different crucibles do not have exactly the same resistance, the resistance at room temperature is tested by the program by sending a short current pulse of twice the speci-

fied minimum current through the crucible while measuring the voltage drop, before the actual control program starts. The control program can operate in two modes, "ramp" and "constant". In the ramp-mode the temperature is increased or decreased with a specified rate, which is important for the lifetime of the crucibles. If they are heated or cooled down too fast, they might break (rates $< 150\,\mathrm{K/h}$ are advised by the manufacturer at absolute temperatures below 600 K). If the desired temperature is reached, the program automatically switches to constant-mode, which holds the temperature in a window of about $\pm 2\,\mathrm{K}$ around the specified value. It should be noted that this way of determining the temperature is not very accurate and uncertainties of $10 - 15\,\%$ of the absolute temperature value have to be expected, however, the reproducibility and the stability are very good. Besides live-control, the program also can save log-files containing all measured and calculated values with a time-stamp.

6.4.3. Operating Instructions

Before switching on the power supplies for the crucibles (EA-PS 9080-100), check that the water-cooling of the cooling shields is on and that the vacuum conditions are sufficient (pressure below $10^{-6}\,\mathrm{mbar}$, otherwise, the beam won't reach the measurement chamber; at ambient conditions the crucibles might be damaged if they are heated). As described above, the current setup is not equipped with temperature sensors, instead the electrical resistance of the setup is taken as a measure for the temperature. The resistance (temperature) readout as well as the control of the heating power can be carried out by a self-made MATLAB program, exploiting the very linear temperature dependence of the resistance of tungsten.
Below a temperature of $\approx 300°\mathrm{C}$, the crucibles should not be heated up or cooled down at a rate higher than 150°C/h, at high temperatures rates of up to 5000°C/h are no problem. With the ramp-function of the Matlab-program, an adequate heating rate can be set and after reaching the desired temperature, the program maintains a stable temperature (typically within $\pm 2°\mathrm{C}$). For safety reasons, a maximum current as well as a maximum voltage can be set. For the 2-crucibles setup, the resistance of the system at room temperature lies around $0.03\,\Omega$ to which the tungsten wires of the crucibles contribute the largest part. When heating up, not only the resistance of the crucible, but also the resistance of the copper wires changes, leading to a systematic error in the temperature measurement. The resistance at a known temperature (*e.g.* room temperature) can be measured by the Matlab program, when checking the respective option (needed *e.g.* after changing the setup), but may also result in a bias. With this method, the absolute error in the temperature measurement might be as high as 15%, but the settings are reproducible (a certain heating power yields the same resistance/temperature). Every time the temperature is increased, gases start to desorb from the crucible, es-

pecially when heating the first time after venting the chamber. In normal operation, pressures below 10^{-6} mbar (which are necessary for good experiments) can be reached without using the liquid nitrogen trap. Nevertheless, the liquid nitrogen trap can be used to improve the vacuum conditions at any time.
If the water-cooling is not switched on for any reason while the crucibles are hot, immediately turn off the power supplies. Do **NOT** turn on the water-cooling - the water will boil and the steam will melt the rubber hoses. Furthermore, the temperature shock might break the pipes inside the vacuum with potentially catastrophic consequences. With the water-cooling off, the crucibles will cool down slowly and likely there won't be any damage. If the crucible temperature without cooling exceeded 400°C, some components of the solder on the cooling shield will evaporate and the chamber needs to be cleaned.
In order to dope the droplets heavily, temperatures corresponding to a vapor pressure of $10^{-4} - 10^{-2}$ mbar of the respective material are needed. If these temperatures are not / no longer sufficient, there is either not enough material left in the crucible or there is another problem. Do not push the temperatures to extremes. When experimenting, always check the un-doped droplet signal first with the TOFMS (helium-comb) as well as with the QMS to determine the He-partial pressure as a reference for the later measurements with doped droplets. If there is no He-signal, control the pressures in all chambers and check the beam-line with the telescope for obstacles and correct alignment.

6.4.4. Maintenance

Depending on the intensity of use, the crucibles will have to be refilled after a certain time. When using small pellets of the material to evaporate, a straw can be plugged through one of the holes for the beam (vapor cell setup) or through the slit at the top (crossed beam setup) into the crucible. The pellets have to be put into the straw with tweezers and slide down into the crucible. The filling level can be checked using an endoscope. This method has the big advantage, that neither the electrical contacts nor the water-cooling have to be disconnected and the alignment is not obstructed.
If the method above cannot be applied, or a different material should be placed in the oven, the simplest method is to disconnect the water-cooling (after turning off the water and dry-blowing the tubes) and the copper-rods (such that the columns on each side of the crucible remain clamped to the base plate) and to remove the whole setup from the rails (by opening the 2 knurled nuts). Once the setup is outside the vacuum chamber, it is much easier to service. When changing the materials, it is best practice to also switch the crucibles (each crucible is only used for one material). To do so, remove the cooling shield and open the clamps on the columns. Remove the old crucibles (be careful, the alumina as well as the tungsten wires are brittle!) and clean the shield as well as the base plate. Collect the material scraped off the shield and the base plate in case it is

valuable (e.g. gold or silver). Mount the new and filled crucibles and assemble the oven again. If all tasks have been carried out very carefully, the alignment might still be alright, but the alignment has to be checked in any case.
When using the crossed beam setup, keep track of the cell temperature needed for a certain beam attenuation. The material condensing at the slit reduces the slit's cross-section, such that higher temperatures are required to get the same doping load. Higher temperatures lead to a faster clogging of the slit, which means that after a while the excess material has to be scraped off.

7. Droplet and Cluster Analysis (Measurement Chamber)

7.1. Abstract: Beam and Cluster Analysis

The nanoparticles assembled in the pickup chamber are carried into the measurement chamber by the droplet beam. There, they can be analyzed *in-situ* or deposited for subsequent *ex-situ* diagnostics. In-flight diagnostics offer the advantage of very cold (ground state) particles which are only very weakly influenced by their surrounding. Measurements on deposited particles have the advantage that the particle density on the substrate can be chosen by adjusting the time span for deposition and instead of measuring averages, single particles can be addressed on the surface. However, during the landing process on a certain substrate, the helium surrounding the nanoparticle will evaporate and the particle will warm up. Additionally, the adsorption of the particles on the substrate may change their shape and morphology and may alter their properties.
The most important detection / analysis techniques at the moment are time-of-flight mass spectrometry (TOFMS) (in flight) and *ex-situ* transmission electron microscopy (TEM) of the deposited clusters. The TOFMS yields data about the composition, abundance and stability of different cluster sizes in the produced cluster collective. The TEM, especially with the element-sensitive detectors, can provide information about single clusters (size, element distribution, morphology). If the samples are exposed to ambient conditions during the transport to external diagnostics, the high reactivity of nanoparticles can become an issue. In order to be able to investigate pre-reactive nanoparticles, a UHV-transfer system was purchased (see Section 7.6). This permits the use of more reactive materials as well as other detection techniques, which are available at *e.g.* the University of Graz. For the protected transfer of samples to the electron microscopes, a specialized TEM-holder, already purchased by the Institute for Electron Microscopy and Nanoanalysis, might be used in the future. A suitable docking port for this holder on our machine is currently under construction.
In addition to this the main investigation methods, *in-situ* microbalance measurements provide information about the absolute cluster mass-flow and helium partial pressure measurements show the influence of the doping on the droplet beam (evaporation).

7.2. Vacuum System

7.2.1. Setup

The vacuum system of the main chamber is a 3-stage system: there are 3 turbo-molecular pumps directly connected to the chamber (Pfeiffer HiPace 700 + Pfeiffer TPU 520 on the bottom and Pfeiffer HiPace 300 on the TOFMS). The compression ratio provided by these pumps is not sufficient to reach UHV conditions ($< 10^{-9}$ mbar) given the rather poor fore-vacuum pressure provided by the oil free multi-Roots primary pump system (Adixen ACP40, $3 \cdot 10^{-2}$ mbar ultimate pressure at the flange of the fore pump which means $1 \cdot 10^{-1}$ mbar at the connection to the turbo pumps, due to the long fore-vacuum line). Therefore a third stage, which is a small turbo pump between primary pump and the turbo pumps on the chamber, was introduced. If this turbo pump is placed between the fore vacuum line and the pumps on the chamber, the fore-pressure provided by the fore-turbo is so low (10^{-6} mbar) that the lubricant of the bearings of the regular 3 turbo pumps might evaporate. To avoid this, the fore-turbo was placed between the primary pump and the fore vacuum line. Because of the length of the line this only leads to an improvement of about an order of magnitude in the fore-pressure compared to the system without the fore-turbo pump. Nevertheless, this is sufficient to reach the 10^{-10} mbar regime, which was one of the objectives of the machine. All the pumps used here are usually working 24/7. In order to reach the lowest possible pressure in the main chamber, bake-out at ≈ 120°C for at least one day is necessary. For the purpose of noise reduction in the lab, the primary pump and the later installed fore turbo pump are located next door.

7.2.2. Operating Instructions

Start-up Procedure Before starting the fore-vacuum system, check that the gate-valve to the differential pumping stage is closed and that the fore-vacuum valve is opened! This is very important because opening the fore-vacuum valve when the fore-turbo pump is at full speed might damage the pump! The two fore-vacuum pumps (multi-Roots + turbo) are connected to the same control line and can be started via the control panel "PREVAC 3" (start with "manual" and switch to "auto" as soon as the pressure falls below the threshold).
The 3 turbo pumps directly mounted to the chamber are linked to the same control line and can be switched on via the control panel "MAIN" (start with "manual"). Check that all 3 pumps are starting up regularly! It might be the case that the pumps were turned off manually (at the respective controllers) because one of the controllers is needed to switch the venting valve of the chamber and during the venting process the other controllers must be switched off. Usually the 3 turbo pumps are water-cooled in series with

the pickup turbo pumps, but air-cooling is also possible ("no water check " - switch on the control panel). If the air-cooling mode is chosen and the water-cooling is turned off, the pumps will eventually become hot if no cooling fans are installed. When going through a bake-out procedure, water-cooling is absolutely necessary!
Since no copper sealed Pirani-manometer was available, only 2 hot cathode manometers are used to monitor the pressure in the TOF- and MAIN-chamber. These manometers may only be turned on below a certain pressure in the chamber. To be safe, wait until all 3 turbo pumps have reached their full speed before turning on the pressure gauges. Very shortly after that, the pressure threshold should be reached and the "MAIN" switch must be set to "auto". Note that the manual mode only works for 10 min, afterwards, the power is switched off (like in the "off" state).

Shut-down Procedure Before shutting down the vacuum system, make sure that the gate-valve to the differential pumping stage is closed and close the valve in the fore vacuum line. Turn off the primary pump and the fore-turbo ("PREVAC 3"-panel), turn off the 3 turbo pumps ("MAIN"-panel) and turn off the pressure gauges! For venting the chamber with dry nitrogen, open the valve at the gas bottle and the valves along the gas line. Check if the electromagnetic valve on the turbo pump "MAIN 1" is connected. Turn off the turbo controllers "TOF" and "MAIN 2". Set the switch on "MAIN" control-panel to manual. Turn off the motor and the pumping station at the turbo-controller "MAIN 1" (options 023 and 010 in the menu), enable the venting valve (option 012) and set venting mode to 2 (option 030). Do not enable the valve as long as the turbo pumps are above 50% of their nominal speed (to go easy on the bearings).
The main chamber is not equipped with an over-pressure valve. The installed safety feature is a burst disk (breaks at 0.6-0.8 bar overpressure), which only works once and is expensive (keep the overpressure below 0.4 bar!). Therefore, listen carefully to a clicking noise stemming from the burst disk while venting. As soon as you hear the noise, the nitrogen valve must be closed and the valve options (012 and 030) must be set back to their original values.

7.3. Time-of-Flight Mass Spectrometer (TOFMS)

The apparatus is equipped with a Stefan Kaesdorf RFT50 time-of-flight mass spectrometer with electron impact ionization and 20 kV post-acceleration, which is especially suited for the measurement of large masses ($m > 10^4$ amu). The ionization region of the spectrometer is located on the beam axis and the ions are extracted perpendicular to the beam, allowing mass spectrometric measurements simultaneously to other experiments

further downstream. The setup is designed such that the initial ionization can be conducted *via* electron impact (built-in electron beam) or *via* laser ionization (external). Data acquisition and the control of the device are executed by the computer underneath the high voltage control units (TOF-PC). In order to avoid software problems, the TOF-PC should not be connected to the internet and no other programs should be installed. The TOF-PC can be operated from the regular laboratory computer using a remote-desktop connection.
For the start-up and shut-down procedure, the checklist in appendix D should be used. Voltage settings for different extraction conditions can be found in the manual of the spectrometer. Typical settings can be found in Section 8.2.
When changing the voltage settings or the region of interest, the grid potentials as well as the deflection potentials have to be fine-tuned in order to maximize the signal in the region of interest. Especially when going form small to large masses, the deflection potentials have to be adjusted.
If there is no signal, its most likely due to a software-bug: when switching between the software modes, the ionization current is switched off (check electrometer current). To switch the current back on, change any of the puls-generator settings (*e.g.* pulse duration). Another reason for a very low ionization current could be a flat battery (9 V battery in wire #1). When replacing the battery, be sure to connect the battery in the right way!
In order for the discriminator to work correctly, the offset at the preamplifier has to be small. As there is a natural drift, the offset at the preamplifier should be checked and corrected monthly. To do so, turn down the MCP-voltage and disconnect the output of the preamplifier (green cable). Connect a voltmeter to the output of the preamplifier and set the offset to zero, using the potentiometer inside the preamplifier box.
After a long time of operation or if the heating current was set to high, the filament emitting the electron beam might break. Suitable filaments are on stock in the laboratory and can be replaced by the user. When replacing tungsten filaments, always wear goggles as the filaments are brittle and chips are hard to remove, even for an eye-doctor.

7.4. Quadrupole Mass Spectrometer (QMS)

The QMS installed on the apparatus is a Balzers (Pfeiffer) Prisma QME 200. The hardware of the QMS consists of two parts, the analyzer (mounted on the chamber) and the control unit (containing the electronics). These two parts are connected via a plug, whose pins are delicate to handle. Ideally, the connection should not be separated. The QMS can be operated with the software QUADSTAR 7.0.3, which is an old software, but works under Windows 7. This mass spectrometer can analyze masses between 0

and 200 amu and is therefore mainly suited to analyze the residual gas as well as the amount of He in the beam. The software can display the whole mass spectrum or the time-dependent intensity of one or more constituents. Suitable templates for both purposes are predefined and can be loaded by the program. In the current setup the main use is to record the decrease of He in the beam due to doping.
In order to work stable, the SEM (secondary electron multiplier) and the filament should be running about half an hour. Note that blocking the beam with the microbalance or the TEM-sample-holder significantly changes the partial pressure measured by the QMS. Comparable measurements can only be recorded if these two elements are in the same position and if the SEM voltage is set at the same value. Before venting the chamber, the QMS has to be switched off!

7.5. Microbalance

The measurement principle of the quartz crystal microbalance is based on the measurement of the resonance frequency of the shear-oscillations of a piezo-quartz. As mass is deposited on the quartz crystal, the resonance frequency f of the oscillation system changes by Δf and allows a very precise measurement of the deposited mass m using the Sauerbrey-equation:

$$\Delta f \approx -\frac{2f^2}{Z}m \tag{7.1}$$

with Z being a constant, depending on the density and shear modulus of the quartz.
In operation, it is striking that the measured frequency does not only depend on the deposited mass, but also on the temperature of the crystal and the electronics. In fact, the resonance frequency is very sensitive to temperature changes and for the most accurate measurements (accuracy: few $10^{-6}\frac{\mu g}{cm^2 s}$) a temperature stabilization to $\pm 0.02°C$ is necessary. This was achieved by heating the microbalance to 50°C and compensating the heat flux to the colder chamber wall by regulating the heating. Furthermore, the electronics of the microbalance and the temperature stabilization have to be in a temperature-controlled environment as well. Without these measures, the most prominent signal would stem from the room temperature oscillations due to the cooling cycles of the air conditioning. In order to reach a constant temperature, the stabilization needs to work for a couple of hours. Especially after a bake-out cycle, several hours are required until the system is ready for measurements.

The software to operate the microbalance is not compatible with Windows 7 or higher and therefore runs on a virtual machine. The built-in live visualization of the deposition rate does not work very well, especially with the very low deposition rates present in typical experiments on this machine. To overcome this limitation, a MATLAB-code

copies the live-stored measurement data and computes and displays the deposited mass as well as the deposition rate.
When conducting measurements, care has to be taken that the microbalance is correctly positioned (xyz-manipulator). The correct position can be checked by using the telescope on the beam axis: the borehole in the center of the back side of the microbalance should lie on the cross hairs. For the alignment procedure of the rest of the apparatus, the microbalance has to be moved out of the beam line (see Section 8.1).

Metal nanoparticles deposited on the crystal do not desorb, limiting the life-time of a crystal. If the software indicates that the life-time of the crystal comes to its end or a clean surface is desired, the crystal can be changed (see manual of the microbalance).

7.6. Vacuum Transfer System

When dealing with reactive samples and in order to guarantee clean surfaces, exposure to ambient air must be avoided. Ideally, the samples which are produced under UHV-conditions in our machine, should be kept in UHV during the transport from our laboratory to the diagnostics (*e.g.* scanning probe microscope on the KFU). For this task, a commercially available system was purchased from Ferrovac, consisting of a chamber fitted with the pumping system, a wobble-stick with pincers, a storage shelf for samples and a suitable gate valve at the connecting flange.
For the transport, a pumping system with low energy consumption is required in order to be able to run the system on battery power. Furthermore, a system without moveable parts (in case of mechanical shocks) is beneficial. Both of these key points are satisfied using a non-evaporable getter (NEG) in combination with an ion getter pump. Thereby, the NEG, which simply adsorbs gas-atoms and -molecules, does not need electrical power. The fact that the NEG is only suitable for certain gas species (especially H_2O, N_2, O_2 and H_2) and cannot adsorb other species (*e.g.* rare gases, CH_4) makes the battery powered ion getter pump necessary. In principle, an ion getter pump alone could also do the trick, but in combination with the NEG, the size and energy consumption of the ion getter pump can be drastically reduced which is essential for this purpose. In the purchased configuration, the pumping system can operate for 3 days using only battery power.
In order to reduce the gas load for the pumping system the linear movements of wobble-stick and sample storage shelf are realized without feedthroughs, using magnetic coupling between a ring on the outside and a piston on the inside which guarantees leak-tight sealing. Additionally, an evacuated buffer volume is connected to the the atmosphere-side of the gate valve during transport, which reduces the permeation through the rubber-

sealed gate valve to a minimum.
For the transfer of samples from the respective apparatus into the UHV-suitcase, a third chamber (lock chamber (LC)) is needed. While the apparatus and the suitcase are maintained under UHV all the time, the LC is installed between them and will be pumped down or vented in order to connect or disconnect the suitcase to or from the apparatus. For the pumping of the LC a HiPace80 turbo-pump backed by an ACP15 multi-Roots fore pump is used. This system reaches a background pressure in the 10^{-10} mbar regime, which is sufficient for all purposes this system is designed for.
A summary of the operating instructions, including all the information needed for regular operation of the device, is attached in appendix F. For extra information consult the manual of the suitcase or the manual of the pumping system.

8. Settings and Typical Readings

8.1. Beam Alignment

A proper alignment of all components of the apparatus along the beam axis is crucial for the success of any experiment. Thereby, the position of the beam is given by the position of the first skimmer, which defines the placement of all other components. For the first alignment of all chambers, a piece of string was connected to the center of the flange-plate on which the skimmer is mounted (reference flange). Using a water level and an engineer's square the string was oriented horizontally, orthogonally to the reference flange. With the string as guidance, the two following vacuum chambers as well as a telescope for optical control of the beam path were installed. Once the telescope was set up, the cross hairs of the telescope could be used to control the position of all further components.
The telescope is shared with other labs and therefore has to be repositioned every now and then. Assuming that the positions of both skimmers in the apparatus do not change, the position of the telescope can be restored by adjusting its tilt as well as its position orthogonal to the beam such, that the cross hairs can be pointed at the center of both skimmers when only changing the focal plane. If this is the case, then the optical axis of the telescope coincides with the beam axis defined by the skimmers.
If the telescope is correctly aligned, the flange-plate with the first skimmer mounted on it can be removed in order to see and position the nozzle. Thereby, the nozzle plate has to be parallel to the skimmer-flange and the nozzle axis has to be horizontal. Once the nozzle is positioned, the flange-plate with skimmer can be mounted again, using the cross-hairs to find the correct position.
While the parts described so far do not move under normal circumstances, the pickup cells along the beam are changed regularly to switch dopants, to refill them or for maintenance. Therefore, these elements have to be aligned much more often. To do so, at first the position of the telescope is controlled by focusing on both skimmers. Then, reinstall the pickup cell, including the electrical wiring and the cooling water pipes (connecting these afterwards may displace the cell again). Using the adjusting screws, the beam-entry and -exit opening of the pickup cell can positioned on the beam axis.
Without additional lighting the apertures for the beam are hard to recognize and distinguish when looking through the telescope. The method of choice is to illuminate the

respective apertures with different colored LEDs while adjusting. This way the contour lines of the orifices should be clearly visible and the color indicates to which orifice the focal plane is set.

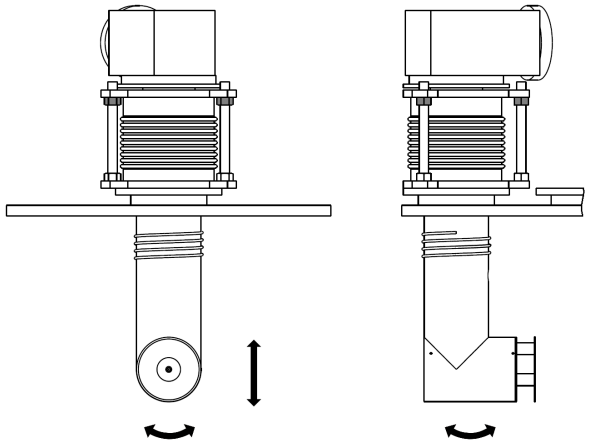

Figure A.20.: Schematics illustrating the adjustment of the nozzle. The left image shows the adjustment of the nozzle position. The tilt shown in the right image must be zero, *i.e.* the beam axis must be horizontal.

8.2. Typical Settings of the Time of Flight Mass Spectrometer

The following tables contain optimized settings for the TOFMS, determined by Johannes Steurer within the course of his master's thesis.[a]

Table A.1.: TOFMS settings used in this thesis to obtain mass spectra of doped or bare He droplets up to a mass < 7000 u. The given values, especially the ones for the deflection unit, correspond to the ones set directly at the TOFMS power supply, not the ones read in by the analog-to-digital converter (ADC).

Ion source	
Filament current	2.1 - 2.2 A
electron energy	89 eV
resulting electrometer current	in the range of 1 μA
Voltage settings	
HV settings	#3 (see TOF-manual) $\rightarrow$ last- and central grid alternately adjusted for best resolution
repeller offset	0
mass filter	off
deflect-x	5.5
deflect-y	5.5
MCP	2.3 - 2.5 kV depending on the mass of interest
Post acceleration	20 kV
Pulse generator	
repetition frequency	10 kHz
duration e-beam	1 μs
delay ion extraction / ionisation	0 μs
duration ion extraction	2.4 μs
duration mass filter	no influence if the mass filter is off
Fast Multiscaler	
number of sweeps	$2 \cdot 10^4$ - several millions
range	$2.8 \cdot 10^5$ (for a bin width of 1)
bin width	1 - 2
Start/Stop Disc.	0.3/-0.15

Table A.2.: TOFMS settings used in this thesis to obtain mass spectra of doped or bare He droplets for big masses up to about 25000 u. The given values, especially the ones for the deflection unit, correspond to the ones set directly at the TOFMS power supply, not the ones read in by the ADC.

Ion source	
Filament current	2.3 - 2.4 A
electron energy	89 eV
resulting electrometer current	15 - 20 μA
Voltage settings	
HV settings	#1 (see TOF-manual) $\rightarrow$ last- and central grid alternately adjusted for best resolution ($U_{\text{centralgrid}} = 2.25\,\text{kV}$, $U_{\text{lastgrid}} = 1.08\,\text{kV}$)
repeller offset	5.2
mass filter	250 V
deflect-x	5.75
deflect-y	5.6
MCP	2.7 kV
Post acceleration	20 kV
1^{st} aperture	2.7
Pulse generator	
repetition frequency	4 kHz
duration e-beam	20 μs
delay ion extraction / ionisation	0 μs
duration ion extraction	6 μs
delay mass filter / ion extraction	1 μs
duration mass filter	3 μs
Fast Multiscaler	
number of sweeps	$5 \cdot 10^5$ - 10^7
range	$2 \cdot 10^5$
bin width	4
Start/Stop Disc.	0.3/-0.15

[a]Steurer, J. *Helium Droplet Mediated Fabrication and Analysis of Noble Metal Nanoparticles.* Master's thesis, Graz University of Technology (2014).

8.3. Settings / Operating Instructions for the QMS

The quadrupole mass spectrometer installed on this machine is a Balzers Prisma QME 200, controlled by the Quadstar 7.0.3-Software. This software is old and only the "Measure" program, which operates the QMS and displays the signals, works under Windows 7 without problems. Usually, this device is used to gain qualitative data (*i.e.* if there is a signal at a specific mass or not), quantitative statement can be made in terms of ratios (*e.g.* helium signal with and without doping). The comparison of different QMS-measurements is difficult due to their dependance on the vacuum conditions and the position of beam blocking elements such as the microbalance and the TEM-substrate holder.

The QMS can be switched on by the I/O - switch on the power supply cable. After that, the software ("QMS Measure"-icon on the desktop) can connect with the detector. Setup → SEM / Emission Control opens a window with two check-boxes which switch on the emission current and the secondary electron multiplier (SEM). The SEM voltage is normally set to **2000 V**. Usually, a drift of the signal intensity occurs during the first half hour of operation, afterwards, the signals are stable. There are two typical modes for measurements: "Analog" and "Versus Time". The former shows a mass spectrum and the latter the evolution of the signal of a specific mass with time. For both modes there are templates available (Scan → Analog → test.sap and MID → Versus Time → he4.mip). After loading one of these templates, the settings can be changed by Parameters → Setup and more importantly Parameters → Channel. In both cases, the changes made in the new windows are saved to the template (!) and activated after closing the windows.

Before switching off the device (I/O - switch on the power supply cable) the SEM voltage and emission current should be turned off by the software (Setup → SEM / Emission Control).

Extensive information on Quadstar can be found in the printed manual (white folder) as well as in the help file "Quadstar 32-bit.chm".

Appendices

A. Engineering Drawings

The following pages contain engineering drawings of the most important home-made parts needed for the buildup of the apparatus, which are:

The new nozzle,

the resistive pickup cells,

and the modifications on the measurement chamber in order to enable laser ionization for the TOFMS.

Besides the drawings here, 3D-CAD constructions for the whole apparatus are available on the laboratory computer. These CAD-constructions were conducted using Pro-Engineer Wildfire, for which the university has a license.

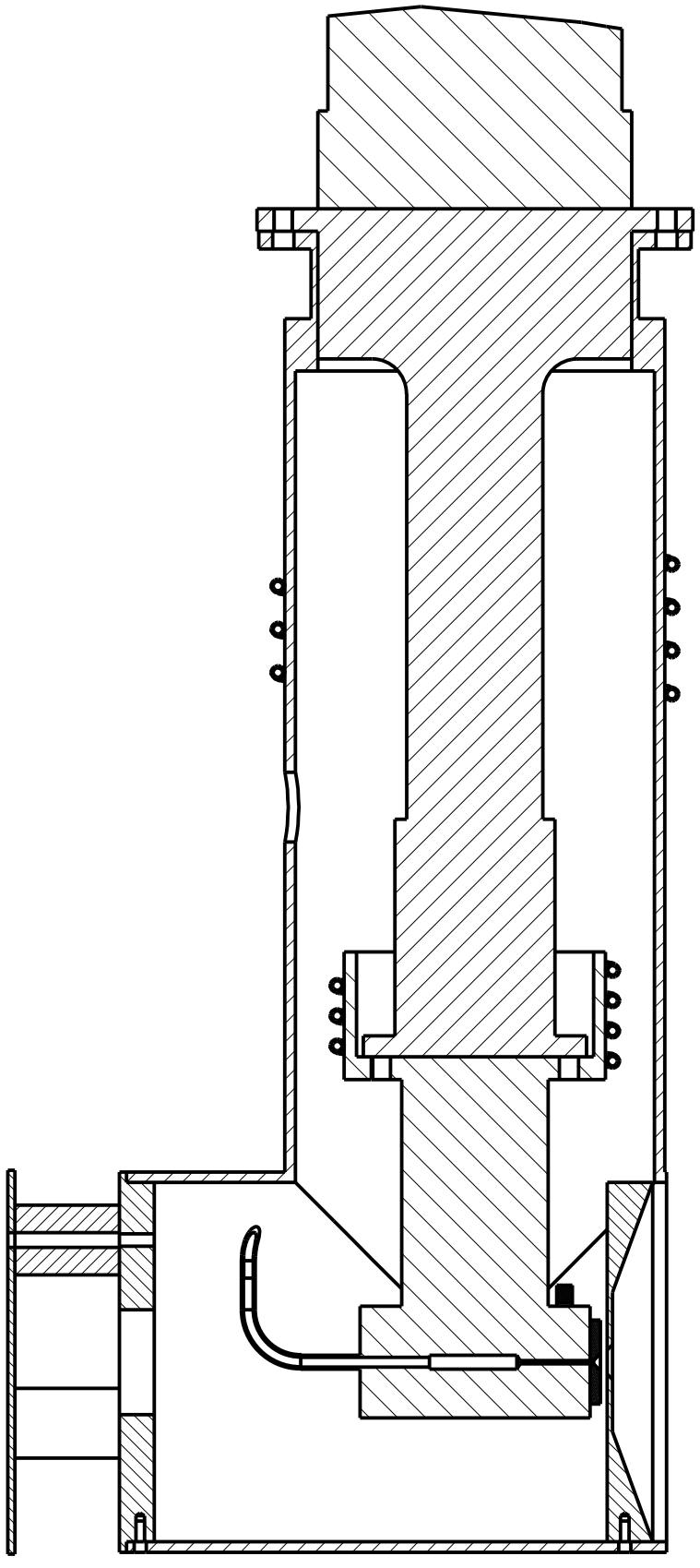

Bemerkung :		Name	Datum	Werkstoff:
	Gez.	Thaler	28-Aug-15	Rohmass:
	Gepr.	–	–	Gewicht: Kg

Zust.	Aenderung	Datum	Name

TUG

Benennung

Nozzle Setup

Dateiname : ASSEMBLY.QUELLKAMMER

Masstab: 1:2

Blatt: 1 von 2

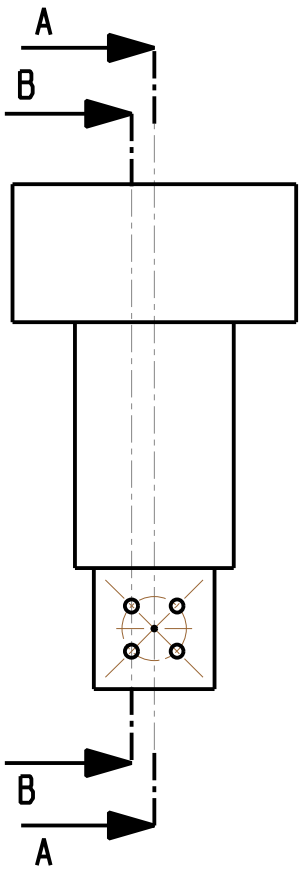

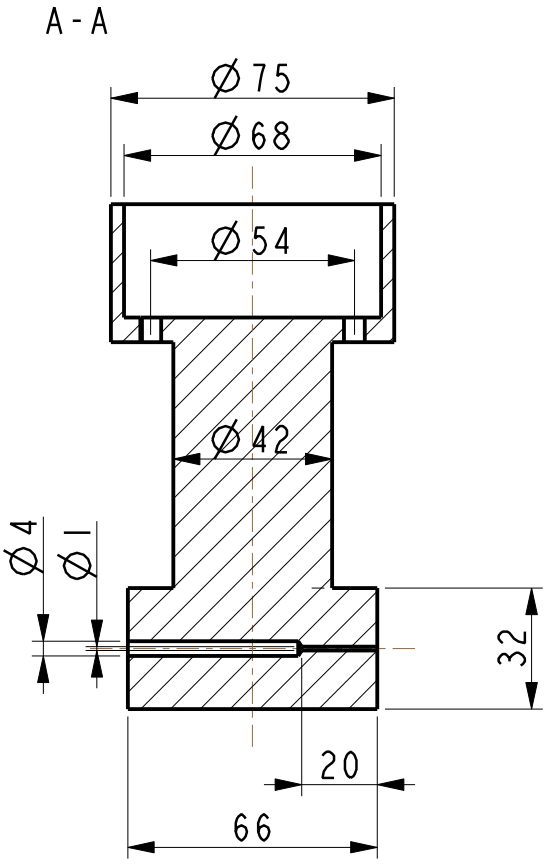

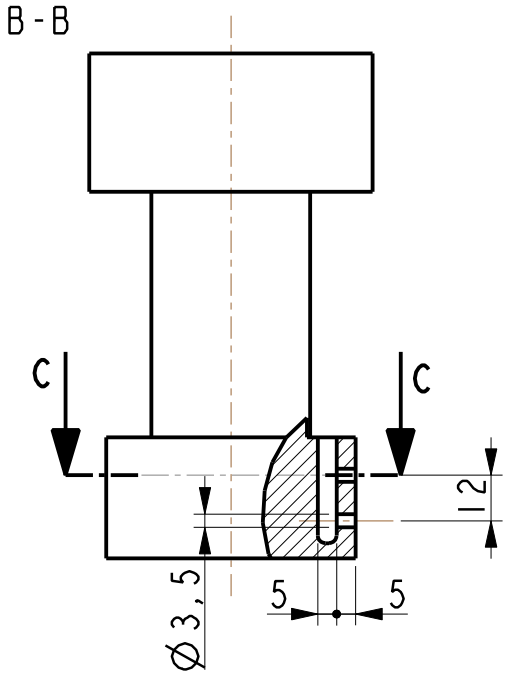

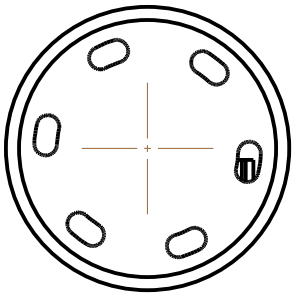

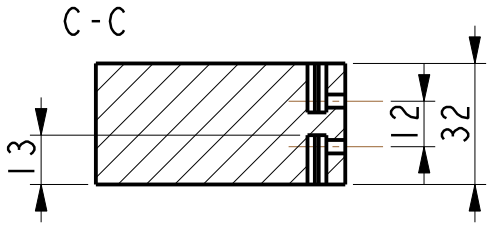

Bemerkung :		Name	Datum	Werkstoff:	Kupfer
	Gez.	Thaler	26-Feb-14	Rohmass:	Durchm. 80mm
	Gepr.	–	–	Gewicht:	Kg

Zust.	Aenderung	Datum	Name

TUG

Benennung

Duese

Dateiname : CONNECTION.FUER.ZEICHNUNG

Masstab: 1:2

Blatt: 1 von 1

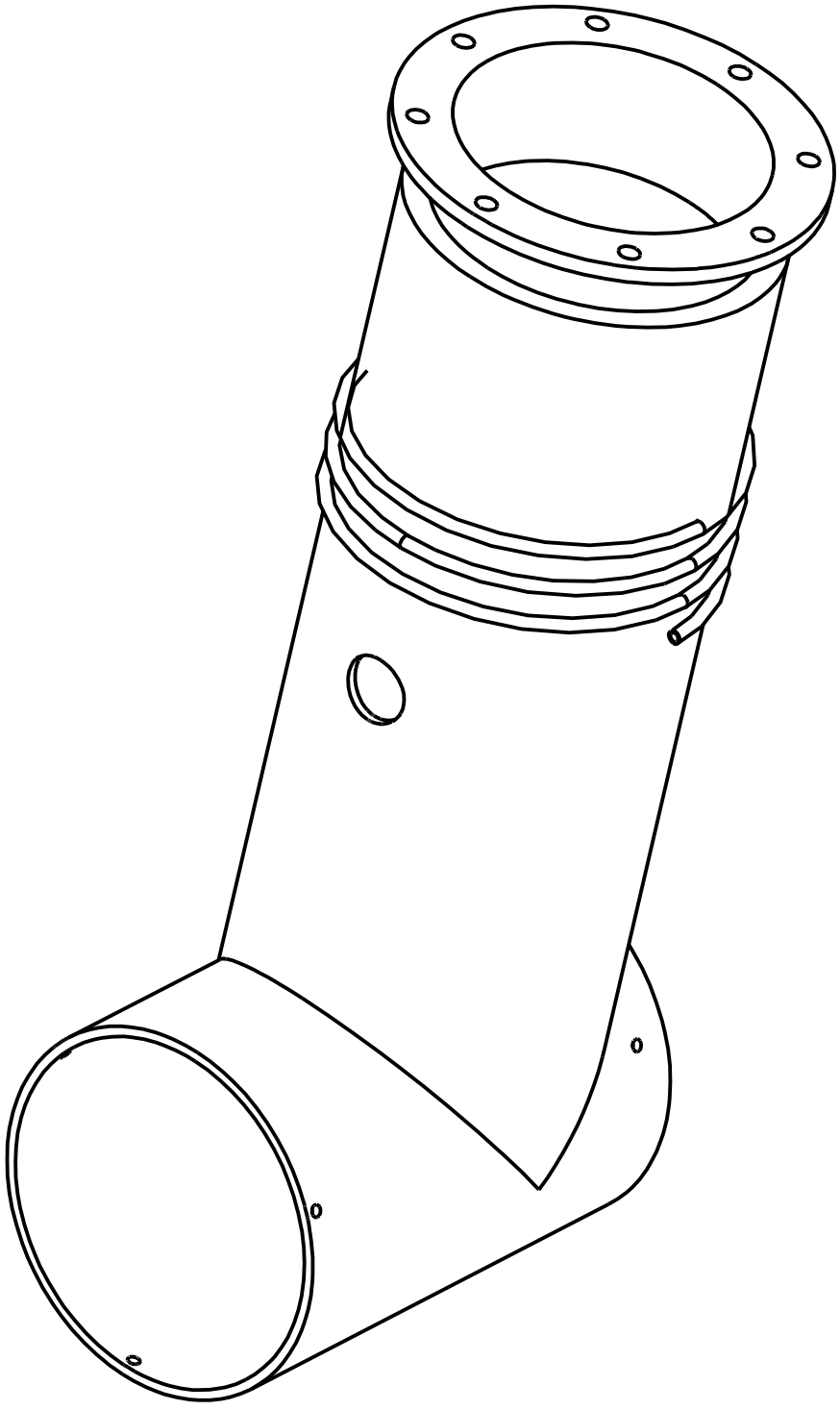

Bemerkung :		Name	Datum	Werkstoff: Kupfer
	Gez.	Thaler	27-Feb-14	Rohmass:
	Gepr.	–	–	Gewicht: Kg

Zust.	Aenderung	Datum	Name

TUG

Benennung

T-Shield

Dateiname : T_SHIELD

Masstab: 1:2

Blatt: 1 von 1

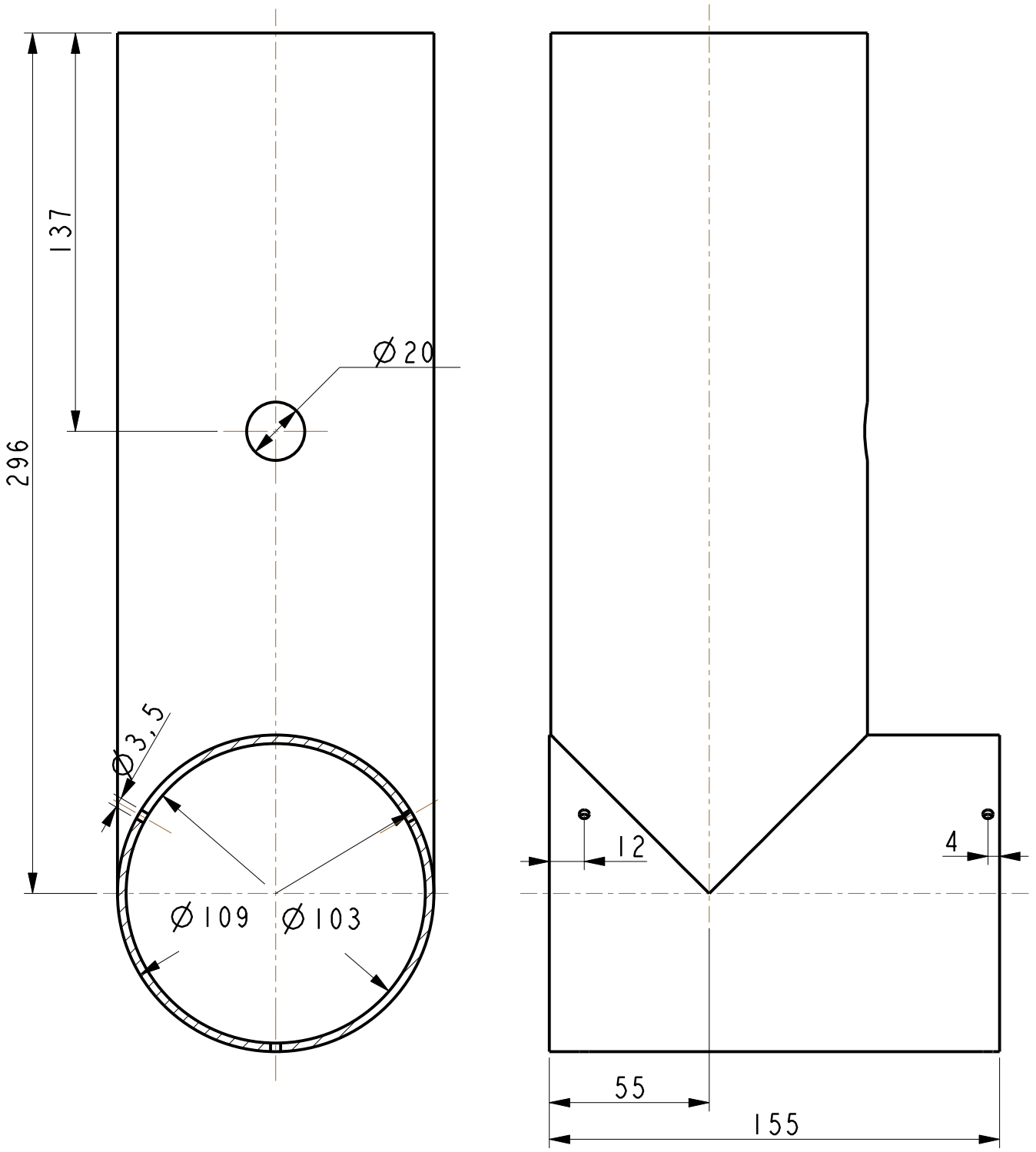

Bemerkung :		Name	Datum	Werkstoff:	Kupfer
	Gez.	Thaler	26-Feb-14	Rohmass:	Rohr, D_innen = 103mm
	Gepr.	–	–	Gewicht:	Kg

Zust.	Aenderung	Datum	Name

TUG

Benennung

Shield-Tubes

Dateiname : SHIELD_TUBES

Masstab 0,200

Blatt: 1 von 1

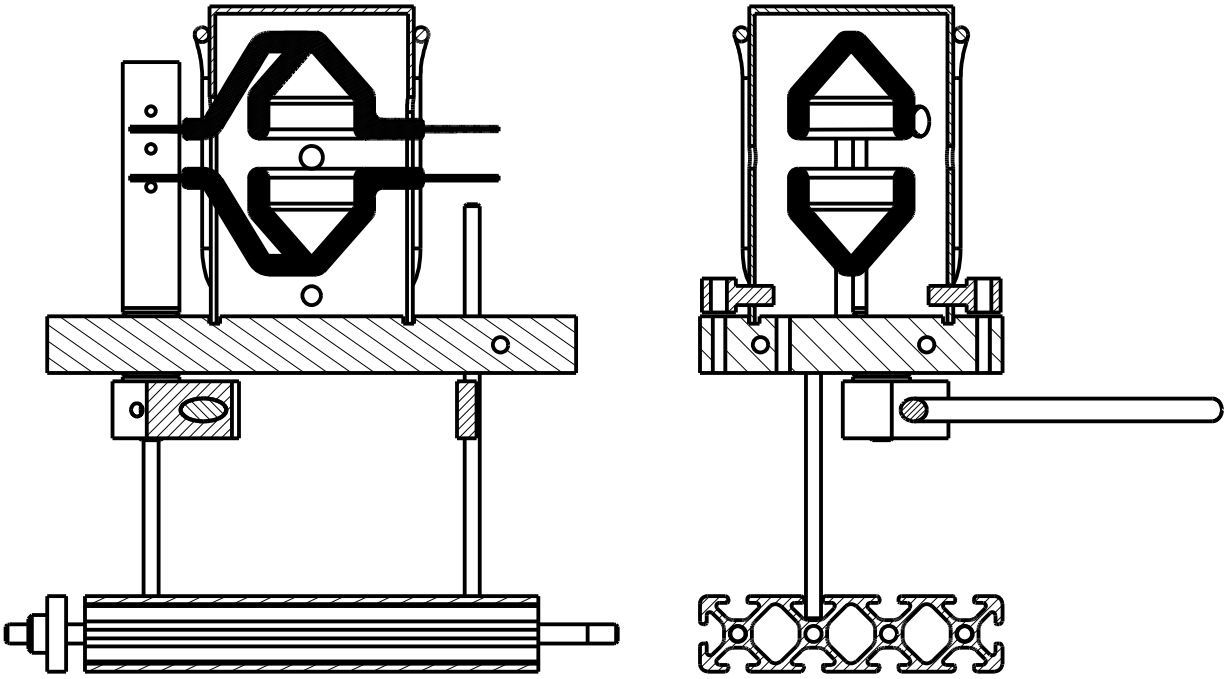

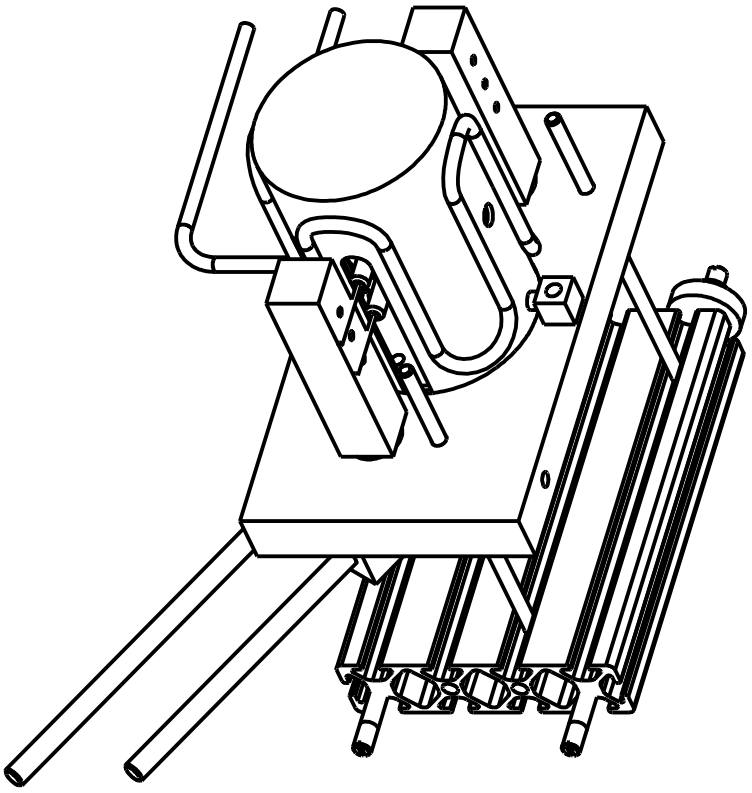

Bemerkung :		Name	Datum	Werkstoff:
	Gez.	Thaler	28-Aug-15	Rohmass:
	Gepr.	–	–	Gewicht: Kg

Zust.	Aenderung	Datum	Name

TUG

Benennung

resistive Quelle

Dateiname : RESISTIVE_QUELLE_PUC5

Masstab: 1:2

Blatt: 1 von 1

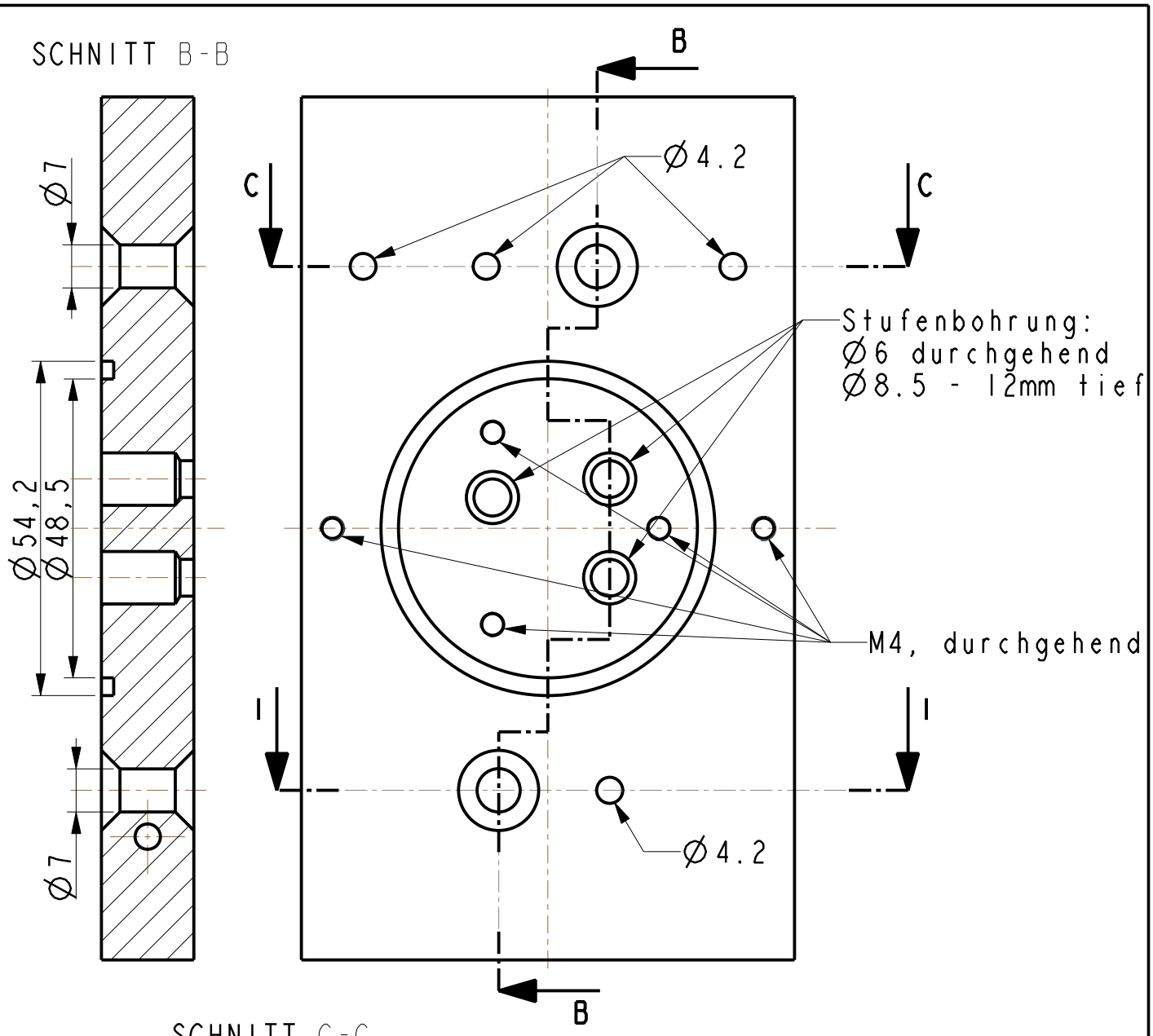

Bemerkung :		Name	Datum	Werkstoff:	Kupfer
	Gez.	Thaler	29-Jun-12	Rohmass:	
	Gepr.	–	–	Gewicht:	Kg

Zust.	Aenderung	Datum	Name

TUG

Benennung

Baseplate

Dateiname : HQ_BASEPLATE

Masstab: 1 : 1

Blatt: 1 von 1

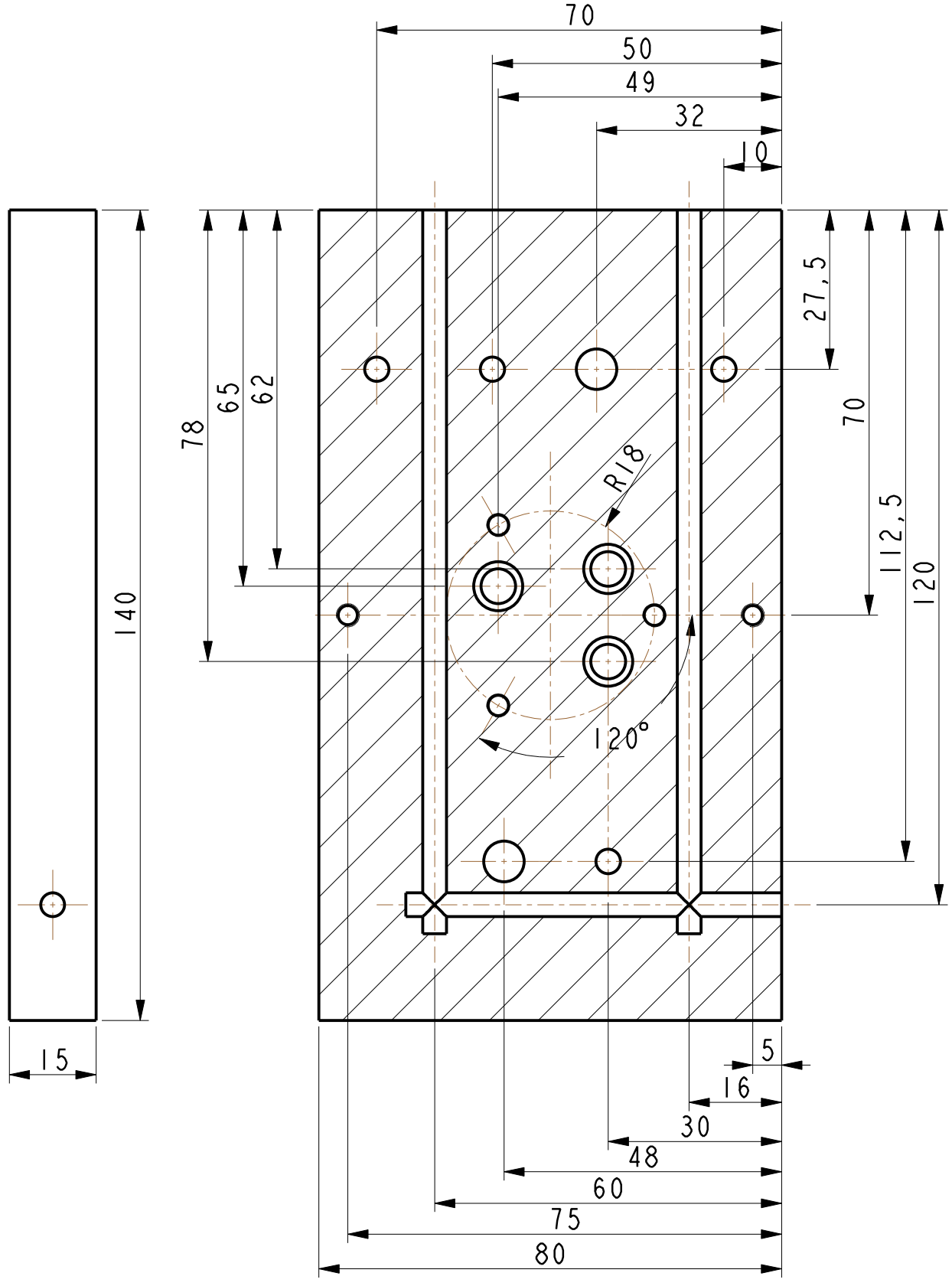

Bemerkung :			Name	Datum	Werkstoff: **Kupfer**
		Gez.	Thaler	29-Jun-12	Rohmass:
		Gepr.	–	–	Gewicht: Kg
Zust.	Aenderung	Datum	Name	**TUG**	Benennung **Grundplatte Verdampferquellen**
				Dateiname : **HQ_BASEPLATE**	Masstab: **1 : 1** Blatt: **1** von **1**

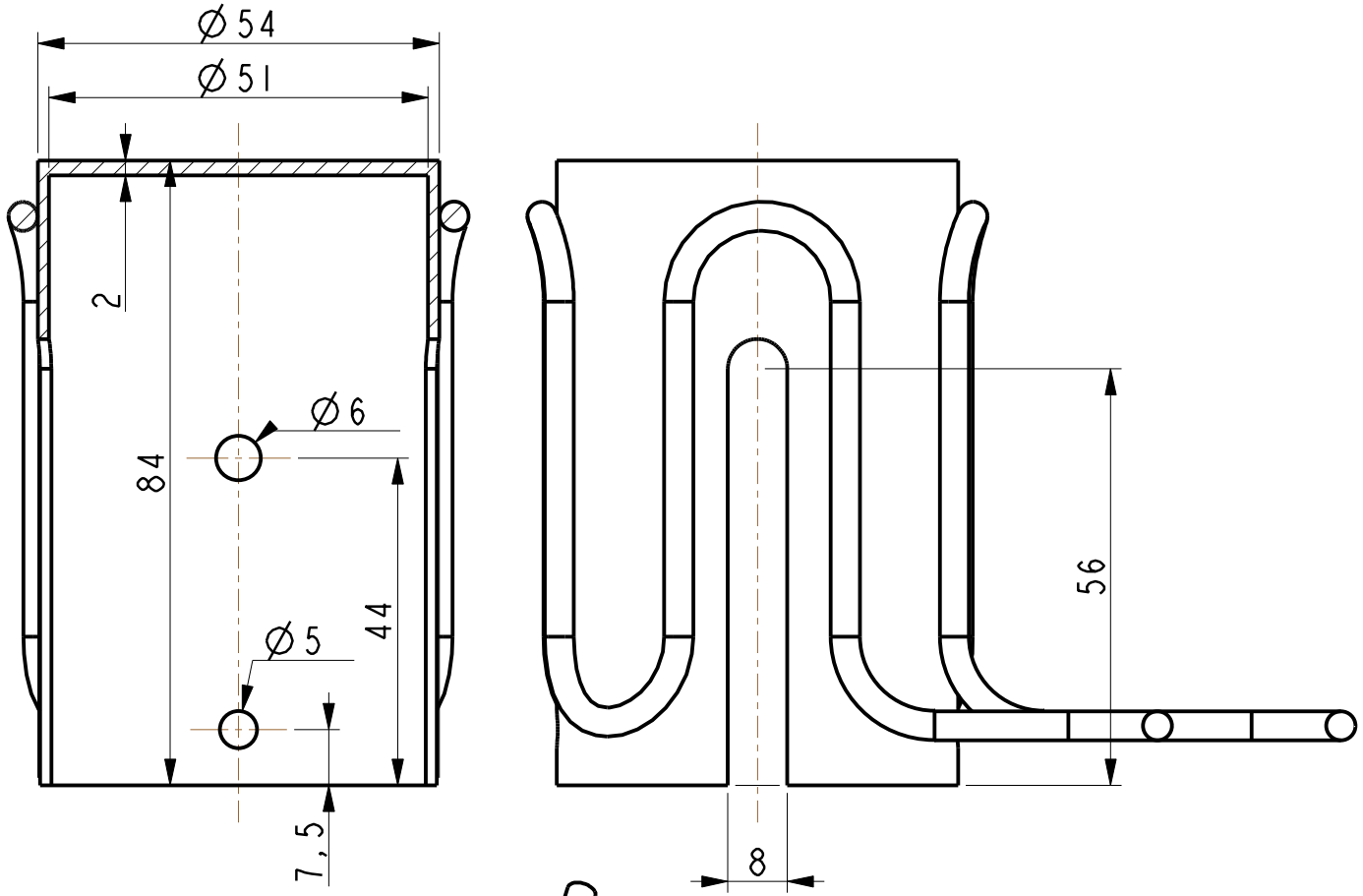

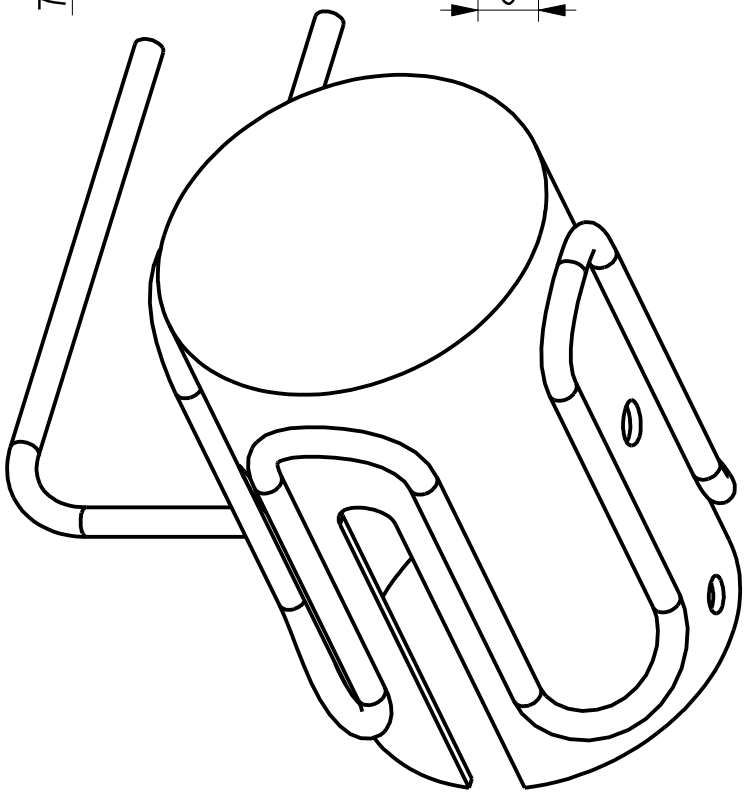

Bemerkung :			Name	Datum	Werkstoff: **Kupfer**
		Gez.	Thaler	28-Aug-15	Rohmass:
		Gepr.	–	–	Gewicht: Kg
Zust.	Aenderung	Datum	Name	**TUG**	Benennung: **Kühlschild hoch**
					Dateiname : RESISTIVE.SOURCE.SHIELD.PUC5
					Masstab: 1:1
					Blatt: 1 von 1

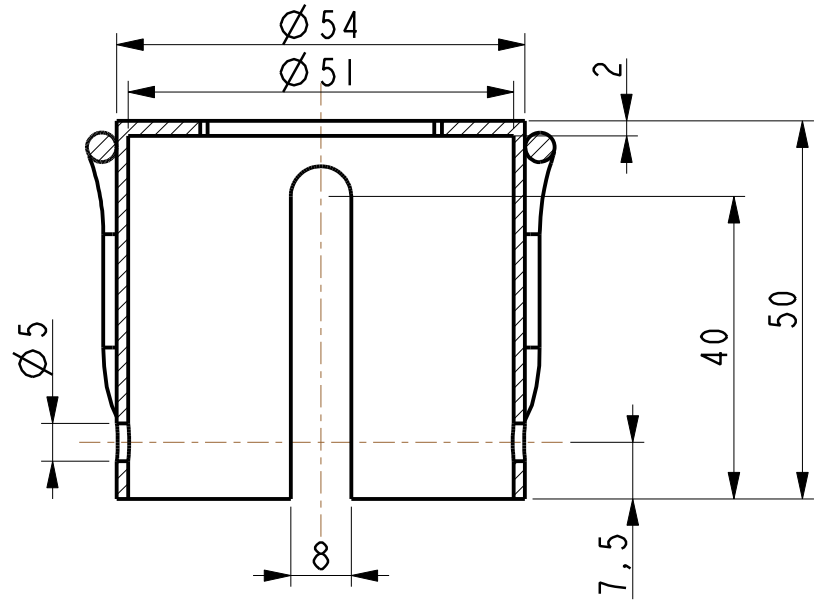

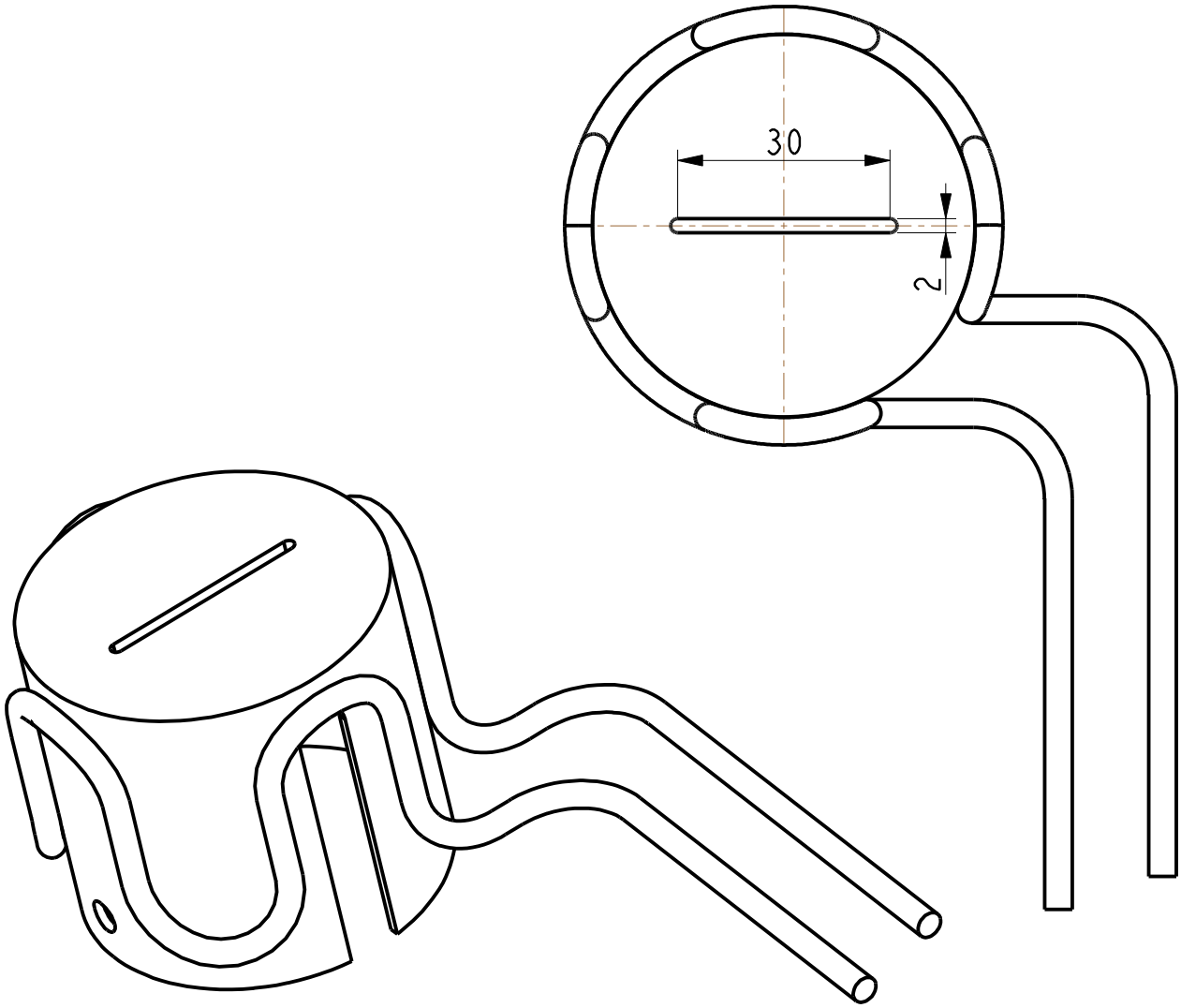

Bemerkung :			Name	Datum	Werkstoff: Kupfer
		Gez.	Thaler	29-Jun-12	Rohmass:
		Gepr.	–	–	Gewicht: Kg
					Benennung
					Kühlschild
Zust.	Aenderung	Datum	Name	TUG	Dateiname : HQ_SHIELD_2
					Masstab: 1 : 1
					Blatt: 1 von 1

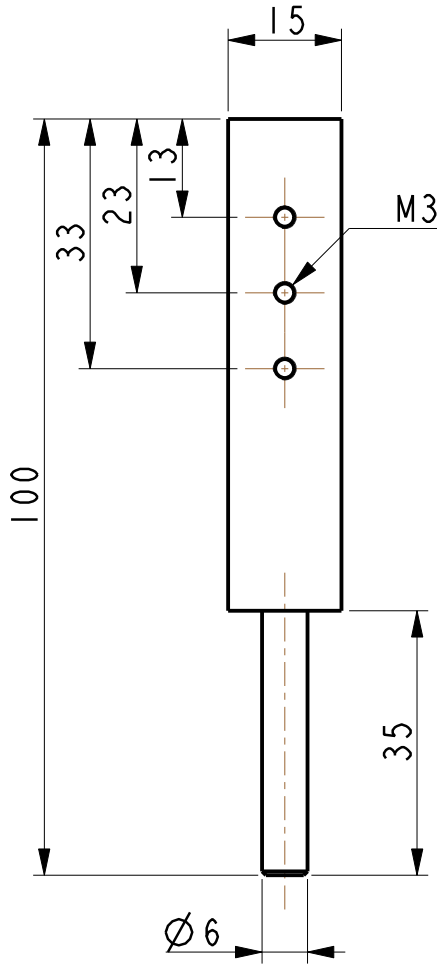

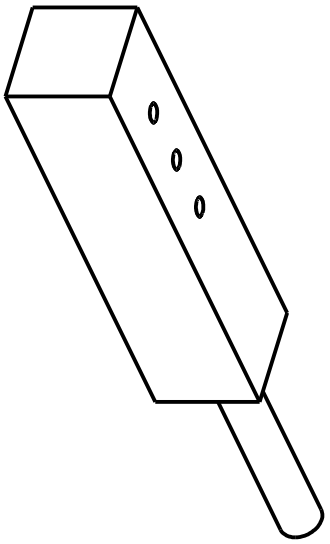

Bemerkung :			Name	Datum	Werkstoff: Kupfer
		Gez.	Thaler	29-Jun-12	Rohmass:
		Gepr.	–	–	Gewicht: Kg
					Benennung
					Säule RS
Zust.	Aenderung	Datum	Name		Dateiname : SAEULE
					Masstab: 1 : 1
					Blatt: 1 von 1

TUG

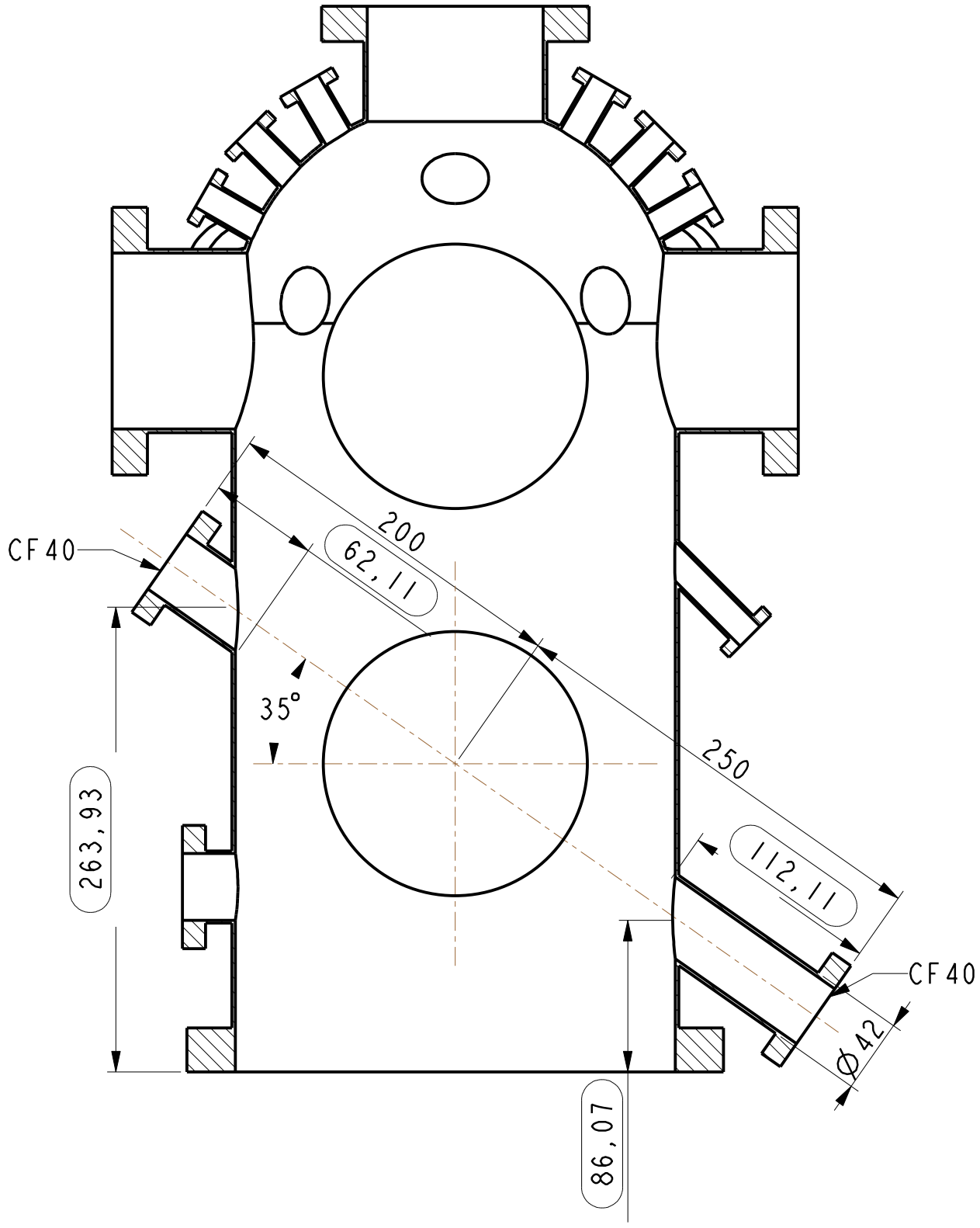

Bemerkung :			Name	Datum	Werkstoff:
		Gez.	Thaler	08-Jan-13	Rohmass:
		Gepr.	–	–	Gewicht: Kg
					Benennung
					Umbau: Messkammer
Zust.	Aenderung	Datum	Name		Dateiname : MESSKAMMER_UMBAU
					Masstab: 1 : 3
					Blatt: 1 von 1

TUG

B. Helium Flux and Droplet Size

For the production of clusters/nanoparticles with a desired size distribution, it is essential to set the adequate droplet size distribution. This is accomplished by setting the expansion conditions accordingly, following the table below (Reprinted with permission from [a]. Copyright 2011, AIP Publishing LLC.):

TABLE I. Nozzle temperature, T_0; attenuation coefficients α_4 and α_8 (in parenthesis) obtained with helium titration; droplet beam velocity, v_D; and average number of He atoms in the droplets, $\langle N_{He} \rangle$, according to Eq. (2). Table I also contains intensity ratios of peak $m = 16$ to $m = 8$ and $m = 12$. Values of $\langle N_{He} \rangle$ obtained previously, using deflection techniques of Refs. 17, 28–30, are shown in the penultimate column. Italicized values of $\langle N_{He} \rangle$ in the last column are beyond the range of the applied technique as described in the text. All measurements are at nozzle stagnation pressure of $P_0 = 20$ bars.

T_0 (K)	α_4/L, (α_8/L), (Pa^{-1} m^{-1})	v_D (m/s)	I_{16}/I_8	I_{16}/I_{12}	$\langle N_{He} \rangle$, previous works	$\langle N_{He} \rangle$, helium titration
5.4	5.98	173[a]	0.512	4.17		1.68×10^{10}
5.7	13.54 (7.99)	173[a]	0.529	3.9		1.43×10^{9}
6	22.39	175[a]	0.531	4.03		3.08×10^{8}
6.5	35.20 (25.11)	194[a]	0.499	3.2	3.5×10^{7} [c]	5.90×10^{7}
7	63.24 (54.5)	200[a]	0.422	3	2.2×10^{7} [c]	9.64×10^{6}
8	74.24 (57.50)	207[a]	0.401	2.6	5.6×10^{6} [d] 9.0×10^{6} [c]	5.31×10^{6}
9	101.76 (85.92)	223[a]	0.28	1.99	1.2×10^{6} [d] 1.8×10^{6} [c]	1.82×10^{6}
9.5	166.10	236[a]	0.226	1.74	150 000 [d] 1.4×10^{5} [c]	3.25×10^{5}
10	293.60 (234.02)	239[b]	0.094	0.85	4.5×10^{4} [d]	*6.39×10^{4}*
10.5	476.58	258[b]	0.036	0.352		*1.4×10^{4}*
11	539.73	276[b]	0.033	0.339	15 000 [b]	*8.1×10^{3}*
12	762.78 (786.53)	300[b]	0.03	0.324	12 000 [b]	*2.4×10^{3}*
13	674.46 (737.46)	323[b]	0.028	0.323	8000 [b]	*2.8×10^{3}*
14	773.78 (1005.91)	340[b]	0.027	0.294	5500 [b]	
15	774.53	357[b]	0.025	0.306	3100 [b]	
16	895.94 (1658.67)	373[b]	0.018	0.271	2100 [b]	
17	597.38	389[b]	0.016	0.257	1300 [b]	
19	409.16	419[b]	0.018	0.264		
23	298.06	466[b]				

[a]Measured in this work.
[b]From Ref. 28.
[c]From Refs. 17 and 30.
[d]From Ref. 29.

[a]Gomez, L.F., Loginov, E., Sliter, R. & Vilesov A.F. Sizes of large He droplets *J. Chem. Phys* **135**, 154201 (2011)

Besides the droplet size also the total He-flux changes with the nozzle temperature, which can be seen in the following graph.

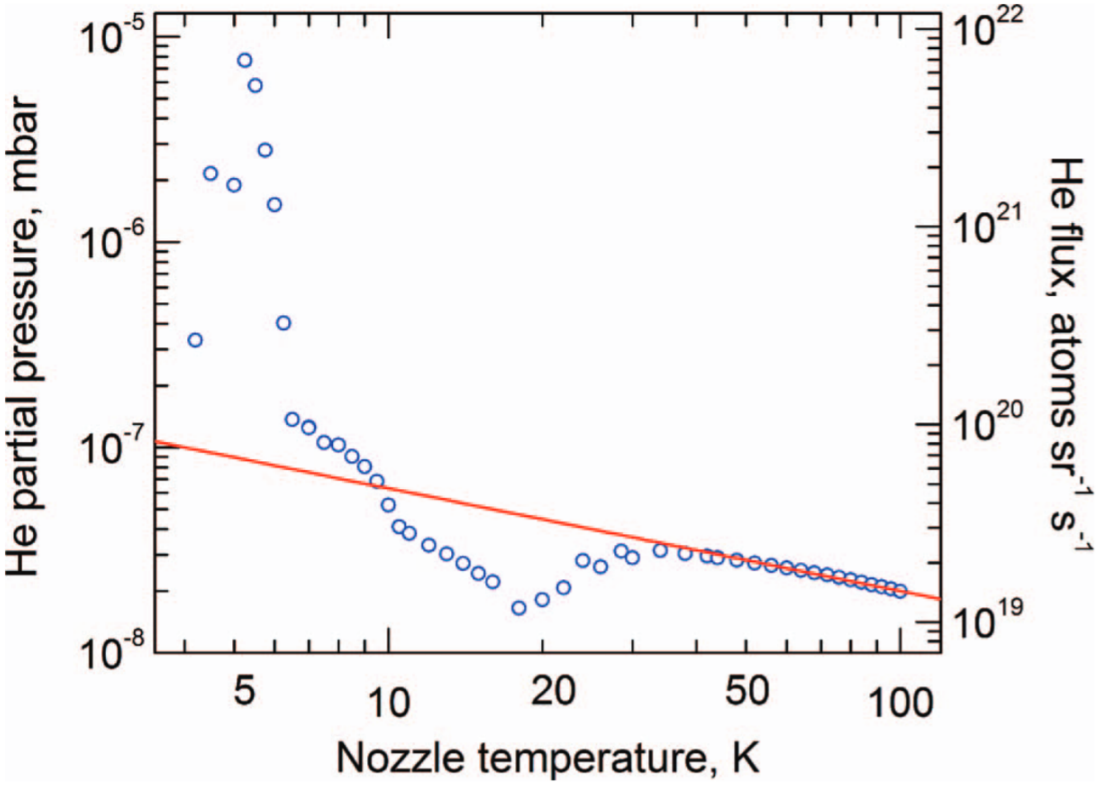

Figure A.21.: Temperature dependent He flux through a cooled nozzle (5 μm diameter) at 20 bar stagnation pressure. The red line symbolizes the theory for free jet expansion, which is no longer valid below $\approx$ 30 K. Reprinted with permission from [a]. Copyright 2011, AIP Publishing LLC.

[a] Gomez, L.F., Loginov, E., Sliter, R. & Vilesov A.F. Sizes of large He droplets *J. Chem. Phys* **135**, 154201 (2011)

C. Vapor Pressure Diagrams

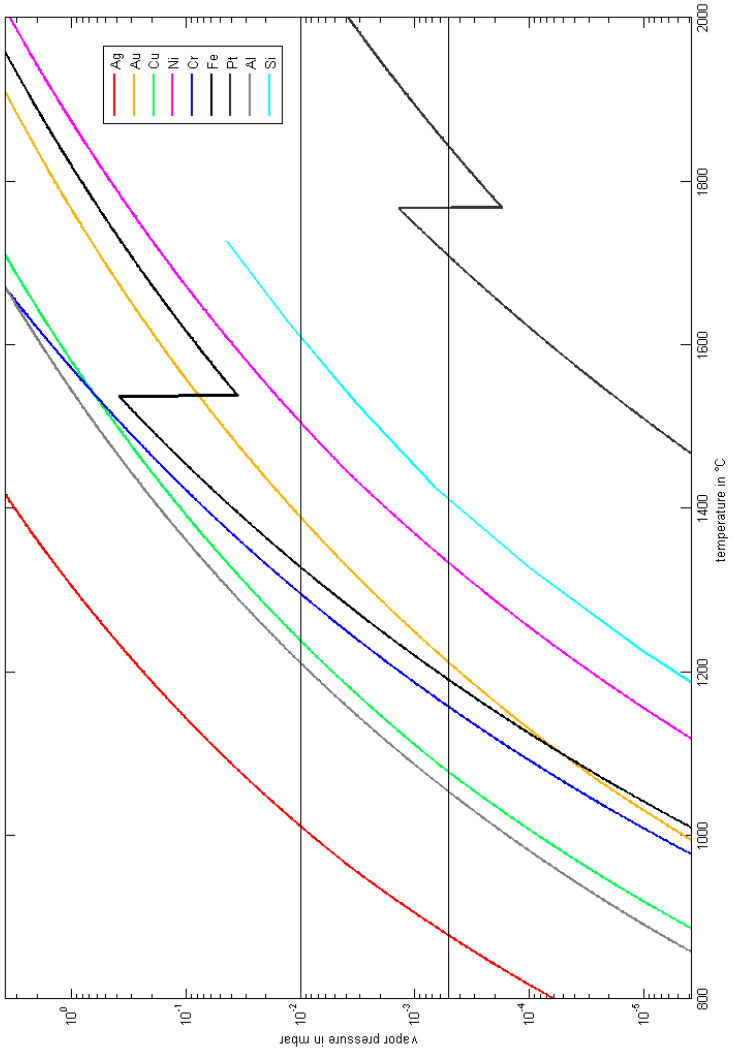

Figure A.22.: Temperature dependent vapor pressures for various materials (data taken from [a])

[a] Lide, D.R. (ed.), *CRC Handbook of Chemistry and Physics* (CRC Press, Boca Raton, FL, 1996), 77th edn.

D. Time of Flight - Checklist

Updated: May 2015

Checklist TOF

Start Up:

- Set the TOF-switch on the control-panel to “auto” (power supply) ☐
- Check pressure in TOF (≤ $5 \cdot 10^{-6}$mbar for 3 hours) and turn off the gauge ☐
- Check if preamplifier is disconnected ☐
- Turn the PC on, start the software ☐
- Check if the HV control knobs for MCP, post acc., liner and lens are at min. ☐
- Turn on the HV control units ☐
- Heat up the filament (-70eV and 2.2A as starting values), turn on the pulse generator, check the electrometer current (≥ µA) ☐
- Slowly increase the HV to operating conditions (values see table in manual) ☐
- Connect preamplifier ☐
- Optimize e.g. the OH peak (adjust central grid, deflection) ☐
- Calibrate / check calibration (are the residual gas peaks at the right positions?) ☐
- Measure ☐

Shut Down:

- Stop measurement, turn off pulse generator, turn off filament ☐
- Turn down HV for MCP, post acc., liner, lens, repeller and extraction ☐
- Turn off the HV control units, shut down the PC ☐
- Disconnect preamplifier ☐
- Turn on the pressure gauge ☐
- Set the TOF-switch on the control-panel to “off” (power supply) ☐

E. Reference: TOF Mass Spectra

The following pages contain exemplary spectra obtained on this machine in different experiments, each followed by a page listing the corresponding TOFMS settings.

The first spectrum shows a measurement of Xe-gas ($1.5 \cdot 10^{-6}$ mbar). Both singly and doubly ionized species are visible in the spectrum.

The second spectrum shows a measurement of undoped helium droplets at 8.0 K nozzle temperature and 20 bar stagnation pressure. In this measurement, the He_N-comb is visible until $\approx$ 500 amu. The missing signal below $\approx$ 40 amu is caused by the mass filter, which kicks out the frequently occurring light ions in order to avoid saturation of the detector. The zoomed spectrum nicely shows that there is no other significant signal except for the He_N.

The third spectrum shows a measurement of silver doped helium droplets at 9.5 K nozzle temperature and 20 bar stagnation pressure. In this measurement not only bare silver clusters (Ag_n) but also silver clusters with 1-3 H_2O molecules attached ($Ag_n(H_2O)_m$) can be seen, as well as the typical multinomial peak distribution at a specific Ag_n, which is caused by the different naturally occurring silver isotopes.

The fourth spectrum shows a measurement of gold doped helium droplets at 9.0 K nozzle temperature and 20 bar stagnation pressure. In contrast to many other elements, gold possesses only a single stable isotope and hence, a specific Au_n only yields a single peak in the mass spectrum. The small peaks in the zoomed spectrum belong to bare He_N. Additionally, a very small signal can be seen at (Au_3He_m with m = [1, 2, 3]).

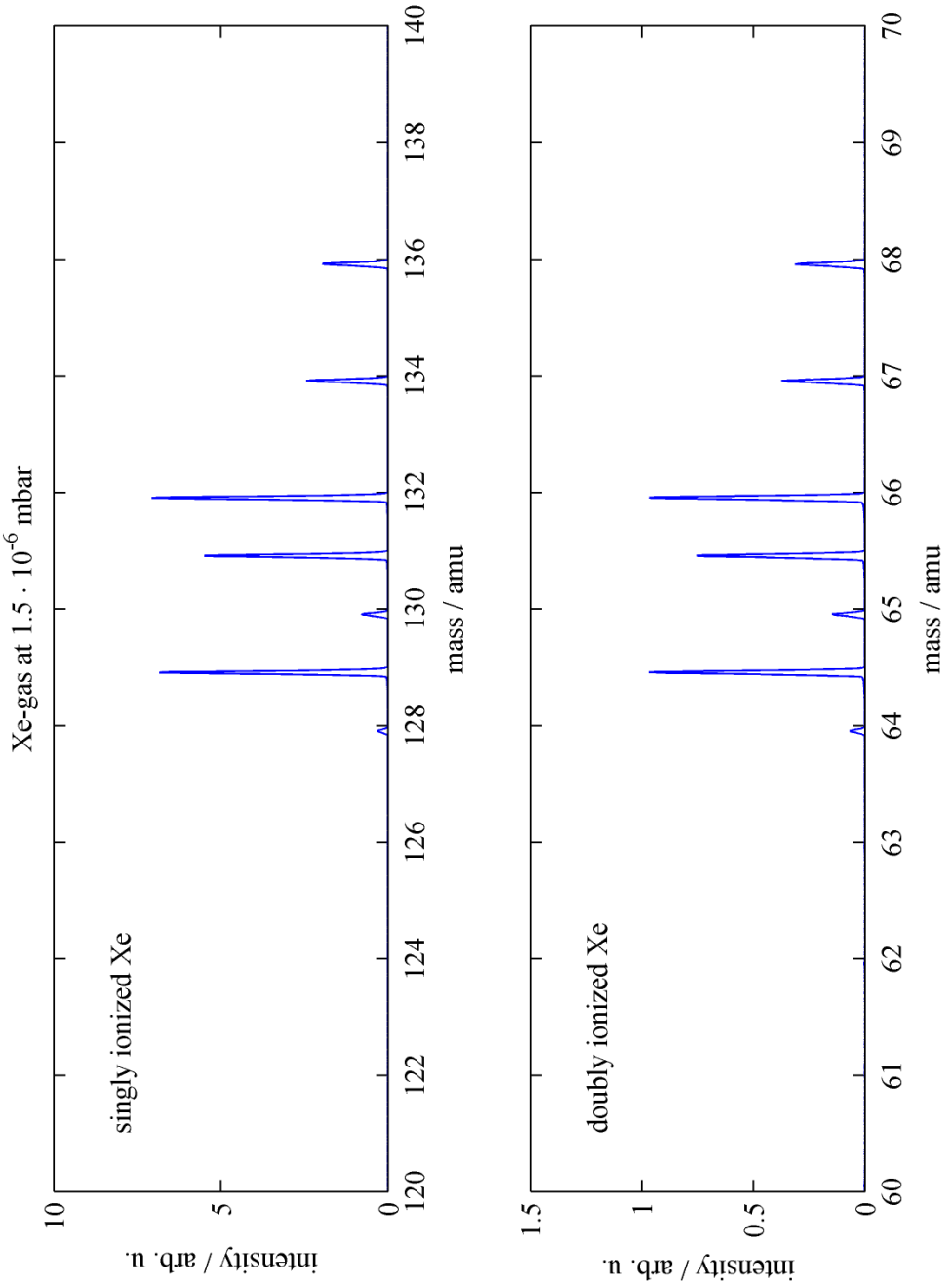
Xe-gas at 1.5 · 10^-6 mbar
singly ionized Xe
intensity / arb. u.
mass / amu
doubly ionized Xe
intensity / arb. u.
mass / amu

Xe - spectrum

bin width=1,000000

sweeps=2000000,000000

time resolution (ps)=250,000000

electron energy (eV)=70,00

frequency (Hz)=10000

duration electron beaml[µs]= 1,000

delay ion extraction / ionisation[µs]= 0,000

duration ion extraction[µs]= 2,000

heating current=2,011450

electrometer current=0,319989

emission current=0,151001

repeller=2,831053

extraction=2,817410

postacceleration=19,911194

MCP=2,204163

last_grid=0,337158

central_grid=0,890808

lens=2,968750

liner=3,015137

deflect_X(+)=2,962036

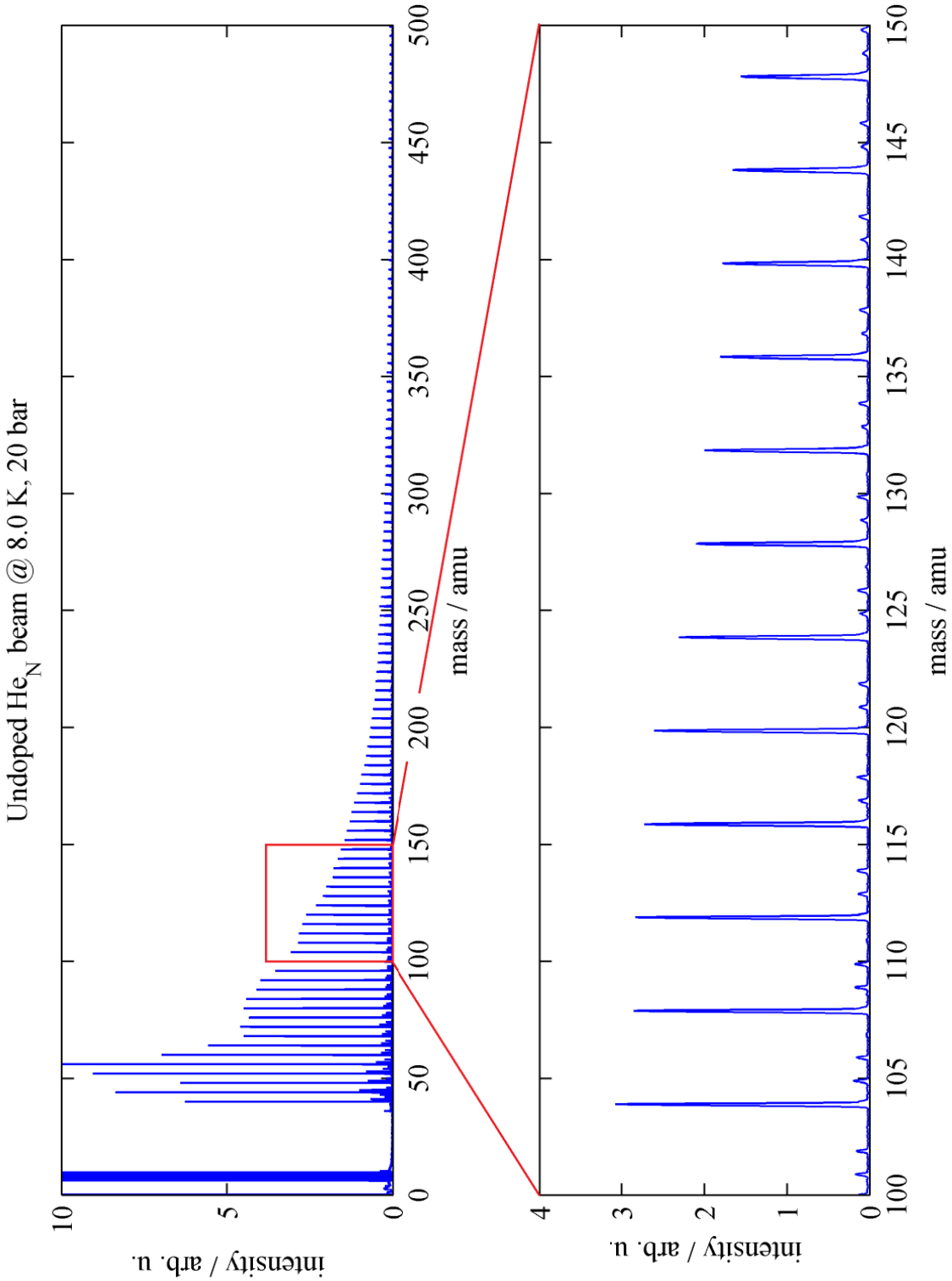
Undoped He_N beam @ 8.0 K, 20 bar
intensity / arb. u.
mass / amu
0
5
10
0
50
100
150
200
250
300
350
400
450
500
intensity / arb. u.
mass / amu
0
1
2
3
4
100
105
110
115
120
125
130
135
140
145
150

He_N - spectrum

bin width=4,000000

sweeps=1000000,000000

time resolution (ps)=250,000000

electron energy (eV)=89,00

frequency (Hz)=4000

duration electron beaml[µs]= 20,000

delay ion extraction / ionisation[µs]= 0,000

duration ion extraction[µs]= 3,000

delay mass filter / ion extraction[µs]= 0,000

duration mass filter[µs]= 3,000

heating current=2,274829

electrometer current=4,075931

emission current=0,612427

repeller=4,511014

extraction=4,481299

postacceleration=19,868469

MCP=2,805618

last_grid=1,114624

central_grid=2,256775

lens=8,021851

liner=8,019409

mass_filter=0,498779

deflect_X(+)=8,247681

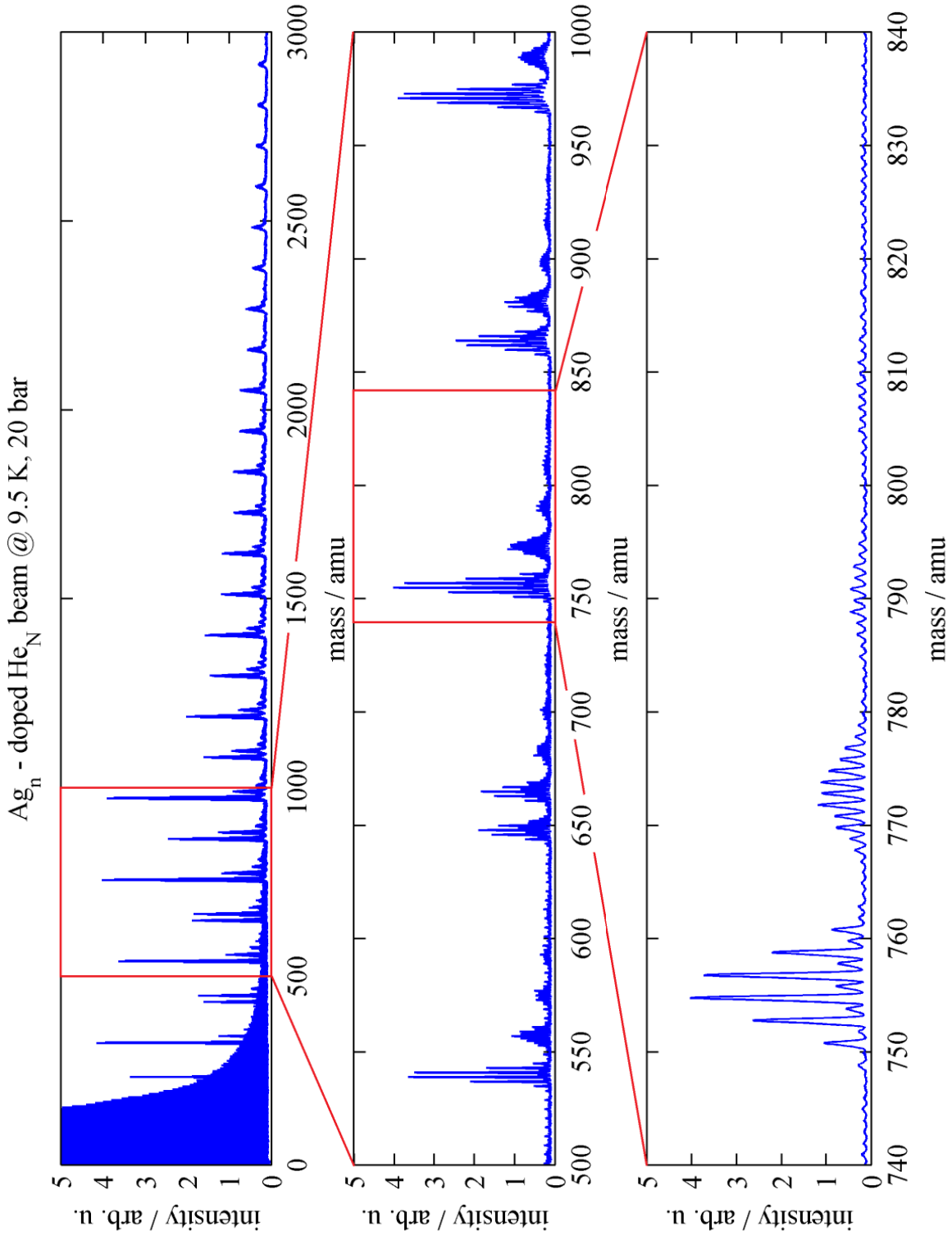
Ag$_n$ - doped He$_N$ beam @ 9.5 K, 20 bar
intensity / arb. u.
mass / amu
0
1
2
3
4
5
500
1000
1500
2000
2500
3000
550
600
650
700
750
800
850
900
950
1000
740
750
760
770
780
790
800
810
820
830
840

Ag_n - spectrum

bin width=2,000000

sweeps=10000000,000000

time resolution (ps)=250,000000

electron energy (eV)=89,00

frequency (Hz)=7000

duration electron beaml[µs]= 1,000

delay ion extraction / ionisation[µs]= 0,000

duration ion extraction[µs]= 3,000

heating current=2,143848

electrometer current=0,608231

emission current=0,398560

repeller=2,832413

extraction=2,794830

postacceleration=19,861603

MCP=2,502380

last_grid=1,385254

central_grid=2,115784

lens=8,013916

liner=8,024902

deflect_X(+)=8,043213

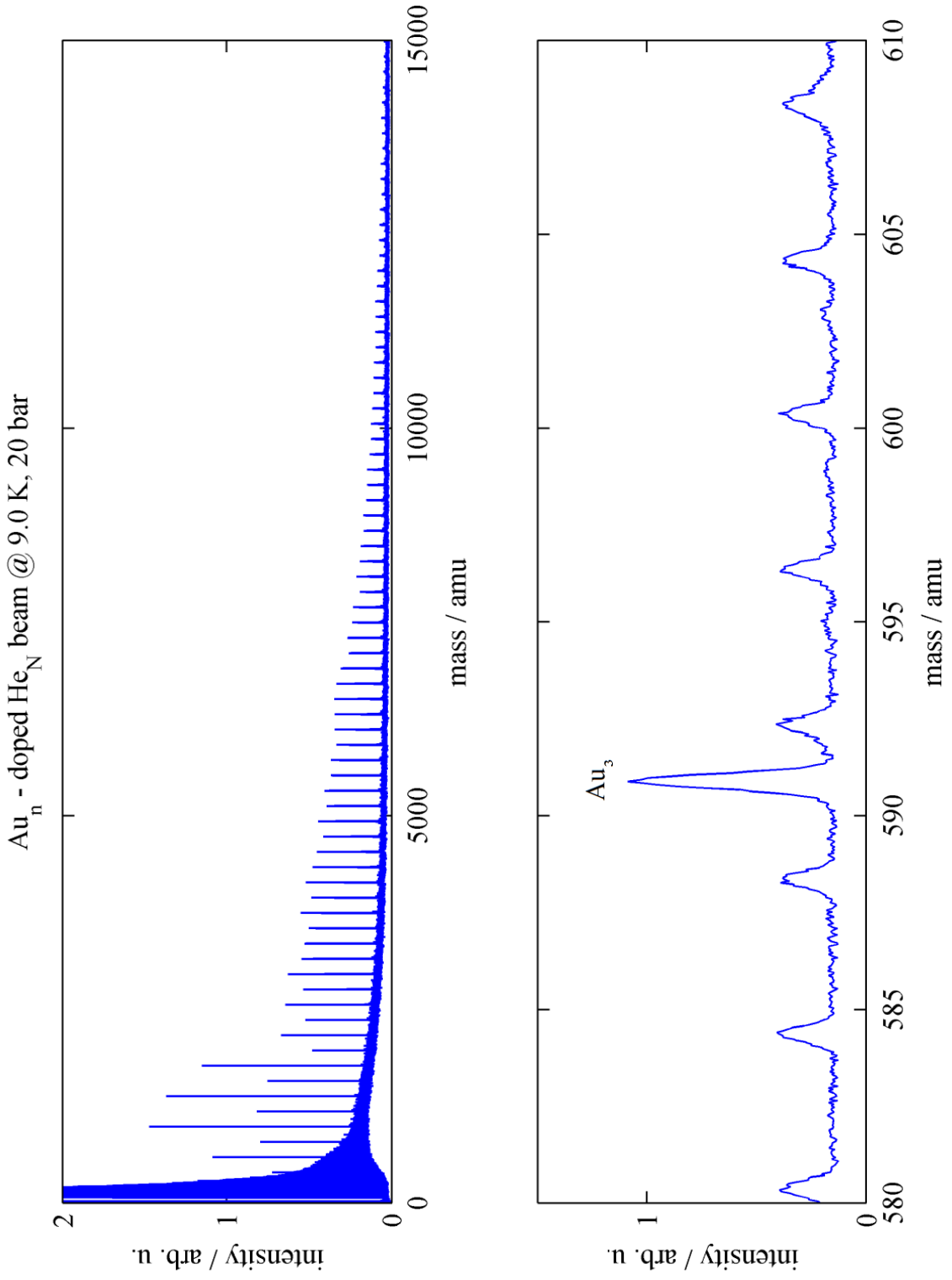
Au_n - doped He_N beam @ 9.0 K, 20 bar
intensity / arb. u.
mass / amu
0
5000
10000
15000
0
1
2
Au_3
intensity / arb. u.
mass / amu
580
585
590
595
600
605
610
0
1

Au_n - spectrum

bin width=4,000000

sweeps=2000000,000000

time resolution (ps)=250,000000

electron energy (eV)=89,00

ramp voltage (V)= 9,99

frequency (Hz)=5000

duration electron beaml[µs]= 20,000

delay ion extraction / ionisation[µs]= 0,000

duration ion extraction[µs]= 5,000

delay mass filter / ion extraction[µs]= 0,000

duration mass filter[µs]= 4,000

heating current=2,491745

electrometer current=3,096161

emission current=0,823486

repeller=4,507388

extraction=4,488626

postacceleration=19,857788

MCP=2,710770

last_grid=1,113647

central_grid=2,283691

lens=8,023682

liner=8,019409

mass_filter=0,499603

deflect_X(+)=8,211670

F. UHV-Suitcase Operating Instructions

UHV – Suitcase: Operating Instructions

1. Controller:

Check if the ion-pump is connected before starting the controller. In order to start the controller, press the start-button (red) for 5 seconds.

The display on the ion-getter-pump controller reads the ion-current in µA. An ion-current of 1 µA corresponds to about 10^{-8} mbar. A display reading of ".000" indicates underrange (< 10^{-11} mbar), a reading of "1." indicates overrange.

If the pressure is higher than 10^{-9} mbar check for the cause! NEG-activation and bakeout might be necessary.

If the display signals overrange ("1."), ***turn off the controller*** - press the off-button (black) for 5 seconds (wait 1 minute before disconnecting any cables) and consult the manual!

2. Standby mode:

When not in use, the UHV-Suitcase should always be kept under vacuum conditions, the lower the baseline pressure, the better. In order to remain UHV conditions in the suitcase:

- ***Keep the ion-getter-pump running*** → the manufacturer guarantees 50.000 hours of operation at 10^{-7} mbar → as the vacuum in the suitcase in standby will be much better, the ion-pump will last forever.
- ***Ensure that there is fore-vacuum pressure (5 mbar or better) at the atmospheric side of the gate-valve*** in order to reduce air diffusion through the rubber sealing of the valve. When using the buffer container provided by the manufacturer, renew the vacuum in the buffer every now and then.

Check the vacuum conditions regularly → the ion-current of the ion-pump is proportional to the pressure inside the suitcase

3. Battery mode:

Before switching to battery mode:

- ***Check the pressure in the suitcase*** → low pressure/ion current necessary for battery runtime and reliable pumping
- ***Ensure that there is fore-vacuum pressure (5 mbar or better) at the atmospheric side of the gate-valve*** in order to reduce air diffusion through the rubber sealing of the valve. When using a buffer container → renew the vacuum in the buffer
- **Ensure that the battery was charged for 8 hours**

In order to switch to battery operation, simply pull the power plug. Battery specifications are 55 hours operation @ 5 µA, battery life span is 1000 cycles. The battery should not be operated outside a 0°C to 40°C window. About 3 hours before the battery runs out of power, the controller will start beeping and the red led turns on.

UHV – Suitcase: Operating Instructions

4. Connecting to and disconnecting from a host UHV system:

Install a turbo-pumped T-piece (lock chamber) between the valve of the host system and the valve of the UHV-suitcase. ***Ensure that the UHV-suitcase is properly aligned and supported by a suitable structure***.

Before opening any valves, pump down the lock chamber to sufficiently low vacuum level (depending on the sensitivity of the samples).

Open the gate valve to the lock chamber and recheck the reading of the ion-pump controller. If the reading is as expected, the valve to the host system can be opened and the sample transfer can be started.

Always retract the wobble-stick after use and close both gate valves.

Check that both valves are firmly closed before starting the disconnection procedure. Then, switch off the vacuum system of the lock chamber, vent the chamber and open the CF40 connection.

Reattach the buffer volume at the atmospheric side of the gate-valve and evacuate the buffer volume to fore-vacuum pressure (5 mbar or better) in order to reduce air diffusion through the rubber sealing of the valve.

5. NEG activation and bakeout:

Activation is necessary after venting or if the pumping speed falls below acceptable limits.

Establish a connection to a turbo-pump, e.g. by using the lock chamber and pump down to vacuum conditions better than $1 \cdot 10^{-6}$ mbar; the ***pressure must be better than $5 \cdot 10^{-5}$ mbar at all times*** during the activation and bakeout. Make sure that the gate valve is open and the ion-pump is turned off during activation and bakeout.

Connect the silicone cable (banana plugs → use a standard lab power supply) for activation of the NEG.

(Re-)activate the NEG before starting the bakeout: 4.8 A for 60 minutes. ***Maximum current: 5 A***

Follow a typical bakeout procedure (heating cords, etc.) but do not exceed 150°C (magnetic manipulators).

Flash the NEG during the cooldown (@ ≈ 80°C) → 3.6 V | 2.5 A for 30 minutes.

Turn the ion-pump back on and close the gate valve, but keep the turbo connected and running until the ultimate pressure is reached (24 h).

6. Venting / pumpdown after venting

If not absolutely necessary, avoid venting the UHV-suitcase. Especially contact with oxygen and humidity is harmful for the NEG. However, the manufacturer guarantees 100 regeneration cycles of the NEG when venting with dry nitrogen. For the venting- and pumpdown-procedures consult the manual!

Danksagung

Eine Dissertation im Fach der Experimentalphysik stellt ein Projekt dar, welches nicht ohne maßgebliche Hilfe durch andere Personen erfolgreich sein kann. Ich möchte hier die Gelegenheit nutzen, um mich bei all jenen zu bedanken, welche mir über den gesamten Zeitraum meiner Arbeit immer wieder mit Rat und Tat zur Seite gestanden haben.
Meinem Betreuer *Prof. Wolfgang E. Ernst* danke ich für die Möglichkeit dieses spannende Projekt mitzugestalten. Obwohl der persönliche wissenschaftliche Freiraum nie zu kurz kam, stand er mir bei etwaigen Fragen jederzeit mit seiner Expertise zur Verfügung.
Andreas W. Hauser, *Markus Koch* und *Florian Lackner* haben sich trotz der dadurch entstehenden Belastung ihrer zeitlichen Ressourcen immer bereitwillig meiner Probleme angenommen. Hierfür und für die vielen freundschaftlichen Gespräche abseits der Wissenschaft möchte ich mich herzlich bedanken.
Meinen Kollegen *Johannes Steurer* und *Philipp Thaler* danke ich für die fruchtbare Zusammenarbeit im Zuge des Laboraufbaus.
Weiters gilt mein besonderer Dank den Mitarbeitern der institutseigenen Werstätten *Reinhard Dämon*, *Josef Friedrich*, *Werner Luttenberger*, *Rupert Maierhofer* und *Uwe Seidl* für die äußerst zeitnahe Fertigung aller benötigten Komponenten und die bereitwillige Unterstützung in unzähligen Fragen welche bei der Neueinrichtung eines Labors naturgemäß auftreten. Ohne sie wäre der Versuchsaufbau in der vorliegenden Form nicht möglich gewesen.
Bei den Mitarbeiterinnen des Sekretariats *Sandra Brunner*, *Bettina Gsöls-Bedenik* und *Elisabeth Weiß* sowie bei *Josef Pichler* bedanke ich mich für die Unterstützung in allen organisatorischen Fragen. Allen anderen Kollegen am Institut für Experimentalphysik danke ich für das freundliche Arbeitsumfeld, welches sich so in dieser Form wohl schwer anderswo finden lassen wird.
Mein ganz besonderer Dank gilt meinen Eltern *Beatrix* und *Franz*, welche mich nicht nur in der Zeit des Diplomstudiums sondern bis zum heutigen Tag in allen Belangen des Lebens unterstützt haben. Ebenso danke ich der besten kleinen Schwester der Welt *Alena* dafür, dass sie da ist wenn ich sie brauche.
Meinen Kindern *Johannes* und *Valentina* möchte ich für all jene Momente danken, in denen ich die wahre Schönheit des Entdeckens und Lernens mit ihnen teilen konnte. Öfter als einmal habt ihr mir die Unbedeutsamkeit meiner Zweifel vor Augen geführt.
Bei dir, liebe *Michaela*, bedanke ich mich für den Rückhalt den du mir gibst. Auch wenn es in der finalen Phase dieser Doktorarbeit nicht immer den Anschein erweckt haben mag, so bin ich doch nirgendwo lieber als an deiner Seite.